The Devil is in the Details:

Tailoring All-Inorganic Perovskite Nanocrystals for Novel Perspectives in Optoelectronic Devices

Dissertation

der Mathematisch-Naturwissenschaftlichen Fakultät

der Eberhard Karls Universität Tübingen

zur Erlangung des Grades eines

Doktors der Naturwissenschaften

(Dr. rer. nat.)

vorgelegt von

Jan Christoph Wahl

aus Reutlingen

Tübingen

2022

Gedruckt mit Genehmigung der Mathematisch-Naturwissenschaftlichen Fakultät der Eberhard Karls Universität Tübingen.

Tag der mündlichen Prüfung:	01.09.2022
Dekan:	Prof. Dr. Thilo Stehle
1. Berichterstatter:	Prof. Dr. Marcus Scheele
2. Berichterstatter:	Prof. Dr. Reinhold Fink

This dissertation was prepared in the time from November 2018 to March 2022 in the group of Prof. Dr. Marcus Scheele at the Institute for Physical and Theoretical Chemistry at the Eberhard Karls University Tübingen.

“Any sufficiently advanced technology is indistinguishable from magic.”

Arthur Clarke in

“Profiles of the Future: An Inquiry into the Limits of the Possible” (1962)

This page was intentionally

left blank.

Abstract

Within this cumulative dissertation the perspectives of all-inorganic caesium lead halide perovskites for novel applications in electroluminescent light emitting devices is investigated. The urge to increase the efficiency and stability of this material for devices is one of the most focused research topics in recent years. Especially the field of nanoscience offers completely novel approaches to functionalizing perovskites, and these will herein be exploited to optimize the system. The main focus will be on tailoring the ligand shell to control the properties of the nanocrystals. The underlying scientific phenomena will be investigated and utilized for more efficient light emitting devices.

Firstly, the underestimated aspect of structure in a nanocrystalline assembly will be discussed. By X-ray nanodiffraction the structural coherence of nanocrystals inside a superlattice was investigated. The experiments revealed an increasing distortion upon approaching the edges of the superstructure, which could be correlated to a significant hypsochromic shift of the photoluminescence signal. An increasing strain, induced by disorder, could be held responsible for the shift in luminance. These findings emphasize the importance of structure for the application of perovskites in a device as the preparation of structurally sound emitter layers emerged as a determining factor for the emitted light.

Subsequently, the ligand shell of the nanocrystals came into focus, because the dynamics on a particle surface are of uttermost importance when considering exchange reactions and solution processed fabrication of thin films. To reveal the dynamics, quasielastic neutron scattering and nuclear magnetic resonance experiments were conducted and combined. They revealed a highly dynamic surface equilibrium for nanocrystals functionalized with a zwitterionic surface ligand. Notably, the dynamics and morphology appeared to be tunable with the absolute ligand concentration. This could be explained by investigating the surface binding situation *via* small angle scattering methods. The zwitterionic character exhibited two possible scenarios, in which either one or both respective functional group(s) is tethered to the particle surface. This drastically affected the surface dynamics, in means of a tunable Fickian diffusion coefficient of the ligand.

During the logical next step, the native ligand shell of perovskites was exchanged with an accordingly functionalized organic semiconductor. The novel ligand partially compensated the surface dipole of the nanocrystal, which effectively lowered the charging energy. This facilitated the charge carrier injection and resulted in a significantly lower electronic resistance. These coupled organic-inorganic nanostructures could be successfully deployed in an electroluminescent light emitting device with increased efficiency.

Lastly, the stability of this novel material was probed because perovskites are intrinsically rather unstable towards external influences. By X-ray photoelectron spectroscopy, the decomposition mechanism of the particles enclosed in the native and exchanged ligand shell was determined. In the native case, the decay into the respective halide salts could be observed. However, the exchanged system

exhibited an increased stability, in terms of a slower decomposition, and a different decay mechanism, *i.e.*, a disproportionation of Pb^{2+} into Pb^{0} and Pb^{3+}. The underlying phenomenon was again the stabilization through the partially compensated surface dipole. Additionally, it was found that a lattice contraction, induced by halide segregation, preceded the decay and likely also initiated it.

In summary, this thesis provides experimental evidence for novel approaches to functionalize perovskite nanocrystals for an optimized application in light emitting devices in terms of enhanced stability, electrical, and optical properties.

Deutsche Zusammenfassung

Im Zuge dieser kumulativen Dissertation werden die Möglichkeiten von anorganischen Cäsium Blei Halogenid Perowskiten für neuartige Anwendungen im Bereich von elektrolumineszenten Leuchtdioden untersucht. Der Wunsch verbesserte Effizienzen und Stabilitäten dieses Materials zu erreichen ist eines der am meisten fokussierten Forschungsfelder der letzten Jahre. Im Besonderen bieten die Nanowissenschaften vollständig neue Ansätze Perowskite zu funktionalisieren, diese sollen im Rahmen dieser Arbeit genutzt werden, um das System zu optimieren. Der Hauptfokus liegt auf der spezifischen Anpassung der Ligandenhülle um die Eigenschaften der Nanopartikel zu kontrollieren. Die grundlegenden wissenschaftlichen Phänomene werden untersucht und für die Herstellung effizienterer Leuchtdioden genutzt.

Zuallererst wird der unterschätzte Aspekt der Struktur eines nanokristallinen Übergitters diskutiert. Mittels Röntgennanostreuung wurde die Kohärenz der Struktur in einem Übergitter untersucht. Die Experimente zeigten eine zunehmende Störung der Struktur je näher man der Kante des Übergitters kam, was mit einer deutlichen hypsochromen Verschiebung des Photolumineszenzspektrums korreliert werden konnte. Zunehmende Spannung, welche durch die Unordnung induziert wurde, konnte für die Verschiebung in der Lumineszenz verantwortlich gemacht werden. Diese Ergebnisse heben die Wichtigkeit der Struktur für die Anwendung von Perowskiten in Dioden hervor, da die Herstellung von strukturell hochwertigen Emitterfilmen als ein bestimmender Faktor für die Emission zutage trat.

Nachfolgend rückte die Ligandenhülle der Nanokristalle in den Fokus, da die Dynamik auf einer Partikeloberfläche von höchster Wichtigkeit für Austauschreaktionen und nasschemisch prozessierte Dünnfilme ist. Um die Dynamik zu untersuchen wurden quasielastische Neutronenstreuung und Kernspinresonanzspektroskopie durchgeführt und kombiniert. Diese deckten ein hochdynamisches Oberflächengleichgewicht der zwitterionischen Liganden, welche die Nanokristalle funktionalisierten, auf. Bemerkenswerterweise schienen die Dynamik und Morphologie mit der Ligandenkonzentration anpassbar zu sein. Dies konnte mit der Untersuchung der Oberflächenbindungssituation mittels Kleinwinkelstreuung erklärt werden. Der zwitterionische Charakter ermöglichte zwei mögliche Szenarien, in welchen entweder eine oder beide funktionelle Gruppe(n) an die Partikeloberfläche

gebunden sind. Hierdurch wird die Oberflächendynamik drastisch beeinflusst, und zwar in diesem Sinne, dass der Fick´sche Diffusionskoeffizient des Liganden veränderbar ist.

Während des nächsten logischen Schrittes wurde die ursprüngliche Ligandenhülle der Perowskite durch einen entsprechend funktionalisierten organischen Halbleiter ausgetauscht. Der neue Ligand konnte den Oberflächendipol des Nanokristalls teilweise kompensieren, was effektiv die Coulomb-Blockade verringerte. Das erleichtert die Ladungsträgerinjektion und resultiert in einem deutlich niedrigeren elektrischen Widerstand. Diese gekoppelten organisch-anorganischen Nanostrukturen konnten erfolgreich in einem elektrolumineszenten Bauteil mit erhöhter Effizienz eingebaut werden.

Zuletzt wurde die Stabilität des neuen Materials untersucht da Perowskite von Natur aus instabil gegenüber externen Einflüssen sind. Mittels Röntgenphotoelektronenspektroskopie wurde der Zersetzungsmechanismus der Partikel, mit nativer und ausgetauschter Ligandenhülle, bestimmt. Im ursprünglichen Falle wurde der Zerfall in die zugehörigen Halogenidsalze beobachtet. Das ausgetauschte System dahingegen zeigte eine verbesserte Stabilität, im Sinne einer langsameren Zersetzung, sowie einen alternativen Zerfallsmechanismus, in Form einer Disproportionierung von Pb^{2+} zu Pb^{0} und Pb^{3+}. Das zugrundeliegende Phänomen war abermals eine Stabilisierung durch den teilweise kompensierten Oberflächendipol. Zusätzlich wurde eine Gitterkontraktion beobachtet, welche durch Halogenidsegregation induziert wurde, die dem Zerfall vorausging und diesen möglicherweise auch initiiert.

Zusammenfassend liefert diese Dissertation experimentelle Belege für neue Ansätze der Funktionalisierung von Perowskitnanokristallen um diese in optimierten Leuchtdioden anzuwenden, genauer mit verbesserter Stabilität, elektrischen und optischen Eigenschaften.

This page was intentionally

left blank.

Table of Contents

1. Introduction

The development of semiconductor-based materials for almost every aspect of modern life has experienced increasing interest for over more than half a century. Semiconductors are used in every electronic device, computers, smartphones, TVs, and solar cells. The everyday life is increasingly shifted onto a digital world in terms of remote meetings (particularly during the COVID pandemic), cryptocurrency and banking, or information access and social media. [1,2] Therefore, the importance of semiconductors is undeniable, and they have become one of the most valuable trading goods in modern times. [3] The impact of processor chips is so striking that preventing access to this technology is even considered a sanction nowadays. [4] Semiconducting materials, as every other resource, are finite and thus the technological development turned towards scaling down the components to maximize their use. However, below a certain size classical industrial and scientific approaches fail to continue this trend and at this point nanotechnology enters the stage. Nanotechnology considers all natural and engineering sciences of materials with at least one dimension below 100 nm ($100 \cdot 10^{-9}$ m), so-called nanomaterials. [5] A prominent example for this trend is Moore´s law which states that the transistor count per circuit doubles every second year. [6] The downsizing of finite or rare materials can also contribute to mitigating the climate change because less resources need to be mined, energy storage capabilities might be increased, CO_2 output might be reduced / mitigated. [7,8] Additionally, tailoring nanomaterials to specific purposes holds the potential to increase the efficiency of devices beyond the limit of macroscopic analogues which could potentially reduce energy consumption. [9]

Especially nanomaterial-based optoelectronic applications like solar cells, light emitting diodes (LED), or optical switches, which rely heavily on semiconducting materials, are increasingly shifted into the focus of optimization. [9–11]

1.1. Motivation

Recent challenges in the field of LEDs are of different origins. The color gamut of devices is a crucial factor, which can be best described by the Commission Internationale de l´Éclairage (CIE) 1931 color scheme. [12] A preferably complete coverage of the visible spectrum is desirable, because images displayed are substantially gaining in color variety. **Figure 1.1 c** compares different LED techniques with respect to their accessible color gamut and shows the potential of QD-based system, which cover a significantly larger portion of the CIE color scheme. [13] Furthermore, the synthetic approaches and materials for the used nanomaterials are crucial since the homogeneity is determined by them. A smaller size distribution leads to more distinct emission peaks and less parasitic emission, which can

be observed as an increased color intensity of the display. [14] Another significant problem of QD-based systems, besides the colored pixels, is the depiction of true black. Currently only organic LEDs are capable of displaying these. [15] Additionally, LEDs on quantum dot (QDLED) basis currently require to be excited by an external light source, typically located behind the actual display (**Figure 1.1 a + b**). [16] The emission process in this setup is therefore a two-step process, which obviously must consider efficiencies during each step. State-of-the-art QLED TVs currently reach external quantum efficiencies of 20.5 %, 21 % and 19.8 % for red, green, and blue pixels, respectively. [17] A highly desired approach is to prepare electroluminescent quantum dot (0-dimensional nanomaterial) LEDs (ELQLED), because of several advantages over their already existing analogue. [16,18] Such ELQLEDs would no longer require the backlight LED to excite the QD emission layer and thus the efficiency might be increased to higher magnitudes, as the charge injection can be shifted onto the QD layer itself (*cf.* **Figure 1.1 b**).

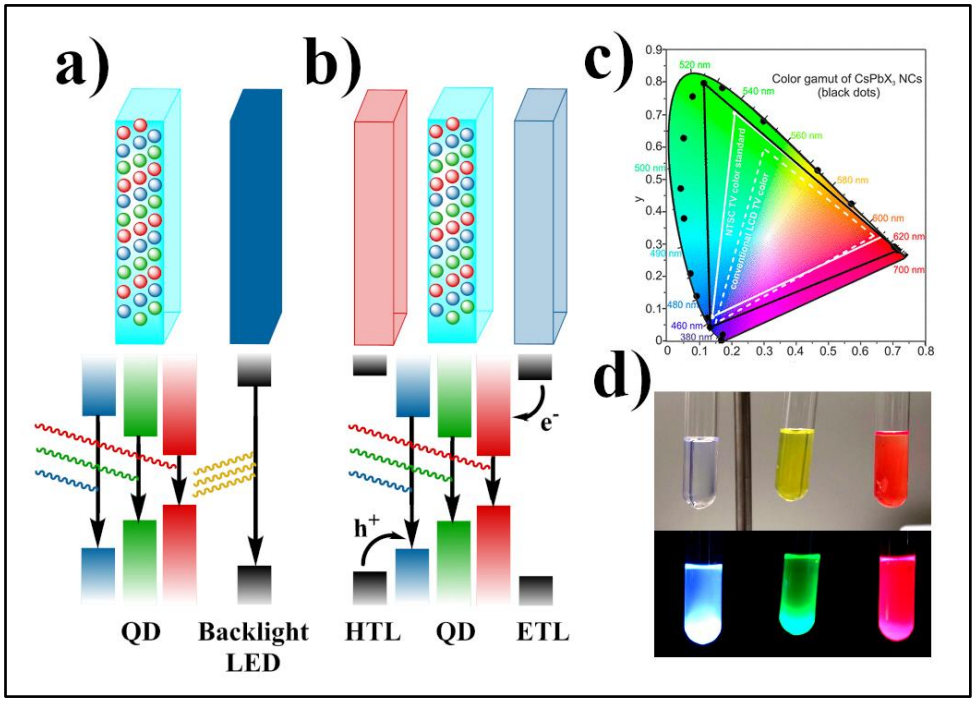

Figure 1.1: a) Working principle of a QDLED with the backlight LED on the right (blue) used to excite the emission layer, containing the QDs. Light is emitted to excite the nanomaterial inside the emission layer, which in turn is responsible for the emission from the display. For generality, all required colors are shown, *i.e.*, red, blue, and green. b) Working principle of an ELQLED, the setup consists of a hole transmitting layer (HTL), electron transmitting layer (ETL), and a QD-containing emission layer. The holes and electrons are injected from the HTL and ETL, respectively. The recombination inside the QDs results in the emission of the display. c) Commission Internationale de l´Éclairage color scheme for different light emitting devices. A conventional liquid crystal TV (white dashed line), and the color gamut of perovskite QDs (black dots). The standard given by the National Television Systems Committee (NTSC) is shown as a white solid line. d) Images of perovskites nanoparticles in solution with emissions ranging over the complete visible spectrum, tunable by the stoichiometry. The top image is taken under ambient light and the bottom picture under UV light illumination. c) Reprinted with permission from Protesescu *et al.* [19] (https://pubs.acs.org/doi/10.1021/nl5048779) and partly edited, further permissions related to the material excerpted should be directed to the ACS.

Many approaches for materials have already been discussed in literature to prepare nanomaterials as efficient emitters in ELQLEDs, with a prominent example being indium phosphide / zinc sulfide (InP/ZnS) core-shell particles. [17,20] These nanoparticles were assembled in so-called coupled organic-inorganic nanostructures (COIN) and analyzed for their optoelectronic properties. [20–22] First results were obtained during the preceding master thesis, and additional experiments were carried out after its completion. [20] By choosing suitable ligands, *viz.* Ni-tetraaminophthalocyanine (Ni4APc) and Zn-tetracarboxyphenylporphyrin (tZnTPP) it was possible to prepare selectively electron and hole conductive thin films, respectively (**Figure 1.2 a**). [20] However, by measuring cyclic voltammetry on the samples it was found that the charge injection could not be realized into the InP core, but into the ZnS shell (**Figure 1.2 b + c**). This can be rationalized by the existence of deep traps in InP, where they are present in larger quantities compared to other materials like cadmium selenide (CdSe). [23] The trap states result in a significantly lower electron transfer rate onto the InP nanoparticle, indicating the difficulty of charge carrier injection (**Figure 1.2 d**). [23] The results for InP strongly suggest changing to a material with a high defect tolerance and better charge carrier screening to prevent the negative influences of trap states in the particle and achieve a better charge carrier injection.

The above arguments demonstrated two major challenges that are significant for the preparation of efficient ELQLEDs, namely the color gamut (optical properties), and charge injection properties (electrical properties). A very promising class of materials to simultaneously tackle both issues are all-inorganic caesium lead halide perovskites. The color gamut of perovskite nanoparticles is extremely pure due to their high homogeneity, trap state tolerance, and high quantum yield. [19,24,25] This results in an almost complete coverage of the CIE color scheme (*cf.* **Figure 1.1 c**) with a very pure emission (**Figure 1.1 d**). [19] Additionally, the little trap state influence and outstanding optoelectronic properties result in good charge injection. This can be seen in ELQLEDs prepared with perovskites as an emitter layer. They reach external quantum efficiencies of 23.4 %, and 8.4 % (21.6 % for hybrid organic-inorganic lead halide perovskites) for green and red emitters, respectively. [26–29] These values are already comparable, or even exceeding, preexisting and optimized LEDs with other, more covalent, nanomaterials.

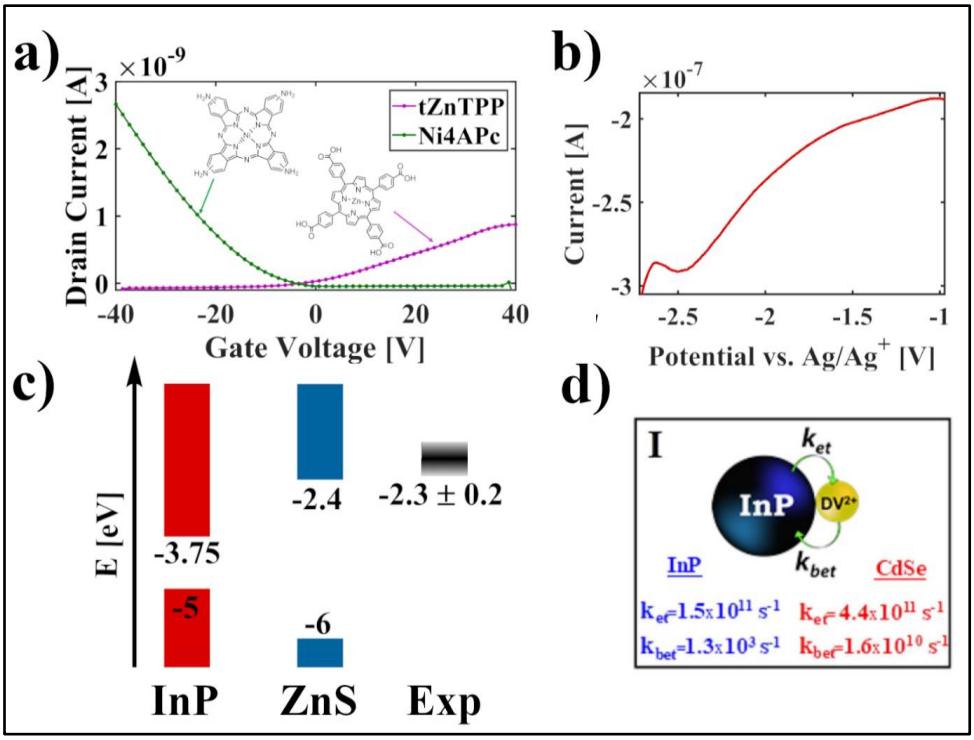

Figure 1.2: a) Field effect transistor measurements with varying gate voltage for investigated COIN systems based on InP/ZnS core-shell particles, functionalized with different ligands. The structures of the corresponding ligands are depicted as well. The voltage dependence for the two systems is different due to the majority carrier nature. In the case of Ni4APc holes and for tZnTPP electrons. The mobility of the respective carriers can be deduced from the slope of the current. [20,30] b) Differential pulse voltammetry (DPV) of InP/ZnS core-shell nanoparticles with their native ligand shell, *i.e.*, oleic acid. A feature at -2.5 V *vs.* a Silver reference electrode can be observed. The measurement is conducted in the reductive regime and thus the signal can be referred to the position of the conduction state. c) Absolute energy levels of InP, and ZnS against vacuum energy, all values are given in eV. The experimentally determined position by cyclic voltammetry (**Figure 1.2 b**) of the charge injection is given as well (Exp). d) Electron transfer rates for InP and CdSe nanoparticles. Two rates are given, where k_{et} is the electron transfer from the nanoparticle, *i.e.*, oxidation, and k_{bet} is the transfer into the particle, *i.e.*, reduction. The reduction rate for CdSe is drastically larger than for InP. [23] b) Cyclic voltammetry measurements conducted by Kai Wurst at the Institut für physikalische und theoretische Chemie (IPTC), Eberhard Karls University, Tübingen. d) Reprinted and edited with permission from Thomas *et al.* [23] Copyright 2018 American Chemical Society.

1.2. Aim and Outline of this Work

Within this work, the aforementioned all-inorganic perovskites are utilized to prepare nanoparticles for optimizing ELQLEDs. Within the framework of this thesis, the potential of nanoscale perovskites for the application in ELQLEDs will be focused. By utilizing nanomaterials many open challenges in the field of LED can be addressed in a unique and novel way. Precisely, the underlying principles of this material class are investigated and their impact on the optoelectronics analyzed. The findings can then provide an approach for improvement in the efficiency of devices.

Nanomaterials are chosen due to the broad possibilities of tuning the properties, exemplarily through their structural integrity, they exhibit interesting properties when it comes to self-assembly, which can be exploited to prepare highly ordered superstructures. Simultaneously, the structure influences the optoelectronics which can be used to further specialize the material. [31] In chapter 3 the impact of the superstructure on the optical properties of perovskite nanocrystals will be discussed. This is an often-underestimated aspect, however the material will be prepared as a solid-state layer in the device. Therefore, the interaction between adjacent particles can no longer be neglected and this can drastically alter the properties of the emitter layer. It will be shown that through misalignment of the particles a strain at the edges of superlattices is induced. The influence of such solid-state interactions on the emissive properties of NC ensembles will be investigated and discussed.

As one advantage of nanomaterials is their stabilization by ligands, which can be exchanged with molecules that induce desired properties to the material, the surface dynamics are of uttermost interest. [11,31–34] During chapter 4 the surface dynamics of perovskite nanoparticles will be revealed. Through knowledge of the ligand surface equilibrium, it is possible to manipulate the system in such a way that the dynamics might be exploited during ligand exchange reactions. Additionally, if thin films are prepared from solution the manipulation of said equilibrium becomes important, because ultimately the ligand density at the surface can be tuned which in turn affects the properties of the particles.

Subsequently, the native ligand shell on perovskite nanoparticles will be exchanged with an accordingly functionalized organic semiconductor and the implications on the optoelectronic properties investigated. By exchanging the native ligand shell, so-called coupled organic-inorganic nanostructures (COIN) are prepared. [21,22] Chapter 5 is focused on the revelation of ligand influence on the charge carrier injection. Underlying phenomena will be discussed and their implications on optoelectronic devices revealed.

Lastly, the stability of the novel material is probed because perovskites are already known to have little resistance against external influences and a low intrinsic stability. [35–39] A low stability when incorporated into a device is undesirable as it reduces the lifetime of the LED significantly. Therefore, the decomposition mechanism of the material under continuous X-ray radiation is revealed and a stabilization induced by the novel ligand shell (organic semiconductor) is measured. By suitably choosing a ligand and investigating the respective decay, the stability of such coupled, mesocrystalline materials possibly can be improved.

2. Theoretical Foundation and Methodology

2.1. Introduction to Perovskites

The widespread research interest on semiconducting materials recently extended to perovskites, a class of materials which excels in optoelectronic properties and is herein shortly introduced. The name perovskite comes from the mineral calcium titanate ($CaTiO_3$), which was first discovered by Gustav Rose in 1839 in the Ural Mountains and named after the Russian mineralogist Lew Perowski. [40,41] $CaTiO_3$ naturally occurs as simple cubic crystals (**Figure 2.1 a + b**), which defined the nomenclature for a whole class of materials with the same crystal structure. [25] The structure in detail is composed of [TiO_6] octahedra with a Ca atom located inside the octahedral gap (**Figure 2.1 a**), which was revealed by Tom Barth in 1925 after the Debye-Scherrer procedure, *i.e.*, X-ray diffraction, was discovered. [42] From geometrical considerations Viktor Goldschmidt formulated the so-called tolerance factor to estimate the crystal structure of ABX_3-type minerals. [43] The factor is calculated from the ratio of the corresponding ionic radii of the components (see **Equation (2.12)**), thus defining a mathematical approach to the definition of perovskites. The formula and implications will be discussed later (chapter 2.3). For a long time, perovskites were nothing more than a mere mineral, however in the 1940s the outstanding optoelectronic properties of perovskite materials initiated an enormous increase in research interest. [44] The focus already extended from oxygen containing materials to other classes, like metal halide-based perovskites (LHP), which will be the focus in this work. [45] An interesting particularity of LHPs is the high defect tolerance: they are very insensitive towards grain boundaries, vacancies, and dangling bonds. [46] This is rationalized by investigation of the electronic structure and taking molecular orbital (MO) theory considerations into account. The frontier states, *i.e.*, the valence and conduction bands or states, are composed of MOs provided by Pb and the halogenides. Universally, the lead 6p orbital interacts with the 3/4/5p-orbital of chloride, bromide, and iodide, respectively. From **Figure 2.1 c**, one can see that the atomic orbitals (AO) are located at energies outside the band gap of crystalline perovskite. This effectively means imperfections, in the form of vacancies or dangling bonds, which are due to AOs that are not coordinated with a respective partner, resulting in trap states not significantly interfering with the optoelectronic properties. [46] Nevertheless, if an antisite or interstitial defect is present, the formation of the bands is distorted due to the breaking of the periodicity, which even in LHPs results in the formation of deep traps. [46,47] However, this requires large energies of formation and thus these states are almost absent. [47] Upon comparing the perovskites with other semiconducting materials, it becomes obvious that many other materials have AOs located in the band gap, which results in trap states being located there. These traps states induce a recombination center for excitons, which drastically affects optoelectronics. Another unique property of LHPs is their nature as a crystalline liquid, which means a long-ranged order is present in the crystal but locally the ions are very mobile. [46,48] The high mobility can be used to exchange ions in

the material, resulting in a highly tunable stoichiometry, readily accessible by simple addition of halide salts. [49] The composition in turn affects the band gap, because the splitting of the MOs can be tuned by the usage of different halides. [46] The band gap is largest for chloride (~ 3 eV) and smallest for iodide (~ 1.8 eV) containing LHPs, which enables the tunability *via* stoichiometry of all values in between these boundaries. [50] Macroscopically, the high local mobility of ions can be observed in the form of ionic conductivity (LHPs are hybrid conductors), and the formation of large polarons, resulting in a highly effective screening of charge carriers and excitons. [48] The formation of polarons results in less scattering of the charge carriers on defect sites and optical phonons, which in turn increases the mobility and leads to a superior conductivity. [48]

The high charge carrier mobilities paired with a high defect tolerance are very interesting for a potential application in solar-cells and light emitting devices (LED). [51] Especially in solar-cells LHPs are expected to exhibit a remarkably high maximum photon energy utilization, which is defined by the ratio of open-circuit potential and the band gap. This value describes the efficiency of the energy conversion from light to electricity and reaches up to 70 % for LHPs. Other solar cells can have losses of up to 50 %. [52] On the other hand the high defect tolerance and high carrier mobilities appear to be very desirable properties for LEDs, as the external quantum efficiency can be drastically increased (*cf.* chapter 1.1).

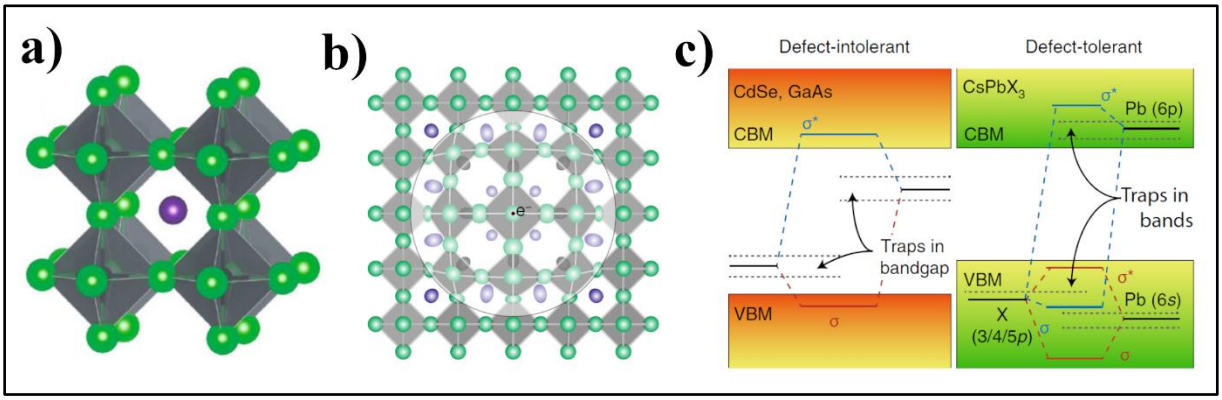

Figure 2.1: a) Crystal structure of perovskites, [BX_6] octahedra in grey. b) Screening in perovskite materials, the formation of a large polaron is indicated by the circle. c) MO Scheme of the electronic structure for a classical semiconductor material (left) and lead halide perovskites (right). Reprinted by permission from Akkerman *et al.*: Springer Nature, Nature Materials, Genesis, challenges, and opportunities for colloidal lead halide perovskite nanocrystals, Akkerman *et al.* [46], Nature materials (2018). Partly edited.

Besides the numerous advantages of LHPs, there are also downsides associated with the material. Most strikingly, the stability of perovskites against environmental influences, like oxygen, humidity, and radiation, is comparably low. [38,39] Additionally, as the material contains lead, the intrinsic toxicity can be considered an issue, depending on the desired application. [53]

The decomposition can be understood in different ways. On the one hand, the material can decay into the corresponding halide salts when exposed to water, heat, or extensive radiation (extrinsic

stability). [37–39] Exemplarily, the decay mechanism of all-inorganic perovskites ($CsPbX_3$) when exposed to X-ray radiation is shown in **Equation (2.1)**. The halogen salts are formed and subsequently the lead salts are even further degraded to elemental Pb and halogen. [37]

$$CsPbX_3 \rightarrow CsX + PbX_2 \rightarrow CsX + Pb^0 + X_2 \tag{2.1}$$

This decay can excellently be tracked by X-ray photoelectron spectroscopy which utilizes the external photoelectric effect to probe specific atoms in the solid. Therefore, the environment of specific electrons can effectively be measured, which can be used to track the dynamics of the decay. [36,37]

On the other hand, perovskites also exhibit a high degree of intrinsic instability, in terms of changes in the crystal structure and composition. [54,55] The phase transition enthalpy between cubic (or precisely pseudocubic) and orthorhombic perovskite phases is typically exceptionally low. [54,56] For $CsPbBrI_2$ exemplarily, the value for this transition equals to $\Delta H = 10.34 \frac{kJ}{mol}$, which only equals ~ $4\, k_B T$ at room temperature (further information can be found in chapter 2.4). [54] Another form of intrinsic instability occurs when the material is exposed to light. The halides are segregated upon exposing perovskites to light and this results in different phases being present at the grain boundaries and inside a grain. [55] This can be rationalized by the fact that a perovskite lattice can be considered an ionic liquid. [48]

LHPs by nature are already highly tunable, nevertheless the usage of nanomaterials (at least one dimension < 100 nm) enables the accessibility to additional tunable parameters. [5] Obviously, nanomaterials can be tuned in size, which alters the band in such a way that smaller nanoparticles exhibit a larger band gap than their macroscopic analogue. [57] Another interesting property, especially for LED applications, is the tunability of the transition dipole moment. By confining at least one of the dimensions the transition dipole moment is restricted to the dimensions of the crystal. [58] These two phenomena are outstanding examples of how nanoparticles can exhibit novel properties. Additionally, the ligand shell can be used to induce specific properties like a reduced charge injection energy by alignment of the energy levels of nanoparticle and ligand or an increased structural integrity by utilizing multidentate ligands. [31,33] The stability can also be increased by using sufficient ligands, in particular for perovskite nanocrystals this was shown to be dependent on the energy of repulsion, which in turn is dependent on the alkyl chain length of the molecule. [24] In sum it can already be seen that the unique properties of nanomaterials can be of great advantage. In the following chapters these concepts will be discussed in further detail.

2.2. Nanoparticle Synthesis

Generally, the synthesis of nanomaterials can be realized by two universal pathways, namely the bottom-up or top-down approach. [59,60] The latter utilizes mainly physical processes like milling, grinding, exfoliation, or arc furnaces to decompose macroscopic materials into smaller parts until finally reaching the nanometer regime. [60–63] The other process is the bottom-up synthesis, which appears more chemical in its nature as it utilizes molecular precursors which are used in a chemical reaction to synthesize nanoparticles (NP). [59,60] Typically, this method is experimentally more expensive than the physical decomposition, nonetheless it is more precise when it comes to size distribution (even up to atom-precise), [64,65] morphology, [66] stoichiometry, [19,24] and quality/stability. [19,24,67] The bottom-up approach can be considered an arrested chemical synthesis, which comes in the form of the macroscopic analogue, *i.e.*, the type of chemical reaction remains the same as on larger scales. However, the usage of suitable surface ligands, which are able to stop the growth of a particle, arrests the reaction at a desired point, resulting in nanoparticles.

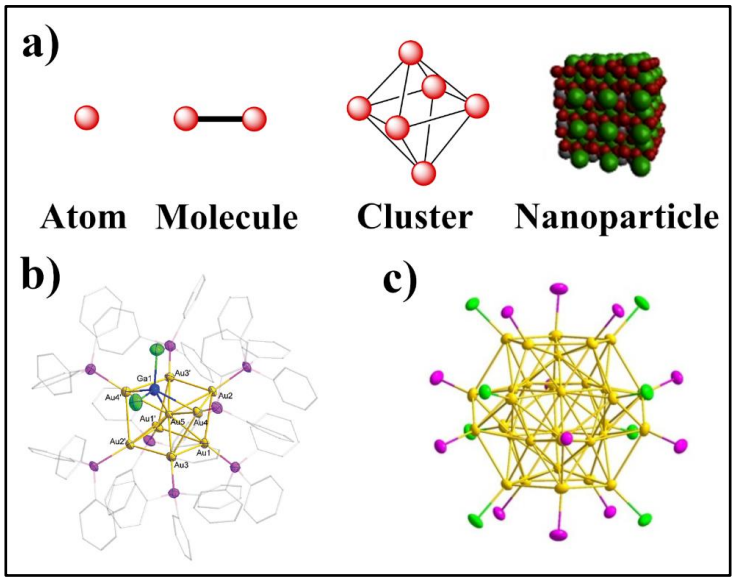

Figure 2.2: a) Schematic representation of a bottom-up nanoparticle synthesis from the atomic precursor *via* molecules and clusters to a particle. b) Experimentally verified gold nanocluster consisting of 9 Au atoms. c) An example of a larger gold cluster containing 32 Au atoms, also experimentally verified. b) Reproduced from Ref. [64] with permission from the Royal Society of Chemistry. c) Reprinted with permission from Ref. [65], with permission from Angewandte Chemie (International ed. In English). © 2019 Wiley-VCH Verlag GmbH & Co. KGaA, Weinheim.

When considering the chemical build-up of nanoparticles, the initial atomic system reacts to molecules (several bonds) and subsequently to a cluster, [68] until finally forming (crystalline) nanoparticles (schematically and exemplarily shown in **Figure 2.2 a**. [59] The formation of clusters during this process occurs in an orderly fashion due to interatomic interactions. [59,69] This potential is number-dependent and thus the atom count defines the amount of energetical minima. This means the larger the atom count, the more stable configurations, *i.e.*, structures, exist for the system.

Interestingly, the most stable clusters are often of specific atom counts, the so-called magic numbers, which explicitly are N = 8, 20, 40, 58, 92, …. [70] Due to the atom number dependent minima in energy, also the structure of the clusters can be determined this way. This can be seen in the experimental examples shown in **Figure 2.2 b + c**, where gold clusters with 9 and 32 atoms and evidently different structures are exemplarily shown. [64,65] To fully comprehend the formation of nanoparticles, the dynamics during the synthesis need to be known and not only the stable products. As the formation of the particles can be considered a nucleation process, two prominent theories are at hand: classical nucleation theory and the LaMer model. [71–73]

2.3. Classical Nucleation and the LaMer Model

2.3.1. Classical Nucleation Theory

Classical nucleation theory (CNT) describes the formation of clusters in thermodynamical means by describing it with the nucleation rate R: [71,72]

$$R = NZj \exp\left\{-\frac{\Delta G^*}{k_B T}\right\}. \tag{2.2}$$

With the number of nucleation sites N, the free enthalpy barrier ΔG^*, Boltzmann's constant k_B = 1.381·10^{-23} m^2 kg s^{-2} K^{-1}, and the temperature T. Furthermore, the probability of cluster formation, the so-called Zeldovich factor, is given by $Zj = 2D/\lambda_f^2$. Containing the diffusion coefficient D and mean free path λ_f of the monomer in solution, as well as rate of nucleation j. [72] Specifically, the Zeldovich factor can be understood as: the faster a particle moves in solution and the shorter its mean free path is, the higher is the probability of a nucleation event. These factors can effectively be tuned by changing the solvent or the concentration of the monomers.

The energy barrier within this theory can be calculated by looking at the interplay of the interface and bulk free energy. The newly formed cluster experiences a lowering in the bulk free energy the larger it becomes. This energetic gain is defined by the volume, density, and chemical potential of the material. On the other hand, the formation of a novel surface costs energy proportional to the surface tension and created surface area, which is represented by the surface free energy change. Overall, the energetic landscape can be expressed by summarizing both contributions: [72]

$$\Delta G = \frac{4}{3}\pi r^3 \rho \Delta\mu + 4\pi r^2 \gamma_{surf}. \tag{2.3}$$

With the cluster radius r, cluster number density ρ, the change in chemical potential between the nucleated and free phase $\Delta\mu$, and the surface tension γ_{surf}.

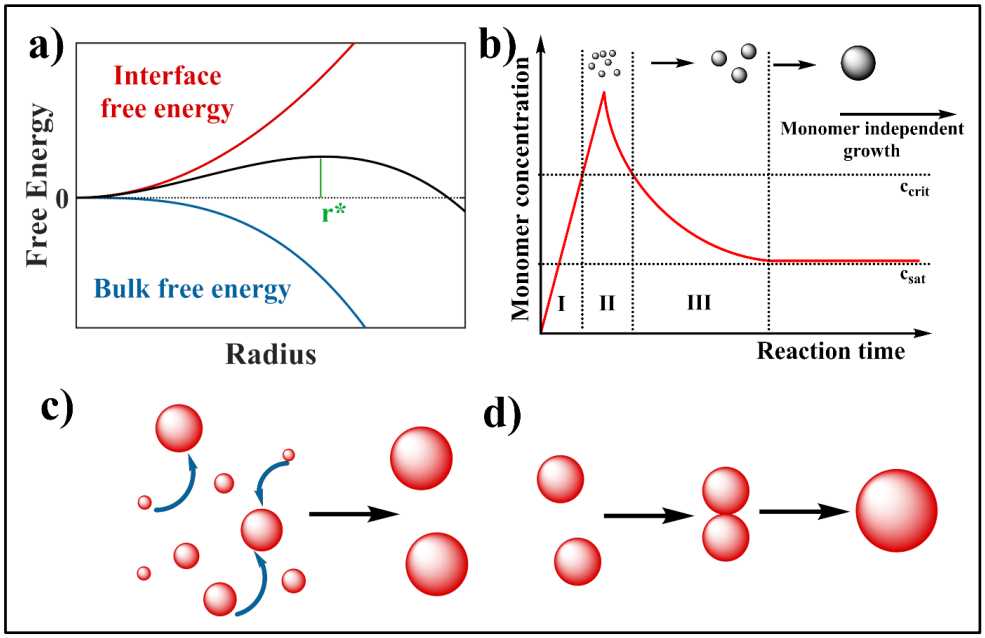

Figure 2.3: a) Energy landscape of the classical nucleation theory with the interface free energy (red) and bulk free energy (blue) contribution, resulting in the complete free energy (black). The maximum of the free energy at the critical radius r^* is the energy barrier of the nucleation rate with the value given in **Equation (3.5)**. b) Schematic concentration progress in the frame of the LaMer model. Three distinct phases of the nucleation can be determined, where (I) denotes the first phase associated with a rapid increase of the monomer concentration. Upon exceeding the critical saturation, phase (II) is initiated during which the formation of nuclei takes place. The formation results in a loss of monomer concentration and as it falls below c_{crit} again, the growth phase (III) begins. As the concentration reaches the saturation limit (c_{sat}) the growth of the cluster ends, resulting in nanoparticles. After phase III, the monomer-independent growth commences. c) Schematic representation of Ostwald ripening, smaller particles are dissolving during this process and the material is then consumed by larger particles, which in turn grow further. This process is indicated by blue arrows. d) Chemical coalescence, during which 2 particles form a larger particle.

To obtain the energy barrier ΔG^* of **Equation (2.2)** the maximum of the free energy (**Equation (2.3)**), associated with a critical radius r^*, needs to be calculated. A graphical representation of ΔG is given in **Figure 2.3 a**, where the r^* and the energy barrier is shown. By maximizing the free energy, *i.e.*, $\partial G/\partial r = 0$, the following expressions are obtained for the critical radius and energy barrier:

$$\Delta G^* = \frac{16\pi\gamma^3}{3|\rho\Delta\mu|^2} \; at \; r^* = \frac{2\gamma}{|\rho\Delta\mu|}. \tag{2.4}$$

2.3.2.LaMer Model

From the thermodynamic description of nucleation, as CNT provides it, the next logical step is to take kinetic aspects into consideration. The LaMer model provides insight into these characteristics, as they are crucial when it comes to morphology and size distribution. [66,73–75] Generally, the LaMer model is separated into 3 distinct phases, as depicted in **Figure 2.3 b**. In the beginning, a rapid increase in monomer concentration defines phase I, and as soon as the monomer concentration exceeds the critical

supersaturation the formation of nuclei is induced (Phase II). The supersaturation is defined by the solubility product of the formed nanoparticles and the concentrations of the precursors. This is where CNT plays a key role, as the formation of nuclei can be described by this theory (see chapter 2.3.1). However, through the formation of nuclei, the concentration of monomers in solution rapidly decreases until it falls below the critical supersaturation. At this point, the formation of novel nuclei is halted, and the system enters the growth phase III. The respective phases and the corresponding monomer concentration are schematically shown in **Figure 2.3 b**.

The sharp increase in monomer concentration during phase I is experimentally realized by the injection of a precursor, commonly referred to as hot injection. [74] An advantage of this method is that the injected precursor is usually added at room temperature to the heated reaction solution, and since supersaturation is temperature dependent, the time the system prevails in phase I is reduced. This is advantageous as a minimization of phase I leads to a faster nucleation and this yields higher homogeneity. [76] The time in the nucleation phase is also affected by the type of reaction by which the nuclei are formed. An outstanding example is the synthesis of perovskite NPs, which is an arrested metathesis. [19] Naturally, such reactions are extremely fast as they only require an exchange of ions, contrary to the synthesis of nanoparticles with a more covalent binding situation. Therefore, the time in phase I is even further reduced and the homogeneity of the samples is extraordinary. [19,24] Additionally, the reaction temperature has dramatic influences on the time spent in phase I. [19,24] This drastically affects the monomer concentration available for the subsequent growth process and can influence the morphology of the particles.

Subsequently, the formed nuclei grow until the monomer concentration is depleted (phase III) and the saturation concentration is reached. While in this phase the influence of the used ligand becomes crucial as it determines the size and morphology. During the growth, different crystal facets are created and exposed to the solution, enabling the ligand to interact with said surfaces. Naturally, the interaction with different crystal surfaces is dependent on the respective binding energies. For instance, the lead sulfide (PbS) crystal planes [001] and [111] planes have significantly different binding energies for oleic acid, explicitly -0.16 eV and -0.52 eV, respectively. [77] Oleic acid has a higher affinity towards the [111] surface and will be more likely to bind there, which means that growth in the other directions, *i.e.*, the {001} and {011} directions, are more likely. This anisotropic growth results, depending on the time of growth termination, in different shapes. For example, if the growth is terminated shortly after the nucleation spherical nanoparticles are synthesized. This has been extensively shown for lead selenide (PbSe) nanoparticles, where the morphology is highly dependent on the ligand density at specific crystal planes. [78] Bealing *et al.* showed that the surface energy is a function of the ligand coverage: [78]

$$\gamma_{hkl} = \gamma^0_{hkl} + \Theta_{hkl} E_{b,hkl}\,, \tag{2.5}$$

with the surface energy γ, undistorted surface energy γ_0, ligand surface coverage Θ, and binding energy E_b of the plane with the Miller indices h, k, l.

From the surface energy, the shape of a crystal can be obtained by the Wulff construction, which effectively relates the surface energy and distance from the center of the crystal to a reference plane: [78,79]

$$\frac{d_{hkl}}{d_{100}} = \frac{\gamma_{hkl}}{\gamma_{100}}, \tag{2.6}$$

with the distance from the center d_{hkl}.

The ratio obtained from **Equation (2.6)** can be used to predict the crystal shape, and thus the NP morphology, *e.g.*, $\frac{d_{111}}{d_{100}} = \frac{\sqrt{3}}{2}$ corresponds to a truncated octahedron, usually denoted as spherical NPs, and values $> \sqrt{3}$ result in cubic particles. [78] The corresponding relative surface energy profile, in terms of ligand coverage (*cf.* **Equation 2.5**), and the resulting morphologies for PbSe are summarized in **Figure 2.4**.

This concept can also be transferred to perovskite nanocrystals (NC), for which the synthesis also appeared to be very ligand dependent both in concentration and composition. [80,81] However, the situation for this type of material is more complicated as a mixture of organic acids and amines is used during the synthesis. [19,80] Nevertheless, the influence of the acids seemed to only affect the size of the as-synthesized particles, the amount of amine on the other hand determines the morphology. [81] At higher temperatures, the chain length of the amine influences the shape of the NP, where long chains resulted in cubic particles (oleylamine) and shorter amines in nanoplatelets. [80] At this point a homogenic NP solution is obtained, however after the initial growth (phase II) monomer independent growth mechanisms, like Ostwald ripening, occur, which alter the size distribution of the particles.

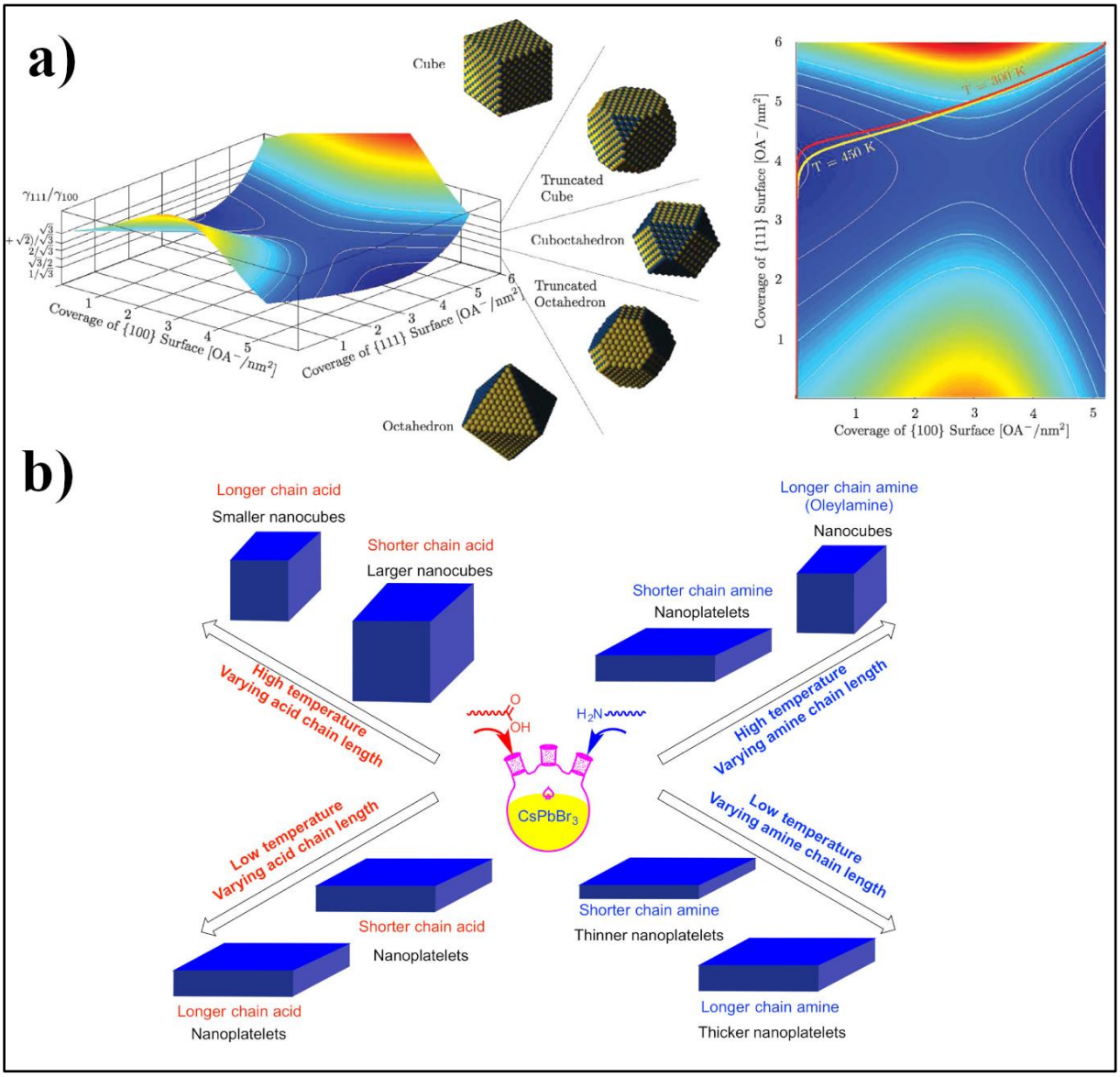

Figure 2.4: a) Relative surface energy profile for the PbSe [100] and [111] surface, dependent on the ligand coverage of oleic acid. Indicated as lines are the ratios given in **Equation (2.6)** and the corresponding morphologies of the nanoparticles. (Left) A birdseye view of the same potential, with isotherms given for the varying the ligand concentration at two temperature (T = 300 K in red and T = 450 K in yellow) depicting which morphologies are accessible. (Right) b) Temperature and ligand type dependence of the morphology of $CsPbBr_3$ perovskites. The temperature dependence is due to the time spent in the nucleation regime (phase I) and the available material for the growth. At higher temperatures, the supersaturation is lowered due to a higher solubility of the product and therefore the time for the nucleation is prolonged. Less material for the growth is available and the anisotropic growth cannot take place, resulting in cubic NPs. The ligand type influences the morphology through the surface energy. The nature of the acid only affects the size of the NPs, whereas the amine can drastically alter the shape. a) Reprinted with permission from Bealing *et al.* [78]. Copyright 2012 American Chemical Society. b) Reprinted with permission from Pan *et al.* [80]. Copyright 2016 American Chemical Society.

2.3.3. Ripening Effects

The most prominent example of a monomer independent growth mechanism, or from here on ripening effects, is Ostwald ripening. [82,83] The underlying principle is the minimization of the surface tension in the system, which results in the disintegration of smaller particles in favor of larger ones. Ostwald showed the surface tension of a particle to be size-dependent and smaller particle experience a higher pressure than larger ones. This means, that the smaller particle will be dissolved and the material flows in a current towards the larger particles increasing their size. This results in an overall broadening of the size distribution for nanoparticles, as the small particles become smaller, and the large particles grow (see **Figure 2.3 c**). Additionally, as the smaller NPs are reduced in size, they will at some point be smaller than a critical radius and dissolve completely.

Two other notable ripening effects are coalescence and oriented attachment, during which two particles are aligning and subsequently form a single particle, as depicted in **Figure 2.3 d**. [83–85] With the main difference between the two mechanisms being the alignment of the crystal planes, specifically for coalescence no such dependency of the orientation of the particles could be observed. [84] The event of coalescence seemed to occur spontaneously and was observed by discontinuities in the NP diameter during the growth process. [84] On the other hand the oriented attachment occurs when the particles are rotated and translated until the lattices of the two adjacent NPs are aligned and the fusion can take place. [85] The fusion process is driven by the minimization of the surface energy after the two particles are in contact and takes place as an atom-by-atom addition. [85]

2.4. Perovskite Synthesis: Thermodynamic and Kinetic Product

The above derived principles are now translated onto a specific system, which will be discussed throughout this work: all-inorganic caesium lead halide perovskites ($CsPbX_3$). Generally, perovskites are synthesized by an arrested‡ metathesis reaction following a typical reaction scheme: [66]

$$CsX_{(aq)} + PbX_{2\,(aq)} \rightarrow CsPbX_{3\,(s)} \downarrow. \tag{2.7}$$

Where *X* denotes a halogen (*X = Cl, Br, I*).

As only an ion exchange is required and the chemical equilibrium is completely shifted towards the product side, as the product typically precipitates, a metathesis usually exhibits very fast reaction kinetics. This makes the differentiation between kinetic and thermodynamic reaction control especially important. [66,86]

‡ Arrested, since the surface ligands are determining the reaction prior to its completion.

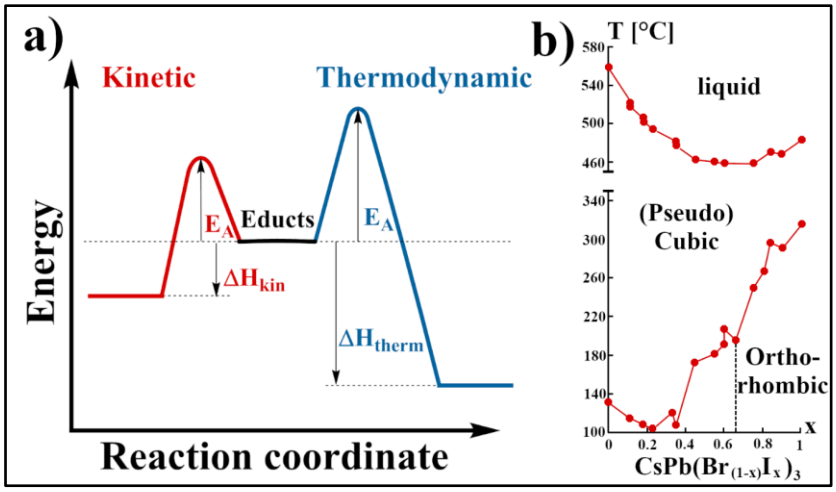

Figure 2.5: a) Schematic reaction energy profile for the kinetic and thermodynamic product, where the activation energy is denoted as E_A, and the enthalpy of reaction as ΔH. The kinetic product shows a smaller activation energy as well as a lower enthalpy of reaction. Therefore, it is the preferred product at lower temperatures. The values for activation energies and enthalpies can be tuned in the case of perovskites by utilizing appropriate educts. [86] b) Phase diagram of the binary $CsPb(Br_{(1-x)}I_x)_3$ system. The graph shows the bulk phases, *i.e.*, (pseudo)cubic and orthorhombic, with the liquid phase on top. The minimum of the (pseudo)cubic phase for a composition of $CsPbBrI_2$ is indicated by a dotted line. Data adapted from Sharma *et al.* [87].

As the hot injection synthesis of $CsPbX_3$ nanocrystals is performed at comparably low temperatures the kinetic product is dominant. [19,24] This is schematically shown in the left part of the energy profile of **Figure 2.5 a**, where at low temperatures the fast reaction kinetics determine the product. At higher temperatures or by utilizing specific ratios and types of precursors the reaction can also be controlled thermodynamically, which results in the more stable product (**Figure 2.5 a, right side**). [86] To determine the kinetic and thermodynamic product the phase diagram of the perovskites can be consulted. **Figure 2.5 b** exemplarily shows the phase diagram for the binary $CsPb(Br_{(1-x)}I_x)_3$ system and the thermodynamically stable phase is identified as the orthorhombic crystal system. On the other hand, the kinetically favorable product is the pseudocubic phase (*cf.* **Figure 2.5 b**). [56,87] The transition from orthorhombic to cubic for this system occurs at relatively low temperatures, a deeper look into the transition enthalpies by calorimetry revealed a phase transition enthalpy of only 10.34 kJ/mol, emphasizing the phase instability of perovskites. [54] Notably, the composition of $CsPbBrI_2$ lies in a local minimum and is thus more stable than other compositions of the iodide containing perovskites. The result of this is exemplarily shown in **Figure 2.6**, where SEM micrographs of nanoparticles with different iodide to bromide ratios are shown. Only the $CsPbBrI_2$ composition appeared as a stable system after several days, as the morphology of the other two depicted compositions drastically changed. For a sample of $CsPbI_3$ the growth of large, elongated crystals occurred, which can be rationalized by 2 scenarios. Th first being, that small distortions of the cubic structure in combination with the ligand result in a favored crystal facette and thus oriented growth. Secondly, the crystal can undergo a phase transition from cubic to orthorhombic because the transition enthalpy only equals 14.1 kJ/mol. [88,89]

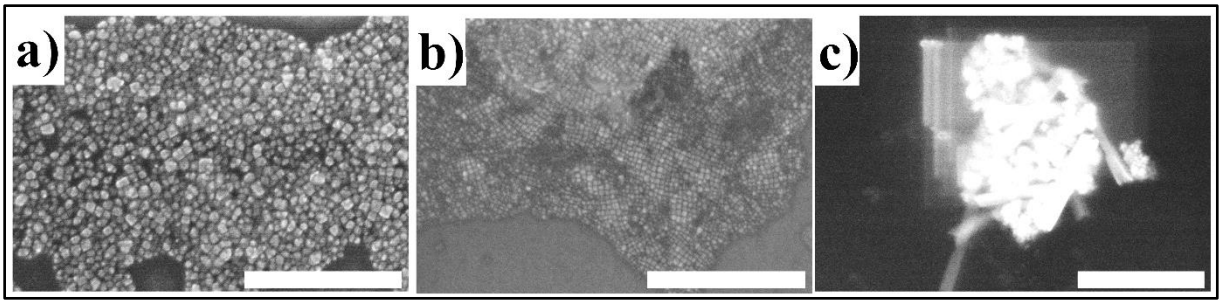

Figure 2.6: Scanning electron micrographs of a) $CsPbBr_{1.5}I_{1.5}$, b) $CsPbBrI_2$, and c) $CsPbI_3$ nanocrystals after storing the samples under ambient atmosphere for several days. In the case of $CsPbBr_{1.5}I_{1.5}$ particles were still visible, but the cubic shape was lost. For the sample shown in c) the particles vanished and macroscopic crystals formed. Scale bars are 500 nm for a) and b) and 1 µm for c).

However, the absolute temperatures depicted in the diagram must be taken with caution as they have to be adjusted for small particle systems. This is called the Gibbs-Thompson effect. The effect relates surface energies of nanoparticles in dependence of the radius to a change in melting temperature: [90]

$$\Delta T_m = T_{m,Bulk} \frac{4\sigma_{sm}}{\Delta H_f \rho_s r}, \tag{2.8}$$

with the melting temperature of the bulk phase $T_{m,Bulk}$, particle-medium interface energy σ_{sm}, bulk enthalpy of fusion ΔH_f, density of the solid ρ_s and particle radius r.

Therefore, the temperatures of the phase diagram shown in **Figure 2.5 b**, need to be adjusted to lower values for nanoparticles, which enables the synthesis of pseudocubic nanoparticles already at lower temperatures as it was shown by Krieg *et al.* and Protesescu *et al.* [19,24] This makes a description by only the phase diagram difficult and to address this, another measure for the stability of a certain perovskite crystal structure, namely the Goldschmidt tolerance factor *t*, which correlates the ionic radii ratio of ABX_3 crystals to certain structures (see **Equation (2.9)** and **Table 2.1**) can be consulted. [43]

$$t = \frac{r_A + r_X}{\sqrt{2}(r_B + r_X)}, \tag{2.9}$$

with the ionic radii of the anion r_X, and the respective cations r_A and r_B.

Table 2.1: Goldschmidt tolerance factors *t*, calculated following **Equation (2.9)**, and corresponding structures. [43]

t	Structure
>1	Hexagonal and tetragonal
0.9-1	Cubic
0.71-0.9	Orthorhombic
<0.71	Indistinguishable

2.5. Core-Shell Nanoparticles

Nanocrystals intrinsically come with particular downsides, *e.g.*, environmental instability, stability against humidity and temperature, as well as oxygen doping of the NCs. [38,91,92] A synthetic approach to mitigate this is the synthesis of a core-shell structure, which can passivate the NC surface and protect it against external influences and incidentally improve optoelectronic properties. Common examples of shell materials for a broad variety of particles are ZnS or SiO_x. [91,93] In the case of semiconductor NCs the energy level arrangement of the core (shell) valence and conduction states determines the nomenclature of the system. These arrangements can be classified in 4 categories as shown in **Figure 2.7 a**. Most commonly used is type I in which the shell has a larger band gap than the core semiconductor. Type II can be divided into 2 subclasses, type IIa and IIb. In both cases lies the shell valence or conduction state in the band gap of the core material, whereas the respective other state is outside. Lastly, the reverse type I arrangement is exactly the opposite of type I and has both states of the shell material lying inside the band gap of the core semiconductor. [94] To practically prepare the shell, 3 experimental approaches are possible, all of which are utilizing organometallic precursors. [76] Two approaches are a classical nucleation (*cf.* chapter 2.3) with either a single-source or separate precursors, exemplarily tetramethoxyorthosilicate (TMOS) or diethyl zinc ($Zn(C_2H_4)_2$) and bis-(trimethyl)-sulfide ($S(Si(CH_3)_3)_2$) for single-source and separate precursor approaches, respectively.

After precursor injection they start to form nuclei on the NC surface, which subsequently grow until the complete surface is covered. Several distinct nucleation sites are formed simultaneously which means the shell growth takes place at all of these sites. After the completion of the shell synthesis this ultimately leads to grain boundaries in the shell, which is generally not desirable. Grain boundaries can be avoided by growing an amorphous shell, which can be realized by the utilization of TMOS or other orthosilicates. They are used as single-source precursor, which can undergo a sol-gel reaction, which is shown for TMOS in **Figure 2.7 b**. In the first step of this sol-gel process a hydrolysis takes place and one of the alkyl chains is removed, resulting in the formation of a more reactive intermediate hydroxy-orthosilicate. Afterwards, this intermediate undergoes a condensation reaction in which Si–O–Si bonds are formed. These steps are repeated until a network of silica is synthesized, however not all alkyl bonds are replaced during this process and therefore the nomenclature SiO_x, rather than SiO_2, is more appropriate. A main advantage of sol-gel processes is the high degree of tunability, *e.g.*, the reactivity of the precursor can be tuned by the alkyl chain length. [93] Additionally, the morphology of the product can be controlled *via* the reaction environment, typically *via* the pH-value. Nevertheless, uncatalyzed reactions of orthosilicates are also possible, as it is the case for TMOS, where the water content of a wet solvent is enough to induce the hydrolysis. [93]

Another synthetical route to avoid grain boundaries is successive ion layer adsorption and reaction (SILAR), during which in subsequent steps the respective precursors are added after each other and separately allowed to react with the surface. Firstly, a precursor like zinc oleate is added at elevated temperatures which results in the formation of a precursor monolayer on the NC surface by forming novel bonds. Following this, a stoichiometric amount of a second precursor, *e.g.*, sulfur, is injected resulting in the formation of a homogenous monolayer of the shell material, ZnS in this example. Through layer-by-layer growth, *i.e.*, the repetition of these steps, the desired shell thickness can be realized. [95]

In a further step, one can also think about growing additional shells of different chemical composition on top of each other, *viz.* a grated core-shell system. [96] This enables further tunability of the desired NC properties and has the ability to enhance the effects of a core-shell system. Specifically, the type of core-shell system can have dramatic influences on the optoelectronic properties of the NCs, *e.g.*, an increase in photoluminescence quantum yield, easier charge carrier injection, facilitated charge carrier separation or exciton leakage. [22,97,98] A more precise discussion of the mentioned phenomena is given further below in the text.

When a shell is prepared on a NC surface the crystal lattice parameters of the respective materials are required to fit reasonably well, especially the lattice constants have to be of comparable magnitude, called epitaxy. Even small mismatches in the lattice parameters lead to a noticeable strain at the core-shell interface, defined by $\varepsilon_s = (a_s - a_c)/a_s$, with the lattice constants of the core and shell material a_s and a_c, respectively. The homogeneous strain induced by the lattice mismatch ε_s can be described by a simple Hookian law in a generalized from $\underline{\sigma_{ij}} = c_{ijkl}\,\underline{\varepsilon_{kl}}$. [99] The applied stress tensor σ_{ij}, elastic stiffness tensor (containing the anisotropic force constants) c_{ijkl}, and strain ε_{kl} are elaborate in their calculation, however for the simplest case, *viz.* a [100] orientation on a cubic NC core lattice (as it is the case for perovskites) the stress tensor is: [100]

$$\varepsilon_{kl}^{[100]} = \varepsilon_s \begin{pmatrix} 1 & 0 & 0 \\ 0 & 1 & 0 \\ 0 & 0 & -\dfrac{2c_{12}}{c_{11}} \end{pmatrix}, \tag{2.10}$$

with the energy density

$$U = \frac{1}{2}\sum_{\lambda=1}^{6}\sum_{\mu=1}^{6} c_{\lambda\mu}\varepsilon_\lambda\varepsilon_\mu = \varepsilon_s^2\left(c_{11} + \frac{c_{12}^2}{c_{11}} + c_{12}\right).$$

This increase in energy density is compensated by the creation of lattice mismatches at the interface of core and shell material. To prevent the formation of mismatches the crystal lattices either must match almost perfectly or the shell needs to be deposited as an amorphous material. Especially in the case of perovskites, which are very vulnerable to any external influences, the synthesis of an amorphous material seems to be most appropriate. The system of choice for perovskites is the

aforementioned TMOS, as the more commonly used tetraethoxyorthosilicate has a higher hydrolysis rate which ultimately leads to the decomposition of the NCs during the shell preparation. [93]

By applying strain to a crystal lattice, the equilibrium position of the atoms in the NC lattice is altered and may break the symmetry of the crystal. If the symmetry is broken, the energy states of the material can be modified, affecting the core material. [100] However, this effect is minimized by the application of an amorphous shell as well, further strengthening the use of an SiO_x shell for perovskites. Despite silica typically being considered an insulator, the utilization of a SiO_x shell does not necessarily lead to complete insulation of the NC core. This is due to the existence of intragap states in amorphous silica, which typically originate in dangling bonds, hydrogenated or non-stoichiometric silicon species (*cf.* discussion on Urbach tail in chapter 2.9). [101–104] These states introduce a non-negligible density of states in the band gap, which only alters the effective mass of the charge carriers but does not suppress charge propagation. [101]

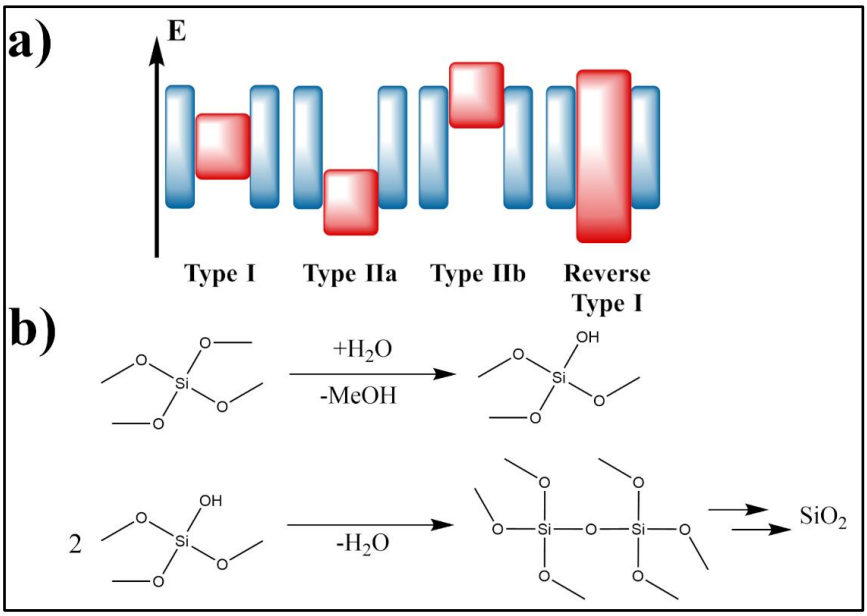

Figure 2.7: a) Possible arrangements of semiconductors in a core-shell system. The core material energy gaps are shown in red, and the corresponding shell gaps in blue. b) The detailed sol-gel mechanism for the synthesis of a SiO_x shell with tetramethoxyorthosilicate (TMOS) as a single-source precursor. In a first step, an alcohol is formed by hydrolysis under the formation of methanol (MeOH). These alcohols can subsequently undergo a condensation to form the corresponding disilylether (disiloxan). These steps can be repeated until SiO_2 is formed. However, often the reaction stops before all alcohols reacted, which results in hydroxy groups still present in the structure (SiO_x).

2.6. Self-Assembly of Nanoparticles

To understand the self-assembly of NCs the interparticle interactions of the particles is of crucial interest. A summary of commonly considered potentials is given in **Table 2.2**.

Table 2.2: Common intermolecular interaction potentials. With the interparticle distance d and particle radius r_{NC}, depth of a potential well α, zero of the potential (~ size of the particles) σ, polarizability of an atom α_0, ionization potential I, relative permittivity of the medium and particle ε_r and ε_1, respectively, as well as the vacuum permittivity $\varepsilon_0 = 8.8542 \cdot 10^{-12}$ *As/Vm*. Furthermore, the dipole moments are μ_i, the absorption frequency ν_e, Planck´s constant $h = 6.626 \cdot 10^{-34}$ m^2kg/s, and the refractive indices of particles and medium n_1 and n_r, respectively. The surface charge is Z, Bjerrum length λ_B, and Debye-Hückel distance $\kappa^2 = 4\pi\lambda_B n$. Where n gives the concentration of charge carriers. Lastly, the partition function of the canonical ensemble is given by Q, the available volume per NC as V_A^N, particle number as N, and de Broglie wavelength as Λ.

Potential	Interaction	Equation
Hard sphere [105]	Pauli exclusion principle	$V_{HS}(d) = \begin{cases} 0, & d > 2\,r_{NC} \\ \infty, & d < 2\,r_{NC} \end{cases}.$
Lennard-Jones [69]	Very short-ranged potentials	$V_{LJ}(d) = 4\alpha\left[\left(\frac{\sigma}{d}\right)^{12} - \left(\frac{\sigma}{d}\right)^{6}\right].$
London dispersion [106,107]	Fluctuating / temporary dipoles	$V_{London}(d) = -\frac{C_{disp}}{d^6} = -\frac{3}{4}\frac{\alpha_0^2 I}{(4\pi\varepsilon_0)^2 d^6}.$
Debye [107]	Dipole-induced dipole	$V_{Debye}(d) = -\frac{\alpha_0 \mu^2}{(4\pi\varepsilon_0\varepsilon_r)^2 d^6}.$
Keesom [107,108]	Dipole-dipole	$V_{Keesom}(d) = -\frac{\mu_1^2 \mu_2^2}{3(4\pi\varepsilon_0\varepsilon_r)^2 k_b T d^6}.$
Van-der Waals [107,109–111]	Summarization of London, Debye and Keesom	$V_{vdW}(d) = -\left[3k_bT\left(\frac{\varepsilon_1(0)-\varepsilon_r(0)}{\varepsilon_1(0)+2\,\varepsilon_r(0)}\right)^2 + \frac{\sqrt{3}h\nu_e}{4}\frac{\left(n_1^2-n_r^2\right)^2}{\left(n_1^2+2\,n_r^2\right)^{\frac{3}{2}}}\right]\frac{r_{NC}^6}{d^6}.$
Coulomb	Charges	$V_{Coulomb} = \frac{1}{4\pi\varepsilon_0}\int \frac{\rho(\vec{r}')}{\lvert\vec{r}-\vec{r}'\rvert} d\vec{r}'.$
Yukawa [112]	Screened charges / electrochemical double layer	$V_{Yukawa}(d) = \frac{Z^2\lambda_B}{k_B T}\left(\frac{\exp(\kappa r_{NC})}{1+\kappa r_{NC}}\right)^2 \frac{\exp(-\kappa d)}{d}.$
Depletion interaction [113]	Excluded volume	$F = -k_B T \ln Q\,; with\ Q = \frac{V_A^N}{N!\Lambda^{3N}}.$
Hydrogen bonds	Intermolecular Hydrogen bridges	n.a.

Some of the potentials are summarized in the Derjaguin-Landau-Verwey-Overbeek (DLVO) theory as a combined potential $V_{DLVO}(d) = V_{vdW} + V_{Yukawa} + V_{LJ}(d)$, which describes the interplay of the attractive vdW and repulsive electrochemical double layer potential, as well as the very strong repulsion when in contact given by the Lennard-Jones potential. [107] This results in a potential, as shown in **Figure 2.8 d**, which exhibits a minimum at a certain distance. This corresponds to the equilibrium distance, where vdW attraction and Yukawa repulsion are of same magnitude and thus defines the median interparticle distance. All interparticle interactions must be considered when constructing the phase diagram of NCs, some examples are given in **Figure 2.8 a - c**, in which different cases of interactions are exemplarily depicted.

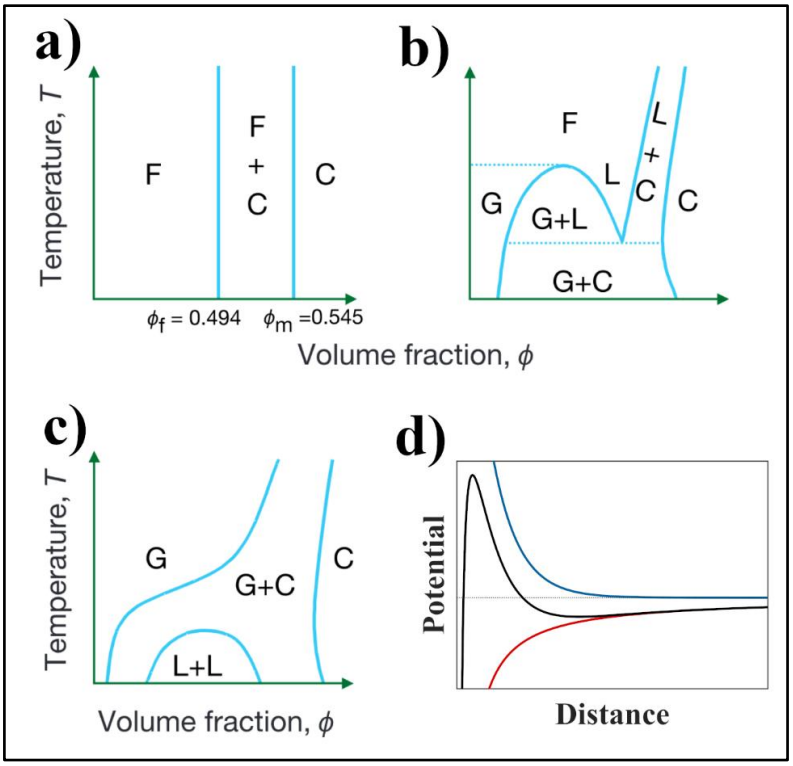

Figure 2.8: Phase diagrams for a) purely hard spheres, b) spheres with long-ranged attraction and c) short-ranged attraction. The shown phases are fluid (F), crystalline (C), liquid (L) and gas (G). Phase transitions are indicated as solid lines and coexisting phases are shown with a plus. d) DLVO potential (black) with corresponding contributions, namely the short-range attraction (van der Waals, red), long-ranged repulsion (Yukawa, blue). a) – c) Reprinted by permission from Anderson *et al.*: Springer Nature, Nature, Insights into phase transition kinetics from colloid science, Anderson *et al.* [117], Nature (2002). Partly edited.

Practically, self-assembly of NCs can be achieved by a variety of methods, with the most common being spin-coating and drop-casting. During spin-coating, the solution is placed on a substrate either prior or during it is rotated. During the spinning process the solution is evenly distributed across the substrate whilst excess solvent is spun off, the remaining solvent is allowed to evaporate. The height of the as-prepared thin film is reciprocally proportional to the square root of the angular velocity $h \propto 1/\sqrt{\omega}$. [114] During drop-casting, the solution is placed on the substrate and the solvent allowed to evaporate. However, despite being very easily accessible, this method typically yields films of less structural quality if the evaporation is taking place too fast. However, if the evaporation is decelerated significantly by covering the substrate, the large NC number can be used to prepare highly ordered superlattices. [115] Another, rather complex, method is the Langmuir-Blodgett interface method, during which the NC solution is placed on top of a liquid face and the solvent of the particles evaporates, leading to self-assembly. Subsequently, the film is deposited by carefully removing the bottom solvent in which the substrate is submerged, effectively depositing the self-assembled film on the substrate. This method also enables the possibility of exchanging the ligand whilst the NC film floats on the solvent. [31,32]

The underlying phenomenon of these preparation methods is, that the concentration of NCs is increased during the process by evaporation / removal of the solvent. To put this into the perspective of phase diagrams, at a given temperature the volume fraction of NCs is continuously increased. This means phase transitions towards a solid or crystal are induced, and the result is a NC mesocrystalline solid. A mesocrystal is defined as an ordered array, that in itself consists of smaller crystalline components, which in this case are NCs. [116]

Subsequently, the structure of the mesocrystalline solid is to be analyzed and the most common method is the utilization of scattering techniques and scanning electron microscopy. An introduction to basic scattering will be given in the next chapter.

2.7. Scattering on Mesocrystalline Samples

To evaluate the scattering on a mesocrystalline sample, at first a time-dependent wavefunction for the incoming and scattered wave $\Psi(t,\vec{x}) \propto \Psi(\vec{x})e^{\frac{iE_k(t-t_0)}{\hbar}}$ can be assumed. [118] However, as typically the sample is illuminated continuously, a steady state can be assumed effectively eliminating the time dependence and solely the time-independent Schrödinger equation must be solved. [118]

$$(\Delta + k^2)\Psi(\vec{x}) = U(\vec{x})\Psi(\vec{x}), \tag{2.11}$$

with the Laplace operator Δ, absolute of the wavevector k given by $k^2 = \frac{2mE_k}{\hbar^2}$, and the reduced potential $U(\vec{x}) = \frac{2mV(\vec{x})}{\hbar^2}$.

This equation can be solved by applying Green´s method for the Helmholtz equation and assuming a plane scattered wave, when far away from the scattering center (1st Born approximation). [118,119] The result is the Lippmann-Schwinger equation: [118,120]

$$\Psi_{\vec{k}}(\vec{x}) = \Psi_0(\vec{x}) + \frac{m}{2\pi\hbar^2}\frac{e^{ik|\vec{x}|}}{|\vec{x}|}\iiint_V e^{-i\langle\vec{q},\vec{x}\rangle}V(\vec{x})d^3x = e^{i\langle\vec{k},\vec{x}\,\rangle} + \frac{f(\vec{q})}{|\vec{x}|}e^{ik|\vec{x}|} \;;\vec{q} = \vec{k} - \vec{k}'.$$
$$with\ \sigma_{tot} = \oint_S \frac{d\sigma}{d\Omega}d\Omega = 2\pi\int_0^\pi \sin(\phi)\,|f(\vec{q})|^2\,d\phi \tag{2.12}$$

With the mass m of the scattered particle wave, reduced Planck´s constant $\hbar = \frac{h}{2\pi}$, momentum transfer $\vec{q}$, and scattering amplitude $f(\vec{q})$, which is the Fourier transformation of the potential, *e.g.*, the transformation of the charge distribution of the electron shell (X-ray scattering) or the Yukawa potential of the nucleus (neutron scattering).

Equation (2.12) can be understood as a sum of an incoming and unscattered plane wave given by the first term and a scattered spherical wave modulated by the scattering amplitude. The scattering amplitude effectively determines the wavevector of the outgoing wave by describing the intensity

distribution along the angular coordinate, and thus also the momentum transfer. [118] Additionally, by squaring the scattering amplitude, the important differential cross section $\frac{d\sigma}{d\Omega}$ (current density of scattered wave divided by the incoming current density) can be determined which is the main measure for the scattered intensity. [118,121] The total scattering cross section σ_{tot} can subsequently be obtained by integrating over all angular directions (**Equation 2.12**). [118]

Especially, when considering multiple scatterers and not an isolated, single scatterer this value can give the scattered intensity in dependence of the momentum transfer by summarizing over the radial distribution function of identical, monodisperse scatterers: [121,122]

$$I_s(\vec{q}) = \frac{d\sigma}{d\Omega} = \frac{N}{V}|f_k(\vec{q})|^2 \cdot \left|\sum_{k=1}^{N} e^{-2\pi i\langle \vec{q},\vec{r}_k\rangle}\right|^2 = \frac{N}{V}P(\vec{q})S(\vec{q}). \tag{2.13}$$

With the scattered intensity I_s, scatterer number density N/V, the square of the scattering amplitude known as the form factor P, and the structure factor S with the reciprocal lattice defined by the momentum transfer q and the real space separation by r_k. **Equation (2.13)** gives a general description of scattering, but the nature of scattering can be distinctively different, it can either be coherent or incoherent (correlated propagation of scattered light) as well as elastic or inelastic (energy preservation after the scattering event). Examples are small- and wide-angle X-ray and neutron scattering for coherent elastic, and quasielastic neutron scattering for incoherent inelastic scattering.

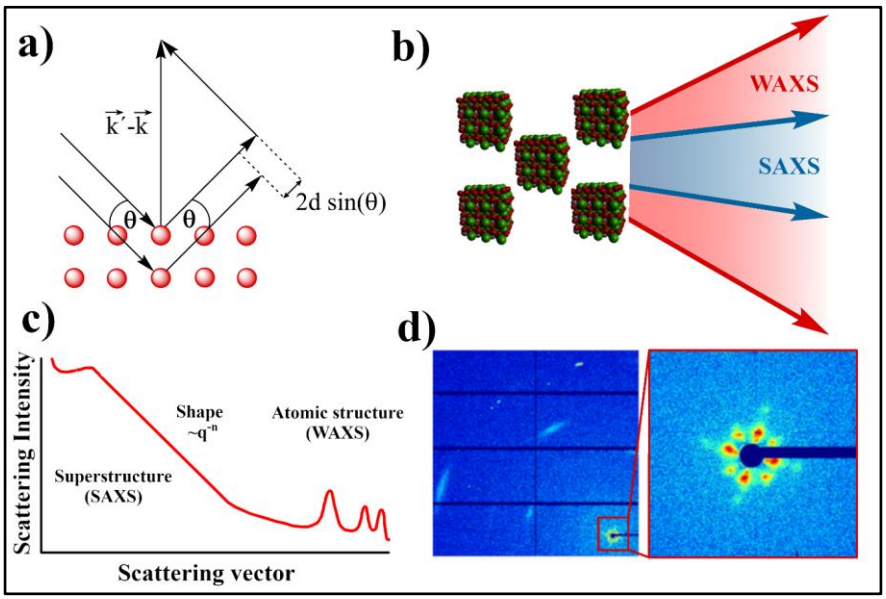

Figure 2.9: a) Depiction of Bragg´s law as given in **Equation (2.14)**, the path difference of incident and outgoing wave is shown as dotted lines. Additionally, geometrical considerations as given in the text are depicted as well. The scattering angle is θ. b) Schematic of the difference between small- and wide-angle X-ray scattering (SAXS and WAXS). The SAXS scattering originates from the superstructure, whereas the WAXS from the atomic lattice. c) Theoretical scattering intensity curve, the information which can be obtained from different regions and techniques are displayed. d) An exemplary scattering map for simultaneous WAXS and SAXS with angular resolution. The left image shows the complete scattering range, *i.e.*, the SAXS and WAXS region. The right image is a magnification of the SAXS region for better visibility.

Within this chapter mainly the structure factor will be discussed, whereas the implications of the form factor will be examined in chapter 2.11.2. The structure factor can be further analyzed by considering the Laue condition, *i.e.*, the condition for destructive interference originating from crystal planes can be expressed as $e^{i(\vec{k}'-\vec{k})(\vec{r_k}-\vec{r_j})} = e^{2i\pi m} = 1$. The exponent of the exponential is in fact the product of a reciprocal and real space lattice vector, and *m* denotes the *m*-th crystal plane, each distanced by the lattice spacing $d_{[hkl]}$. From geometrical considerations the absolute of the reciprocal lattice vector at each plane must satisfy $\left|(\vec{k}'-\vec{k})\right| = m\left|(\vec{k}'-\vec{k})\right| = \frac{2\pi m}{d_{[hkl]}}$ (periodicity of the reciprocal lattice) and $\left|(\vec{k}'-\vec{k})\right| = 2k\sin\Theta = \frac{4\pi}{\lambda}\sin\Theta$ (compare **Figure 2.9 a**). Combining these considerations results in the famous Bragg condition to calculate the lattice spacing: [123]

$$m\lambda = 2d_{[hkl]}\sin\Theta\,; and\ a = d_{[hkl]}\sqrt{h^2+k^2+l^2}\ (simple\ cubic). \tag{2.14}$$

With the Laue indices *h*, *k*, *l* defining the lattice plane and the lattice constant *a*.

Exemplarily, a scattering experiment at the Deutsche Elektronen Synchrotron (DESY) P10 Coherence Application beamline of the PETRA III storage ring will be discussed, because it provides the possibility to perform simultaneous wide angle and small angle X-ray diffraction (WAXS and SAXS, for details *cf.* chapter 3). [124] At first the distinction between WAXS and SAXS shall be explained, as the different angles offer different information of the sample. An incident beam can be diffracted by either large, *i.e.*, the nanocrystals, or small structures, *i.e.*, the atomic lattice of the material (schematically shown in **Figure 2.9 b**). Nevertheless, all contributions to the overall scattered intensity follow **Equations (2.13)** and **(2.14)** and are simply summarized. [99,125] At a low momentum transfer range, the small angle scattering is used to determine the structure of the lattice of nanocrystals, which from here on will be called superlattice. [31] The form factor for all NCs is assumed to be equal, neglecting the size distribution or in other words assuming a homogenic sample. At larger *q*-values, the structure of the atomic lattice inside a nanocrystal can be accessed. [31] This aspect is shown in the example intensity plot of **Figure 2.9 c**, where the different regions and corresponding information is depicted.

Additionally, by using a 2D detector angular information can be obtained, the result of a typical diffraction experiment on $CsPbBr_3$ nanocrystal superlattices is shown in **Figure 2.9 d**. The SAXS and WAXS signals are shown at larger and smaller momentum transfer values, respectively. From the diffraction pattern and corresponding labeling (see below) of the peaks it can be deduced that both, the atomic as well as the superlattice, are of simple cubic structure. The as obtained diffractograms can be fitted by a two-component Gaussian function to obtain the peak positions in radial and angular direction, as well as their FWHMs. By doing so, the FWHM can subsequently be used to calculate lattice distortions by following the Williamson-Hall Method. [31,126] A more detailed description of this procedure is given in chapter 3 of the results part.

The labelling of the peaks can be realized as a summation of the intensity over all angular coordinates (data reduction). This results in an intensity plot against the radial coordinate, *i.e.*, the momentum transfer. [125,127,128] From these, peaks at different *q*-values can be fitted and analyzed by the Bragg equation (**Equation (2.14)**) to obtain the lattice spacings. Additionally, the overall peak distribution can be analyzed by calculating the expected patterns from the scattered intensity given in **Equation (2.13)**. For example, the caesium chloride (CsCl) structure is a simple cubic (sc) lattice with a 2-atomic basis (Cs located at (0,0,0) and Cl at (1/2,1/2,1/2)), thus the scattered intensity for this crystal is given by:

$$I_s = \left(\sum_{k=1}^{2} f_k e^{-2\pi i(hx_k+ky_k+lz_k)}\right)^2 = \left(f_{Cs} + f_{cl}e^{-i\pi(h+k+l)}\right)^2 = \left(f_{cs} + f_{cl}(-1)^{h+k+l}\right)^2$$
$$I_s = \begin{cases}(f_{Cs}+f_{Cl})^2, & h+k+l\ even\\ (f_{Cs}-f_{Cl})^2, & h+k+l\ odd\end{cases} \quad (2.15)$$

With the indices *1* and *2* indicating Cs and Cl, respectively, x_k, y_k, z_k being the cartesian coordinates of the atoms in real space, and *h*, *k*, *l* the Miller indices defining the reciprocal lattice vector.

For a simple cubic crystal, reflexes for all Miller indices occur, only the absolute intensity depends on the form factors. However, for other crystal systems such as face-centered or body-centered cubic, some reflexes are cancelled out due to destructive interference. Which reflexes are deleted can be found by following the same procedure as shown in **Equation (2.15)**. Notably, the structure factor can be modelled differently for samples which are not as perfect as the above-described atomic lattices. Especially for small angle scattering of large scatterers this becomes particularly important. Prominent examples are the structure factors of hard spheres or fractal aggregates, which are discussed in further detail in chapter 4.7. Finally, by integrating over all angular coordinates, the intensity profile can be analyzed, and the underlying structure clearly identified. To support the above derived scattering results and obtain additional information like height of a thin film or local distortions from ideality, scanning electron microscopy or atomic force microscopy are useful. Especially if smaller regions are of interest, these techniques offer a high degree of information as SAXS and WAXS typically are averaging over a larger area.

2.8. Quantum Confined Semiconductors

As mentioned before, the size of nanocrystals has dramatic implications on the properties of the material. To further evaluate this phenomenon, the basics of the electronic band structures of semiconductors needs to be discussed. Generally, the bands in a semiconductor are formed by Bloch wavefunctions $\Psi(\vec{r}) = u(\vec{r})\exp(i\vec{k}\cdot\vec{r}), with\ u(\vec{r}) = u(\vec{r}+\vec{T})$, which can be thought of as a product of a plane wave and the periodicity of the lattice. [129] By solving the Schrödinger equation for a one-

dimensional, periodic potential of δ-functions in the Kronig-Penney model one finds the following energy dispersion: [99,130]

$$\left(\frac{mAa^2}{2\hbar^2}\right)\left(\frac{2mE}{\hbar^2}a\right)^{-1}\sin\left(\frac{2mE}{\hbar^2}a\right)+\cos\left(\frac{2mE}{\hbar^2}a\right)=\cos(ka);\ \ \cos(ka)\ \in[-1,1]. \tag{2.16}$$

With the energy eigenvalue *E*, constant *A*, absolute of the wavevector *k*, lattice constant *a*, and mass *m*.

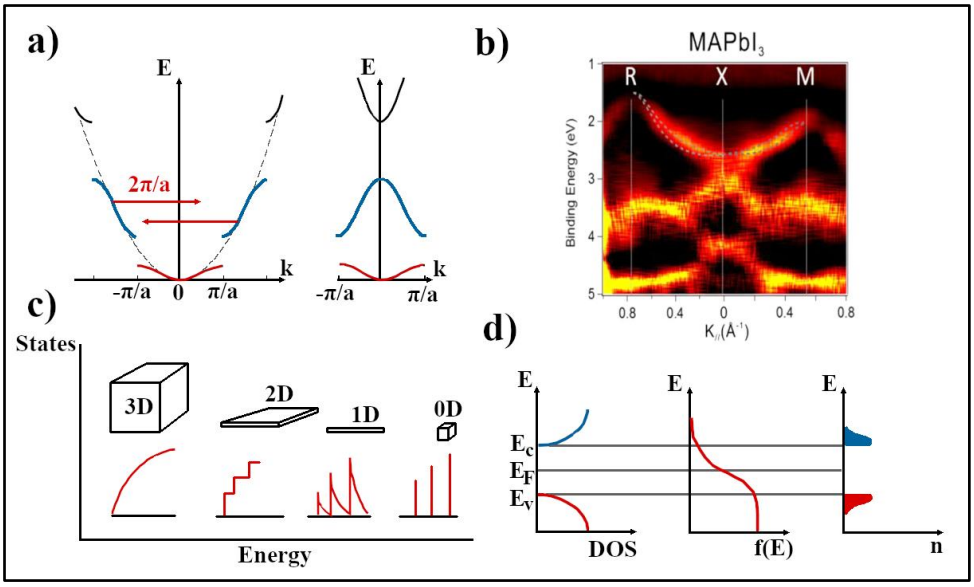

Figure 2.10: a) Dispersion relation of free electrons (dashed line) and dispersion for an electron in a periodic potential (**Equation (2.16)**, full lines). The contribution from the 1st Brillouin zone is depicted in red, whereas the dispersion relation from neighboring zones is shown in blue. The dispersion from translationally moved cells, *i.e.*, neighboring ones, can be projected onto the first Brillouin zone to obtain the reduced zone scheme (right part), also called band scheme. b) Experimentally measured band structure for methylammonium lead iodide ($MAPbI_3$), measured *via* angle resolved photoelectron spectroscopy. The R, X, and M point correspond to the corner point, center of a face, and center of an edge of the cubic structure. c) Density of states (DOS) for different dimensions and the correspond plot *vs.* energy (red). d) The DOS of a 3D semiconductor (left), the Fermi-Dirac distribution (middle) and their product, which is the charge carrier density (right). E_c, E_F, and E_v are the conduction band edge, fermi energy, and valence band edge, respectively. b) Reprinted with permission from Zu *et al.* [131]. Copyright 2019 American Chemical Society.

From the solution (**Equation (2.16)**) it can easily be seen that it only holds true if the modulus of the left side is ≤ 1, therefore, all other values are forbidden which is the origin of the band gap. Phenomenologically, the origin can be understood as the creation of standing waves at the edge of the 1st Brillouin zone. Away from the edges a degenerate family of waves traveling on both directions is present. Solving the Schrödinger equation yields the energy dispersion relation $E(\vec{k})$ which has discontinuities where **Equation (2.16)** is not defined, which is shown in **Figure 2.10 a**. [99] Nevertheless, the equation holds true for every elementary cell, which means the solution can be shifted by the translation vector $\vec{T}$. Effectively, this means that the dispersion relation of each cell can be projected onto the 1st Brillouin zone which results in the reduced zone scheme shown in **Figure 2.10 a**, also known as the band scheme. It can be seen that away from the edge of the Brillouin zone, ($k << \pi/a$) the dispersion relation can reasonably be approximated by the dispersion for free or quasi-

free electrons $E(\vec{k}) = \left(\frac{\hbar^2}{2m^*}\right)\vec{k}^2$ (dashed line in **Figure 2.10 a**, since the Taylor series[§] of a cosine approximates as $\cos(ka) \propto (ka)^2$). On the other hand, near the edge of the Brillouin zone (k ≈ π/a) the dispersion differs significantly from those of free electrons and therefore the energy dispersion in **Equation (2.16)** needs to be considered. [99] The band structure is experimentally accessible *via* angle-resolved photoemission spectroscopy, as it is exemplarily shown for simple cubic methylammonium lead iodide perovskites in **Figure 2.10 b**. [131]

Each primitive elementary cell contributes a total of 2 states to the resulting band, thus *2N* states are available, with *N* being the number of elementary cells in the crystal and the factor 2 coming from the electron spin. [99] If we transform this result to NCs we find that no infinite crystal is present, and the number of elementary cells is countable. Therefore, the number of available states is drastically reduced compared to a macroscopic analogue. This results in a tearing of the band structures and the availability of less states. [57,132,133] This effect can best be visualized by the density of states (DOS), which gives a measure of the magnitude of available states per energy interval. [99] The DOS can be thought of as the summation over all *k*-values at a fixed energy in the band scheme. After the summation, the highest filled state at the lower end of the band gap will be referred to as the valence band maximum (E_v) or valence state ($1S_h$), and the lowest unfilled state above the band gap is named conduction band minimum (E_c) or conduction state ($1S_e$). [22]

The DOS is generally calculated by: [99]

$$D(E) = \frac{dN}{dE} = \frac{dN}{dk}\frac{dk}{dE}. \tag{2.17}$$

With the number of states *N*, energy *E*, and absolute of the wavevector *k*. *N* can also be calculated as the ratio of the volume/cross section/radius of a sphere with radius $|\vec{k}|$ in k-space divided by the volume/area/length of a single state in k-space in the form of a cube with length π/*L*. The first term on the right-hand side in **Equation (2.17)** corresponds to the number of states per infinitesimal *k*-space interval, and the second to the energy dispersion. For different dimensions, the result varies significantly due to the absence of states, as explained above. The densities of states for different dimensions are summarized in **Table 2.3** and depicted in **Figure 2.10 c**, for simplicity a quasi-free electron dispersion is assumed. This assumption can be considered sufficient for the description of electrons in semiconducting and metallic materials, if the coupling of the charge carrier to the lattice is small enough and/or the electron is far away from the Brillouin edge. [99]

[§] $\cos(x) = \sum_n (-1)^n \frac{x^{2n}}{(2n)!}$

Table 2.3: Densities of states for free electrons in different confinement environments, the energy dispersion for the corresponding dimensions are *E(k)*, the number of available states is *N*. *N* is calculated by assuming the volume in *k*-space to be $(\pi/V)^D$, where *V* is either the volume of a cube (3D), the area of a square (2D) or the length of a line (1D), and *D* the dimension (*D* = 1,2,3). The DOS is calculated following **Equation (2.17)**. E_c is the conduction band edge, for holes this value is to be replaced by the valence band edge. Θ is the Heaviside function, and δ the Dirac delta-function.

Dimension	*E(k)*	*N*	*DOS(E)*
3D (Bulk)	$\frac{\hbar^2}{2m^*}\left(k_x^2+k_y^2+k_z^2\right)$	$\frac{4k^3L^3}{3\pi}$	$\frac{1}{2\pi^2}\left(\frac{2m^*}{\hbar^2}\right)^{\frac{3}{2}}\sqrt{E-E_c}$
2D (Platelet)	$\frac{\hbar^2}{2m^*}\left(k_x^2+k_y^2\right)$	$\frac{k^2L^2}{2\pi}$	$\frac{m^*}{\pi\hbar^2}\Theta(E-E_c)$
1D (Wire)	$\frac{\hbar^2}{2m^*}k_x^2$	$\frac{kL}{\pi}$	$\frac{m^*}{\pi\hbar}\sqrt{\frac{m^*}{2(E-E_c)}}$
0D (Quantum Dot)	-	-	$2\delta(E-E_c)$

With the DOS known, the states are filled according to the Fermi-Dirac statistic $f(E) = 1/\left(\exp\left(\frac{E-E_F}{k_BT}\right)+1\right)$. [99] The Fermi energy E_F usually refers to the energy of the highest occupied state at zero temperature. [99] However, for an intrinsic semiconductor, *i.e.*, no doping and the same numbers of electrons and holes is present, E_F lies directly in the middle of the band gap. [99] Subsequently, the Fermi distribution can be multiplied with the DOS to obtain the charge carrier density, as exemplarily shown in **Figure 2.10 d**. The middle panel shows a distribution at finite temperature with the turning point located at E_F. From this image one can see that some electrons are located inside the conduction band (which was neglected in the discussion before). Only at 0 *K* the electrons are solely in the valence band. Another important classification about how electrons are excited into the conduction band is when a phonon is required, namely indirect or direct band-gap semiconductors, respectively. If a phonon is needed, the electron is moved in the *k*-space by the absorption of the phonon and is therefore called indirect semiconductor. Additionally, as only electrons in the conduction and holes in the valence band contribute to the conductivity, a higher temperature means higher conductivity for semiconductors. This is exactly contrary to the behavior of metals, which show a lower conductivity at higher temperatures due to more scattering.

From quantum statistics (*cf.* **Figure 2.10 d**) it can be seen that in an intrinsic semiconductor some electrons are thermally excited to the conduction band and leave a hole in the valence band. This effectively means that an exciton (electron-hole pair) is created. This quasiparticle can be described with a wavefunction and by reducing the dimensions continuously, less states are available for the particle to occupy. Finally, at small enough sizes the particle dimensions are so small that the wavefunction does not fit completely into the crystal, *i.e.*, the particle is smaller than the exciton Bohr radius. Consequently, the exciton must be described as a particle in a box and the corresponding

energy levels are discretized. This obviously affects the absolute energies of the valence and conduction states and can be thought of as a particle in a box with an infinitely high potential barrier. As the electronic energy levels in this model are proportional to n^2, orbitals / bands of higher quantum numbers n are more destabilized than the ones with lower n. Effectively, this results in the broadening of the band gap, as the frontier states are energetically drifting apart when the particle size decreases. This is schematically shown for different sizes in **Figure 2.11**.

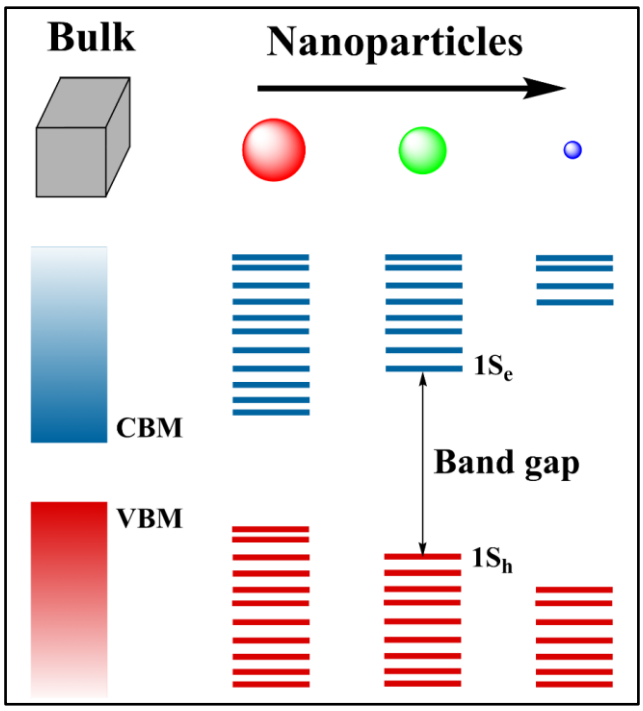

Figure 2.11: The broadening of the band gap for differently sized nanoparticles in comparison to the bulk material. The conduction band minimum and valence band maximum are given as CBM and VBM, respectively. The frontier states for nanoparticles are denoted as $1S_e$ and $1S_h$, due to the tearing of the bands. The band gap is present in all cases, however for better visibility only shown for one example.

However, the presence of excitons contributes another, stabilizing factor in the form of the exciton binding energy, *i.e.*, the Coulomb interaction of the electron and hole (second term in **Equation (2.18)**). Therefore, the overall broadening of the gap can be described with the Brus equation: [57]

$$\Delta E_g = \frac{h^2}{8r_{NC}^2}\left(\frac{1}{m_e^*}+\frac{1}{m_h^*}\right) - \frac{1.8e^2}{4\pi\varepsilon_{NC}\varepsilon_0 r_{NC}}. \tag{2.18}$$

With the change in the width of the band gap ΔE_g, effective masses of the electron and hole m_e^* and m_h^*, respectively, the permittivity of the NC material ε_{NC}, and elementary charge $e = 1.602 \cdot 10^{-19} C$.

Upon decreasing the size of a crystal, the formation of defects has much greater impact on the properties, as already small quantities can drastically affect the electronic structure. This is because the electronic structure is formed by a comparably small number of atoms and is therefore more susceptible to defects. The defects in a nanocrystal are of different nature and can be summarized

under the term trap states. Exemplarily, the surface-to-volume ratio is increased continuously for smaller particles, thus, a higher percentage of the atoms is located at the surface which means they are not completely saturated. This creates dangling bonds, which are orbitals that are not contributing to the overall electronic structure of the NC. The energy levels of these orbitals can be located inside the band gap and are one origin of trap states. As discussed in chapter 2.1 a peculiarity of perovskites is that these dangling bonds are not inside the band gap, which contributes to their outstanding electronic properties. [46] However, dangling bonds are not the only source of trap states for NCs, other, energetically more demanding traps like interstitials or antisites are also possible. Traps of this type are interrupting the symmetry of the crystal which interferes with the band formation, as it is described above, resulting in the formation of novel energy states. Generally, states within the band gap can be classified as either deep or shallow traps, depending on the energy difference between trap state and frontier state of the NC. Trap states are interfering with electronic properties as they decrease the conductivity. Also, the optical properties are affected because traps provide non-radiative recombination centers for excitons which lowers the luminescence quantum yield. [23,46]

2.9. Optical Properties of Nanocrystals

From the chapter above it becomes apparent that the transition between bands / states of charge carriers is of crucial interest for many properties and applications of semiconductor-based materials and devices. In order to excite an electron from the valence to the conduction state, it has to be exposed to an external perturbation which can be described by the time-dependent first order perturbation theory. [134] A main finding of said theory is Fermi´s Golden rule for the transitions into continuous states. [134] It correlates the transition rate $W_{f\to i}$ to the matrix element (Hamiltonian) of the distortion $|V_{fi}|$ and the density of states by: [134]

$$W_{f\to i} = 2\pi\hbar|V_{fi}|^2 DOS(E_f). \tag{2.19}$$

With the matrix element of the perturbation $|V_{fi}|$, *e.g.*, an incident electromagnetic wave, and the density of states at the final state $DOS(E_f)$. The initial and final state are denoted by the subscripts *i* and *f*, respectively.

However, the transition not necessarily finalizes in a continuous state distribution and a different description for discrete states is required. One approach is given by the Franck-Condon principle for vibronic (*i.e.*, vibrational + electronic) transitions. [134–136] The basic model to derive such transitions is the anharmonic oscillator. [137] The transition probability can be obtained by applying a product ansatz for the wavefunction $\Psi = \Psi_v\Psi_e$, where the spin is neglected for simplicity, and the operator for the dipole moment is applied onto the function. [134] The probability is then given by:

$$\langle \varepsilon' \nu' | \hat{\mu} | \varepsilon \nu \rangle = \int_{-\infty}^{\infty} \Psi'^{*}_{\nu} \Psi_{\nu} d\tau_{\nu} \int_{-\infty}^{\infty} \Psi'^{*}_{e} \hat{\mu} \Psi_{e} d\tau_{e} \qquad (2.20)$$

$$with\ \hat{\mu} = -e \sum \vec{r}_i + e \sum Z_I \vec{R}_I.$$

Where the vibrational state and wavefunction is denoted with ν, the electronic state with e, the integration over all spatial coordinates is represented by τ. The dipole operator $\hat{\mu}$ is explicitly given, with the location of the electron $\vec{r}_i$ and nuclei $\vec{R}_I$ with charge Z.

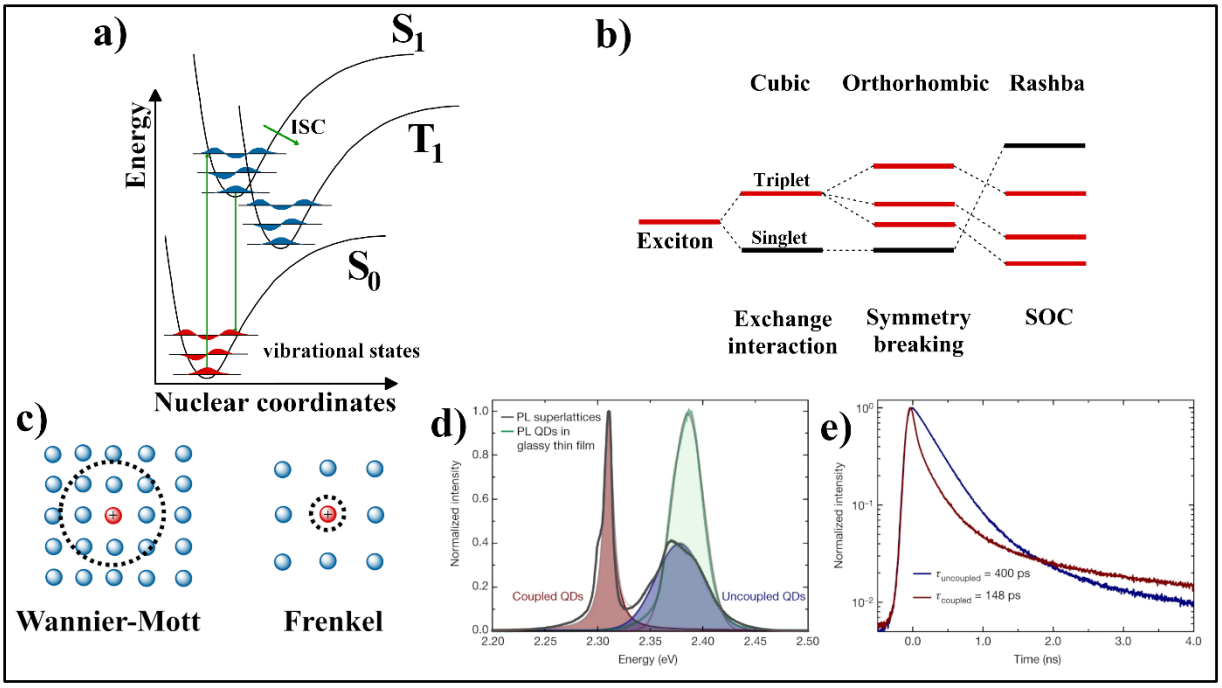

Figure 2.12: a) Visual depiction of vibronic transitions (green arrows) from the electronic ground state S_0 to the excited state S_1. Succeeding the excitation, the system can either relax radiatively (fluorescence) or non-radiatively *via* thermal equilibration to S_0 or intersystem crossing (ISC) to the triplet state (T_1) with subsequent radiative relaxation to the ground state again (phosphorescence). The triplet state is lowered due to increased exchange interactions between two electrons. The lowest 3 vibrational states for each state are represented by their wavefunction in the Morse potential. b) Excitonic fine structure of perovskites. The exciton is adjusted in a first step by the exchange interaction of electron and hole. For the cubic structure this results in a triple degenerate triplet state and a singlet state. However, by breaking the symmetry (transition to orthorhombic) the degeneracy is lost. By additionally adding spin-orbit coupling (SOC) in a crystal system with inversion center (Rashba effect) the energetics are reversed. Optically active and passive states are depicted in red and black, respectively. c) Simplified picture of excitons, shown are a Wannier-Mott (left) and Frenkel exciton (right). The hole is depicted in red and the orbit of the electron as a dashed line. d) Superfluorescence spectra of $CsPbBr_3$ QDs, the superfluorescence signal is shown in red and denoted by "coupled QDs". The uncoupled analogue, *i.e.*, a structural incoherent sample, is shown in blue and green. e) Photoluminescence lifetimes for the superfluorescence (red) and uncoupled case (blue). d) + e) Reprinted by permission from Rainò *et al.*: Springer Nature, Nature Superfluorescence from lead halide perovskite quantum dot superlattices, Rainò *et al.* [139], Nature (2018). Partly edited.

The two integrals in **Equation (2.20)** can be rationalized as the so-called Franck-Condon factor (FCF) (first term) which is the overlap of the vibrational part of the wavefunction and the transition dipole moment (TDM) (second term). A graphical depiction of the FCF is given in **Figure**

2.12 a, one can see that only transitions with a large overlap are favorable. However, it must be noted that only vertical transitions are allowed due to the Born-Oppenheimer approximation. From the FCF and TDM, the selection rules can be deduced and allowed transitions identified. [134] A simplified picture and correlation to the measurable spectra (absorption and emission) gives the Jablonski term scheme, in which the available states and transitions are shown simultaneously. [138] The allowed transitions finally define the absorption and luminescence spectra of a material, which are experimentally accessible. The oscillator strength of a transition (magnitude of the integral given in **Equation (2.20)**) gives rise to the extinction coefficient which is used for example in Lambert-Beer´s law.

Through vibronic transitions, excitons are created where the electron and hole pair can either be spatially separated extremely (Wannier-Mott) or be in close proximity (Frenkel) as shown in **Figure 2.12 c**. The latter is typically associated with excitons in organic semiconductors where the wavefunction of the exciton is confined to the molecule. [140] On the other hand, the Wannier-Mott excitons are more relevant for semiconductors and NCs. The electron is excited to the conduction band and moves in an orbit around the hole, which remains stationary. [141] In either case the separation of electron and hole results in a coulombic interaction, which is the exciton binding energy. The magnitude of the binding energy can be approximated by the hydrogen atom model and for a Wannier-Mott exciton is given by: [142]

$$E_b^{exc} = -\frac{1}{2}\frac{\mu^* e^4}{(4n\pi\varepsilon_0)^2 \varepsilon_r^2 \hbar^2}. \tag{2.21}$$

With the effective mass μ^*, and principal quantum number n.

The exciton binding energy acts as a stabilizing force, which positions the energy levels of the excitons below the conduction or above the valence band, or for molecular excitons the highest occupied molecular orbital (HOMO) and lowest unoccupied molecular orbital (LUMO). The magnitude of the binding energy differs significantly for the two types of excitons, with the Wannier-Mott exciton typically exhibiting energies of ~ 10 meV, and Frenkel excitons of ~ 1 eV, a factor of 100 times larger. This is due to the different radii of the electron orbit, ~ 10 nm for Wannier-Mott and ~ 1 nm for the Frenkel analogue. [142]

If a nanocrystal becomes smaller than the respective exciton Bohr radius of the exciton the quasiparticle is confined. If the dimensions of the NC are significantly smaller than the exciton radius the system is considered to be in strong confinement, whereas for comparable radii the weak confinement regime is reached. For perovskite materials the stoichiometry dependent exciton Bohr radii are calculated to be 5 nm, 7 nm, and 12 nm for $CsPbCl_3$, $CsPbBr_3$, and $CsPbI_3$, respectively. [19] Additionally, quantum confined systems show a size-dependence of the exciton binding energy, the trend for 2D perovskites was found to be a reciprocally exponential increase of the binding energy

with the width of the quantum well. [143] Meaning, that excitons are more tightly bound in smaller structures.

The overall energy of an exciton is $E_{exc} = E_g + E_b^{exc} + E_{kin} + E_{exch}$, where E_{exch}[**] is the electron-hole exchange interaction. Upon considering this exchange interaction of the exciton one finds that the singlet state is lower in energy, as the triplet state does not contain this contribution. This is schematically shown in **Figure 2.12 b**, where the respective states are split, with the singlet state lower in energy. Typically, the lowest exciton state is considered a dark state because the relaxation is electric dipole forbidden, and transitions must follow the selection rules of dipoles. [144,145] Additionally, the transition from the bright state to the energetically lower dark state is not easily accessible, as it requires 2 phonons. [146] Therefore, in perovskites the emission is obtained from the excitonic triplet states, despite the dark-bright splitting being comparably small (~ 0.5 – 2 meV) and large spin-orbit coupling. [144–148] The single dark singlet state in perovskites is generated from the Pb 6s and halide Xp orbitals, and the triplet states from the Pb 5p orbitals. [147] The three p orbitals of Pb generate the threefold degeneracy of the triplet state, which becomes apparent upon breaking the symmetry of the crystal. [147] If the symmetry is lowered (cubic → orthorhombic) the degenerate states split up due to the different lattice constants for each spatial direction. [147] The splitting can be observed as three distinct luminescence signals at low temperature. [146] By including spin-orbit coupling in a crystal without inversion center (Rashba effect) the absolute energies of singlet and triplet are switched (see **Figure 2.12 b**). [144,146,147] Perovskites are for now the only known material to exhibit such an effect, where the lowest exciton state is emissive. [145]

The excited state has a certain lifetime, *i.e.*, the time spent in this state, which decays exponentially as the wavefunction is time-dependent $\Psi(\vec{r},t) = \Psi(\vec{r})e^{-iEt/\hbar - t/\tau}$. Therefore, the intensity of the emitted light also follows this exponential decay, *i.e.*, $I(t) = I_0 \exp(-t/\tau)$. This decay can also include several decay mechanisms and thus consist of multiple contributions with distinct lifetimes. In order to decay, the excited state has to emit energy. Without external stimulation, this can be realized by either light emission, in the form of fluorescence (electron singlet → singlet transition) or phosphorescence (electron triplet → singlet transition), internal conversion (thermal equilibration) or external quenching, where the latter 2 cases are non-radiative processes. [134,149] Another notable non-radiative relaxation mechanism is trap state recombination, as trap states provide energetically favorable recombination centers for excitons. The ratio of radiative to overall recombination gives a measure for the quantum yield (QY).

$$QY = \frac{k_r}{k_r + \sum k_{nr}}, \tag{2.22}$$

with the radiative rate constant k_r, and non-radiative rate constants k_{nr}.

[**] E_{exch} is the energy which occurs due to exchanging two otherwise similar particles: $E_{exch} = \langle \Psi_a \Psi_b | \hat{H} | \Psi_b \Psi_a \rangle$

Another remarkable property of excitons in perovskites is the creation of trions, *i.e.*, charged excitons, composed of either 2 electrons and a hole (negative trion) or 2 holes and an electron (positive trion). [150,151] In a charged NC, as it could be created in an ELQLED through charge carrier imbalance, the excitation of excitons results in the formation of trions. These quasiparticles have implications on the optical properties, especially the lifetime. Perovskites mostly exhibit a lifetime composed of multiple contributions, and the creation and annihilation of trions is an explanation for extremely fast lifetime decay components. [151]

With the formation of excitons, electrons are excited into a state in which they can move more freely. This inflicts the formation of polarons, created by the interaction of longitudinal optical phonons and electrons. [99] These polarons can experience strong coupling to the phonon (small polaron) and be strongly localized or weak coupling (large polarons) and are still able to move comparably free. [152–155] As electrons and (longitudinal optical) phonons are coupled, the quantum mechanical description yields a coupling constant, the so-called Fröhlich interaction: [152,153]

$$\alpha = \frac{e^2}{\kappa}\left(\frac{m_e}{2\hbar^3\omega_{phonon}}\right)^{\frac{1}{2}}, with\ \kappa^{-1} = \varepsilon_\infty^{-1} - \varepsilon_0^{-1}. \tag{2.23}$$

With the electron mass m_e, phonon frequency ω, as well as static (ε_0) and high frequency (ε_∞) dielectric constant of the material.

Among other influences, the electron-phonon coupling can be observed in the Urbach energy of the absorption spectrum. [156] This energy describes the energetic disorder near the absorption onset, thus summarizing effects like polarons, trap states, structural coherence, and others. [157,158] Experimentally, the Urbach energy can be seen as an exponential decay of the extinction coefficient into the band gap (Urbach tail), and its magnitude is proportional to degree of disorder. [159] This effect can also be used to explain the conductivity in hydrogenated, amorphous silica (comparable to the aforementioned SiO_x shell). [104,159]

On the other hand, polarons also inflict easily measurable implications for the photoluminescence spectra, namely (temperature-dependent) broadening of the emission. [160,161] The signal broadening is mainly due to the coupling to longitudinal optical (LO) phonons, as the lattice deformation induced by the electron has the same symmetry and can be derived by: [160]

$$\Gamma(T) = \Gamma_0 + \Gamma_{ac} + \frac{\gamma_{LO}}{e^{\frac{E_{LO}}{k_B T}} - 1}. \tag{2.24}$$

Where Γ_0 is an intrinsic broadening due to *e.g.*, scattering by disorder, Γ_{ac} is a linear broadening due to the coupling to acoustic phonons ($\Gamma_{ac} \ll \Gamma_{LO}$ at high temperatures), γ_{LO} is the coupling strength of the phonon and electron, and E_{LO} is the phonon energy. Despite being small compared to the coupling to LO phonons, the coupling to acoustic phonons is important to understand bandgap renormalization in perovskites. [162] The symmetry of acoustic phonons results in larger or smaller binding distances,

which affects the interaction strength of Pb and halide. If the distance is increased, the interaction is lowered and *vice versa*. This results in a broadening / narrowing of the band gap (not to be confused with thermal expansion), which is known as bandgap renormalization. An outstanding feature of LO phonon coupling is the detection of phase transitions because different phases also differ in phonon frequency which in turn changes the coupling strength and thus the temperature dependence of the phonon broadening. [161]

Another important influence on the PL signal and QY of quantum confined semiconductors occurs when the shell (both inorganic in core-shell systems and organic in case of the ligand) is considered in addition. Firstly, only the inorganic core-shell system shall be considered, especially the electronic structure and absolute energy levels of both materials. By appropriately aligning the energy levels of core and shell the wavefunction for the electron or hole can be delocalized if the energy difference is small enough. [94,163] A similar effect, however due to different reasons, occurs for the ligand shell (*cf.* **Figure 2.13 a**). [164] Depending on the electronic structure and energetic composition, the delocalization of the exciton can be increased, which means a significant probability of observing the electron or hole on the ligand shell can be induced. [164] Both effects are summarized under the term exciton leakage and can experimentally be observed as a bathochromic (red-) shift in the PL signal. Additionally, the delocalization, *i.e.*, dislocation of the charge carriers induced by *e.g.*, exciton leakage has dramatic influences on the efficiency of the material. [163] The dislocation of the charge carriers can result in the separation of the exciton if an external field is applied (voltage). As the exciton is in spatial partition the recombination is far less likely, which results in a lowering of the QY because non-radiative relaxation becomes more likely (**Figure 2.13 b**). [163] On the other hand, the dislocation can also be beneficial as it can reduce Auger recombination in the NC. If one of the respective wavefunctions is more delocalized than the other, the probability for Auger recombination (**Figure 2.13 c + d**) decreases drastically. This is due to the spatial separation and therefore the absence of energy transfer between two neighboring excitons. [163] The last non-radiative process is trap state recombination, which was already discussed above. Most of these traps are located at the NC surface, mostly in the form of dangling bonds, and can be saturated very effectively by the synthesis of a shell. These effects emphasize how complex the shell design for NCs is and that a broad variety of effects affects the outcome.

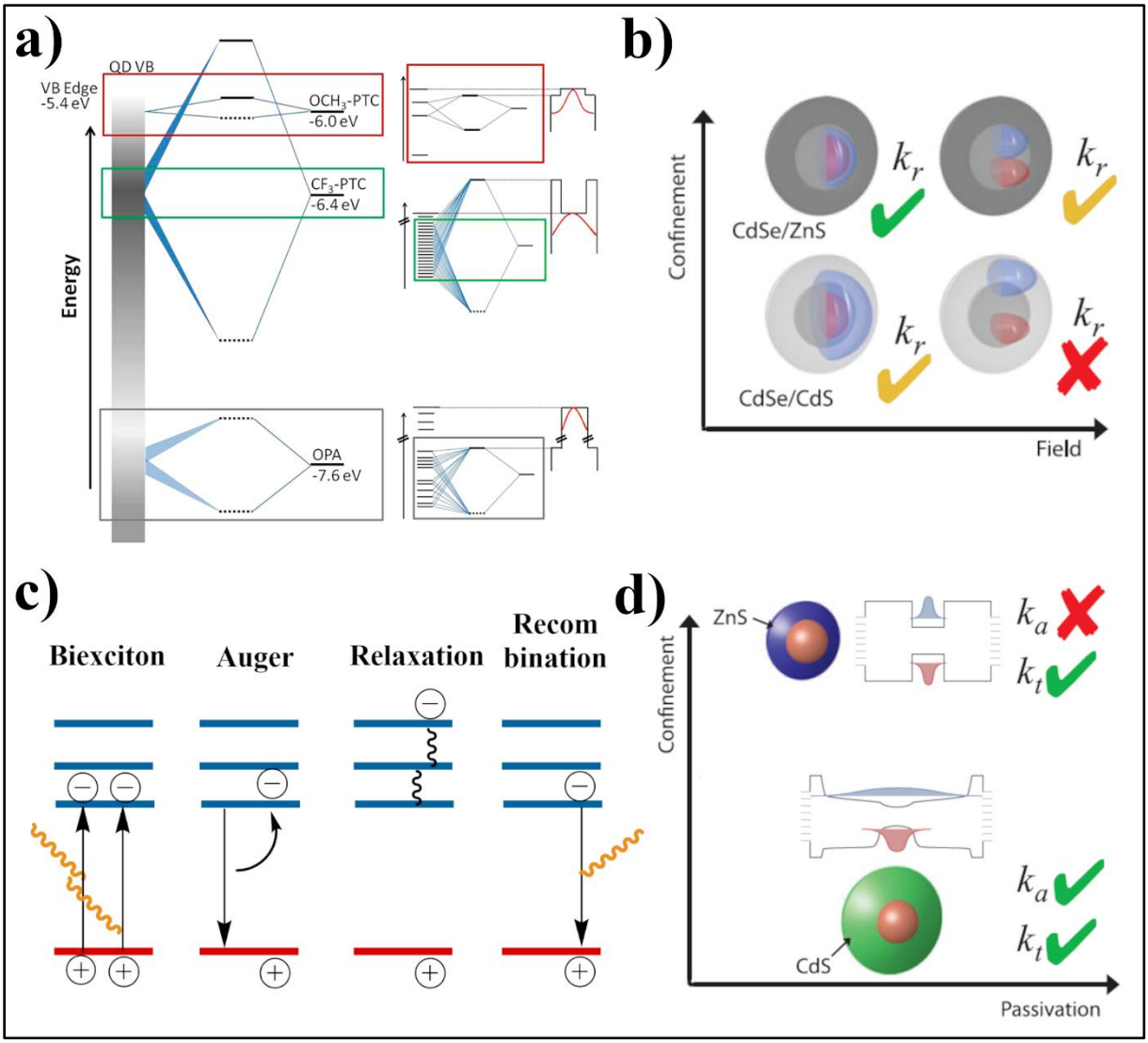

Figure 2.13: a) Interaction of NC and ligand electronic structures resulting in exciton leakage. The NC is depicted by a continuum of states as a grey bar on the left and the ligand frontier states are on the right. The orbitals created upon binding are in the middle. Upon achieving resonant alignment of the frontier states, the excitonic wavefunction can extend onto the organic ligand shell (red and green box). If the frontier states of the ligand are not located near the valence band edge and resonance cannot be achieved, the localization of the wavefunction is maintained (grey box). b) Field induced quenching for two systems. For the top case of CdSe/ZnS the stronger electric field does not result in field induced quenching because the energy difference between core and shell is large enough. Therefore, the excitonic wavefunction (blue and red for electron and hole, respectively) is not separated. The lower case shows a splitting of the exciton where the electron is dislocated onto the shell. c) Auger assisted quenching which requires the formation of a biexciton. The first exciton recombines non-radiatively whilst the second absorbs the energy and is thus elevated in energy. After thermal equilibration (relaxation) the second exciton recombines radiatively, resulting in a loss of half of the excitons. d) Prerequisites for Auger quenching, if the wavefunctions are in proximity this process becomes less likely, as the radiative combination is much more likely (top). Whereas if the functions are separated Auger processes are more likely (bottom). a) Reprinted with permission from Frederick *et al.* [164] Copyright 2013 American Chemical Society. b) + d) Reprinted by permission from Bozyigit and Wood: Springer Nature, MRS Bulletin, Challenges and solutions for high-efficiency quantum dot-based LEDs, Bozyigit & Wood, MRS Bulletin (2013). Partly edited.

One outstanding property of perovskites is superfluorescence. [139] Main characteristics of superfluorescence are a hypsochromic (blue-) shift of the emission combined with a decrease in

FWHM and a shortened PL lifetime (**Figure 2.12 d + e**). [139] Both effects can be deduced from the coupling of individual NCs in a superlattice, which can drastically alter the optical properties (*cf.* results chapter 3). Notably, the emission of photons from superfluorescence is coherent, whereas for uncoupled NCs the emitted light is incoherent. [139] It was shown for $CsPbBr_3$ NCs, when situated in a highly ordered superlattice, that the particles can couple *via* photon fields (comparable to electromagnetic fields from a Hertzian dipole) to establish a coherent state. [139] Precisely, this means that the dipoles of the excited states are aligned, and the subsequent emission experiences the above states properties. [139] An important requirement for superfluorescence is the confinement of the individual emitters (that are NCs) into a volume of λ_{em}^3, where λ_{em} is the emission wavelength of an isolated NC. [165] This highlights the necessity of the superlattices for the phenomenon to occur.

2.10. Electrical Properties of Nanocrystal Arrays

In order to access the conductivity in nanocrystal arrays, the force $\vec{F} = \hbar(d\vec{k}/dt) = q\vec{E} + q\nabla\vec{\epsilon} \times \vec{B}$ acting on a charge carrier must first be considered. It contains the influence of the lattice $(d\vec{k}/dt)$ as well as external electrical and magnetic fields.[99] The force can be of differing nature, for simplicity only constant fields will be considered. If solely a constant magnetic field is applied the electron will experience the Lorentz force and this results in the movement along surfaces of constant energy. The path therefore not necessarily is a straight line, rather the electron moves along the Fermi surface. [99] On the other hand, the application of a constant electrical field, like it is the case if a voltage is applied, results in the electron moving with an effective mass given by: [99]

$$\frac{1}{m^*} = \frac{1}{\hbar^2}\frac{d^2\epsilon}{dk^2}. \tag{2.25}$$

Effectively, this means the periodic potential determines the effective mass *via* the dispersion relation, or more precisely by its curvature. The effective mass of an electron in the conduction band is distinct, however due to spin-coupling, the holes (in the valence band) are experiencing two different dispersion maxima which results in two effective masses, namely light and heavy holes. Notably, the dispersion is dependent on the spatial direction inside the crystal, therefore the effective mass is a tensor and spatially dependent. [99] Since the dispersion relation of electrons is proportional to a cosine (**Equation (2.16)**) and $\vec{k}$ becomes time-dependent by applying an electrical field, the sign of the effective mass oscillates upon moving through the lattice. This means electrons oscillate inside the first Brillouin zone with a period of $\omega_B = \frac{e}{\hbar} \cdot E_0 \cdot a$, proportional to the strength of the external field E_0 and lattice constant a, because a negative sign refers to a movement in the opposite direction [129]

However, in real solids the lattice constant is small enough that the charge carrier propagates faster than it oscillates, this means these Bloch oscillations are suppressed and the electron can propagate.

An external electrical field thus results in the acceleration of the charge carriers, and the movement can then be described by the (extended) Drude equation: [99,166,167]

$$\sigma = \sigma_e + \sigma_h + \sigma_{ionic} = e\left(n\mu_e + p\mu_p\right) + FZc(\mu_+ + \mu_-). \tag{2.26}$$

With the conductivities σ_i, for electrons, holes, and ions, the charge carrier densities n and p for electrons and holes, respectively, the mobilities μ_i, Faraday constant $F = 9.6485 \cdot 10^4\ A \cdot s \cdot mol^{-1}$, ionic charge Z, ionic concentration c, and mobilities $\mu_\pm$ for anions and cations.

The Drude model drastically simplifies the movement of charge carriers in NC solids. As nanocrystals are separated entities the transport is mostly dominated by tunneling processes. [22,33,168] The transfer integral β gives a measure for the tunneling efficiency of a NC system, as it is linked to the tunneling rate τ by $\beta = \frac{h}{\tau}$. Guyot-Sionnest´s approach to model the tunneling rate of weakly coupled NC ensembles is as follows: [169]

$$\tau^{-1} = \frac{2E_A}{h}\exp\left(-2\frac{\sqrt{2m^*\Delta V}}{\hbar}\,(D-2r)\right)\exp\left(-\frac{E_A}{k_BT}\right). \tag{2.27}$$

With the hopping activation energy E_A, height ΔV and width $D - 2r$ of the tunneling barrier.

As previously discussed, charge carriers in semiconductors couple to phonons, especially LO phonons which are connected to charge transport. Therefore, the model by Guyot-Sionnest can be extended to small polarons. These quasiparticles were first described by Holstein and their transport/tunneling can be described by the Marcus` theory of electron transfer: [154,155,170]

$$\tau_{pol}^{-1} = \frac{E_A^2}{\hbar\pi^2}\exp\left(-4\frac{\sqrt{2m^*\Delta V}}{\hbar}(D-2r)\right)\sqrt{\frac{\pi}{k_BT\,\lambda_{reorg}}}\exp\left(-\frac{\left(\lambda_{reorg}+\Delta V\right)^2}{4\lambda_{reorg}k_BT}\right). \tag{2.28}$$

With the reorganization energy λ_{reorg}.

The tunneling barrier is not the only obstacle that needs to be overcome by a charge carrier that moves in a mesocrystal. As charges are injected into an adjacent NC the overall charge balance is altered, this results in a coulombic repulsion and is known as the charging energy or Coulomb blockade. [171–173] By following the modified Laikthman-Wolf model, the charging energy E_C is given by: [173]

$$E_C = \frac{e^2}{2(C_s + nC_m)}. \tag{2.29}$$

Where C_s is the self and C_m the mutual capacitance, n denotes the number of nearest neighbors.

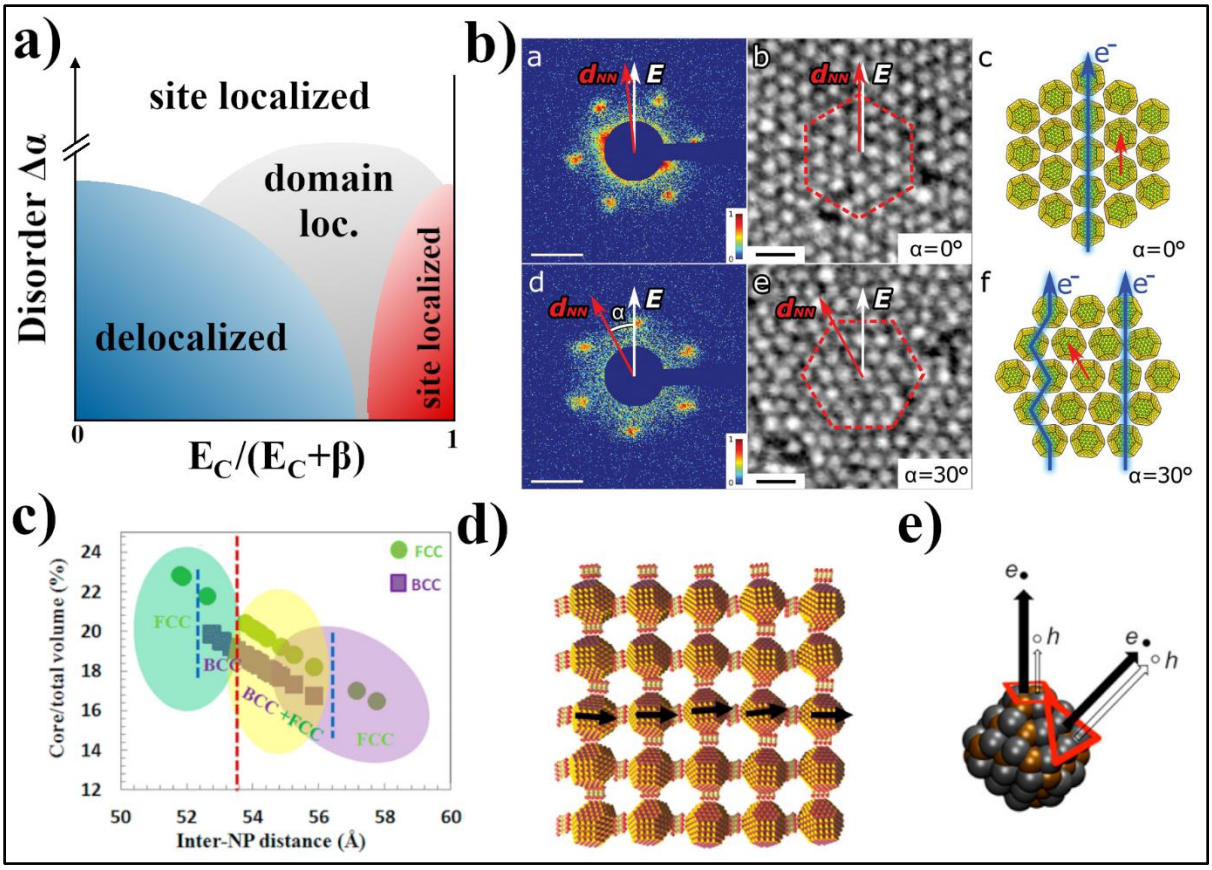

Figure 2.14: a) Interplay of charging energy, transfer integral and energetic disorder. The different possible transport regimes are depicted in blue (delocalized), red (site localized or Mott insulator), grey (domain localized), and white (site localized or Anderson insulator). b) Charge carrier propagation anisotropy induced by the orientation of the NC SL. If the nearest-neighbor distance and electrical field are in line, charge transport can take place more easily (top). If not, the electron has to move along the nearest-neighbor direction rather than along the electrical field, which lowers the current (bottom). This effect contributes to the energetic disorder depending on the local orientation of the SL. c) Packing density of fcc, bcc and distorted (fcc + bcc) PbS superlattices. A bcc lattice always exhibits a denser packing, which in turn affects the nearest-neighbor distance. d) Local distortions between the atomic and superlattice. The direction of the atomic lattice is given as a black arrow, which are slightly alternating for every NC, due to its orientation, and thus are not directed in the same direction as the superlattice lattice vector. e) Coupling of electron and holes to the lattice in PbSe NCs, where facets show different coupling strengths (indicated as arrows). The result is a facilitated carrier transport along a facette with high coupling for electron or hole, respectively. a) Adapted with permission from Ref. [174], with permission from ChemPhysChem. © 2001 Wiley-VCH Verlag GmbH & Co. KGaA, Weinheim. b) Reprinted with permission from Ref. [31], with permission from Advanced Materials. © 2020 Wiley-VCH Verlag GmbH & Co. KGaA, Weinheim. c) Reprinted with permission from Wang *et al.* [177] Copyright 2013 American Chemical Society. d) Reprinted with permission from Zaluzhnyy *et al.* [178] Copyright 2017 American Chemical Society. Partly edited. e) Reprinted with permission from Kaushik et al. [179] Copyright 2014 American Chemical Society. Partly edited.

The components of **Equation (2.29)** are discussed in chapter 5. Both influences, *i.e.*, charging energy and transfer integral are in direct competition and can be expressed as a dimensionless parameter $E_C/(E_C+\beta)$ describing the charge injection between adjacent NCs. This parameter can have values between 0 and 1 and very basically describes the coupling between NCs and can be used to estimate the type of conductivity in a mesocrystal. If the parameter is small, delocalized transport occurs, whereas if the value increases domain and site localized (Mott insulator) transport occurs

(**Figure 2.14 a**). [172,174,175] The Mott insulator transition takes places when the system can no longer overcome the charging energy. Another crucial parameter, especially for NC samples, which intrinsically have a size distribution, is the average energetic fluctuation $\Delta\alpha$. If the mesocrystal exhibits a large structural, and thus energetical, disorder this can lead to so-called Anderson localization, and the system can no longer maintain the delocalized transport and charge carrier propagation mainly occurs as site localized. [176]

Anderson localization can occur due to a variety of reasons, exemplarily the orientation of the external field and direction of the nearest-neighbor distance d_{NN} was found to be a determining factor in PbS superlattices. [31] If d_{NN} is directed in the same way as the electrical field, charge carrier transport is facilitated, whereas if an offset exists charge carriers have to move along a path following the NCs which increases the resistance of up to 40–50% (**Figure 2. 14 b**). [31] Another factor is the structure of the superlattice because it determines the interparticle distance which in turn is one of the most important factors for the tunneling efficiency (**Equations (3.52)** and **(3.53)**). If the SL exhibits a face-centered cubic (fcc) structure, d_{NN} is larger than in the body-centered (bcc) or hexagonal closed packed (hcp) analogs (**Figure 2.14 c**). [177] This means for a bcc structure a higher conductivity is to be expected, which could be shown in PbS SLs. [31,180] Until here the NCs in a SL were assumed to be homogeneous, however in reality they have a distinct size distribution which results in deviations from perfection whilst assembling. This results in imperfections of the orientation and is schematically shown in **Figure 2.14 d**, where an assembly of PbS NCs is shown with a distinct crystal direction. The imperfection can be described by correlating the SL with the atomic lattice (AL) and determining the angles between crystallographic axes. [31,178] The correlation can be obtained by simultaneous small and wide-angle scattering (SAXS and WAXS) and the gaussian widths of the reflexes can be used to calculate the deviation from a perfect alignment of SL and AL (*cf.* chapter 3). For the mentioned PbS sample the disorder could be measured to be up to 10%. [178] Lastly, as mentioned before the effective mass of charge carriers is an anisotropic property, which means the movement along differing axes cannot be equally effective. For example, in PbSe NCs electrons are more easily transported towards the edges of the nanocrystal, whereas the holes are more likely to move towards the facettes of a particle (**Figure 2.14 e**). This results in different mobilities and is another factor that influences the energetical disorder. [179] All in all, the energetic disorder is a factor which is hard to calculate due to the large variety of complex phenomena summarized within, however it is a crucial factor that must be kept in mind. If the charge carrier transport in NC arrays is described, all of the above explained factors (E_C, β and $\Delta\alpha$) and the interplay of them needs to be considered, as graphically summarized in **Figure 2.14 a**. [174] It can be seen that only for a low energetical disorder and a facile charge carrier injection delocalized transport is theoretically possible, however in practice this is hardly achieved. There are many properties that can be altered to improve the charge carrier injection and thus the transport properties. This will be discussed in further detail in the following chapters.

The above considerations mainly focus on the estimation of charge carrier propagation but contain no information on the actual movement of a charge carrier. The easiest approach to determining the conduction mechanism is to measure the temperature dependence. Contrary to metals, semiconductors have lower conductivities at lower temperatures, because the charge carrier density obeys the Fermi-Dirac distribution and thus at lower temperatures, less free charge carriers are available, such that they exhibit a thermally activated conductivity. However, as NCs are isolated entities and charge carriers couple to the lattice, typically only hopping propagation is possible. At higher temperatures enough thermal energy is available to realize Arrhenius type nearest-neighbor hopping (NNH), where the charge carriers simply hop to the next available site. This mechanism follows a simple exponential behavior: [181,182]

$$\sigma(T) = \sigma_0 \cdot \exp\left(-\frac{E_A}{k_B T}\right), \tag{2.30}$$

with the conductivity σ_0, and hopping activation energy E_A.

If the temperature is lowered, less energy for the hopping process will be available which results in the unavailability of certain states. This effectively means that charge carriers cannot jump to the next available site, but rather jump to a site that is energetically more favorable. Since this site is often not located next to the initial site, this process is known as variable range hopping (VRH) and was first discussed by Mott. [182–184]

$$\sigma(T) = \sigma_0 \exp\left(\left(\frac{T_M}{T}\right)^{\frac{1}{1+n}}\right) \quad with\ T_M = \frac{21.2}{k_B g_0 \xi^3}. \tag{2.31}$$

Where T_M is a characteristic temperature, n the dimensionality, g_0 the local density of states, and ξ the localization length. Within Mott VRH the charging energy, *i.e.*, the coulomb interaction is neglected since the thermal energy is still comparably large. However, upon further decreasing the temperature, the Hubbard gap opens, and this effect can no longer be neglected. [174,182] Therefore, the model needs to be adjusted, which was done by Efros and Shklovskii (ES VRH): [185]

$$\sigma(T) = \sigma_0 \exp\left(\left(\frac{T_{ES}}{T}\right)^{\frac{3}{3+n}}\right) \quad with\ T_{ES} = \frac{\beta_{ES} e^2}{k_B \varepsilon_r \xi}. \tag{2.32}$$

With the characteristic temperature T_{ES}, a numerical constant near unity β_{ES}. The transition from Mott to ES VRH can be estimated by comparing the characteristic temperatures $T_{cross} = \frac{16 T_{ES}^2}{T_M}$.

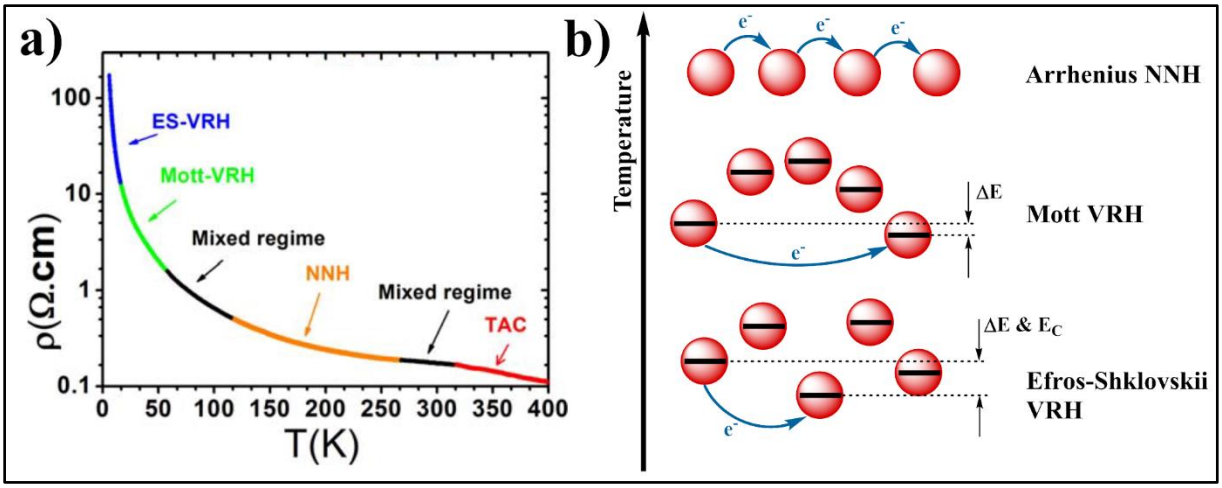

Figure 2.15: a) Temperature dependence of the specific resistance in SbO_2 nanobelts. The slope of the curve represents the conduction mechanism at the respective temperature regimes, and the corresponding mechanism is denoted as well. TAC is temperature activated conductivity, which is delocalized. b) Depiction of hopping type conductivity at different temperatures. For NNH the electrons propagate to adjacent NCs, whereas for Mott VRH hopping the electron is transferred to an energetically favorable site. The different energies are represented by the black bars. In the case of Efros-Shklovskii VRH the charging energy is considered as well, changing the availability of sites. a) Reprinted with permission from Ref. [182], with permission from Physica Status Solidi Rapid Research Letters. © 2012 Wiley-VCH Verlag GmbH & Co. KGaA, Weinheim.

2.11. Ligand Exchange

For nanocrystal samples the ligand shell has drastic implications (*cf.* chapter 2.12), therefore it is of enormous interest to develop procedures to exchange the ligand shell and tune the NCs to specific needs. In rather simple approaches the exchange is carried out either in solution or solid state, in which the surface equilibrium at the NC is utilized. This equilibrium is created between the bound species (native) and the novel ligand:

$$[native]_{bound} + [novel]_{free} \rightleftharpoons [native]_{free} + [novel]_{bound}$$

$$K_{surf} = \frac{[native]_{free}[novel]_{bound}}{[native]_{bound}[novel]_{free}} \tag{2.33}$$

With the concentration of the respective species given in brackets and their binding situation as subscript, K_{surf} denotes the surface equilibrium constant. The equilibrium, just like any other chemical equilibrium, can be manipulated by changing the prerequisites as the system will react to any change in *status quo* by (partly) compensating it (LeChâtelier principle). [186,187] Most importantly for the exchange on NCs is the reaction of the system towards concentration alterations. As a dynamic equilibrium is assumed, an increase in concentration (or even the addition) of novel ligand will shift the equilibrium towards the product side. Especially beneficial is the usage of a ligand with a higher

affinity to the NC surface, because this alters the reaction enthalpy. The equilibrium can also be shifted by changing the temperature, as K_{surf} is temperature dependent: [167]

$$\begin{gathered} \Delta G^0 = \Delta H^0 - T\Delta S^0 \\ and\ \Delta G^0 = -RT \ln K_{surf} \\ gives\ \frac{\partial \ln K_{surf}}{\partial T} = \frac{\Delta H^0}{RT^2}. \end{gathered} \tag{2.34}$$

Where ΔG^0, ΔH^0, and ΔS^0 are the standard free enthalpy, reaction enthalpy and entropy, respectively. $R = 8.314\,J/(mol \cdot K)$ is the universal gas constant. The last equation is known as the van´t Hoff equation **(Equation (2.34))** and can be used to calculate the temperature dependent behavior of the equilibrium constant. Explicitly, the equilibrium can be shifted to the product side (*i.e.*, exchanged side) by increasing the temperature if the reaction is exothermic (enthalpy $\Delta H^0 < 0$).

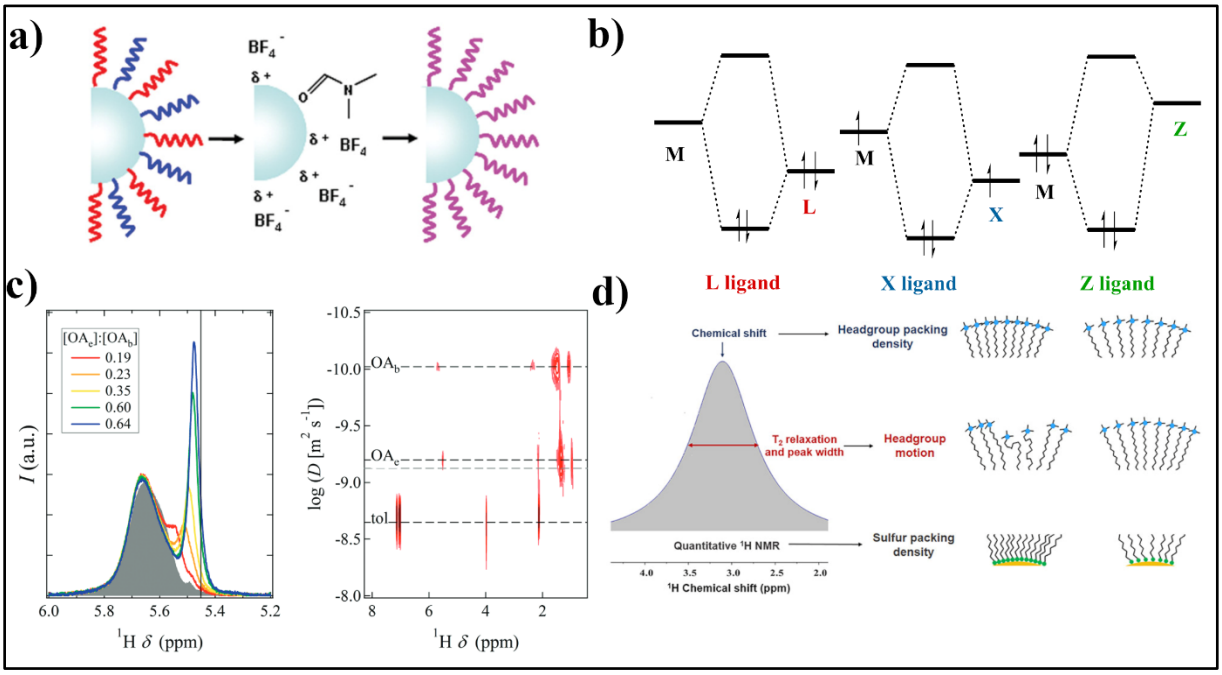

Figure 2.16: a) Schematic of the ligand exchange with oxidizing agents (here: $NOBF_4$), with the electrostatically stabilized particle in the middle, native ligands are shown in red and blue and the novel ligand in purple. b) MO schemes of L, X, and Z type ligands with a depiction of the electrons for the dative, covalent and reverse dative case. c) 1D ^{1}H-NMR of oleic acid on CdSe NCs, where the tethered ligand signal is underlaid in grey (left) and the corresponding DOSY which clearly shows the bound species at larger diffusion coefficients (left). d) Schematic of how the NMR signal is affected when the ligand is attached to a NC surface in the case of thiol-functionalized Au nanoparticles. a) Reprinted with permission from Dong *et al.* [189] Copyright 2011 American Chemical Society. Partly edited. c) Reprinted with permission from Fritzinger *et al.* [191] Copyright 2010 American Chemical Society. d) Reprinted with permission from Wu *et al.* [192] Copyright 2019 American Chemical Society.

A more drastic approach to exchange the native shell is by utilizing appropriate oxidation agents which react with the ligand. [188–190] Such oxidizing agents can oxidize the native ligand shell and form ethers, esters, phosphonates, or amines. [190] The organic reaction products are no longer able to tether at the NC surface and, to prevent a loss of stability of the particles, need to be replaced. After

the native ligand is removed, the now partially positively charged NC surface is passivated by the anionic counterions of the used salts, *i.e.*, BF_4^- or S^{2-} (**Figure 2.16 a**). [188–190] Subsequently, these counterions can easily be replaced by a desired, novel ligand (Schematic **Figure 2.16 a**). [189]

Next, possible ligand configurations need to be classified and the classical coordination number often does not represent the actual binding situation, or more precisely electronic situation, of a ligand. Therefore, Green introduced the novel $ML_lX_xZ_z$ system to better describe the situation in organometallic complexes, which are comparable to the binding situation on a NC surface. [193] Within this model it is differentiated between ligands that can contribute an electron pair (dative bond, L-type), an unpaired electron (covalent bond, X-type), and a free orbital (reverse dative bond, Z-type) (*cf.* **Figure 2.16 b**). [193] Notably, a ligand not necessarily only contributes a single type of character, for example chelate ligands can provide mixed L- and X-type functional groups, the number of such groups is reflected in the subscripts of $ML_lX_xZ_z$. [193] Depending on the surface of the NC, precisely the orbitals of the surface atoms that can interact, the character of the ligands can be decisive about the bonding. Exemplarily, in a Cs terminated facette of perovskites a Z-type ligand will not be able to bind effectively, as there are no available electrons in Cs^+ to be provided for the dative bond. With this nomenclature, qualitative evaluation of possible ligands and ligand exchange reactions can be understood in further detail. [194]

In nonpolar solvents the exchange of X-type ligands is strongly inhibited due to charge neutrality and these ligands will therefore remain strongly attached to the NC surface. [194] However, the exchange of neutral L- and Z-type ligands is easily accessible in such an environment (**Equation (2.35) a + b**). This results in a continuous adsorption and desorption of L-type ligands and can be described by a chemical equilibrium, as already stated above. Neutral Z-type ligands also readily exchange in aliphatic solvents; however, the exchange requires the displacement of metal complexes, which might be unfavorable for the stability of the NC. [195] Exemplarily, the exchange reactions will be shown for LHPs:

a) $(CsPbX_3)_m(X_5Pb)L + L` \rightarrow (CsPbX_3)_m(X_5Pb)L` + L$

b) $(CsPbX_3)_m(X_5Pb)_nL_n + Z \rightarrow (CsPbX_3)_m(X_5Pb_{n-1})ZL_{n-2} + PbL_2$ (2.35)

c) $(CsPbX_3)_m(X_5Pb)X + HX` \rightarrow (CsPbX_3)_m(X_5Pb)X` + HX$

Here, the term in brackets with subscript *m* denotes the NC, which does not participate in the exchange. (X_5Pb) represents the surface site at which the exchange takes place, *L* and *L`* are the native and exchanged ligand, respectively. Despite being inherently suppressed, X-type ligands are still able to exchange in aliphatic solvents, however they require an associated proton exchange, and the establishment of an equilibrium is inhibited (**Equation (2.35) c**). [191]

The situation drastically changes in polar solvents, as charge neutrality is no longer required. Therefore, X-type ligands can desorb easily (**Equation (2.36) a**). [196] An extreme case, which includes

the formation of a charged NC, of this is the exchange *via* $NOBF_4$ or Et_3OBF_4, as it was mentioned before (**Equation (2.36) b**). [189,190,194]

$$\text{a)}\ (CsPbX_3)_m(X_5Pb)X + X`^- \rightarrow (CsPbX_3)_m(X_5Pb)X` + X^-$$
$$\text{b)}\ (CsPbX_3)_m(X_5Pb)L + X`^- \rightarrow [(CsPbX_3)_m(X_5Pb)X']^- + L \qquad (2.36)$$

Obviously, exchange reactions should be monitored, and this can be very effectively done by nuclear magnetic resonance (NMR) as the environment of a proton affects the resonance enormously. [191,192,197] Most significantly for NCs, the immediate environment of the ligands, *i.e.*, either bound or free, affects the signal drastically. [191,192] Two main observations can be made if a ligand is tethered to the NC: the chemical shift is downfield shifted and broadened when compared to the free counterpart. [191,194] The downfield shift originates in intermolecular interactions of the ligand with other ligands and the NC, which contributes an additional term to the shielding constant. [198] The interaction obviously is distance-dependent and therefore accommodating ligands at the NC changes the packing density and this alters the potential, as shown in **Figure 2.16 d**. [192] The additional shielding changes the effective magnetic field at the probed nucleus and therefore its shielding:

$$\nu_i = \frac{\gamma_{mag}}{2\pi} B_0(1 - \sigma_i - \sigma_{int}). \qquad (2.37)$$

With the chemical shielding ν_i of the i-th nucleus, the gyromagnetic ratio γ_{mag}, the external magnetic field B_0, and the shielding of the nucleus and the interaction potential σ_i and σ_{int}, respectively.

The broadening also originates in the packing of the ligands on the surface, however the reason for this is the loss of rotational degrees of freedom. The loss results in a higher interaction between neighboring molecules and this decreases the transversal relaxation time T_2, meaning the transversal (spin-spin) relaxation is facilitated through the vicinity of the ligands. [194] The line width in the spectrum can then be estimated by the width of the peak $h_{1/2}$, and the effective transversal relaxation time T_2^* as $h_{1/2} = 1/(\pi T_2^*)$. Notably, T_2^* is not the actual relaxation time T_2, to transform them a correction factor is required. However, T_2^* is a lot easier to access as it is the decay constant of the free induction decay (FID) which is readily measured during an NMR experiment.

One of the most prominent peaks analyzed with respect to these two factors is the allyl peak in oleic acid since it shows a very prominent behavior (**Figure 2.16 c**). [191] However, not every peak exhibits these distinguishable features and other NMR techniques are required to deconvolute the peaks. Especially, diffusion ordered NMR spectroscopy (DOSY) is of enormous use for this purpose, because it can arrange the peaks observed in 1D NMR by the diffusion coefficient of the molecule. Therefore, tethered ligands are found at significantly lower diffusion coefficients and the peaks can be separated from the ones originating from the free ligand (**Figure 2.16 c**). [191,194] However, if the composition and morphology of the shell should be probed additional techniques like nuclear Overhauser effect NMR spectroscopy (NOESY) are required. [199,200]

Additionally, less expensive information is also contained in NMR spectra, *e.g.*, the quantitative analysis of bound and free peaks can be conducted. This is achieved by the application of a standard to reference the chemical shifts and, more importantly, the amount of substance. If the concentration of the standard is known, the concentration of the ligand can be calculated by:

$$c_{Ligand} = \frac{A_{Ligand}}{A_{standard}} \cdot \frac{N^H_{Ligand}}{N^H_{standard}} \cdot c_{standard}. \tag{2.38}$$

Where the concentrations *c*, area of the NMR peak *A*, and number of protons N^H are used for ligand and standard. **Equation (2.38)** enables the calculation of attached and free ligand, and thus the determination of the surface equilibrium given in **Equation (2.33)** and thus exchange dynamics.

2.11.1. Quasielastic Neutron Scattering

A drawback of NMR is that the dynamics of the ligands on the NC surface cannot be resolved. To access these, another technique is required, and quasielastic neutron scattering (QENS) provides exactly this. [125] Again, referring to **Equation (2.13)** the scattered intensity is proportional to $I(q) \propto P(q)S(q)$. As dynamics in solution are of interest, the time-dependent structure factor is important because the temporal behavior describes the movement of the scatterers. [125] Quasielastic neutron scattering can be performed at the IN16B beamline in the backscattering and time-of-flight (BATS) configuration at the Institute Laue-Langevin (ILL) in Grenoble, France (**Figure 2.17 a**). Firstly, neutron scattering is the method of choice for the analysis of ligands, as the scattering of neutrons is very sensitive towards protons. This is due to the scattering length density (*SLD*), which is a measure of the scattering cross section at low energies, as it is the case in QENS. It is given by the limit of the elastic scattering cross section $\lim_{k\to 0} d\sigma_e/d\Omega = 4\pi(SLD)^2$ and can easily be related to basic molecular quantities like the molecular volume V_m. By utilizing specific coherent scattering lengths of the present atoms ($b_{c,i}$) the *SLD* can be calculated as $SLD_{molecule} = \sum_i b_{c,i} / V_m$. [201,202] As deuterium has a much lower *SLD* than hydrogen, measuring QENS in deuterated solvents enables a facile way to measure the dynamics of the non-deuterated ligand on a NC surface. [125] **Figure 2.17 a** schematically shows the QENS experiment in the BATS configuration, and it can be seen that the angle dependence can be translated into the momentum transfer *q* and the ToF component, *i.e.*, the time the neutron takes from being scattered to the detector, is directly related to the energy transfer.

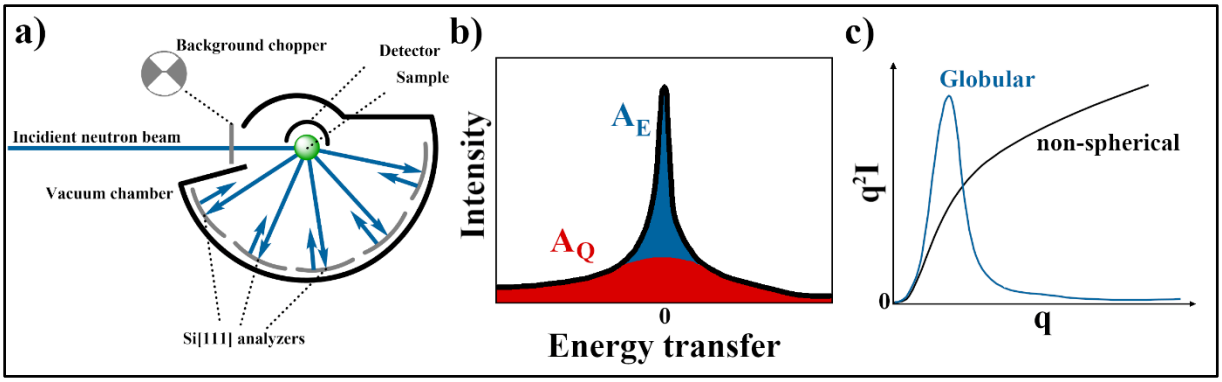

Figure 2.17: a) Schematic setup of the IN16B BATS beamline at the ILL, Grenoble (France). The incident beam is chopped by a background chopper to enable the time-of-flight measurement. After the beam is scattered by the sample it is backscattered at the Si[111] analyzers. The backscattered neutrons are then detected at the detector, which lies behind the sample. This way, the angular dependence can be resolved. Additionally, the time-of-flight (ToF) data is obtained as the detection is time resolved. Therefore, the momentum transfer is accessible *via* the angle and the energy transfer *via* the ToF data. b) Calculation quantities for the EISF, the elastic scattering (A_E) Lorentzian is depicted in blue and the quasielastic contribution (A_Q) in red. c) Exemplary Kratky plot for a spherical / globular and non-spherical scatterer.

It is reasonable to assume Brownian motion for the scatterers in solution, more specifically diffusion which follows Fick´s 2nd law.

$$\frac{\partial c}{\partial t} = D\frac{\partial^2 c}{\partial x^2}$$
$$c(x,t) = \frac{1}{\sqrt{4\pi D t}}\exp\left(-\frac{x^2}{4Dt}\right), \tag{2.39}$$

with the concentration c, and diffusion coefficient D. To translate the result of Fickian diffusion to the QENS experiment, one has to perform 2 subsequent Fourier transformations (FT), for the spatial and temporal component. The first transformation in space results in the intermediate scattering intensity $I_s(q,t) = \exp(-Dq^2t)$. The second FT in time results in the (Lorentzian) incoherent scattering function S_{inc}: [203]

$$S_{inc}(q,\omega) = \frac{1}{\pi}\frac{\Gamma(q)}{\omega^2 + \Gamma(q)^2} \equiv A_{E/Q}. \tag{2.40}$$

Where ω is the energy transfer, and $A_{E/Q}$ are the areas of the elastic and quasielastic Lorentzian. The Lorentzian function contains a broadening Γ due to the diffusion. For the broadening, a general expression can be assumed: [125]

$$\Gamma(q) = \frac{D_{jump}q^2}{1 + D_{jump}q^2\tau}. \tag{2.41}$$

With the jump diffusion coefficient D_{jump}, absolute of the momentum transfer q, and jump time τ. **Equation (2.41)** assumes a general jump diffusion model, in which the ligand resides at a certain site for the time τ. However, for small jump times $\lim_{\tau\to 0}\Gamma(q)$ the diffusion follows simple Fickian diffusion

again, with $\Gamma = Dq^2$. From the scattering function, the elastic incoherent structure factor can be calculated:

$$EISF = \frac{A_E}{A_E + A_Q}. \tag{2.42}$$

Therein, the EISF gives a direct measure for the space which is available for the scatterers to access and typically exhibits a monotonic decay with momentum transfer. [203] However, obtaining both quantities requires extensive, independent fitting of the results for all *q*-values, which in turn are dependent on the applied model. Additionally, the diffusion coefficient can then be used to calculate the hydrodynamic radius r_H, which is a value that can be compared to the results from SAS. [204,205]

$$D = \frac{k_B T}{6\pi\eta r_H}, \tag{2.43}$$

with η is the solvent viscosity.

2.11.2. Small Angle X-Ray and Neutron Scattering in Solution

In small angle X-ray and neutron scattering (SAXS and SANS), the intermolecular interactions in solution play an important role (see chapter 2.6). By balancing the different interactions, the system enters an equilibrium which can be probed by SAS and the quantities obtained are directly relatable to the intermolecular interactions. In sufficiently dissolved solutions the structure factor can be assumed to equal unity and thus only the form factor contributes to the scattering. By measuring such samples, the morphology of the scatterers, their size and even composition can be resolved. [206] Before explicitly fitting the scattered intensity, simple analysis techniques can be performed to obtain the most basic characteristics of the scatterers. At first, the exponent *m* of the intensity decay at intermediate to large *q*-values can be fitted by $I(q) = 2\pi(\Delta SLD)^2 S/(Vq^m)$. [206,207] The intensity in this regime follows Porod´s law and depends on the morphology of the particle. The different exponents and the corresponding geometries are given in **Table 2.4**. [207]

Table 2.4: Intensity decay exponents and the corresponding morphologies.

Power law	Morphology
q^{-4}	Spherical
q^{-2}	Thin circular disk
q^{-2}	Gaussian chain
q^{-1}	Thin rod

Additionally, the behavior at small momentum transfers can be analyzed by performing a Guinier fit. [208] The intensity in this regime follows an exponential decay: [208]

$$I(q) = I(0)\exp\left(-\frac{1}{3}q^2R_G^2\right). \quad (2.44)$$

Where the radius of gyration R_g is a measure for the mass distribution. However, to obtain the actual size, a correction factor needs to be employed, *e.g.*, 1.29 for a spherical particle. [208] From the Guinier Fit, *i.e.*, the natural logarithm of the intensity *vs.* the square of absolute of the momentum transfer, it can also de deduced if particles are dominated by repulsive or attractive interactions. If the plot exhibits an upturn, which can be calculated from the derivative of *ln(I)*, attractive forces dominate, and *vice versa*.

Complementary to the Guinier analysis is the Kratky plot, in which $I \cdot q^2$ is plotted against the absolute of the momentum transfer. [121,209] From the shape of the Kratky plot one can estimate if the scatterer is of spherical or non-spherical shape (**Figure 2.17 c**). Also, the peak position of the "bell" can be used to calculate the radius of a spherical scatterer and thus eventual changes in the morphology during exchange processes. Lastly, it is possible to perform an indirect Fourier transform of the measured intensity to obtain a real space size distribution $p(r) = \int_{-\infty}^{\infty}(qr)I(q)\sin(qr)\,dq$.

However, all the above-mentioned analysis methods can be used to calculate first results and observe trends between samples. To obtain a precise picture, the form factor must be explicitly fitted. This is efficiently performed with software like SASfit. [210] Many approaches for *P(q)* are possible and generally the intensities can be summed up $I(q) = \sum_i I_i + I_{bkg} + I_{OZ}$. The background is used to subtract any unwanted scattering, transmission or reflection intensity which originates from the spectrometer or substrate of choice. Additionally, the Ornstein-Zerneke (I_{OZ}) contribution is required for samples in the nanocrystalline regime. Very basically this contribution describes the interaction of 2 nanocrystals, either directly or indirectly. [125,211] The indirect interaction in this case is *via* a third NC which is influenced by the first NC, and subsequently can also affect the second, target particle and *v. v.* [211] Explicitly, this can be fitted by: [211]

$$I_{OZ}(q) = \frac{I_{OZ}(0)}{1 + q^2\xi_{OZ}^2}. \quad (2.45)$$

Therein, ξ_{OZ} is the correlation length. As the intensity in this case mainly depends on the form factor, a suitable model is required. The form factor can be modelled depending on the morphology of the scatterer, and possible models are summarized in **Table 2.5**.

Table 2.5: Form factors of a variety of geometries. ΔSLD is the difference in scattering length density between particle, ligand shell, and solvent. R is the radius for spherical scatterers, A, B, C are the lengths and α, β, γ the angles of the parallelepiped. V denotes the respective volume of the scatterer. θ is the angle between scattering vector and the z-axis. [125,212–214]

Morphology	Formula $P(q)$
Sphere	$\begin{cases} 36\pi(\Delta SLD)^2 V_{sphere}^2 \frac{\left(\sin(qR) - qR\cos(qR)\right)^2}{(qR)^3} \; ; q \neq 0 \\ 4\pi(\Delta SLD)^2 V_{sphere}^2 \; ; q = 0 \end{cases}$
Core-shell sphere	$36\pi\left\{(\Delta SLD_{shell})^2 V_{R+t}^2 \frac{\left(\sin(q(R+t) - q(R+t)\cos(q(R+t))\right)^2}{(q(R+t))^3} + (\Delta SLD_{core-shell})^2 V_R^2 \frac{\left(\sin(qR) - qR\cos(qR)\right)^2}{(qR)^3}\right\}$
Parallelepiped	$(\Delta SLD)^2 V^2 sinc^2\left(\frac{1}{2}qA\cos(\alpha)\right) sinc^2\left(\frac{1}{2}qB\cos(\beta)\right) sinc^2\left(\frac{1}{2}qC\cos(\gamma)\right)$
Ellipsoid	$\begin{cases} 18\pi(\Delta SLD)^2 V^2 \int_0^\pi \frac{\left(\sin(qR_\theta) - qR_\theta\cos(qR_\theta)\right)^2}{(qR_\theta)^3} \sin(\theta)\, d\theta \; ; q \neq 0 \\ 4\pi(\Delta SLD)^2 V^2 \; ; q = 0 \end{cases}$ $with\ R_\theta = R_r\sqrt{\sin^2(\theta) + \epsilon^2\cos^2(\theta)}$

2.12. Ligand Shell

To evaluate the influence of a ligand on the nanocrystal surface, it is convenient to look at the interacting orbitals of the surface. Exemplarily, this will be done for a Pb terminated surface of LHPs as they are the focus of this work. Practically, molecular orbital theory provides the perfect toolset to interpret the interacting orbitals. [134] In a perovskite Pb can be assumed in an octahedral (O_h symmetry) ligand field. The halides surrounding the central atom can be summarized in symmetry adapted linear combinations (SALC) of the interaction orbitals (p orbitals of the halides) which interact with the 6s and 6p orbitals of lead, as shown in **Figure 2.18 a**, the result of the interaction are the frontier states. On the surface however, the symmetry is broken and the O_h symmetry is lowered to a C_{4v} symmetry, because only 5 of the 6 halides are available. This results in a destabilization of the surface since the lowering in symmetry increases the variety of states and therefore the entropy: [215,216]

$$S = R\ln\left(\frac{8\pi^2}{\sigma}\left(\frac{2\pi e k_B T}{h^2}\right)^{\frac{3}{2}} m_{red}\right). \tag{2.46}$$

Where σ is a dimensionless parameter given by the point group, for O_h equal to 24, whereas for C_{4v} only 4, showing the drastic increase in entropy. [217] However, by saturating the surface with a ligand the symmetry is restored and the NC stabilized. On the other hand, by tethering a ligand to the surface several additional phenomena occur as well. Most notably the ligand can provide an intrinsic dipole moment which is able to (partially) compensate the surface dipole on the NC surface. The orientation

and the magnitude of the resulting dipole can drastically shift the absolute energy levels of the system, without altering the band gap size. This has been extensively shown for PbS NCs where the shift of valence/$1S_h$ and conduction/$1S_e$ states can be of orders up to 1 eV or more (**Figure 2.18 b**). [34,194,218] If the dipole is oriented away from the NC surface, the energy levels are shifted to higher energies, and if the dipole is directed towards the surface the energy is lowered. [218] This effect can be understood by the concept of mirror charges, where the functional group of a ligand acts as a charge above the NC surface. This induces a potential of the form: [219]

$$V_{mirror}(\vec{r}) = \frac{1}{4\pi\varepsilon_0}\left(\frac{q}{|\vec{r} - \vec{r_q}|} + \frac{q_{mirror}}{|\vec{r} - \vec{r}_{mirror}|}\right). \tag{2.47}$$

Where q represents the charge, and $\vec{r}$ the position vectors. This potential can further be modified if an intrinsic dipole on the ligand is present, which adds an additional term. This term can increase or decrease the magnitude of the resulting potential and enhances or compensates the surface dipole, respectively.

Another effect which can be observed at the interface is Fermi level pinning, which means the alignment of the Fermi levels of ligand and NC (**Figure 2.18 c**). The most straight-forward case is the interface between a metal and a semiconductor, where the work function, *i.e.*, Fermi level, of the metal and the Fermi level of the semiconductor are aligned at the same energy. The energy states, or bands, of the semiconductor have to bend towards the shifted Fermi level near the interface in order to balance the change. [220,221] The bending of the bands leads to an accumulation of charges near the interface and thus charges will be exchanged between the metal and semiconductor until the potential difference is compensated. The influence of the junction not only affects the absolute energies of the semiconductor energy levels, but also their density of states. Exemplarily for perylenetetracarboxylic dianhydride (PTCDA) it could be shown that the distribution of the HOMO and LUMO changes upon tethering it to a metal surface. Far away from the surface both states are well described by a gaussian distribution, however upon approaching the interface between metal and PTCDA the distribution is altered to a Voigt profile. [222] This results in more states being located inside the HOMO-LUMO gap of PTCDA.

The situation changes if two semiconductors are brought into contact, commonly known are homojunctions of p- and n-doped Si (np-junction). However, in the case of an inorganic and organic semiconductor, as it is the case for NC functionalized with an organic semiconductor as ligand, the alignment is not trivial. This heterojunction (a junction between two materials, contrary to the homojunction) exhibits the same Fermi level pinning, however the band bending behaves differently as both semiconductors must adjust to the novel electronic situation. This results in a built-in voltage which is given by the difference of the Fermi levels of the isolated semiconductors. When the difference between the respective Fermi levels is large, the band bending cannot compensate the Fermi

level bending, and this results in discontinuities of the alignment at the interface. The magnitude of the discontinuities between the valence and conduction bands can be estimated by Anderson´s rule: [223]

$$\Delta E_c = (\chi_2 - \chi_1)$$
$$\Delta E_v = (\chi_1 - E_{g1}) - (\chi_2 - E_{g2}). \quad (2.48)$$

Where χ_i are the electron affinities of the respective semiconductors.

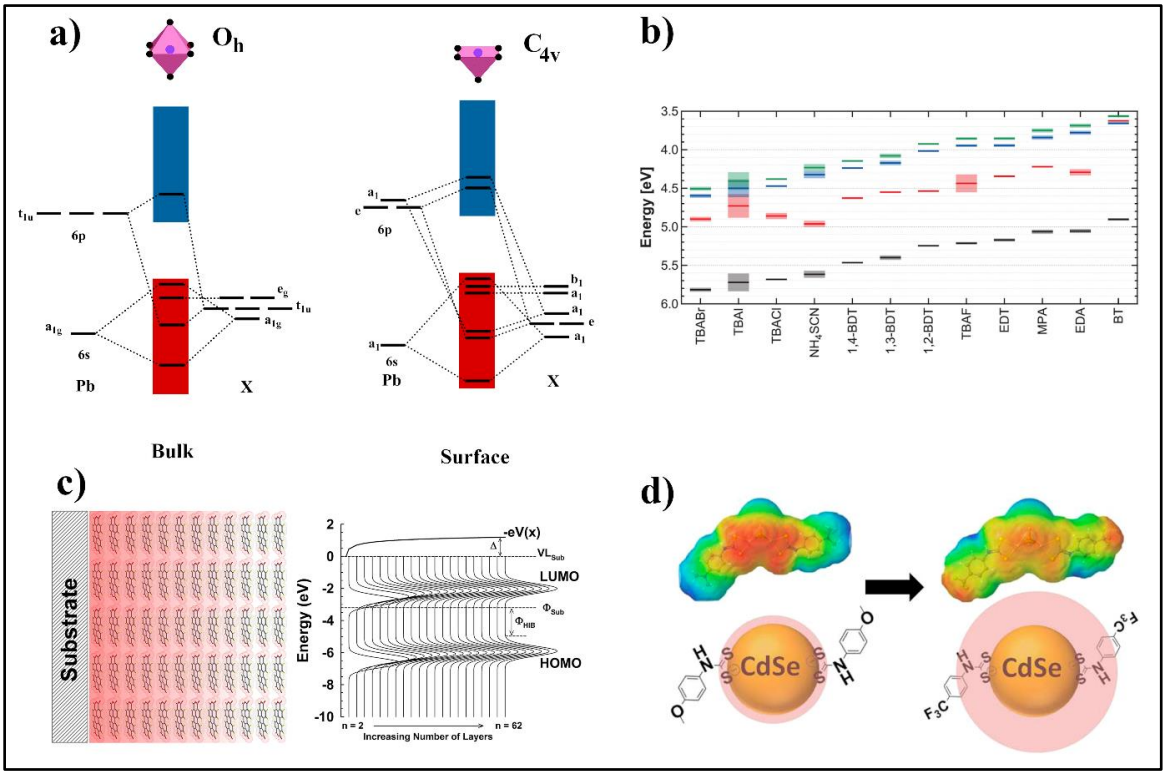

Figure 2.18: a) MO scheme for bulk (O_h symmetry) and surface (C_{4v} symmetry) PbX_n. The valence and conduction band are shown in red and blue, respectively, the electrons are not depicted for simplicity. In the C_{4v} MO scheme the states are split due to the loss in symmetry, which results in a larger variety of states. b) Absolute energy levels of PbS NCs functionalized with different ligands. The surface dipole is pointing towards the surface for ligands on the left side of the graph and away from the surface on the right side. In between the magnitude of the dipole is gradually altered. c) Fermi level pinning of PTCDA on a substrate. The states are bend towards the substrate Fermi level near the surface. Additionally, the profile of the HOMO and LUMO changes from a Gaussian to a Voigt profile, when approaching the surface. d) Spreading of the wavefunction onto the ligand shell by resonant alignment in CdSe NCs. b) Reprinted with permission from Brown *et al.* [218] Copyright 2014 American Chemical Society. Partly edited. c) Reprinted from "The role of the density of interface states in interfacial energy level alignment of PTCDA" by Khoshkhoo *et al.* [222], Copyright 2017, with permission from Elsevier. d) Reprinted with permission from Frederick *et al.* [164] Copyright 2013 American Chemical Society.

A model to explain the discontinuity at the interface is the formation of a dipole layer, but the underlying principle is yet to be found. [224] When a semiconducting ligand is in contact with a NC surface and the energy levels are suitably aligned after above considerations are regarded, the confinement of charge carries inside the NC can be altered. This is due to the spreading of the wavefunction onto the ligand, which can occur if the offset between NC $1S_e$ / $1S_h$ and the ligands

HOMO / LUMO is small enough. This results in so-called exciton leakage and can be seen as a bathochromic shift of the first excitonic transition. [164]

2.13. Coupled Organic-Inorganic Nanostructures

The functionalization of NCs with organic semiconductors (OSC) was shortly mentioned before, this chapter will discuss the possibility of coupling the two components in two ways: electronically and structurally. These so-called coupled organic inorganic nanostructures (COIN) hold enormous potential for applications in optoelectronics (**Figure 2.19**). [21,22,32,33,225] The structural coupling of NCs and OSCs is realizable by tethering novel ligands, *viz.* functionalized OSCs, *via* ligand exchange reactions to the surface. [21,22] The chemical bond between NC and OSC is the first structural component in the framework of COINs. Additionally, the self-assembly properties of nanoparticles can be exploited, precisely by allowing NCs to self-assemble and exchanging the ligand subsequently a high degree of order is accessible. This successive ligand exchange with a di- or tetra-functionalized OSC can stabilize the structure obtained from the assembly and make it more rigid towards external influences. [31,33] A more structured material is desirable as it can benefit the charge carrier mobility, which is shown to be dependent on the local structure of the superlattice (*cf.* discussion on $\Delta\alpha$ in chapter 2.10). [31] Another beneficial factor by functionalizing the NCs with an OSC is the reduction of the interparticle spacing, which drastically increases the tunneling probability as discussed before. This increases the mobility of charge carriers in the mesocrystal by decreasing the tunneling barrier width d_{NN}. [32,33,168,180] Secondly, by near-resonant alignment of the energy levels between NC and OSC the height of the barrier ΔV can be tuned, as the ligand typically determines this value. [32,33,164] This again results in a higher charge carrier mobility. [32,33] Lastly, OSCs typically have higher dielectric constants compared to ligands used during NC synthesis. This affects the charge carrier injection in means of the charging energy E_C and facilitates the propagation of charge carriers. [21,22] In sum, by preparing COINs it is possible to increase the structural order, increase the tunneling rate and reduce the charge injection energy, which all contribute to improved optoelectronic properties (compare **Figure 2.14 a**).

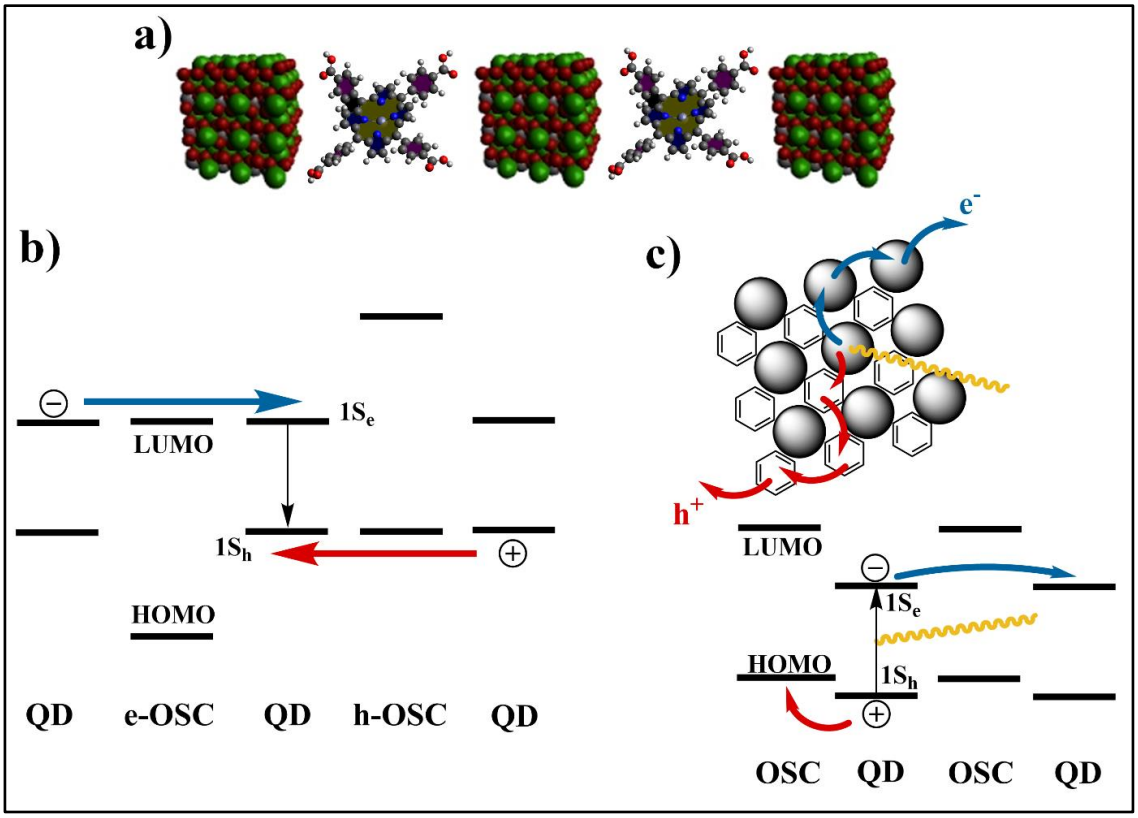

Figure 2.19: a) Schematic of coupled organic-inorganic nanostructures (COIN) with the QDs coupled electronically and structurally *via* the organic semiconductor (OSC). b) Working scheme of COINs used as photodiodes. The electron is injected through an electron conducting COIN system (indicated by e-OSC) and the hole through a hole conducting system (h-OSC). As the charge carriers are injected into a QD they are able to recombine (QD in the middle). Notably, by suitable ligand choice both HOMO and LUMO can be aligned simultaneously as the charge carriers are injected from different sides. c) COINs used as solar cells, the exciton is created on a QD with the ligand acting as a hole and the QDs as an electron transport material. This results in a separation of the charge carriers. The movement of electrons and holes is depicted in blue and red, respectively.

When COINs are realized they can be used in optoelectronic devices as solar cells or LEDs and by carefully tuning the properties *via* suitable ligand choices they can be optimized for the application in such devices. [22] Exemplarily, by using a OSC which has a HOMO energetically higher than the $1S_h$ of the NC and a LUMO higher than the $1S_e$ it is possible to separate excitons which are created on a NC (**Figure 2.19 c**). [226] Therefore, the charge separation, as it is required in solar cells, can already be intrinsically induced to the absorption layer which can increase the efficiency. A requirement for this principle is the possibility of charge carrier propagation in the OSC ligand shell as one of the respective charge carriers needs to propagate *via* the OSC. Luckily, charge carriers can propagate either by Förster resonance energy transfer (FRET, singlets) or Dexter energy transfer (triplets). [227] Generally, the charge carrier propagation follows Fermi´s golden rule (**Equation (2.49) a**), however the coupling integral H_{DA} must be adjusted for singlets and triplets as it originates from different potentials (**Equation (2.49) b + c**). [134,227,228] Additionally, to calculate transfer rate constants it must be differentiated between a transfer of energy (FRET) and an actual charge carrier (Dexter), for

the latter case Marcus theory of electron transfer approximates the Franck-Condon density of states (*FCWD*). [170,227]

$$\text{a) } k_{DA} = \frac{2\pi}{\hbar}|H_{DA}|^2(FCWD)$$

$$\text{b) } Singlets: V_{dip-dip} \approx \frac{\kappa\mu^2}{n^2}\left(\frac{1}{\alpha\mu + r_{DA}}\right)^3 ; with\ \kappa = \mu_D\mu_A - 3(r_{DA}\mu_D)(r_{DA}\mu_A)$$

$$\text{c) } Triplets: V_{Dexter} = A\exp(-\zeta r_{DA}) \qquad (2.49)$$

$$\text{d) } k_{singlet} = \frac{\kappa^2\pi^{3/2}\mu^4}{n^4(\alpha\mu + r_{DA})^6\sigma}\exp\left(-\frac{\Delta_{DA}^2}{4\sigma^2}\right)$$

$$\text{e) } k_{triplet} = \frac{2\pi}{\hbar}|A\exp(-\zeta r_{DA})|\sqrt{\frac{1}{4\pi k_B T\lambda}}\exp\left(-\frac{(\Delta G^0 + \lambda)^2}{4\lambda k_B T}\right)$$

With the transfer rates *k*, dipole moments μ, distance r_{DA}, constant *A*, spatial overlap of the donor and acceptor wavefunctions ξ, refractive index *n*, constant parameter α, Gaussian width σ, and energy difference between donor and acceptor Δ_{DA}.

On the other hand, the application in LEDs can be realized by preparing COINs and utilizing them as an emitter layer. To prepare a mesomaterial suitable for light emission the charge carriers must be injected separately, *i.e.*, from different sides of the emission layer. This can be applied to the COIN approach by functionalizing NCs with a set of 2 different ligands, where one aligns with the $1S_e$ and the other with the $1S_h$ state (**Figure 2.19 b**). This way the charge carrier injection of electrons and holes is restricted to either side, whichever allows mobility for the respective charge carrier. [22]

2.14. Electroluminescent Quantum Dot Light-Emitting Devices

To practically realize an electroluminescent quantum dot LED (ELQLED) the device has to be setup with two electrodes, electron and hole injection layers, an emitter layer (NCs), as well as electron and hole blocking / transport layers. Such a device is typically prepared by spin-coating the bottom layers, including the emitter layer, and subsequently depositing the top layers, *e.g.*, by vapor deposition. After device fabrication, the properties are analyzed by current-voltage-luminance (*jVL*) curves, as they combine the electrical and optical properties in a single measurement. Additionally, the setup can be complemented by a spectrometer to measure the emission wavelength. Overall, the combination of these measurements allows for a complete characterization of the device. [229,230] From the *jVL* curve it is possible to calculate the current efficacy by comparing the luminance (dependent on the NC QY) and current at a given voltage. Furthermore, the external quantum efficiency (EQE) can be derived from this value by adding a constant experimental setup factor. Generally speaking, the following trends are desirable for the EQE. Firstly, obviously a higher EQE means the ELQLED can be operated

at lower voltages, because the injected carriers are more likely to recombine in the emission layer. The EQE is reduced if the charge carriers are already lost inside the injection layers (*cf.* charging energy) or if the resistance inside the emission layer is too small, so the carriers are moving across the central layer and are thus unlikely to recombine. Additionally, the QY of the NC itself plays a role, the more trap states are present in the NC the lower the QY will be and thus the EQE is reduced. [163] Secondly, the maximum of the EQE should be at small currents, as this gives a measure of quenching in the sample and less quenching means higher recombination rates. [163] The origin of the quenching is the applied electric field, or voltage, which separates the charge carriers that are already injected into the emission layer. [163] This type of quenching is enhanced if the resonant alignment between NC and ligand is exceedingly high, as the leakage of the wavefunction onto the ligand increases the probability of charge carrier separation as more space is available due to a lowering of confinement. [163,164] On the other hand Auger recombination also contributes herein, however this type of quenching is increased if the confinement is increased, just the opposite trend as for field induced quenching. [163,231] Mathematically the EQE is given by: [229]

$$EQE = \gamma \cdot q_{eff} \cdot \eta_{out}. \tag{2.50}$$

Where γ is a charge carrier balance factor, q_{eff} relates to the quantum yield of the emitter layer, and η_{out} is the outcoupling factor.

The last factor in **Equation (2.50)** corresponds to emitted light that needs to exit the device. This factor strongly depends on the emission angle of the emitters in the emission layer, and thus on the transition dipole moment. [229,232] The emitted light in a NC is emitted perpendicular to the transition dipole moment, and if the angle is large enough the light can be internally reflected by the transparent cathode of the LED and thus is not able to leave the device. [58,232] The angle can effectively be measured by angular resolved photoluminescence measurements. For $CsPbBr_3$ perovskites, with a QY near unity, the EQE due to η_{out} in **Equation (2.50)** was found to be ~ 20%, due to a transition dipole moment of ~ 45–50°. [233]

For perovskites, a possibility to reduce the above stated problems is the application of Li-salts (*e.g.*, LiTFSI) to create a passivating surface layer. [234,235] The Li-salts are passivating dangling bonds and vacancies, by which also the transition dipole moment is tuned in a way that allows for a more efficient light emission, and additionally the hole injection is facilitated through tuning of the surface energy levels. For a more detailed discussion of this topic, the interested reader is referred to Naujoks *et al.*[††]

The variety of influences on the EQE behavior of such a system suggest an in-depth error analysis, therefore the error in the EQE can be calculated by Gaussian error propagation, which is given by: [236]

[††] Naujoks, T. *et al.*, ACS Appl. Mater. Interfaces **2022**, *14*, 25, 28985. DOI: 10.1021/acsami.2c04018.

$$\Delta EQE = \Delta\left(\frac{L}{I}\right) = \sqrt{\left(\frac{\partial EQE}{\partial I}\right)^2 \sigma_I^2 + \left(\frac{\partial EQE}{\partial L}\right)^2 \sigma_L^2} = \sqrt{\left(-\frac{L}{I^2}\right)^2 \sigma_I^2 + \left(\frac{1}{I}\right)^2 \sigma_L^2}. \quad (2.51)$$

With the standard deviations σ, luminance L, and current density I.

3. Spatially Resolved Fluorescence of Caesium Lead Halide Perovskite Supercrystals Reveals Quasi-Atomic Behavior of Nanocrystals

Dmitry Lapkin[1,*], Christopher Kirsch[2,*], Jonas Hiller[2,*], Denis Andrienko[3], Dameli Assalauova[1], Kai Braun[2], Jerome Carnis[1], Young Yong Kim[1], Mukunda Mandal[3], Andre Maier[2,4], Alfred J. Meixner[2,4], Nastasia Mukharamova[1], Marcus Scheele[2,4,+], Frank Schreiber[4,5], Michael Sprung[1], **Jan Wahl**[2], Sophia Westendorf[2], Ivan A. Zaluzhnyy[5], Ivan A. Vartanyants[1,6,+]

1. Deutsches Elektronen-Synchrotron DESY, Notkestraße 85, 22607 Hamburg, Germany

2. Institut für Physikalische und Theoretische Chemie, Universität Tübingen, Auf der Morgenstelle 18, 72076 Tübingen, Germany

3. Max Planck Institute for Polymer Research, Ackermannweg 10, 55128 Mainz, Germany

4. Center for Light-Matter Interaction, Sensors & Analytics LISA$^+$, Universität Tübingen, Auf der Morgenstelle 15, D-72076 Tübingen, Germany

5. Institut für Angewandte Physik, Universität Tübingen, Auf der Morgenstelle 10, 72076 Tübingen, Germany

6. National Research Nuclear University MEPhI (Moscow Engineering Physics Institute), Kashirskoe shosse 31, 115409 Moscow, Russia

* These authors contributed equally

+To whom correspondence should be addressed

This chapter is based on the publication published in Nature Communications: Nat. Commun. **13,** 892 (2022), DOI: 10.1038/s41467-022-28486-3.

ArXiv Preprint: https://doi.org/10.48550/arXiv.2109.05502

3.1. Abstract

We correlate spatially resolved fluorescence (-lifetime) measurements with X-ray nanodiffraction to reveal surface defects in supercrystals of self-assembled caesium lead halide perovskite nanocrystals and study their effect on the fluorescence properties. Upon comparison with density functional modelling, we show that a loss in structural coherence, an increasing atomic misalignment between adjacent nanocrystals, and growing compressive strain near the surface of the supercrystal are responsible for the observed fluorescence blueshift and decreased fluorescence lifetimes. Such surface defect-related optical properties extend the frequently assumed analogy between atoms and nanocrystals as so-called quasi-atoms. Our results emphasize the importance of minimizing strain during the self-assembly of perovskite nanocrystals into supercrystals for lighting application such as superfluorescent emitters.

3.2. Introduction

Advances in the self-assembly of colloidal nanocrystals (NCs) from solution into three-dimensional arrays with long-range order have enabled the design of microscopic "supercrystals" that approach the structural precision of atomic single crystals. [237] The individual NCs, which are the building blocks of a supercrystal, are often regarded as "artificial atoms", and hence analogies between atomic crystals and such supercrystals have been made. [238,239] NC supercrystals are susceptible to doping, [240] and they can exhibit exceptional mechanical properties, [241] quasicrystal formation, [238] enhanced electronic coupling, [242] and engineered phonon modes. [243] In view of the recent progress in exploiting the massive structural coherence in NC supercrystals to generate collective optoelectronic properties, [139,244,245] a critical question remains whether this artificial atom analogy can be extended towards the optical properties of NC supercrystals. Due to surface dangling bonds and surface reconstruction, even the purest and most carefully prepared atomic crystals are not structurally perfect. [246,247] For *atomic* crystals, such surface defects strongly affect the fluorescence spectra, lifetime and quantum yield. [248–252] For supercrystals, this is much less understood.

In this work, we show that in close analogy to atomic crystals, [253,254] $CsPbBr_2Cl$ and $CsPbBr_3$ NC supercrystals exhibit structural distortions near their surfaces which significantly alter their fluorescence properties. This finding is of high relevance for the application of these materials as tunable, bright emitters with superfluorescent behavior. [139,244,245] Superfluorescence is a key property for the design of spectrally ultra-pure laser sources [255] or highly efficient light-harvesting systems. [256] Recent quantum chemical simulations have suggested that structural disorder in $CsPbBr_3$ supercrystals and its effect on the thermal decoherence plays a pivotal role in the efficiency of the

superfluorescence. [257] Previous structural investigations of ensembles of $CsPbBr_3$ supercrystals by grazing-incidence small angle X-ray scattering (SAXS) indicated a primitive unit cell with slight tetragonal distortion, [258] and wide-angle X-ray scattering (WAXS) showed a high degree of structural coherence. [259] Electron microscopy of individual supercrystals revealed a frequent occurrence of local defects in the supercrystals, such as isolated NC vacancies. [260] Confocal fluorescence microscopy of individual $CsPbBr_3$ supercrystals displayed spatial variations in the fluorescence peak wavelength and intensity, indicating that local structural inhomogeneities may substantially affect the fluorescence properties of the entire supercrystal. [115] Our approach is based on simultaneous WAXS and SAXS measurements with a nano-focused beam to probe the structural defects and crystallographic orientation of the supercrystal and the constituting NCs on a local level with dimensions of ~3 µm and 7 – 9 nm, respectively. [31,178,261] By correlation with diffraction-limited confocal fluorescence microscopy and modelling with density functional theory (DFT) we present proof that compressive strain, a loss of structural coherence and an increasing atomic misalignment between adjacent nanocrystals at the edges of $CsPbBr_2Cl$ NC supercrystals are responsible for a blueshifted emission and decrease of the fluorescence lifetimes.

3.3. Results

We study self-assembled $CsPbBr_2Cl$ and $CsPbBr_3$ NC supercrystals on glass substrates (see Methods for details on synthesis and self-assembly of NCs). Spatially resolved photoluminescence spectra of the NC supercrystals under 405 nm excitation in a confocal laser scanning microscope with a step size of 250 nm and 100 nm, respectively, are shown in **Figure 3.1**. When approaching an edge of the supercrystal, we find a continuous blueshift of the emission peak wavelength. This blueshift is strongest for relatively small (few µm edge length) and highly facetted supercrystals, where it reaches up to 20 meV for $CsPbBr_2Cl$. We observe the same blue-shifting behavior for supercrystals composed of $CsPbBr_3$ NCs, although to a lesser extent (up to 12 meV).

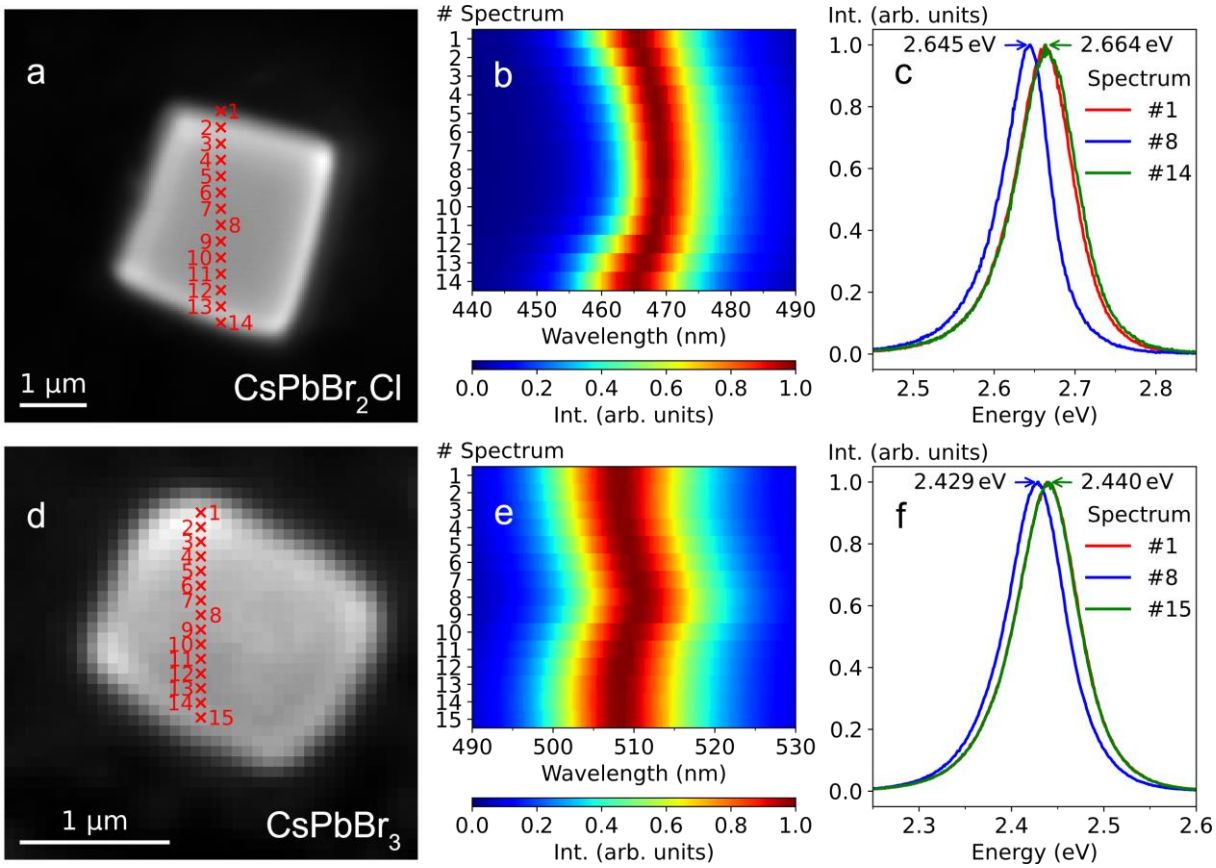

Figure 3.1: Spatially resolved fluorescence. a) Optical micrograph of a $CsPbBr_2Cl$ NC supercrystal. Positions of the measured photoluminescence spectra are indicated. b) The corresponding normalized spectra. c) Selected normalized spectra, acquired at the edges and the center of the supercrystal. d-f) Corresponding data for a $CsPbBr_3$ supercrystal.

In **Figure 3.2**, we display fluorescence lifetime images of self-assembled $CsPbBr_2Cl$ and $CsPbBr_3$ supercrystals measured on glass substrates with a lateral resolution of 200 nm under 405 nm excitation. For both supercrystal compositions, we obtain good fits of the experimental time-resolved fluorescence by pixel-by-pixel monoexponential reconvolution using an instrument response function acquired on a clean glass coverslip (Supplementary **Figure S3.2, S3.3**). In the case of supercrystals composed of $CsPbBr_2Cl$ NCs, we measure typical fluorescence lifetimes around 2.2 ns in the center which decrease by approximately 20% when scanning from the center of a supercrystal towards its edges. Supercrystals composed of $CsPbBr_3$ NCs exhibit typical lifetime values around 1.5 ns in the center, which shorten by approximately 30% when approaching the edges. We note that this holds true only for freshly prepared NC supercrystals. After several days of exposure to air, the trend in the spatially resolved τ-values is reversed in that such aged supercrystals exhibit longer lifetimes at the edges. However, the overall blueshift of the fluorescence peak wavelength towards the edges is preserved.

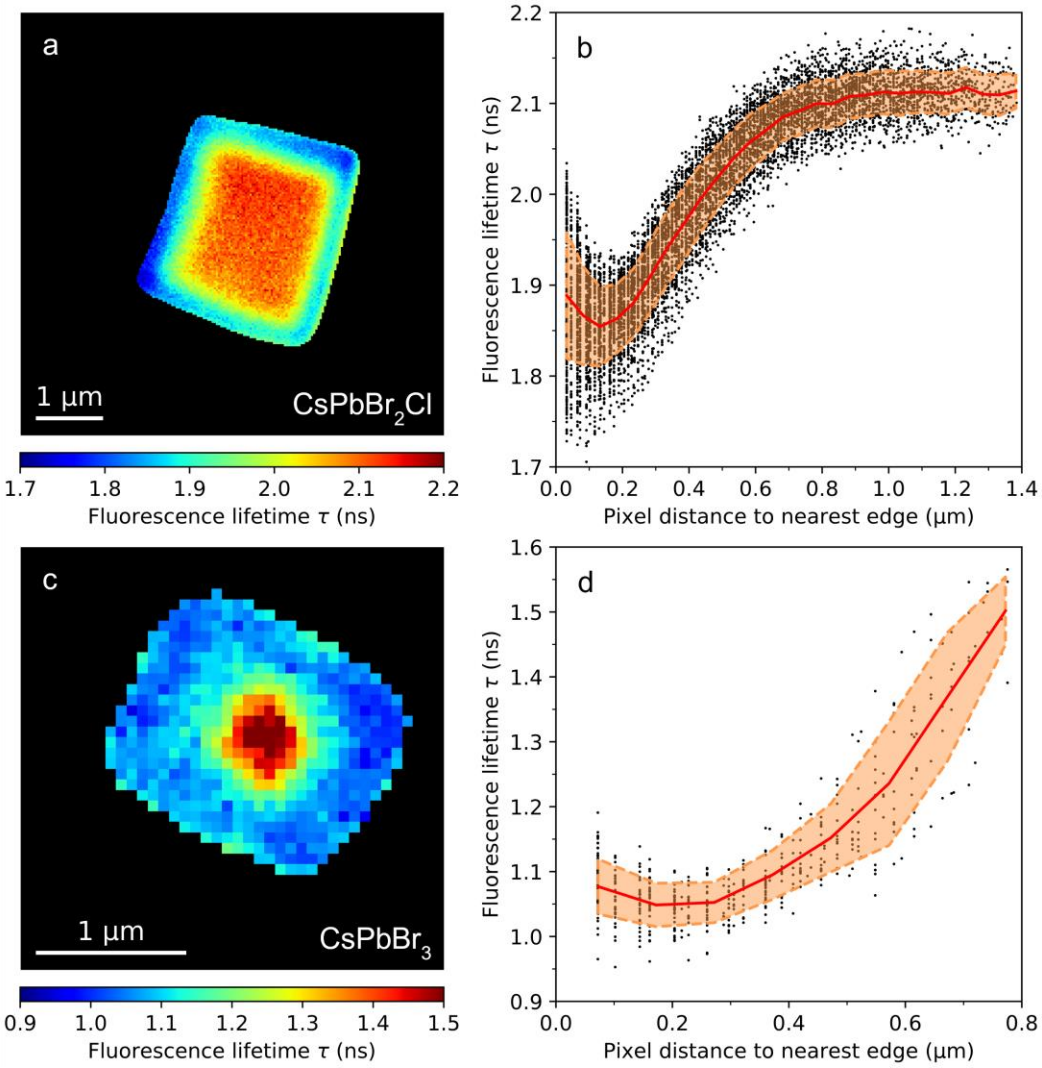

Figure 3.2: Spatially resolved fluorescence lifetime imaging. a) Fluorescence lifetime image of a $CsPbBr_2Cl$ NC supercrystal obtained by fitting the experimental time-resolved fluorescence with a monoexponential decay function. b) Fluorescence lifetime values obtained at each pixel inside the supercrystal as a function of the distance to the nearest edge, where the red line shows the mean value, and the dashed lines indicate the confidence interval of $\pm\sigma$. c-d) Analogous results for a $CsPbBr_3$ NC supercrystal.

To correlate the fluorescence data with the structure of the supercrystals, we carry out X-ray synchrotron measurements by SAXS and WAXS at PETRA III facility (Hamburg, Germany) (see **Figure 3.3 a** and Methods for details). Using a 400×400 nm^2 X-ray beam, we perform a spatially resolved scan of a typical $CsPbBr_2Cl$ NC supercrystal on a Kapton substrate. While the results presented here are for one typical supercrystal, examples of more supercrystals are provided in the Supplementary information (**Section S9**). First, all individual patterns are integrated to obtain the average structure. The averaged background-corrected WAXS and SAXS diffraction patterns are shown in **Fig. 3.3 b** and **3.3 c**, correspondingly. The signal in the WAXS region contains three orders of Bragg peaks from the atomic lattice (**Fig. 3.3 b**), and the SAXS region (shown enlarged in **Fig. 3.3 c**) displays several orders of Bragg peak from the supercrystal. A real-space map of the scan based on the integrated SAXS intensity at $q < 2$ nm^{-1} is shown in **Fig. 3.3 d**. The map represents a square area of

high intensity corresponding to a single supercrystal. For comparison, we display a scanning electron micrograph of a similar supercrystal (see inset in **Figure 3.3 a** and **Figure S3.8**) from which we determine an average NC diameter of 7.3±0.4 nm and an interparticle distance of 2.5±0.5 nm. For strongly facetted supercrystals, the NC diameter is rather uniform over the whole crystal. For less facetted supercrystals, occasional ensembles of smaller NCs are found in the vicinity of the edges. However, the spatial extent of such smaller NC populations is always limited to ~200 nm (see Supplementary Information, **Section S3**).

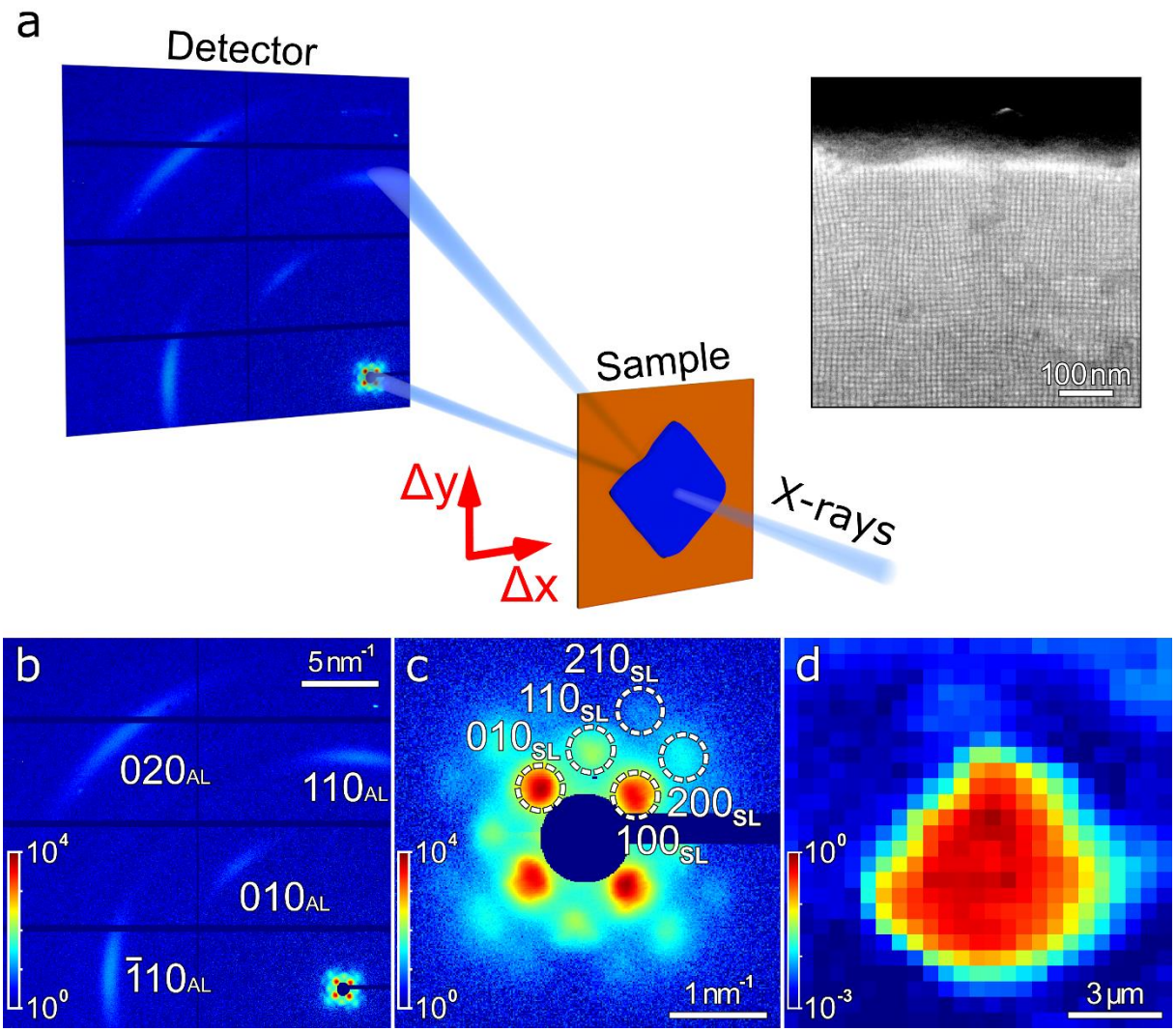

Figure 3.3: Spatially resolved X-ray nanodiffraction experiment and average diffraction patterns. a) Scheme of the X-ray experiment. EIGER X 4M 2D detector is positioned downstream from the sample. The arrows show the directions Δx and Δy of spatial scanning. Inset (top right): a SEM micrograph of the $CsPbBr_2Cl$ NC supercrystal. b) Average diffraction pattern for a supercrystal. Several orders of WAXS and SAXS Bragg peaks from the atomic and supercrystal structure, respectively, are well visible. The WAXS Bragg peaks are indexed using pseudo-cubic notation. c) Enlarged SAXS region of the averaged diffraction pattern. The Bragg peaks are indexed according to a simple cubic structure. d) Diffraction map for a scan based on the integrated intensity of the SAXS diffraction patterns at $q < 2$ nm^{-1}. The pixel size (the step size) is 500 nm.

The average diffraction pattern in the WAXS region (see **Fig. 3.3 b**) contains four prominent Bragg peaks, originating from the atomic lattice (AL) of the NCs. Their radial positions at

q = 10.93 nm^{-1}, 15.44 nm^{-1}, and 21.90 nm^{-1} (see Supplementary Information, **Figure S3.10**) can be attributed to a cubic AL. We note that although a cubic phase for $CsPbBr_2Cl$ has been reported, [262,263] the most stable phase at room temperature is expected to be orthorhombic. Due to the small NC size and the resulting broadening of the Bragg peaks, it is impossible to distinguish between these two very similar structures. Thus, we use a pseudocubic notation to index the WAXS peaks: 110 and 002 orthorhombic peaks correspond to 100_{AL} pseudocubic peak, 112 and 200 – to 110_{AL}, and 220, 004 – to 200_{AL} peaks. The present peaks and their azimuthal positions indicate a primary orientation of the NCs along the $[001]_{AL}$ axis with respect to the incident beam. We find the unit cell parameter to be a_{AL} = 0.575±0.003 nm, which is in good agreement with previously reported values for $CsPbBr_2Cl$. [264] From the peak broadening, we extract the NC size (d) and lattice distortion (g) using the Williamson-Hall method with d = 6.8±0.1 nm and g = 2.3±0.1% (see Supplementary Information, **Section S4**). The obtained NC size is in good agreement with the SEM results.

The SAXS pattern in **Figure 3.3 c** represents the typical 4-fold pattern of a simple cubic lattice oriented along the $[001]_{SC}$ axis with four visible orders of Bragg peaks that can be attributed to 100_{SC}, 110_{SC}, 200_{SC}, and 210_{SC} reflections of the supercrystal of NCs. We determine an average unit cell parameter of a_{SC} = 9.9±0.4 nm. Considering the NC size obtained by SEM, we obtain an interparticle distance of 2.6±0.4 nm, which is in a good agreement with the SEM result (2.5±0.5 nm). All crystallographic axes of the NCs are aligned with the corresponding axes of the supercrystal (e.g. $[100]_{AL}||[100]_{SC}$ and $[010]_{AL}||[010]_{SC}$), which is consistent with Ref. [260].

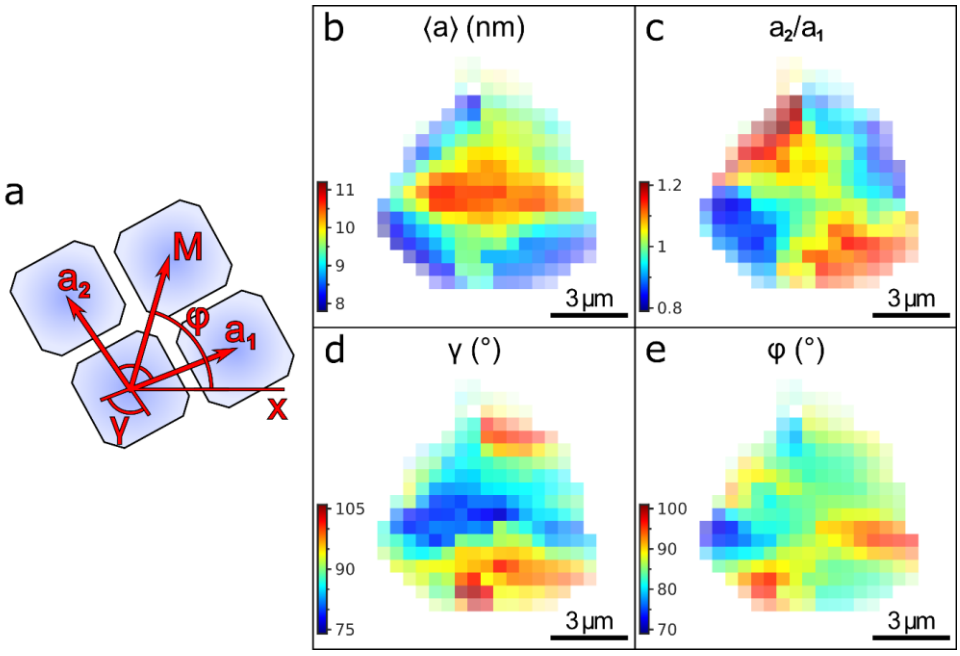

Figure 3.4: Spatially resolved SAXS. a) Definition of the geometrical parameters of a superlattice unit cell: the basis vectors a_1 and a_2 with the angle γ between them, and the mean line M between the basis vectors at the angle φ; b) average unit cell parameter $\langle a \rangle = (a_1+a_2)/2$; c) ratio a_2/a_1 of the unit cell parameters along the basis vectors a_2 and a_1; d) angle γ between the basis vectors a_1 and a_2; e) azimuthal position φ of the mean line M between the basis vectors a_1 and a_2. The pixel size in b-e) is 500 nm.

Analyzing individual SAXS patterns from different locations on the supercrystal, we find substantial local deviations from the average structure (see Supplementary Information, **Figure S3.12** for examples of single diffraction patterns). To illustrate this, from the Bragg peak positions, we extract the basis vectors a_1 and a_2, the angle γ between them, and the average azimuthal position φ, which are defined in **Figure 3.4 a** (see the Methods section for details). As depicted in **Fig. 3.4 b**, the mean unit cell parameter is largest in the center of the supercrystal with 10.7 nm and smallest at the edges with 7.8 nm. Although both unit cell parameters a_1 and a_2 decrease at the edges (see Supplementary Information, **Figure S3.16**, for separate maps of a_1 and a_2 values), we observe that this lattice contraction is anisotropic. The ratio of the in-plane unit cell parameters a_2/a_1 differs from unity by ±20% in such a way that the NC spacing in the directions along the nearest supercrystal boundary is smaller than normal to it, as shown in **Fig. 3.4 c**. We note that the mean value $\langle a \rangle = 9.4 \pm 0.7$ nm is slightly smaller than the unit cell parameters extracted from the average diffraction pattern. We attribute this to the low intensity of scattering from the supercrystal edges, which reduces their contribution to the average pattern. We do not observe a clear trend in the size of the SAXS Bragg peaks (see Supplementary Information, **Figure S3.15**, for the maps). The instrumental peak broadening, determined by the incident X-ray beam size is about 0.015 nm^{-1} (FWHM). The observed peak sizes are much larger and vary in the range from 0.05 nm^{-1} to 0.2 nm^{-1} and, as such, they depend mainly on the superlattice distortion. The characteristic lengthscale on which this distortion evolves is, most probably, smaller than the incident beam. Thus, the areas with different lattice parameters simultaneously illuminated by the incident beam lead to the peak broadening.

The angle γ between the $[100]_{SC}$ and $[010]_{SC}$ axes differs from its average value of $\langle \gamma \rangle = 90 \pm 6°$ in a range of 76° to 105° over the whole supercrystal as shown in **Fig. 3.4 d**. Specifically, we find $\gamma > 90°$ close to the top and bottom corners of the supercrystal and $\gamma < 90°$ close to the left and right corners. Thus, the angle pointing towards the corner of the supercrystal is always obtuse. We further calculate the azimuthal position φ of the mean line $\boldsymbol{M}$ between the $[100]_{SC}$ and $[010]_{SC}$ axes. This angle can be interpreted as the azimuthal orientation of the unit cell of the supercrystal. The orientation changes inhomogeneously throughout the superlattice in the range from 72° to 97° as shown in **Fig. 3.4 e**. There is no obvious correlation between the lattice orientation and the spatial position within the sample. Overall, these results suggest that the supercrystal is simple cubic on average, but it exhibits substantial local monoclinic distortions.

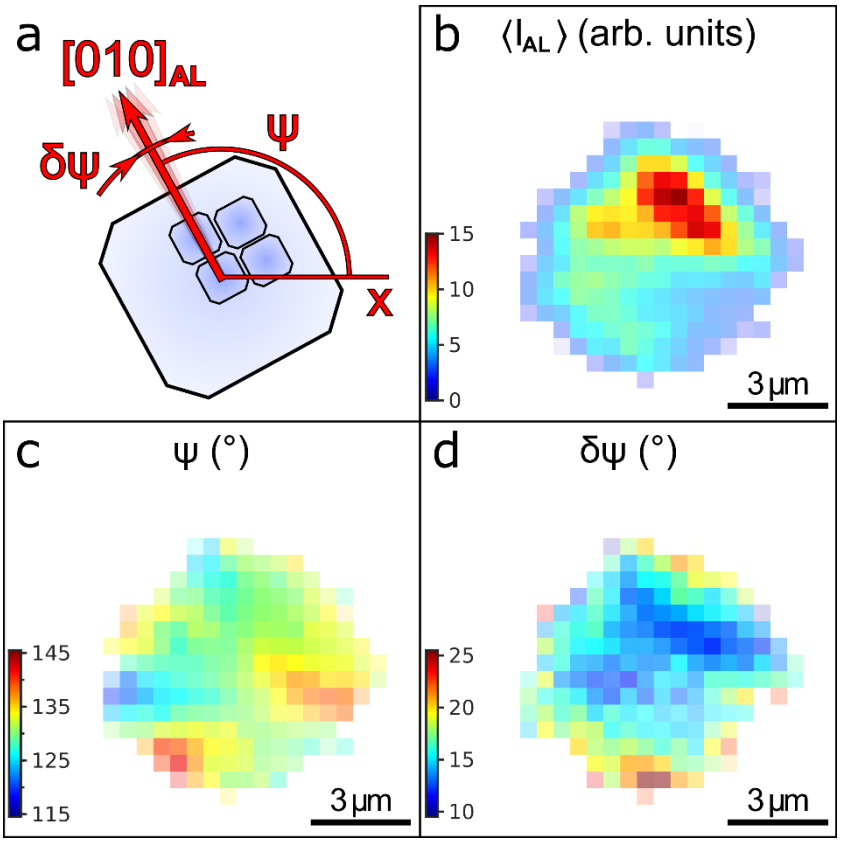

Figure 3.5: Spatially resolved WAXS. a) Definition of the geometrical parameters of the atomic lattice extracted by fitting of the Bragg peaks; b) mean intensity of the WAXS Bragg peaks $\langle I_{AL} \rangle$; c) azimuthal position ψ of the 100_{AL} crystallographic axis of the NCs; d) FWHM $\delta\psi$ of the angular disorder of the NCs around the mean azimuthal position ψ extracted from the azimuthal FWHMs of the Bragg peaks by the Williamson-Hall method. The pixel size in b-d) is 500 nm.

We analyze the Bragg peaks in the WAXS region of individual diffraction patterns at different locations to study the angular orientation of the NCs inside the superlattice. From the WAXS Bragg peak analysis, we extract the average WAXS intensity $\langle I_{AL} \rangle$ and the azimuthal position ψ of the $[010]_{AL}$ axis defined in **Fig. 3.5 a** (see Methods section and Supplementary Information, **Section S6**). In contrast to the intensity of the SAXS Bragg peaks, the WAXS intensity $\langle I_{AL} \rangle$ decreases towards the edges, as shown in **Fig. 3.5 b**, indicating an out-of-plane rotation of the NCs that shifts the Bragg peaks slightly out of the Ewald sphere. [261] We find that ψ changes in a wide range from 120° to 142° as shown in **Fig. 3.5 c**. The map of ψ resembles that of the azimuthal orientation φ of the mean line ***M***, shown in **Fig. 3.4 e**. The 45° offset between the $[010]_{AL}$ axis and the mean line ***M*** indicates the alignment of the $[110]_{AL}$ axis with the mean line ***M*** between the $[100]_{SC}$ and $[010]_{SC}$ axes (see Supplementary Information, **Figure S3.23**).

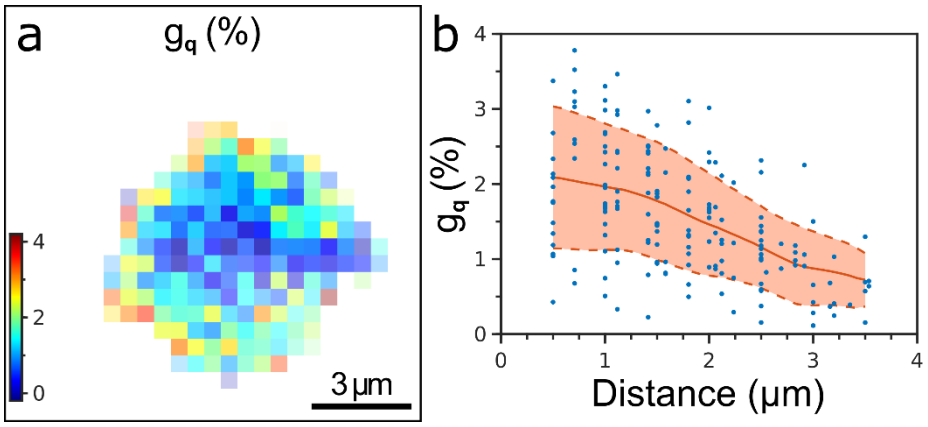

Figure 3.6: Spatially resolved atomic lattice distortion a) Atomic lattice distortion g_q extracted from the radial FWHMs of the WAXS Bragg peaks by the Williamson-Hall method. The pixel size is 500 nm. b) The same value g_q for each pixel plotted against the distance from this pixel to the nearest edge of the supercrystal. The red line shows the mean value, the dashed lines indicate the confidence interval of $\pm\sigma$.

From the azimuthal FWHMs of the WAXS Bragg peaks, we extract the angular disorder $\delta\psi$ of the individual nanocrystals at each spatial point by the Williamson-Hall method as shown in **Fig. 3.5 d** (see Methods for details). The disorder is smallest in the center of a supercrystal (9.9°) and increases to a maximum of 24.0° at the edges. The mean value of the angular disorder is $\langle\delta\psi\rangle$ = 16.1±2.8°, which is consistent with previously observed values for similar superstructures. [31,178,260,261]

Despite the fact that the atomic lattice parameter a_{AL} is constant within the error bars throughout the whole supercrystal (see Supplementary Information, **Figure S3.20**, for the map of a_{AL}), we find a difference in the radial width of the Bragg peaks at different locations. By the Williamson-Hall method, we extract the lattice distortion g_q (the ratio $\delta a_{AL}/a_{AL}$, where δa_{AL} is the FWHM of the unit cell parameter distribution around the mean value a_{AL}) at each spatial point (see Methods section for details). We find a clear trend of increasing atomic lattice distortion towards the edges of the supercrystal with a maximum of 2% at the edge, while it is about 1% at a distance 3 µm into the center, as shown in **Fig. 3.6**. The trend is even more evident for another supercrystal with particularly good signal-to-noise ratio of the WAXS intensity (see Supplementary Information, **Figure S3.29**).

To rationalize the experimental trend of increased fluorescence energies at the edges of the supercrystal as compared to its center, we carry out density functional modelling of the system. We consider three individual contributions in this regard. First, we recognize that the number of nearest neighbors at the surface of the supercrystal is lower than that in the center, leading to stronger exciton confinement and hence increased fluorescence energies at the edges. Indeed, our DFT calculations confirm this trend in **Figure 3.7 a**, which is consistent with the blueshift of the fluorescence spectra observed experimentally for the NCs at the edges. “Nearest neighbors” refers here to adjacent NCs with near-perfect orientational order, that is, a low value of $\delta\psi$ (**Figure 3.5 d**). A large orientational misalignment ($\delta\psi$) is likely to have a similar effect on nearest neighbor coupling as a reduced number of nearest neighbors. Second, we anticipate that the shorter interparticle spacing (**Fig. 3.4 b**) should

facilitate better electronic coupling between the nanocrystals at the edges and, therefore, a decrease in the optical gap at the edges is anticipated. While this expectation is confirmed computationally in **Figure 3.7 b**, we note that it is exactly opposite to what is observed experimentally in **Figures 3.1 b, e** (see Discussion section for details). Third, the supercrystal is compressed at the edges, as evident from **Figure 3.4 b**. While it is reasonable to assume that the compressive strain will mostly manifest in a denser packing of the soft oleylamine/oleic acid ligand sphere of the NCs, we also consider a partial compression of the hard-inorganic lattice-core. In **Figure 3.7 c** we calculate the effect of such compression on the HOMO–LUMO gap (E_{gap}) of the NC. While axial stress applied to the CsCl-terminated surface of the $CsPbBr_2Cl$ particle results in a steady increase of the optical gap consistent with the experiment, similar stress on the CsBr-terminated surfaces of both particles are found to both increase or decrease E_{gap}, depending on the magnitude of the applied stress.

Overall, our computational modelling suggests that the spectral blueshift of the fluorescence from the edges of the supercrystal can be caused mainly due to a reduced NC coordination number at the edges as well as the compressive atomic lattice strain in some cases, knowing that the third factor — the shorter inter-particle distance — works in the opposite direction, facilitating electronic coupling between adjacent nanocrystals and decreasing the optical gap. However, since the experimentally measured spectral shift is seemingly a combination of all three effects discussed above, a fully quantitative prediction would require more detailed knowledge on their relative contributions as well as the relative orientation and positions of individual nanocrystals, which are currently not available.

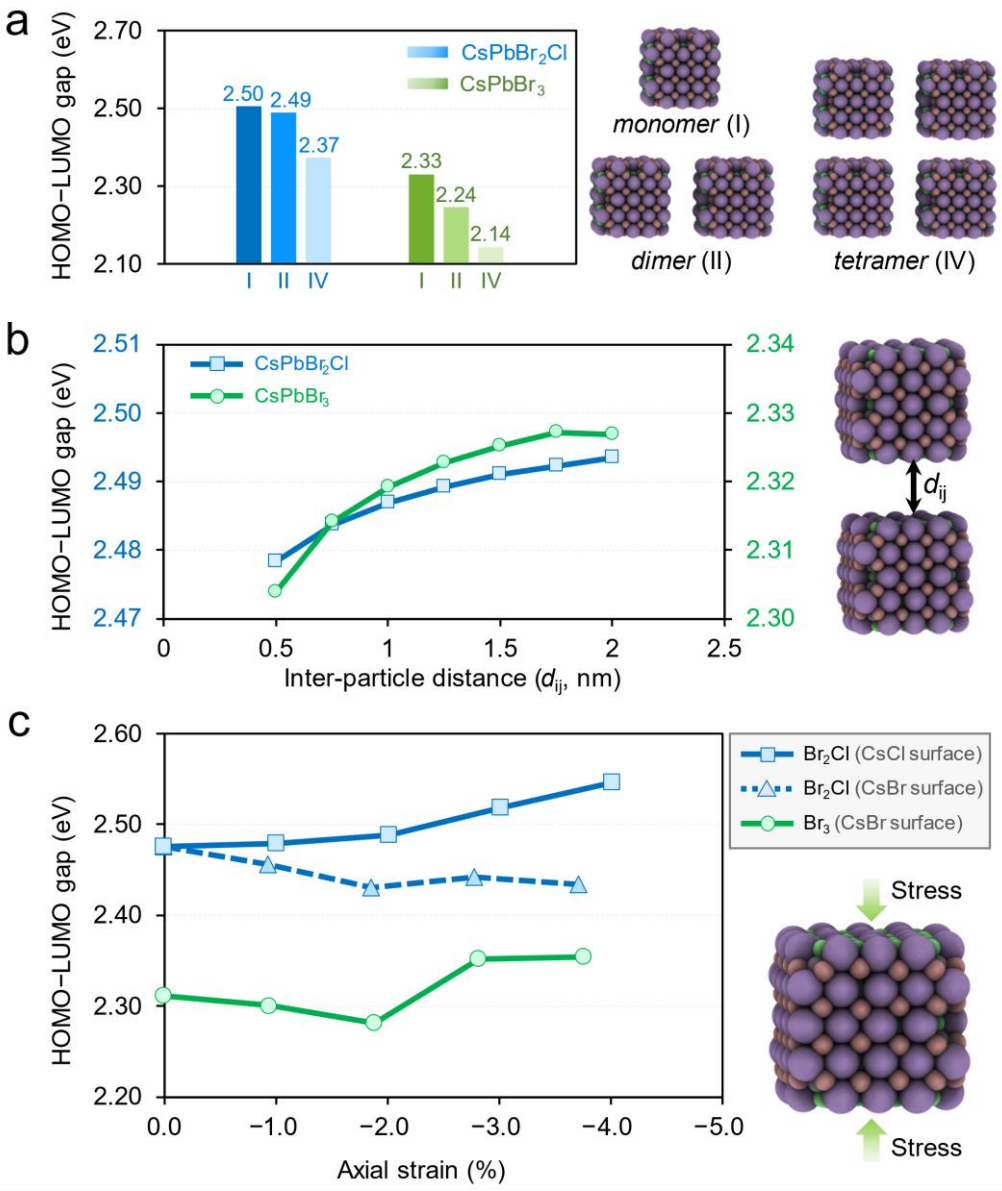

Figure 3.7: Density Functional Modelling. Computed HOMO–LUMO gaps as a function of a) number of neighboring particles considered (dimers and tetramers are 0.5 nm apart), b) distance between two adjacent particles, and c) applied axial strain, for both $CsPbBr_2Cl$ and $CsPbBr_3$ particles. All energies are in eV computed at PBE/DZVP level of theory.

3.4. Discussion

When NCs are self-assembled into supercrystals from colloidal solution via slow drying, the increasing curvature and surface tension of the evaporating solvent invokes compressive strain on the supercrystal. [265,266] We hold such a strain responsible for the observed compression of the unit cell parameter by over 20% of the $CsPbBr_2Cl$ NC supercrystals in **Fig. 3.4 b**. This compression is possible due to the softness of the oleylamine/oleic acid ligand shell of the NCs, enabling a large decrease of the interparticle distance by growing interdigitation of adjacent ligand spheres. We note that the

compression occurs gradually over a length scale of many lattice planes (>1 µm), meaning that it is not a localized surface reconstruction as commonly observed in atomic crystals. [247] The accompanying loss in angular correlation of the constituting NCs with the superlattice fits to a scenario where strain in the supercrystal is partially relieved by forming local structural defects. The comparison of the average (**Fig. 3.3 c**) *vs.* the local (**Fig. 3.4**) structure of the supercrystal shows that such distortions are indeed frequently present. We note that recent work on $CsPbBr_3$ NC supercrystals reported perfect structural coherence exclusively in the out-of-plane direction. [259] Since our experiment is only sensitive to in-plane structural features, the findings here are not contradictive to that report.

Our results in **Fig. 3.4 c** support the view of Kapuscinsky et al. that strain during the self-assembly is initially isotropic but later becomes increasingly anisotropic. [265] In a simple cubic supercrystal, the preferred direction for anisotropic structural changes to manifest is the $<111>_{SC}$, which will result in a shear deformation of the ligand spheres. [267] The expected structure of the supercrystal after this shear deformation is reasonably resembled by the local structure depicted in **Fig. 3.4**.

The compression in the supercrystals is not exclusively limited to the soft ligand sphere. With an interparticle distance of <1 nm close to the edges of a supercrystal, the space for the two ligand spheres of adjacent NCs is so constrained, that the inorganic cores of the NCs become compressed as well (**Fig. 3.6**). Strain in lead halide perovskite thin films plays an important role for their optoelectronic properties and application in photovoltaic devices. [268] Our fluorescence and fluorescence lifetime data in **Figures 3.1 and 3.2** suggests that this is also the case for lead halide NC supercrystals. A comparison of **Figure 3.1** with **Figure 3.4 b** reveals a strong correlation between the gradual blueshift of the fluorescence peak wavelength and the progressive compression of the supercrystal. We suggest that the shift by up to 20 meV is the result of three, partially competing phenomena: 1) a loss in structural coherence as well as isoorientation of NCs (**Fig. 3.5 c** and **d**) 2) a decrease of the interparticle distance (**Fig. 3.4 b**), and 3) the distortion of the atomic lattices of the NCs (**Fig. 3.6**). Our DFT calculations in **Figure 3.7 a** suggest that the first effect should be associated with a significant blueshift of the fluorescence due to reduced coupling, consistent with a previous report about the importance of structural coherence for electric transport in supercrystals. [242] While the second effect can only lead to a red shift (**Fig. 3.7 b**), the third effect is also shown to invoke a blueshift for specific facets or magnitudes of strain (**Fig. 3.7 c**).

With reference to several studies on $CsPbBr_3$ NCs which reported a red-shifted fluorescence after assembly into supercrystals, we note that the resultant peak wavelength may further be affected by the concomitant changes in the dielectric environment, aging, miniband formation as well as cooperative emission. [139,269–271] However, most of these observations were made under markedly

different conditions, such as low temperature, prolonged exposure to air or self-assembly at the liquid/gas interface, which may be the reason that they are not a dominating factor in our study.

We note a previous report on the spatially resolved fluorescence of $CsPb(I_{0.28}Br_{0.72})_3$ NC supercrystals with a similar fluorescence blueshift between the center and the edge. [115] As a main conclusion, gradual release of I_2 gas under intense laser illumination led to the blueshift since lead bromide perovskites exhibit a larger bandgap than the corresponding lead iodide perovskites. The authors argued that the I_2 loss commenced from the edges towards the center, which would explain the spatial fluorescence variations. In $CsPbBr_2Cl$ however, this mechanism is not easily applicable since the reduction potential of Br^- is much lower than that of I^-. In line with this, $CsPbBr_3$ NC supercrystals without a halide mixture show a similar blueshift, indicating that a change in the mixed halide composition is not required to observe the effects reported here.

The decrease of the fluorescence lifetime in **Figure 3.2** is also strongly correlated with the gradual compression of the supercrystal towards the edges. Moreover, many supercrystals exhibit particularly decreased lifetime values at the corners, which bears similarities with the anisotropic changes in the lattice spacings in **Figure 3.4 c**, highlighting again the correlation between structural and optical properties. We speculate that the increased atomic lattice distortion and loss of structural coherence near the edges of the supercrystals result in a reduced stability of the excited state of the emitting NCs. This view is supported by the decreased radiative lifetime values from these locations as well as previous reports on the fluorescence lifetime at grain boundaries of large organic-inorganic perovskites. [272,273] In view of the currently pursued application of lead halide NC supercrystals as superfluorescent emitters, [139,245] this would imply that bright and coherent emission originates from the center of the supercrystals as long as they are freshly prepared. Conversely, for aged $CsPbBr_2Cl$ NC supercrystals, the lifetimes are longest at the edges, which points to an increased stability of the excited state, potentially due to the formation of a protective oxide shell. [274]

As an alternative explanation for the spatial differences in the fluorescence (-lifetime) in the supercrystals, we also consider a photon propagation effect, that is, multiple emission and (re-)absorption events, which become more likely with increasing thickness of the emitter material. [269] Therefore, reabsorption should occur predominantly in the center of the supercrystals but not at the edges. This effect results in an overall red-shift of the fluorescence and an increase of the fluorescence lifetime, which would be in line with the observations in this work. [275,276] Moreover, we would expect the absolute fluorescence intensity *per emitter* to be lower for an area with frequent reabsorption events and the time-resolved fluorescence decay to be increasingly multiexponential due to the non-radiative losses and multi-step nature of the photon propagation effect. However, we find the fluorescence decay to be monoexponential (**Figure S3.2 c + S3.3 c**) and the fluorescence intensity to be highest in the center, from where it gradually decreases toward the edges (**Figures S3.6 b** and **S3.7 b**). This decrease extends over a much larger distance than the flattening of the edges which we

occasionally observe on less facetted supercrystals (**Figure S3.9 c**), such that the high fluorescence intensity in the center cannot be a mere thickness effect. We note that we would expect a negative correlation between the fluorescence intensity with its corresponding lifetime if reabsorption was dominant in the supercrystals, but we do not find such a correlation in our data (**Figures S3.6 f** and **S3.7 f**). In summary, given the relatively high fluorescence quantum yield of lead halide perovskite NCs, reabsorption is likely to partially contribute to the spatially varying optical properties of supercrystals thereof, [277] but our data is inconsistent with it as the dominant cause.

In conclusion, supercrystals of lead halide perovskite NCs self-assembled from solution exhibit a loss in structural coherence, an increasing atomic misalignment between adjacent NCs, and compressive strain near their surfaces. These structural distortions are strongly correlated with a blue-shifted fluorescence and decreased radiative lifetimes. We note that structural distortion and surface defects have been shown to strongly affect the fluorescence properties in *atomic* crystals, such as transition metal dichalcogenides. [248–252] The structure-fluorescence correlations in *supercrystals* revealed here are thus another example for the analogy between atoms and NCs as so-called quasi-atoms.

Acknowledgement

We acknowledge DESY (Hamburg, Germany) for the provision of experimental facilities. Parts of this research were carried out at PETRA III synchrotron facility and we would like to thank the beamline staff for assistance in using the Coherence Application P10 beamline. This work was supported by the Helmholtz Associations Initiative Networking Fund (grant No. HRSF-0002), the Russian Science Foundation (grant No. 18-41-06001) and the DFG under grants SCHE1905/8-1, SCHE1905/9-1, AN680/6-1 and SCHR700/38-1. D.L., N.M., D.As., Y.Y.K., M.Sp., and I.A.V. acknowledge support of the project by Edgar Weckert.

Authors contribution

D.L., C.K., and J.H. contributed equally to this work. D.L., D.As., J.C., Y.Y.K., N.M., I.Z. and M.Sp. performed the X-ray scattering experiments. C.K., S.W. and J.W. synthesized the NCs, conducted optical absorption and fluorescence measurements in solution and prepared all samples. J.H. carried out the confocal fluorescence (-lifetime) measurements. M.M. performed DFT calculations and A.M. undertook the SEM and AFM measurements. F.S., A.J.M., K.B., D.A., I.A.V. and M.S. conceived and supervised the project. D.L., J.H., M.M., I.A.V. and M.S. wrote the manuscript with input from all authors. All authors have given approval to the final version of the manuscript.

Competing interests

The authors declare no competing interests.

Data availability

The X-ray and optical data that support the findings of this study are available in Zenodo.org at https://zenodo.org/deposit/5607366. [278]

3.5. Methods

Chemicals

1-Octadecene (ODE), technical grade, 90%, Sigma Aldrich; Oleic acid (OA), 97%, Acros Organics; Oleylamine (OAm), 80 - 90%, Acros Organics; Caesium carbonate (Cs2CO3), 99.99% (trace metal basis), Acros Organics; Lead(II)chloride (PbCl2), 99.999% (trace metal basis), Sigma Aldrich; Lead(II)bromide ($PbBr_2$), ≥98%, Sigma Aldrich; Toluene, 99.8%, extra dry, AcroSeal, Acros; Tetrachloroethylene (TCE), ≥99%, Acros Organics; Kapton® polyimide membranes (125 µm thickness) were purchased from DuPont; Si/SiOx wafers (200 nm SiOx thickness) were purchased from Siegert Wafer GmbH. All chemicals were used as purchased.

Preparation of Cs-oleate

203.5 mg Cs_2CO_3 (0.625 mmol) was loaded into a 25 mL three-neck flask along with 10 mL 1-octadecene and 0.625 mL oleic acid, dried for 1 h at 120 °C and then heated to 150 °C under nitrogen atmosphere until all Cs_2CO_3 reacted with oleic acid. The mixture was kept in a glovebox and heated to 110 °C before injection.

Synthesis of $CsPbX_3$ nanocrystals

$CsPbX_3$ NCs were made by a hot-Injection synthesis using a modified literature method. [19] To synthesize 9 nm $CsPbBr_3$ or 7 nm $CsPbBr_2Cl$ NCs, 138 mg (0.38 mmol) $PbBr_2$ or 92 mg (0.25 mmol) $PbBr_2$ and 35 mg (0.125 mmol) $PbCl_2$ were degassed in 10 mL ODE in a 25 mL three-neck flask under reduced pressure at 120 °C for 2 h. Then, 1 mL of dried oleylamine (OAm) and 0.5 mL of dried oleic acid (OA) were injected at 120 °C under nitrogen atmosphere with continuous stirring and the reaction mixture was heated to 160 °C. After the solubilization was completed, 0.8 mL of a previously prepared solution of Cs-oleate in ODE (0.125 M) was swiftly injected, and the reaction mixture was cooled to room temperature using an ice-bath.

Isolation and purification of $CsPbX_3$ nanocrystals

$CsPbX_3$ NCs were collected by centrifuging the suspension (7000 rpm, 10 min), decanting the supernatant, and collecting the precipitate. The precipitate was centrifuged again without addition of a solvent (7000 rpm, 5 min), and the resulting supernatant was removed with a syringe, to separate the traces of residual supernatant. The precipitate was dissolved in 2 mL hexane and centrifuged again (2500 rpm, 5 min) to remove aggregates and larger particles. The resulting supernatant was filtered

through a 0.2 µm PTFE syringe filter and stored as stock solution inside of a glovebox with a typically concentration of 16 mM following Maes *et al*. [279]

Self-assembly of NC superlattices

For the growth of supercrystals, different substrates (Si wafer, Kapton, glass) were used, depending on the desired experiment. The self-assembly experiment was set up in a glass Petri dish (with a 60 mm diameter), for this purpose three substrates each were placed in such a Petri dish together with a PTFE-lid filled with 1 mL tetrachloroethylene. To each of these substrates, 40 µL of a 1 - 3 mM solution of the perovskites in TCE was added. The lid of the Petri dish was closed, covered with aluminum foil, and allowed to stand for 24 h. After that, the lid was opened and left for another 5 h to dry completely. All self-assembly preparations were performed under inert atmosphere. The more monodisperse the size distribution of the perovskites, the better the resulting superlattices

Spatially resolved optical measurements

All spatially resolved optical measurements were performed using a home-built inverted confocal laser scanning microscope. The measurements were performed on glass substrates utilizing a high numerical aperture oil immersion objective (NA = 1.4) and a 405 nm pulsed diode laser (Picoquant LDH P-C-405) with variable repetition rates (Picoquant PDL 800-D laser driver) as the excitation source. Under these conditions the lateral resolution of the instrument is approximately 200 nm. A single photon avalanche diode (MPD PDM Series) was used in conjunction with the Picoquant HydraHarp 400 as a time-correlated single photon counting system to detect time-resolved fluorescence. Time-resolved data acquisition and analysis was performed using Picoquants SymPhoTime 64 software package. The spectral data was recorded using an Acton Spectra Pro 2300i spectrometer with a 300 grooves/mm grating. The detector temperature (Princeton PIXIS CCD) was kept steady at -45 °C.

X-ray diffraction experiment

The nano-diffraction experiment was performed at the Coherence Applications beamline P10 of the PETRA III synchrotron source at DESY. An X-ray beam with the wavelength λ = 0.0898 nm (E = 13.8 keV) was focused down to a spot size of approximately 400 × 400 nm^2 (FWHM) with a focal depth of about 0.5 mm at the GINIX nano-diffraction endstation. [280] The two-dimensional detector EIGER X 4M (Dectris) with 2070 × 2167 pixels and a pixel size of 75 × 75 µm^2 was positioned 412 mm downstream from the sample. The detector was aligned ~6 cm off-centre in both directions normal to the incident beam to allow simultaneous detection of SAXS and WAXS. We performed a spatially resolved scan of the sample on a Kapton substrate by 25 × 25 spatial points with 500 nm step size and collected 625 diffraction patterns in transmission geometry. The exposure time was set to 0.5 s to prevent radiation damage of the sample. The background scattering pattern from a pure Kapton film was subtracted from every collected pattern.

Bragg peak analysis

Each diffraction pattern was interpolated onto a polar coordinate grid with the origin at the direct beam position. The radial profiles were obtained by averaging along the azimuthal coordinate. To extract parameters of the WAXS and SAXS Bragg peaks separately, we fitted each of them by the 2D Gaussian function

$$I(q,\varphi) = \frac{I_0}{2\pi\sigma_q\sigma_\varphi}\exp\left[-\frac{(q-q_0)^2}{2\sigma_q^2} - \frac{(\varphi-\varphi_0)^2}{2\sigma_\varphi^2}\right],$$

where I_0 is the integrated intensity, q_0 and φ_0 are the radial and azimuthal central positions, and σ_q and σ_φ are the corresponding root mean square (rms) values. The FWHMs of the Bragg peaks were evaluated according to relations: $w_q = 2\sqrt{2ln2}\sigma_q$ and $w_\varphi = 2\sqrt{2ln2}\sigma_\varphi$. The fitting was done in the appropriate region of the polar coordinates with a single isolated Bragg peak.

For the SAXS peaks, the parameters were pairwise averaged for the corresponding Friedel pairs of the Bragg peaks to improve statistics. The resulting momentum transfer values and angles were used to calculate the real space parameters of the unit cell: the length of the basis vectors a_1 and a_2, the angle γ between them and the average azimuthal position φ counted counterclockwise from an arbitrary horizontal axis (see Supplementary Materials for details).

For the WAXS peaks, we calculated an average Bragg peak intensity I_{AL} and the azimuthal position ψ of the $[010]_{AL}$ axis. To obtain the average azimuthal position ψ, we averaged all four azimuthal positions for 010_{AL}, 020_{AL}, 110_{AL}, and $\bar{1}00_{AL}$ Bragg peaks, but corrected the last two values by +45° and -45°, respectively. We used the Williamson-Hall method [281] to analyze the size of the WAXS Bragg peaks at each spatial point of the supercrystal. The FWHM of the Bragg peak is determined by the NC size and the lattice distortion as follows:

$$w_{q,\varphi}^2(q) = \left(\frac{2\pi K}{L}\right)^2 + \left(g_{q,\varphi}q\right)^2, \tag{3.1}$$

where $w_{q,\varphi}$ is the FWHM of the Bragg peak at q in radial or azimuthal direction, respectively, L is the NC size, $g_{q,\varphi}$ is the radial or angular lattice distortion of the atomic lattice, respectively, K is a dimensionless shape parameter that is about 0.86 for cubic NCs. [282] The radial lattice distortion g_q calculated from the radial FWHM w_q is equal to the ratio $\delta a_{AL}/a_{AL}$, where δa_{AL} is the FWHM of the unit cell parameter distribution around the mean value a_{AL}. The angular lattice distortion g_φ calculated from the azimuthal FWHM w_φ is equal to the FWHM $\delta\psi$ of the angular distribution of the NCs around their average azimuthal position ψ. For the spatially resolved analysis of the FWHMs, the NC size L was fixed at the value, obtained from the average radial profiles. For details of the analysis, see Supplementary materials.

Scanning electron and atomic force microscopy

SEM imaging of supercrystals on Si/SiO_x devices was performed with a HITACHI model SU8030 at 30 kV. To estimate the thickness of micro-crystals, samples were titled by 45° with respect to the incoming electron beam. AFM investigations were conducted with a Bruker MultiMode 8 HR in contact mode.

Density functional theory calculations

All computations are performed using the CP2K 5.1 program suite using the Quickstep module. [283] The PBE exchange correlation functional, [284] a dual basis of localized Gaussians and plane waves (GPW) [285] with a 350 Ry plane-wave cutoff, double-ζ basis-set augmented with polarization functions (MOLOPT variant), [286] and GTH pseudopotentials [287] for core electrons are used for all calculations. The van der Waals (VDW) interaction was accounted for by employing Grimme's DFT-D3 method. [288] SCF convergence criterion was set at 10^{-6} for all calculations.

Initial geometries of $CsPbX_3$ (X = Cl, Br) nanocrystals were obtained by cutting small cubes (~2.4 nm) from the bulk, exposing the CsX layer at the surface and maintaining overall charge neutrality of the particle. [289] All structures were then optimized in vacuum using the BFGS optimizer imposing non-periodic boundary conditions with a wavelet Poisson solver, [290] setting a maximum force of 5 meV·Å^{-1} (10^{-4} hartree/bohr) as convergence criteria. For these non-periodic systems, axial strain was simulated by fixing the length of one side of the cube. If the relaxed cubic nanocrystal has side length $a \times b \times c$, and stress is to be applied along the Z-direction, "c" is fixed at some c′ by constraining the z coordinates of both the top and bottom surface-atoms along the z-direction, with all other coordinates of all atoms relaxed. % Strain is reported as $(c' - c)/c \times 100\%$. For calculations involving dimers and tetramers, 2/4 monomers were explicitly considered, but *periodic* boundary condition was imposed with at least 10 Å vacuum above the surface of the nanocluster to avoid spurious interaction with its periodic image.

3.6. Supplementary Information

Spatially resolved fluorescence of caesium lead halide perovskite supercrystals reveals quasi-atomic behavior of nanocrystals

Dmitry Lapkin[1,*], Christopher Kirsch[2,*], Jonas Hiller[2,*], Denis Andrienko[3], Dameli Assalauova[1], Kai Braun[2], Jerome Carnis[1], Young Yong Kim[1], Mukunda Mandal[3], Andre Maier[2,4], Alfred J. Meixner[2,4], Nastasia Mukharamova[1], Marcus Scheele[2,4,+], Frank Schreiber[4,5], Michael Sprung[1], **Jan Wahl**[2], Sophia Westendorf[2], Ivan A. Zaluzhnyy[5], Ivan A. Vartanyants[1,6,+]

1. Deutsches Elektronen-Synchrotron DESY, Notkestraße 85, D-22607 Hamburg, Germany

2. Institut für Physikalische und Theoretische Chemie, Universität Tübingen, Auf der Morgenstelle 18, D-72076 Tübingen, Germany

3. Max Planck Institute for Polymer Research, Ackermannweg 10, D-55128 Mainz, Germany

4. Center for Light-Matter Interaction, Sensors & Analytics LISA+, Universität Tübingen, Auf der Morgenstelle 15, D-72076 Tübingen, Germany

5. Institut für Angewandte Physik, Universität Tübingen, Auf der Morgenstelle 10, D-72076 Tübingen, Germany

6. National Research Nuclear University MEPhI (Moscow Engineering Physics Institute), Kashirskoe shosse 31, 115409 Moscow, Russia

* These authors contributed equally

+To whom correspondence should be addressed

Section S1. Optical absorption and fluorescence of $CsPbBr_2Cl$ and $CsPbBr_3$ nanocrystals in solution

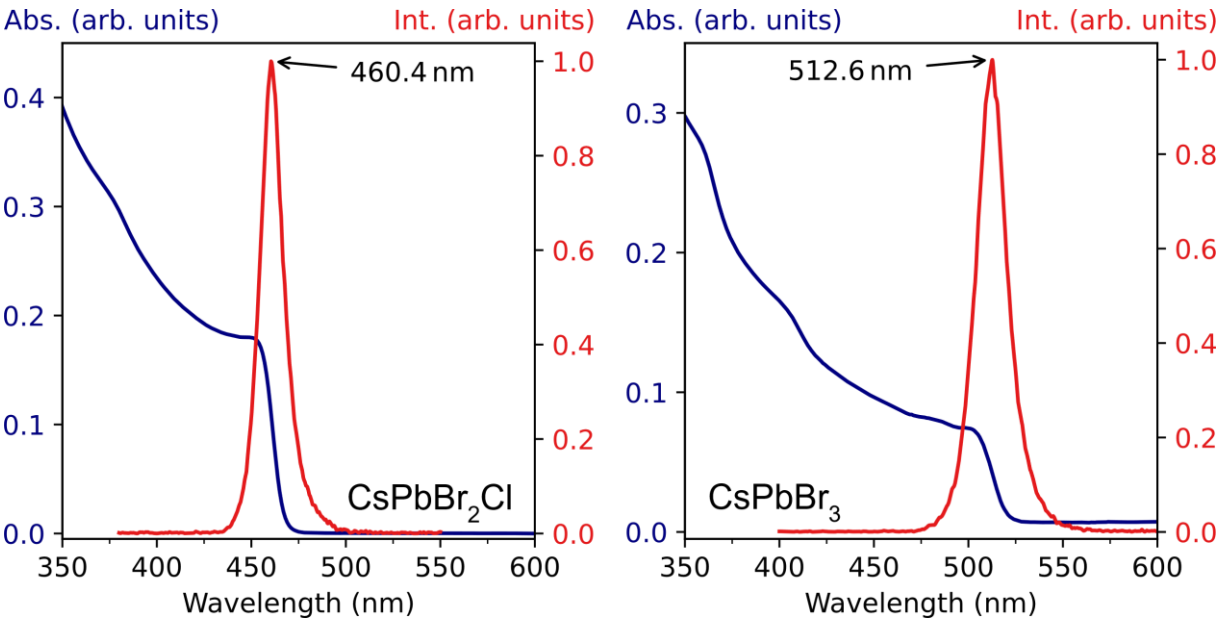

Figure S3.1: a) Absorption and emission spectrum of $CsPbBr_2Cl$ NPs dispersed in Toluene. b) Absorption and emission spectrum of $CsPbBr_3$ NPs dispersed in Hexane.

Optical measurements were performed on a UV-vis-NIR spectrometer (Agilent Technologies, Cary 5000) and a fluorescence spectrometer (PerkinElmer FL8500). All spectra were acquired under ambient conditions in Toluol at room temperature (25 °C) in a cuvette of 1 cm pathlength.

Section S3.2. Fluorescence lifetime imaging

A fast fluorescence lifetime imaging microscopy (fast FLIM) image is recorded by scanning the excitation laser over an area of interest while recording the time-resolved fluorescence in the form of a time-correlated single photon counting (TCSPC) histogram at each pixel. The fast lifetime hereby obtained for each pixel is to be understood as the mean photon arrival time after the excitation laser pulse and therefore includes the time the light takes to travel through the instrument. The histogram of the excitation pulse is called the instrument response function (IRF) and was directly measured by the means of scattered light from a clean glass substrate. The physical decay of the sample is obtained by fitting the experimental decay curves recorded at each pixel by employing the IRF in an n-exponential reconvolution with a maximum likelihood estimation method employed for fit optimization.

For both compositions of the investigated self-assembled supercrystals, good results were obtained by fitting a monoexponential reconvolution to the experimental decay curves. Exemplary fits for the center pixels in the FLIM images of the self-assembled supercrystals composed of $CsPbBr_2Cl$ NCs and $CsPbBr_3$ NCs are depicted in **Fig. S3.2** and **Fig. S3.3,** respectively.

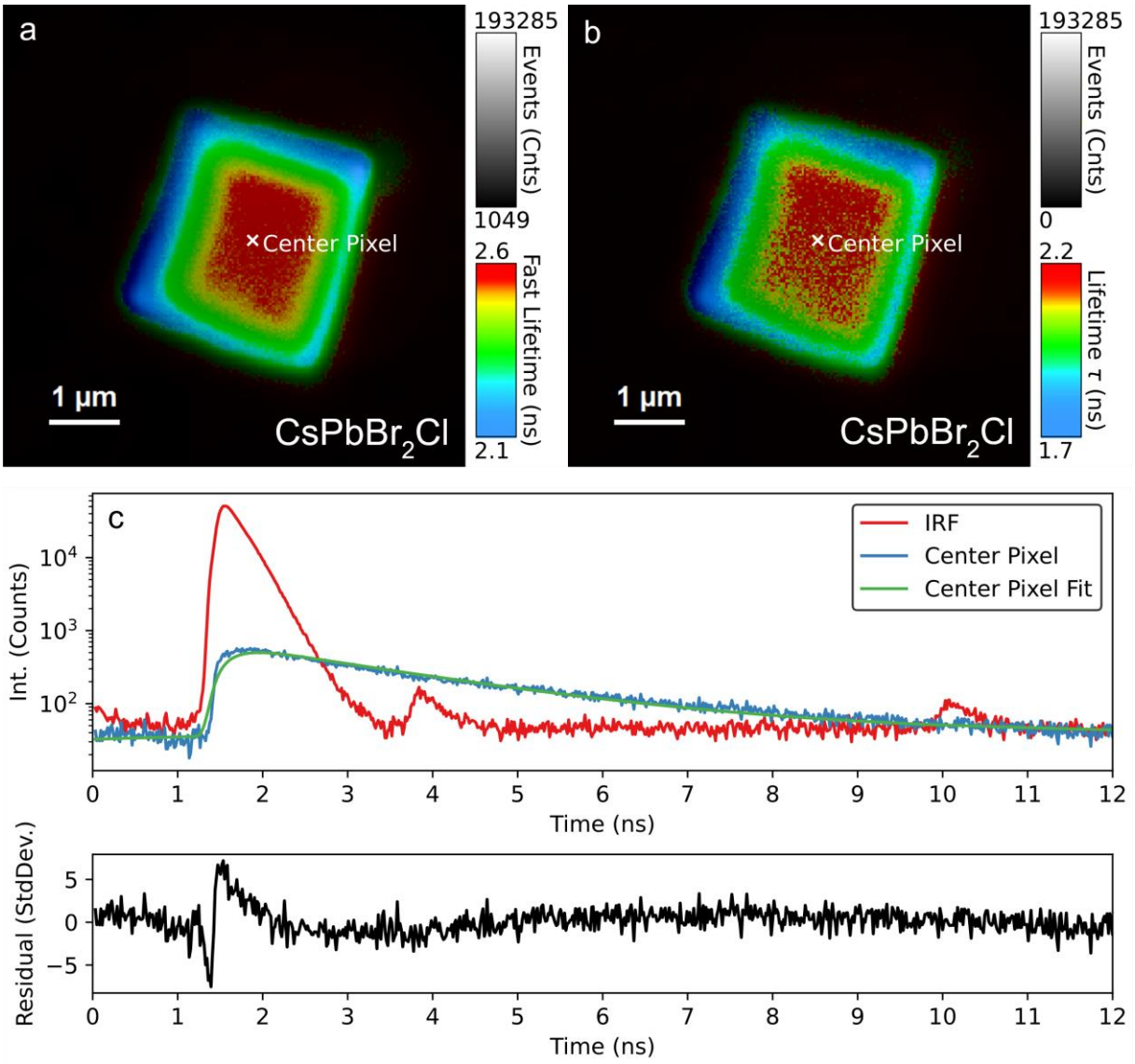

Figure S3.2: For each pixel of the FLIM images the fluorescence intensity is encoded on a brightness scale while fast lifetimes and fluorescence lifetimes are displayed in RGB false color. a) Fast FLIM image of a self-assembled $CsPbBr_2Cl$ supercrystal and b) the corresponding fitted FLIM image obtained through a pixel-by-pixel monoexponential reconvolution. c) The experimentally acquired IRF as well as an exemplary decay curve of a pixel in the center of the supercrystal and its corresponding monoexponential fit.

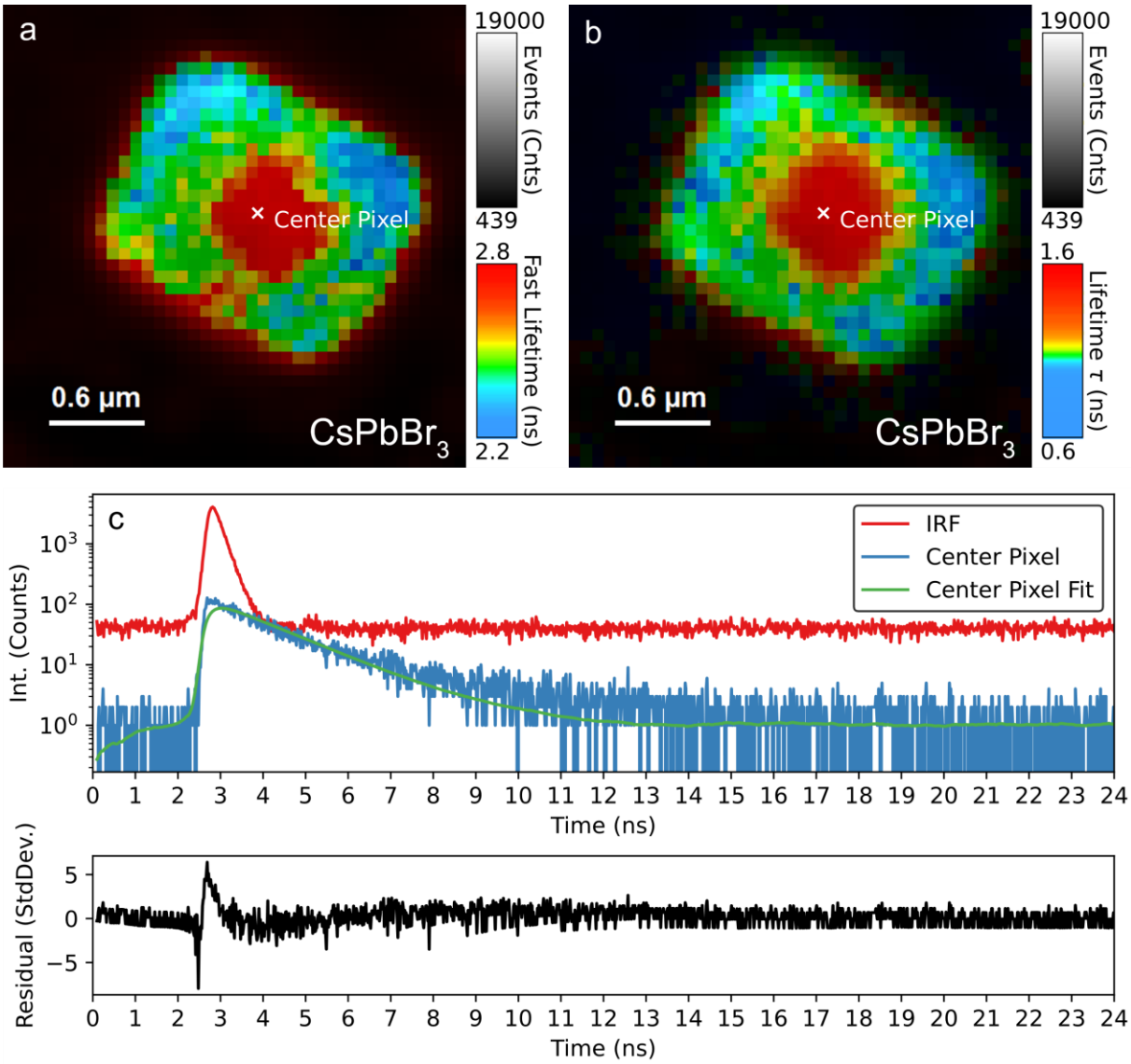

Figure S3.3: For each pixel of the FLIM images the fluorescence intensity is encoded on a brightness scale while fast lifetimes and fluorescence lifetimes are displayed in RGB false color. a) Fast FLIM image of a self-assembled $CsPbBr_3$ supercrystal and b) the corresponding fitted FLIM image obtained through a pixel-by-pixel monoexponential reconvolution. c) The experimentally acquired IRF as well as an exemplary decay curve of a pixel in the center of the supercrystal and its corresponding monoexponential fit.

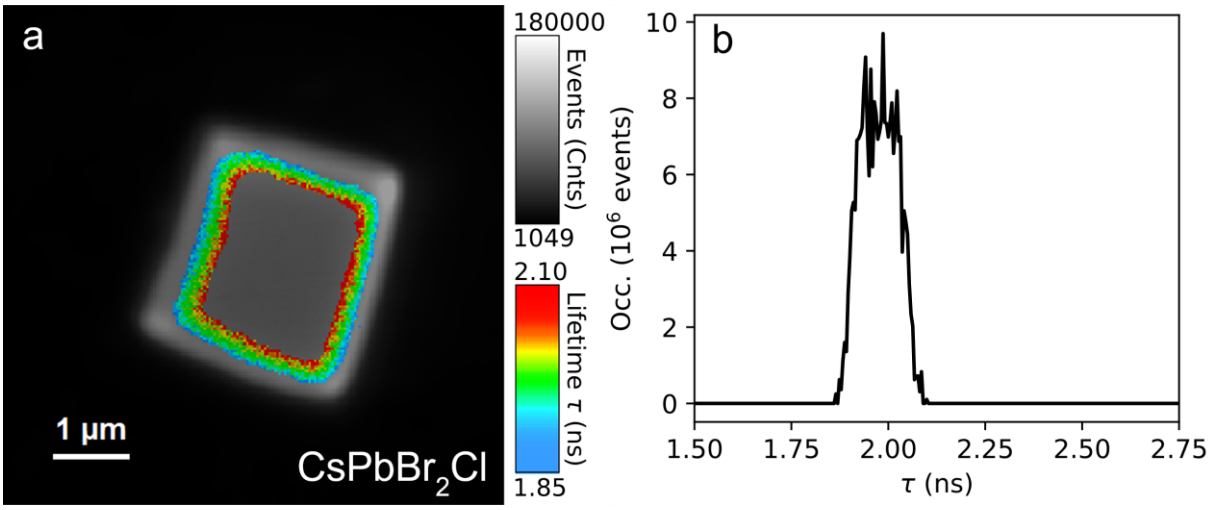

Figure S3.4: a) Region of interest (ROI) FLIM image of the intermediate area of the $CsPbBr_2Cl$ supercrystal depicted in Fig. S2. b) The occurrence of the τ-values associated with the monoexponential decay throughout the ROI FLIM image. This ROI FLIM image demonstrates that the decrease of the τ-values when scanning from the center of the supercrystal towards its edges is rather gradual. The "step-like" decrease that **Fig. S2** seems to imply is due to the chosen RGB color-scaling.

Section S3.2.1. Determining the shortest euclidean distance to the supercrystal edge for each pixel

The first step in the analysis is differentiating between the pixels located inside and those located outside of the supercrystal. This was achieved by assigning the lifetime value 0 to each pixel for which the measured fluorescence intensity is less than half the maximum recorded fluorescence intensity. Because the transition between the inside and the outside of the supercrystal is characterized by a steep drop in the recorded fluorescence intensity, all pixels inside the supercrystal are unaffected and keep their non-zero lifetime value, while all pixels outside of the supercrystal are assigned the lifetime value 0. The masking process for the $CsPbBr_2Cl$ supercrystal is depicted in **Fig. S3.5**. The pixel-to-edge distance for all pixels inside the supercrystal is then the shortest distance between a pixel with a non-zero lifetime value and a pixel with the associated lifetime value 0. The free Python machine learning library Scikit-learn was employed for the actual calculations.

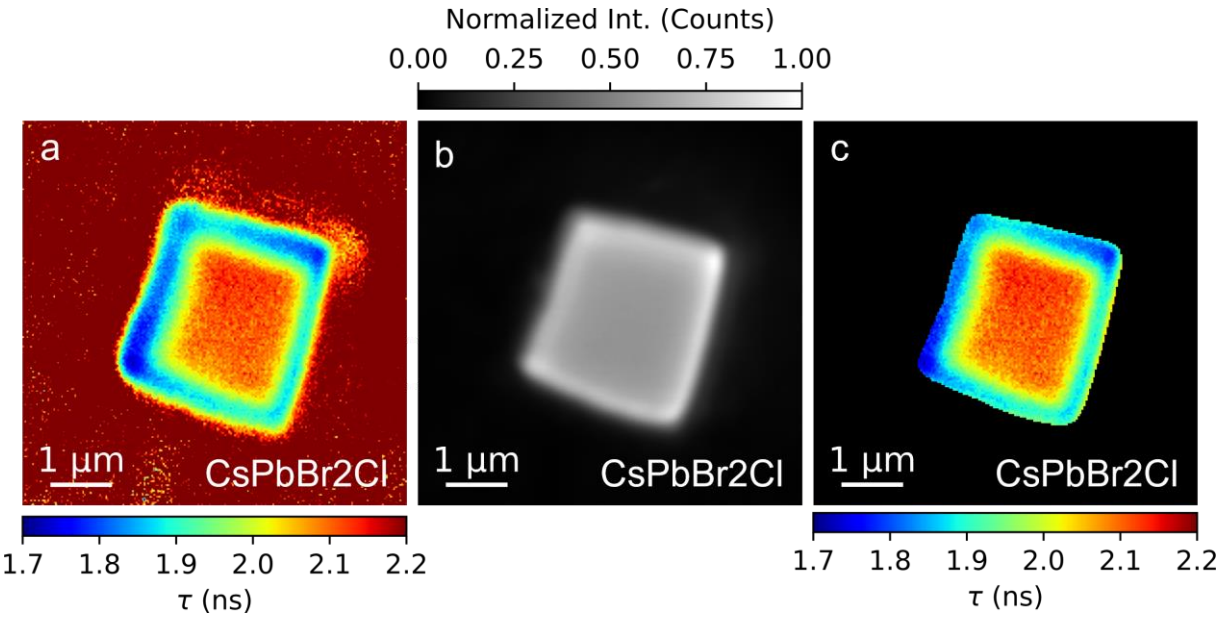

Figure S3.5. For each of the 200x200 pixels the fluorescence lifetime a) as well as the fluorescence intensity b) are recorded. c) Result of assigning the lifetime value 0 to all pixels for which the recorded fluorescence intensity is less than half the maximum recorded fluorescence intensity. All pixels inside the supercrystal remain unaffected and keep their non-zero lifetime value as determined by the measurement.

Section S3.3. Electron microscopy of $CsPbBr_2Cl$ supercrystals

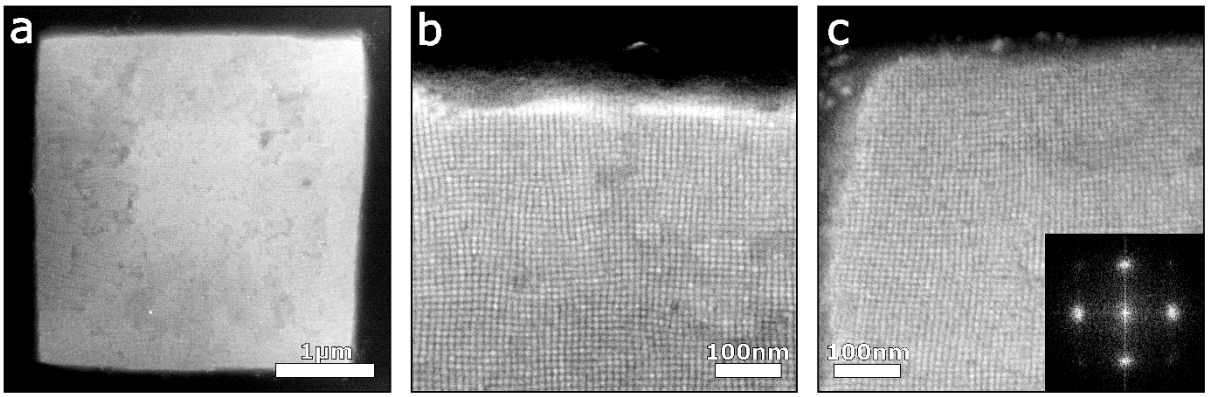

Figure S3.6: a) SEM micrograph of self-assembled supercrystals of $CsPbBr_2Cl$ NCs. The NC diameter is rather uniform over the whole crystal (7.3±0.4 nm), as indicated by the high-resolution micrograph of an edge b) and a corner c). The inset of c) corresponds to the FFT of the corresponding micrograph, indicating a homogeneous four-fold symmetry of the NC arrangement.

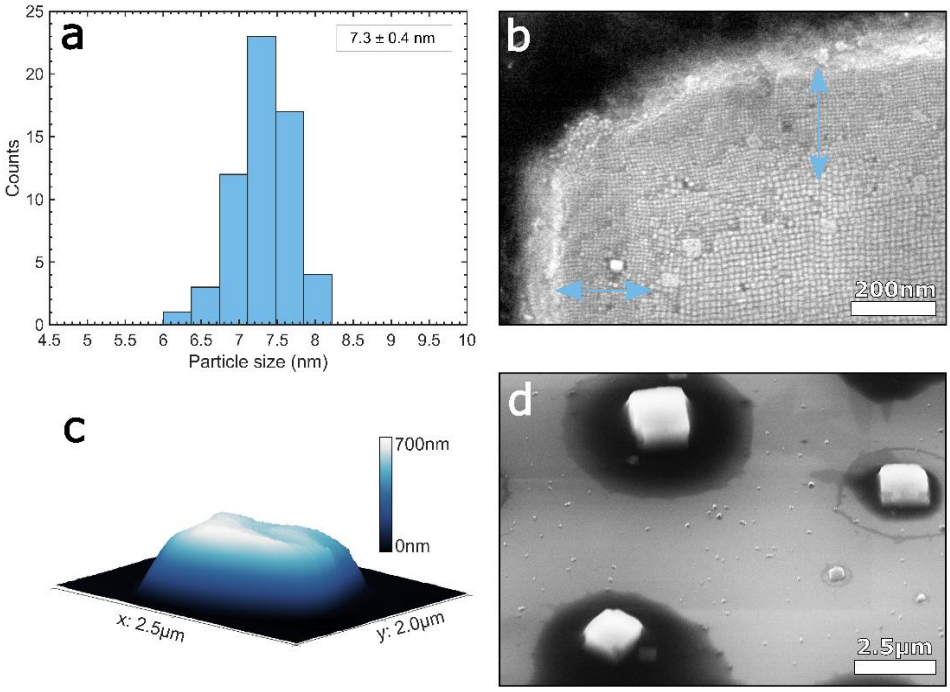

Figure S3.7: a) Distribution of the diameter of the $CsPbBr_2Cl$ NCs, measured by SEM. The mean value is 7.3±0.4 nm (size distribution of ~5%). b) SEM micrograph of the corner of a less facetted supercrystals occasionally featuring NCs of smaller size. The spatial extent of this subpopulation is limited to ~200 nm from the edges, indicated by the blue arrows. c) 3D AFM map of a supercrystal on a Kapton membrane. d) SEM micrograph of three supercrystals on a Si/SiOx wafer under a view angle of 45°. Typical supercrystal thicknesses of 580±120 nm can be observed.

Section S3.4. Atomic structure of the constituting $CsPbBr_2Cl$ NCs

The azimuthally averaged WAXS intensity calculated for the mean pattern for a supercrystal is shown in **Fig. S3.8**. There are three prominent peaks originating from the atomic lattice of the $CsPbBr_2Cl$ NCs. The peaks can be attributed to 100_{AL}, 110_{AL} and 200_{AL} reflections of a cubic superlattice. The peaks at $q \sim 24.5$ nm^{-1} can be attributed to 210_{AL} reflection which is only partially covered by the detector. The structured background in the range of q = 17-20 nm^{-1} is from the Kapton film. It cannot be fully subtracted due to the anisotropy of scattering from the Kapton film in different spatial point of the scanned area. The peaks were simultaneously fitted by three Gaussian functions:

$$I(q) = \sum_{i=1}^{3} \frac{I_i}{\sqrt{2\pi\sigma_i^2}} \exp\left[-\frac{(q-q_i)^2}{2\sigma_i^2}\right], \quad \text{(S3.1)}$$

where I_i is the integrated intensity, q_i is the momentum transfer and $w_i = 2\sqrt{2ln2}\sigma_i$ is the FWHM of the i-th Bragg peak. The peaks are at q_{100} = 10.930±0.005 nm^{-1}, q_{110} = 15.442±0.002 nm^{-1} and q_{200} = 21.900±0.003 nm^{-} giving the unit cell parameter a_{AL} = 0.574±0.001 nm. The error bars are the fitting errors. One should note that the expected atomic lattice structure for cesium lead halide perovskites at room temperature is orthorhombic. [262] However, the deviation of the unit cell parameters of such orthorhombic lattice from a cubic lattice is < 2%. We are not able to resolve the

peaks of the same order with so small separation due to the size-dependent Scherrer broadening of the Bragg peaks. Thus, we used the pseudocubic indexing of the Bragg peaks, where the 100_{AL} index corresponds to 110_{AL} and 002_{AL} reflections of the orthorhombic structure, the 110_{AL} – to 200_{AL} and 112_{AL}, the 200_{AL} – to 220_{AL} and 004_{AL}.

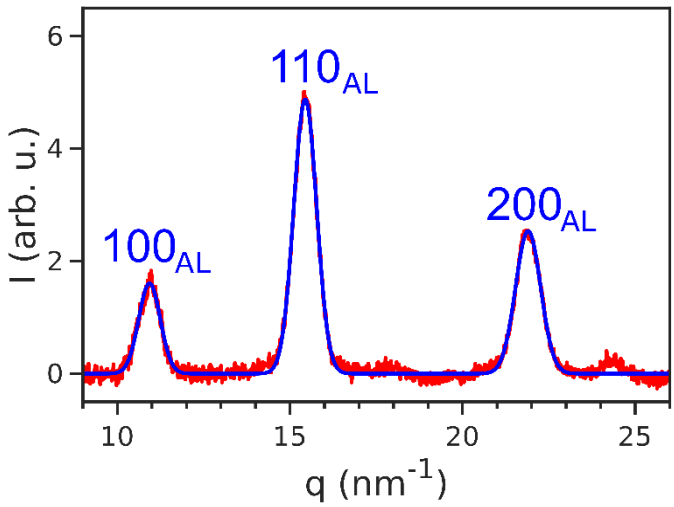

Figure S3.8: Azimuthally averaged intensity profile in WAXS region (red line) and Gaussian fitting including three peaks (blue line). The peaks are indexed according to a pseudocubic structure.

The FWHMs of the peaks extracted by the fitting are w_{100} = 0.736±0.011 nm^{-1}, w_{110} = 0.784±0.004 nm^{-1}, w_{200} = 0.856±0.08 nm^{-1}. We analyzed the FWHMs of the peaks by the Williamson-Hall method. [281] According to the method, the FWHMs of the Bragg peaks are defined by two factors: the size of coherently scattering domain L and the lattice distortion g (the ratio $\delta a_{AL}/a_{AL}$ of the FWHM δa_{AL} of the unit cell parameter distribution around the mean value a_{AL}). If we assume that the coherently scattering domain is a NC, the Williamson-Hall equation can be written as follows:

$$w^2(q) = \left(\frac{2\pi K}{L}\right)^2 + (gq)^2, \qquad \text{(S3.2)}$$

where $w(q)$ is the FWHM of the Bragg peak at momentum transfer q, K – a dimensionless shape factor, L – the NC size and g – the lattice distortion.

The first term is the pure Scherrer broadening, where the shape factor K is about 0.85 for the reflections of low orders for a cubic crystallite. [282] One should note, the size of coherently scattering domain can be bigger than a single NC if there are perfectly aligned NCs scattering coherently to the same direction. However, the fact that the WAXS Bragg peaks are much broader in the azimuthal direction than in the radial (see the main text for the WAXS pattern), indicate a high degree of angular disorder of the NCs (will be discussed below) leading to low probability of such a scenario.

To extract the NC size L and the lattice distortion g, we fitted the experimentally obtained FWHMs and q-values for the present 100_{AL}, 110_{AL} and 200_{AL} peaks with **Eq. S3.2** as shown in **Fig. S3.9**. The resulting parameters are L = 6.8±0.1 nm and g = 2.3±0.1%. The resulting NC size L is

even smaller than the size L_{SEM} = 7.3±0.4 nm obtained from SEM measurement that indicates the correctness of the assumption that the coherently scattering domain consist of a single NC. The smaller size can be explained by the lattice twinning inside the NC leading to smaller domains and by the limits of the method.

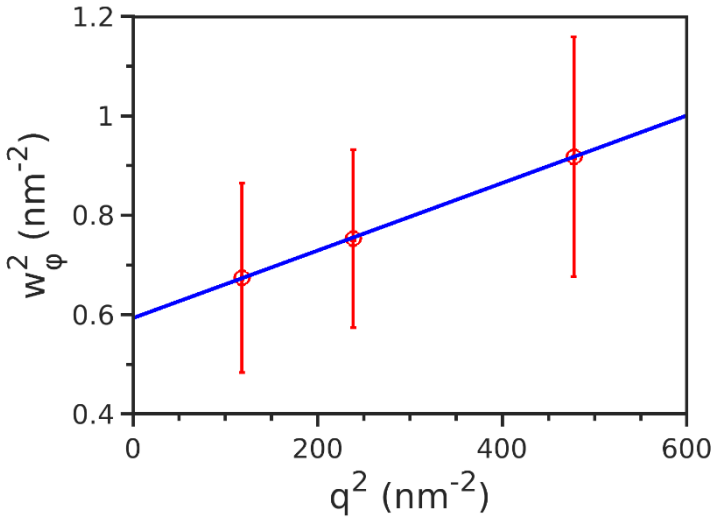

Figure S3.9: Williamson-Hall plot for the radial FWHM values of the WAXS Bragg peaks. The red points are experimental values, the blue straight line is the best fit.

Section S3.5. Local superlattice structure

The single SAXS diffraction patterns at different spatial points of the supercrystal are quite different from the average diffraction pattern shown in **Fig. 3.3 c** in the main text. Examples of the single patterns are shown in **Fig. S3.10**. Clearly, the Bragg peaks do not maintain their positions in both radial and azimuthal directions and change their shape from point to point.

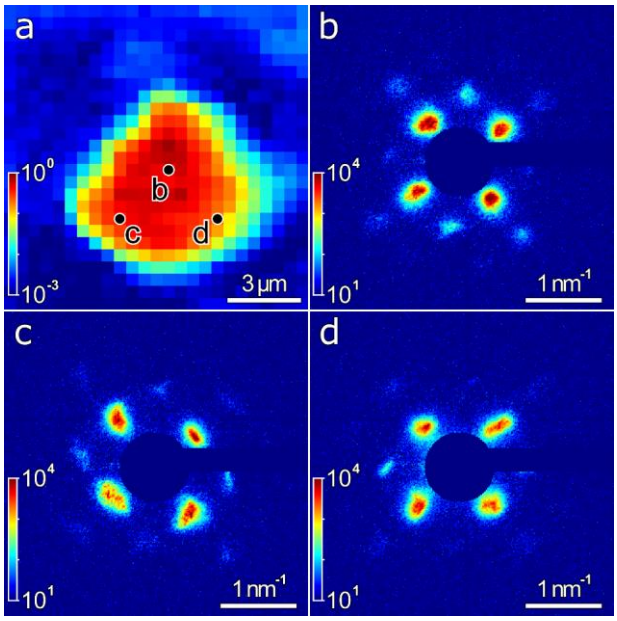

Figure S3.10: a) SAXS intensity-based map of the sample. The pixel size is 500 nm. b-d) Examples of single SAXS diffractions patterns collected at the points indicated in panel a).

To study dependence of their parameters on the spatial position within the sample, we evaluated each single diffraction pattern separately. We fitted each of the first order Bragg peaks in the SAXS region by the Gaussian function:

$$I(q,\varphi) = \frac{I_0}{2\pi\sigma_q\sigma_\omega}\exp\left[-\frac{(q-q_0)^2}{2\sigma_q^2} - \frac{(\omega-\omega_0)^2}{2\sigma_\omega^2}\right], \quad \text{(S3.3)}$$

where I_0 is the integrated intensity, q_0 and ω_0 are the radial and azimuthal positions, $w_q = 2\sqrt{2ln2}\sigma_q$and $w_\omega = 2\sqrt{2ln2}\sigma_\omega$ are the corresponding FWHMs of the Bragg peak. The fitting was done in the appropriate region of the polar coordinates with single isolated Bragg peak.

There are two Friedel pairs of the Bragg peaks corresponding to reflections from the $(100)_{SL}$ and $(010)_{SL}$ superlattice planes. Counting from the right-pointing horizontal axis, the 1st and 3rd peaks correspond to the $(100)_{SL}$ plane and the 2nd and 4th – to the $(010)_{SL}$ plane. We averaged the intensities, the radial and azimuthal positions and the FWHMs within each pair to get more reliable characteristics of the superlattice planes. The azimuthal coordinates of the 3rd and 4th peaks were corrected by -180° prior to the averaging. Finally, we have two sets of the characteristics defined in **Fig. S3.11 a**. The reciprocal space coordinated were converted into the coordinates of the real-space basis vectors $\boldsymbol{a_1}$ and $\boldsymbol{a_2}$.

The azimuthal positions are converted into real space as follows:

$$\varphi_1 = \omega_2 - 90° \quad \text{(S3.4)}$$

$$\varphi_2 = \omega_1 + 90° \quad \text{(S3.5)}$$

The nearest-neighbor distances a_1 and a_2 are calculated as:

$$a_1 = \frac{2\pi}{q_1 \cdot \sin\gamma} \quad \text{(S3.6)}$$

$$a_2 = \frac{2\pi}{q_2 \cdot \sin\gamma} \quad \text{(S3.7)}$$

We also used additional azimuthal coordinates that are the azimuthal position of the mean line $\boldsymbol{M}$ between the $\boldsymbol{a_1}$ and $\boldsymbol{a_2}$:

$$\varphi = \frac{\varphi_1 + \varphi_2}{2} \quad \text{(S3.8)}$$

and the angle γ between the real space basis vectors $\boldsymbol{a_1}$ and $\boldsymbol{a_2}$, calculated as:

$$\gamma = \varphi_2 - \varphi_1 \quad \text{(S3.9)}$$

The definition of the real space coordinates is shown in **Fig. S3.11 b**.

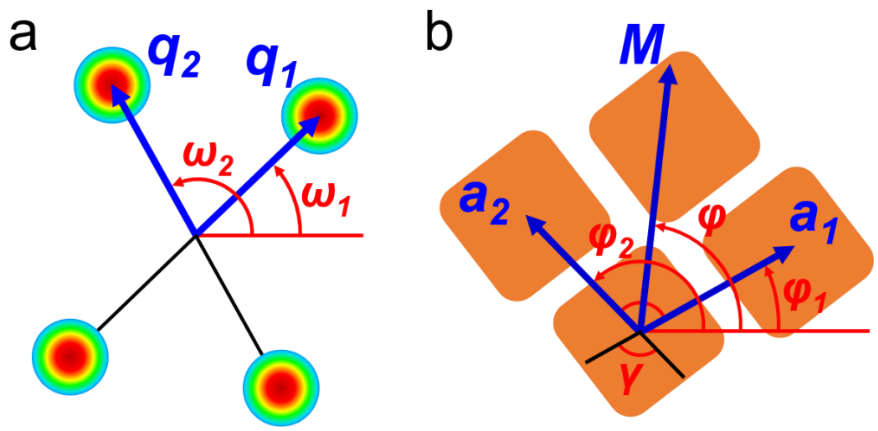

Figure S3.11: a) Scheme of the SAXS diffraction pattern from the superlattice. Only the first order Bragg peaks are shown. Two pairs of Bragg peaks are at momentum transfer values q_1 and q_2 and azimuthal positions ω_1 and ω_2, respectively. b) Scheme of the real space unit cell of the superlattice. The nearest neighbors are at distances a_1 and a_2 with azimuthal positions φ_1 and φ_2, respectively. The mean line $\boldsymbol{M}$ between $\boldsymbol{a_1}$ and $\boldsymbol{a_2}$ is at azimuthal position φ. The angle between $\boldsymbol{a_1}$ and $\boldsymbol{a_2}$ is equal to γ.

The extracted intensities I_1 and I_2 of the Bragg peaks are shown in **Fig. S3.12 a, d**. The scattering areas basically coincide except the upper and right corners. Vanishing of the 1st Bragg peak possibly indicates out-of-plane rotation of the SL on these supercrystal edges as soon as such rotation bring the peak out of the Ewald sphere.

The extracted momentum transfers q_1 and q_2 associated with the superlattice plane spacings are shown in **Fig. S3.12 b, e**. As it is clear from the figure, the momentum transfers grow on the edges of the supercrystal. It indicates contraction of the superlattice that is thoroughly discussed in the main text as well as its anisotropy.

The extracted azimuthal positions ω_1 and ω_2 are shown in **Fig. S3.12 c, f**. They clearly indicate rotation of the superlattice around the incident beam (normal to the substrate). The rotation is also discussed in the main text.

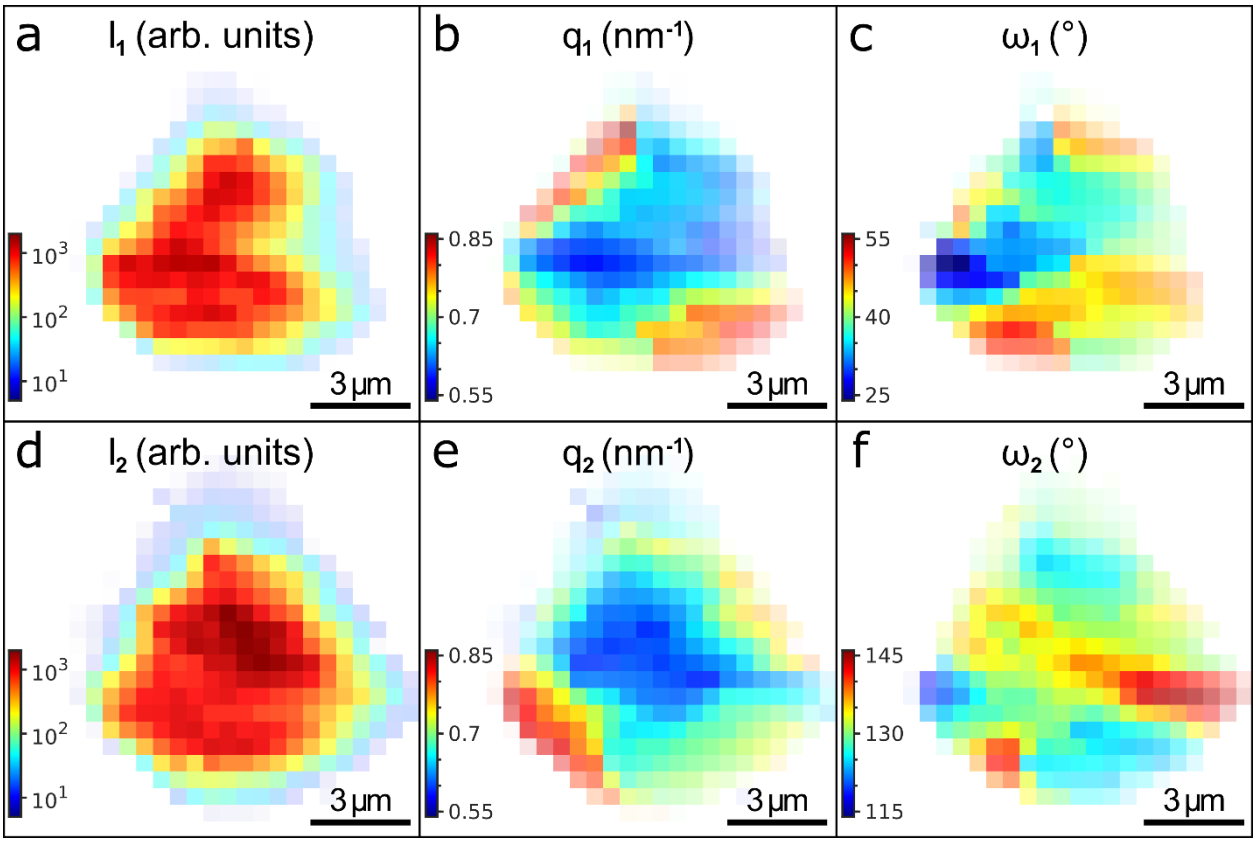

Figure S3.12: Mean extracted parameters: a, d) intensities, b, e) momentum transfer values and c, f) azimuthal positions of a-c) the 1st and 3rd and d-f) the 2nd and 4th Bragg peaks. The azimuthal positions are counted counterclockwise from a horizontal axis pointing to the right. The azimuthal position of the 3rd and 4th were corrected by -180° before averaging with their counterparts. The pixel size is 500 nm.

The extracted FWHMs in the radial direction w_{q1} and w_{q2} are shown in **Fig. S3.13 a, c**. Interestingly, in contrast to the momentum transfer values q_1 and q_2, the main deviations in FWHMs happen on the edges to which the crystallographic axes are perpendicular. This means lower dispersion in the superlattice plane separation normal to the edge of the supercrystal.

The extracted FWHMs in the azimuthal direction $w_{\omega 1}$ and $w_{\omega 2}$ are shown in **Fig. S3.13 b, d**. There is no clear trend in the behavior of these parameters in respect to the spatial position inside the supercrystal. But most of the point having high FWHM values are located in the middle of the supercrystal, indicating higher dispersion of the angle γ between the lattice vectors a_1 and a_2 as well as of the superlattice orientation angle φ.

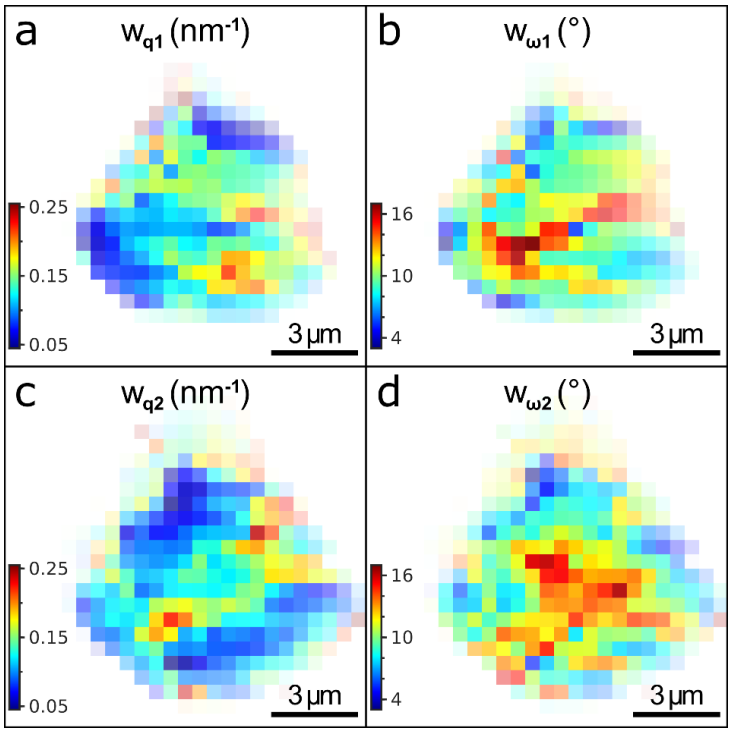

Figure S3.13: Mean extracted FWHMs in a, c) radial and b, d) azimuthal directions of a,b) the 1st and 3rd and c,d) the 2nd and 4th Bragg peaks. The pixel size is 500 nm.

The calculated lengths of the lattice vectors a_1 and a_2 are shown in **Fig. S3.14**. The distance between the adjacent NCs decrease in both directions on the edges of the supercrystal, but the effect is higher in the direction parallel to the nearest supercrystal edge. For example, in the point 1 in **Fig. S3.14**, the distance along $\boldsymbol{a_1}$, which is pointing to the top-right parallel to the nearest edge, is smaller than along $\boldsymbol{a_2}$, which is normal to the nearest edge. On the contrary, in the point 2, where $\boldsymbol{a_2}$ is parallel to the nearest edge, the distance along this direction is smaller than along $\boldsymbol{a_1}$. The anisotropy of the lattice shrinkage is better visible on the map of the a_2/a_1 ratio that is shown and discussed in the main text.

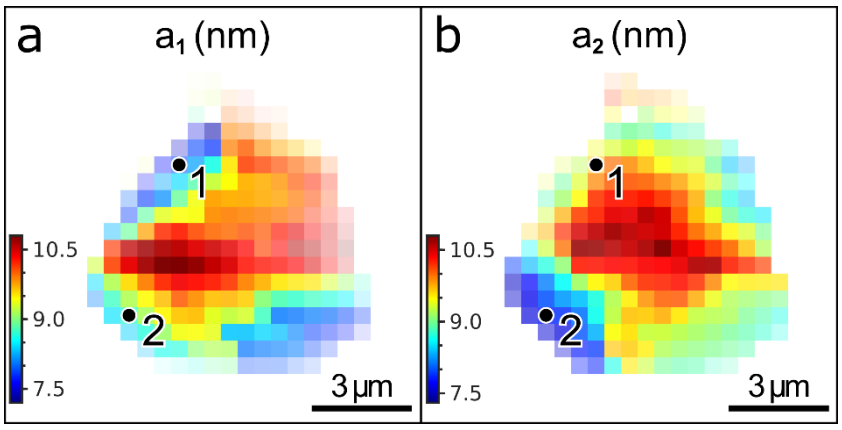

Figure S3.14. Maps of the calculated lengths of the lattice vectors a_1 and a_2. The points 1 and 2 are discussed in the text. The pixel size is 500 nm.

Section S3.6. NCs orientation inside the SL

In WAXS region, there are four Bragg peaks present on most of the diffraction pattern, as shown on the average one in **Fig. S3.15**. Analogous to the SAXS analysis, we fitted each of the peaks separately for each spatial point within the sample with the 2D Gaussian functions (**Eq. S3.3**).

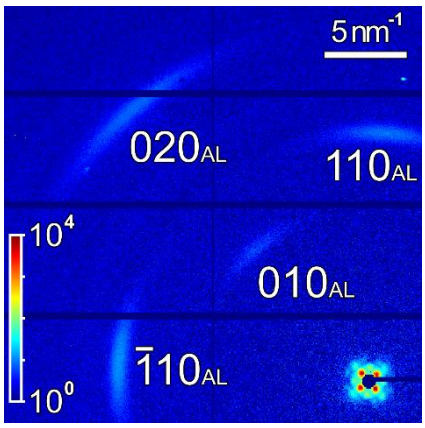

Figure S3.15: Average WAXS diffraction pattern with four prominent Bragg peaks. The indexes are given for pseudocubic atomic lattice oriented along [001] axis.

Extracted this way intensities of the Bragg peaks are shown in **Fig. S3.16**. 010_{AL}, 020_{AL}, 110_{AL} and $\bar{1}10_{AL}$ peaks are detected in the spatial points within the supercrystal, though lower intensity of the WAXS reflections did not allow detecting them on the very edges. The 010_{AL} reflection is registered on even smaller area, because it has the lowest intensity among the peaks.

The intensities are not uniform within the supercrystal that can indicate different thickness of the sample or slight out-of-plane rotation of the NCs. The intensities of 010_{AL}, 020_{AL} and 110_{AL} reflections change the same way, while the intensity of $\bar{1}10_{AL}$ reflection stay almost constant. The inhomogeneous thickness would lead to the similar changes in intensities of all reflections, thus, the change most likely is due to the out-of-plane rotation of the NCs. The constant intensity of $\bar{1}10_{AL}$ reflection indicates that the rotation happens around an axis close to the $[\bar{1}10]_{AL}$ one. The changes in intensity of 010_{AL} and 020_{AL} reflections are qualitatively similar to the changes in intensity I_2 of 010_{SL} reflection (see **Fig. S12 d**) that indicates simultaneous rotation of the NCs and SL keeping their mutual orientation. The changes in SAXS intensity are smaller due to lower effect of the Ewald's sphere curvature.

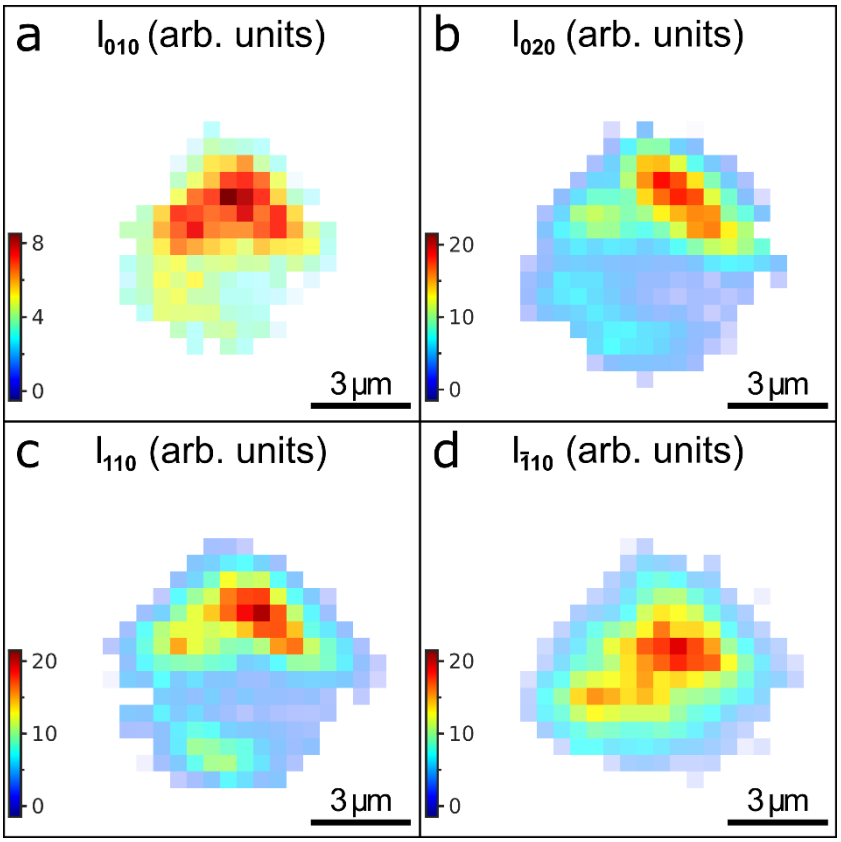

Figure S3.16: Extracted intensities of the WAXS Bragg peaks: a) 010_{AL}, b) 020_{AL}, c) 110_{AL} and d) $\bar{1}10_{AL}$. The pixel size is 500 nm.

The mean extracted momentum transfer values are q_{010} = 10.87±0.05 nm^{-1}, q_{110} = 10.85±0.05 nm^{-1}, $q_{\bar{1}10}$ = 10.91±0.03 nm^{-1}, q_{020} = 21.86±0.04 nm^{-1}, that is in a good agreement with the values obtained from the average radial profiles discussed above in **Section S3.5**. The error bars here represent the standard deviation of the values across the sample. The momentum transfer values do not depend on the spatial position on the sample, as shown in **Fig. S3.17**. The deviation is due to the noise together with the low intensities of the peaks themselves.

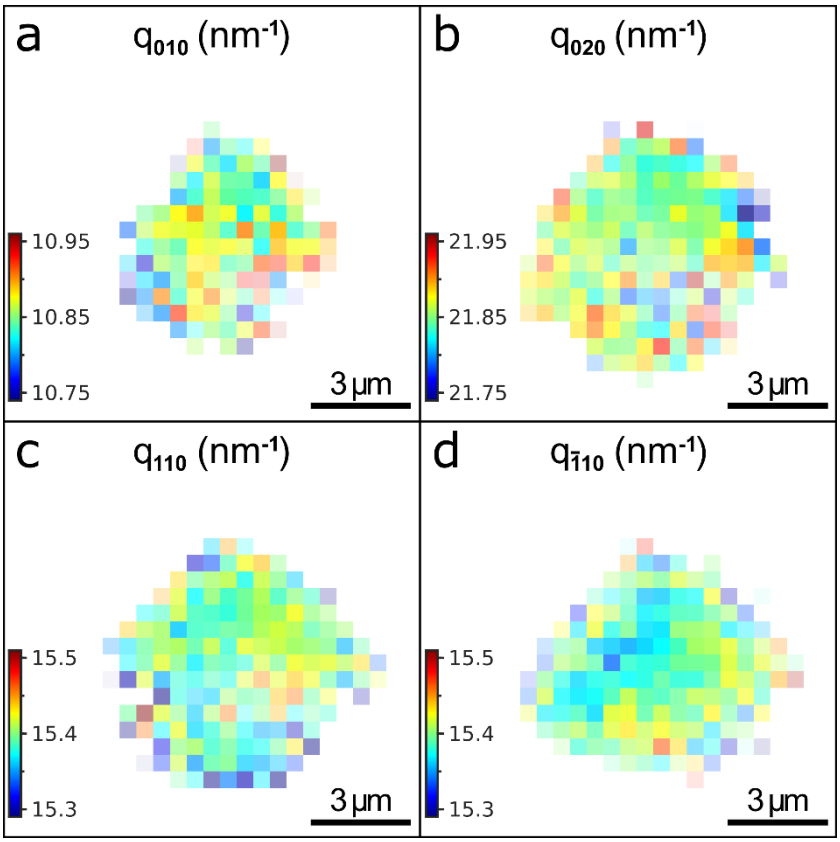

Figure S3.17: Extracted momentum transfers of the WAXS Bragg peaks: a) 010_{AL}, b) 020_{AL}, c) 110_{AL} and d) $\bar{1}10_{AL}$. The pixel size is 500 nm.

The calculated from the q-values unit cell parameter is shown in **Fig. S3.18 a**. It does not change within the supercrystal and remains constant at the value of a_{AL} = 0.576±0.002 nm. To better visualize the change in the unit cell parameter, we plot the values for each pixel against the distance of this pixel to the nearest supercrystal edge in **Fig. S3.18 b**.

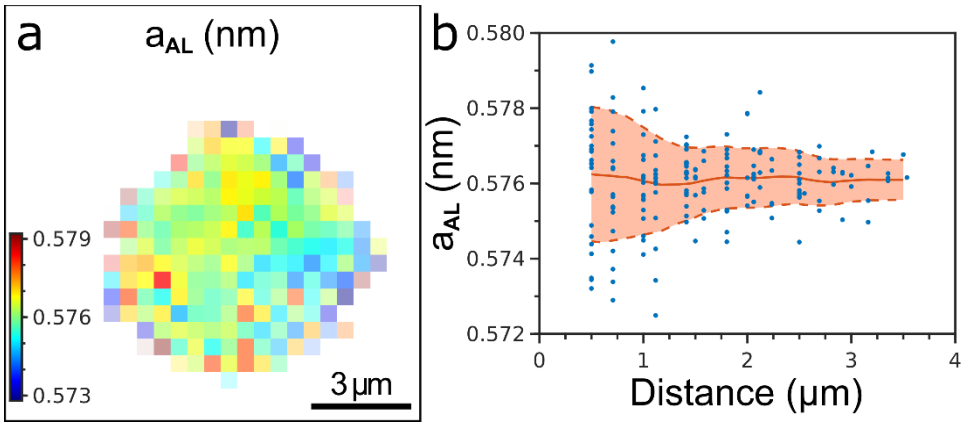

Figure S3.18: a) Calculated unit cell parameter a_{AL} of the pseudo-cubic atomic lattice of the NCs and b) the same value for each pixel against the distance from this pixel to the nearest edge of the supercrystal. The red line shows the mean value, the dashed lines indicate the confidence interval of ±σ. The pixel size in a) is 500 nm.

The FWHMs in radial direction, shown in **Fig. S3.19**, do not show any correlations with the spatial position on the sample as well. The mean values are $w_{q,010}$ = 0.73±0.10 nm^{-1},

$w_{q,110}$ = 0.75±0.09 nm^{-1}, $w_{q,\bar{1}10}$ = 0.73±0.07 nm^{-1} and $w_{q,020}$ = 0.85±0.11 nm^{-1}, that is in good agreement with the values from the average radial profile discussed above in **Section S3.4**. The error bars here represent the standard deviation of the values across the sample.

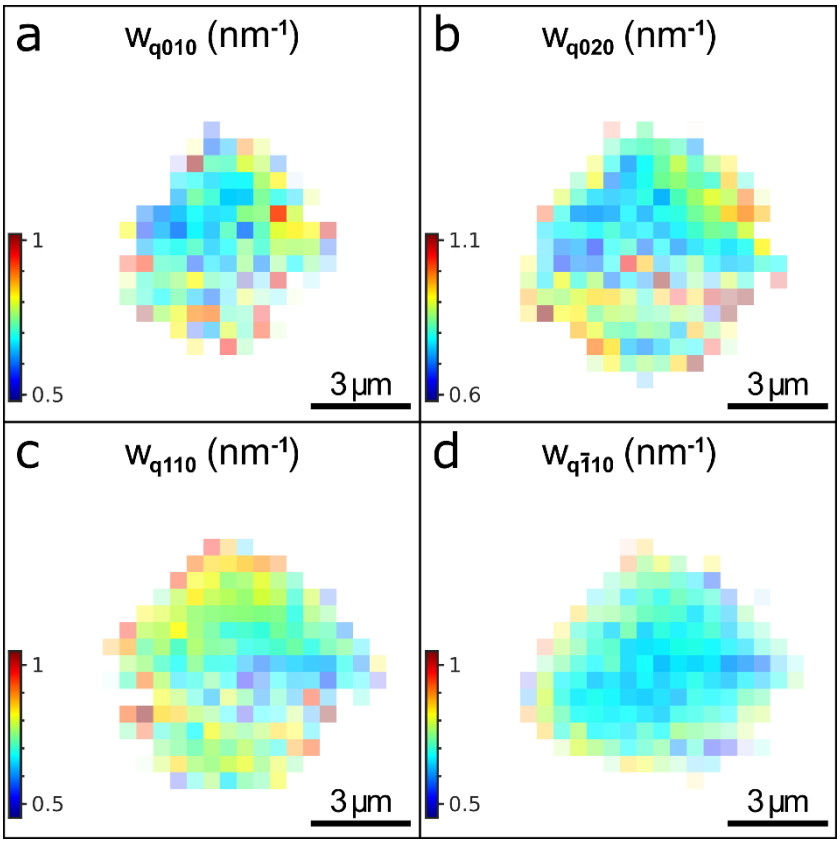

Figure S3.19: Extracted radial FWHMs of the WAXS Bragg peaks: a) 010_{AL}, b) 020_{AL}, c) 110_{AL} and d) $\bar{1}10_{AL}$. The pixel size is 500 nm.

We used the radial FWHMs to extract the atomic lattice distortion of the NCs by the Williamson-Hall method (**Eq. S3.2**). The lattice distortion g_q (the ratio $\delta a_{AL}/a_{AL}$ of the FWHM δa_{AL} of the unit cell parameter distribution around the mean value a_{AL}) was calculated as follows:

$$g_q = \langle \frac{1}{q_i} \sqrt{(w_i)^2 - \left(\frac{2\pi K}{L}\right)^2} \rangle_i, \tag{S3.10}$$

where w_i are the radial FWHMs for the present peaks, q_i are the momentum transfer values of the corresponding peaks, K is the shape constant, L is the NCs size, and the averaging is performed over all present Bragg peaks. The shape constant K was discussed in **Section S3.4**; the NCs size was fixed at L = 6.8 nm obtained from the radial profile as described in the same **Section S3.4**. The resulting values of the atomic lattice distortion are shown in **Figure 3.6** in the main text. The mean value is g_q = 1.5 ± 0.9% that is in good agreement with the values obtained from the average radial profile discussed in Section S1. The distortion gets slightly higher on the edges of the supercrystal that can be explained by the contraction of the NCs together with the superlattice. To better visualize the change in distortion, we plot the values for each pixel against the distance of this pixel to the nearest

supercrystal edge in **Fig. 3.6 b** in the main text. The atomic lattice distortion grows from < 1% in the middle of the supercrystal up to > 2% on the edges. The trend is even more evident for another sample, described in **Section S3.7**. Here the effect is less pronounced, probably, because of lower intensity of the WAXS Bragg peaks causing higher noise.

Since the NCs have pseudocubic atomic lattice (all angles are equal to 90°), the azimuthal position of the WAXS Bragg peaks directly correspond to the azimuthal orientation of the supercrystal unit cell basis vectors $\mathbf{a}_1$ and $\mathbf{a}_2$**.** Thus, the azimuthal positions in real space are equal to the azimuthal positions in reciprocal space $\varphi_{hkl} = \omega_{hkl}$**.** The extracted azimuthal positions for all four peaks are shown in **Fig. S3.20**. The NCs are clearly rotating in-plane as soon as the positions change for different peaks together from point to point. As expected, the difference between the positions remains constant, *e.g.*, $\varphi_{\bar{1}10} - \varphi_{110} = 90°$, $\varphi_{\bar{1}10} - \varphi_{020} = 45°$ etc. We calculated the average azimuthal NC position ψ collinear to the 010_{AL} vector as $\psi = \langle \varphi_{010},\ \varphi_{020},\ \varphi_{110} + 45°,\ \varphi_{\bar{1}10} - 45° \rangle$, where the angle brackets denote averaging over the four angles. The angle ψ is used to study the azimuthal position of the NCs. It is shown in **Fig. 3.5c** and discussed in the main text.

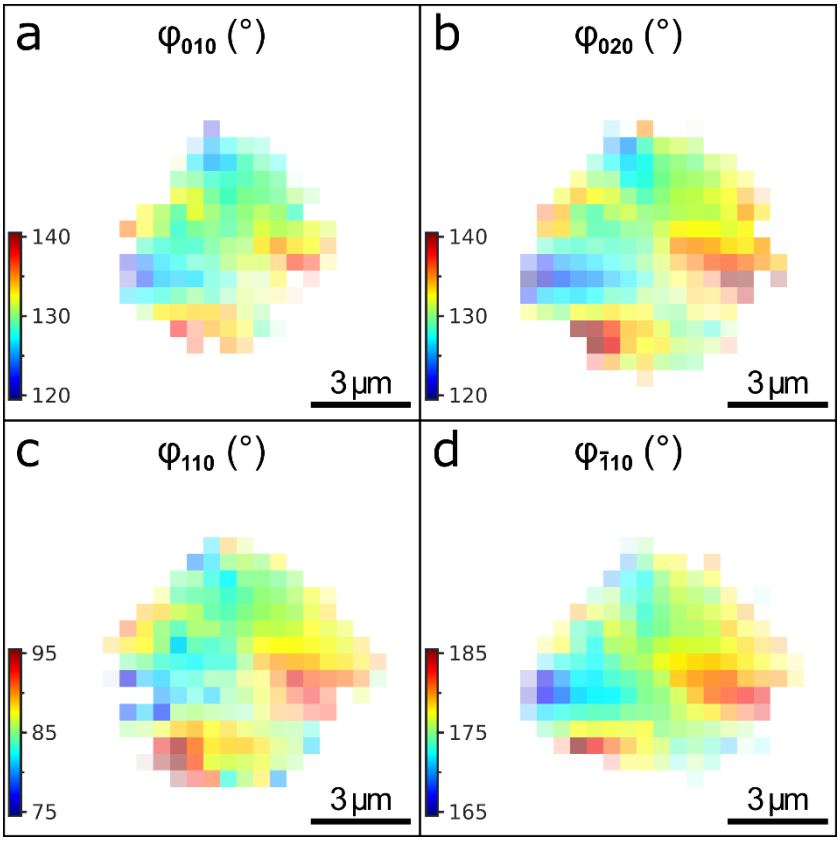

Figure S3.20: Extracted azimuthal positions of the WAXS Bragg peaks: a) 010_{AL}, b) 020_{AL}, c) 110_{AL} and d) $\bar{1}10_{AL}$. The positions are counted counterclockwise from a horizontal axis pointing to the right. The pixel size is 500 nm.

We studied the relative azimuthal orientation of the NCs and the SL comparing the azimuthal positions of the lattice vectors obtained from the Bragg peak analysis described above. The differences in angles between the $[010]_{AL}$ axis of the NCs and the mean line $\boldsymbol{M}$ between the superlattice vectors $\boldsymbol{a_1}$

and $\boldsymbol{a_2}$ $\Delta = \psi - \varphi$; between the $[010]_{AL}$ and $\boldsymbol{a_1}$ $\Delta_1 = \psi - \varphi_1$; between the $[010]_{AL}$ and $\boldsymbol{a_2}$ $\Delta_2 = \psi - \varphi_2$ are shown in **Fig. S3.21**. Clearly, the angle Δ has narrower distribution with the mean value $\langle\Delta\rangle$ =45.2±1.7°. For comparison, the angles Δ_1 *and* Δ_2 have broader distribution with the mean values $\langle\Delta_1\rangle$ = 90.1±3.5° and $\langle\Delta_2\rangle$ = 0.8±3.8°. This is rather expected, because the angles between the NC crystallographic axes are constant, while the angle between the superlattice vectors changes from point to point in relatively broad range, as shown in **Fig. 3.4 d** and discussed in the main text. At the same time, the angle between the mean lines between the superlattice vectors (e. g. ***M*** between $\boldsymbol{a_1}$ and $\boldsymbol{a_2}$ and ***M'*** between $\boldsymbol{a_1}$ and $\boldsymbol{-a_2}$) is always equal to 90° and does not depend on the length and orientation of the vectors $\boldsymbol{a_1}$ and $\boldsymbol{a_2}$. It makes possible keeping the mutual orientation between the $[100]_{AL}$ and $[010]_{AL}$ axes and the mean lines ***M*** and ***M'***.

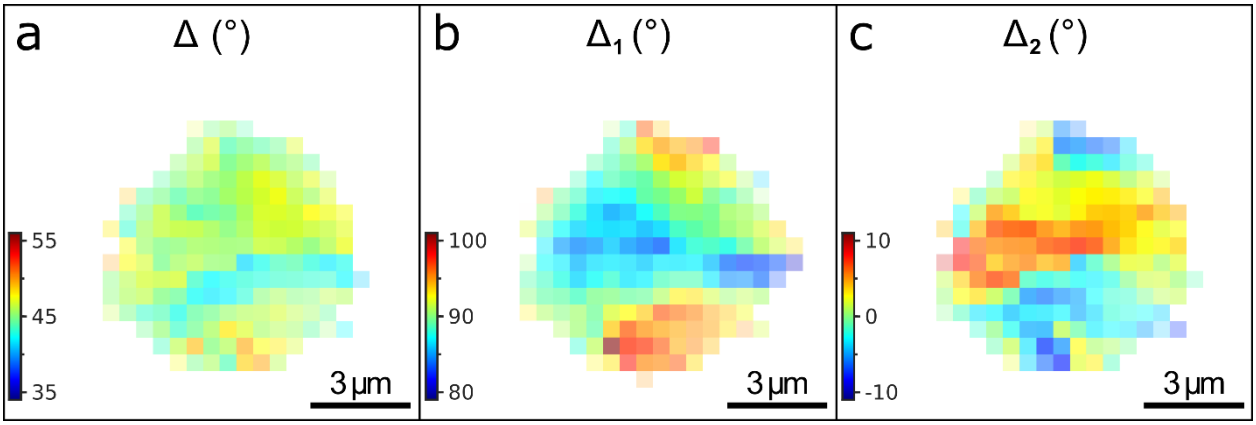

Figure S3.21: Relative angle between the direct lattice vectors of the NCs and the SL: a) between $[010]_{AL}$ and the mean line ***M*** between the $\boldsymbol{a_1}$ and $\boldsymbol{a_2}$; b) between $[010]_{AL}$ and $\boldsymbol{a_1}$; c) between $[010]_{AL}$ and $\boldsymbol{a_2}$. The pixel size is 500 nm.

The azimuthal FWHMs shown in **Fig. S3.22** show clear dependence on the spatial position within the supercrystal. The FWHMs grow from 12° in the middle of the supercrystal up to 24° on the edges indicating higher azimuthal disorder of the NCs there.

We used the azimuthal FWHMs to extract the NCs angular disorder by the Williamson-Hall method. In this case, the lattice distortion g from **Eq. S3.2** is the FWHM $\delta\psi$ of angular distribution of the NCs around their mean position given by the azimuthal peak positions. The FWHM $\delta\psi$ was calculated as follows:

$$\delta\psi = \langle\frac{1}{q_i}\sqrt{(w_i q_i)^2 - \left(\frac{2\pi K}{L}\right)^2}\rangle_i, \tag{S3.11}$$

where w_i are the azimuthal FWHMs (in radians) for the present peaks, q_i are the momentum transfer values of the corresponding peaks, K is the shape constant, L is the NCs size, and the averaging is performed over all present Bragg peaks. The shape constant K was discussed in **Section S3.4**; the NCs size was fixed at L = 6.8 nm obtained from the radial profile as described in the same **Section S3.4**. The resulting values of the FWHM are shown in **Figure 3.5 d** and discussed in the main text.

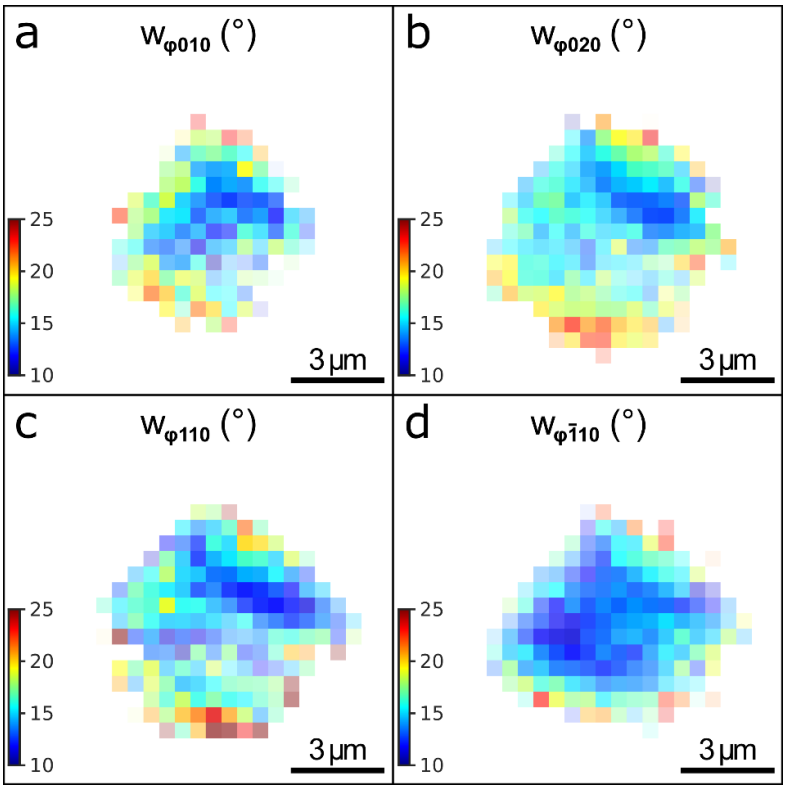

Figure S3.22: Extracted azimuthal FWHMs of the WAXS Bragg peaks: a) 010_{AL}, b) 020_{AL}, c) 110_{AL} and d) $\bar{1}10_{AL}$. The pixel size is 500 nm.

Section S3.7. Another example of a supercrystal

All studied supercrystals behave similarly. Here we present the main results obtained for one more supercrystal. The average WAXS and SAXS patterns as well as the SAXS-based diffraction map are shown in **Fig. S3.23**. The patterns look very similar to the ones observed for the sample described in the main text. The local structure was analyzed the same way as described above. The only difference is the WAXS analysis, performed only for three peaks 010_{AL}, 020_{AL} and $\bar{1}10_{AL}$. The fourth 110_{AL} peak hardly fitted into the detector in this case and was excluded from the consideration.

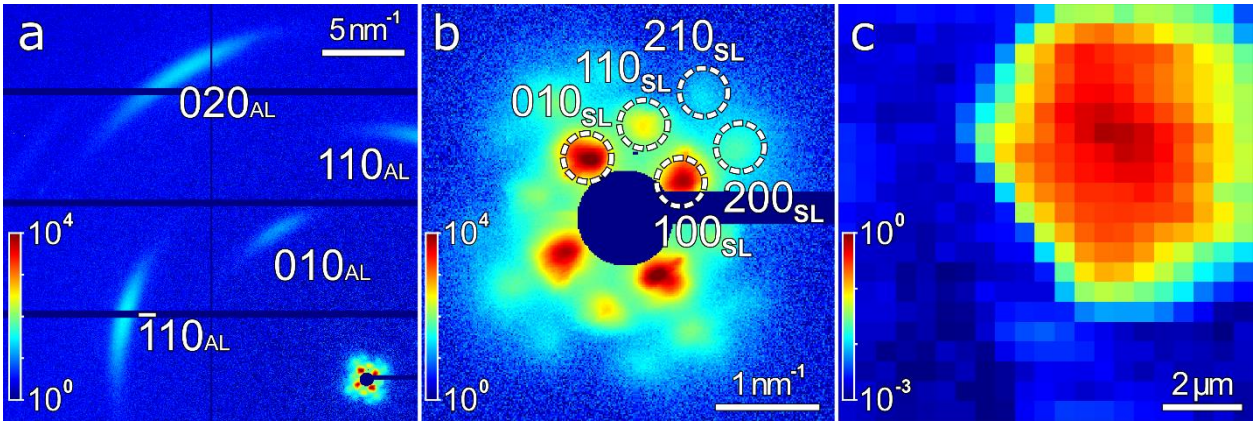

Figure S3.23: Average WAXS a) and SAXS b) patterns and c) SAXS-based diffraction map of the second sample. The Bragg peaks are indexed according to the "pseudocubic" structure of the atomic lattice and simple cubic structure of the superlattice. The pixel size in c) is 500 nm.

The main extracted parameters of the superlattice are shown in **Fig. S3.24**. The main observations are the same as for the sample described in the main text. The superlattice anisotropically shrinks on the edges of the supercrystal. The contraction happens preferentially in the directions parallel to the nearest supercrystal edge. The angle between the basis vectors $\boldsymbol{a_1}$ and $\boldsymbol{a_2}$ changes in the range of 75-105° and the superlattice rotates in-plane as indicated by the azimuthal position φ of the mean line $\boldsymbol{M}$ between $\boldsymbol{a_1}$ and $\boldsymbol{a_2}$.

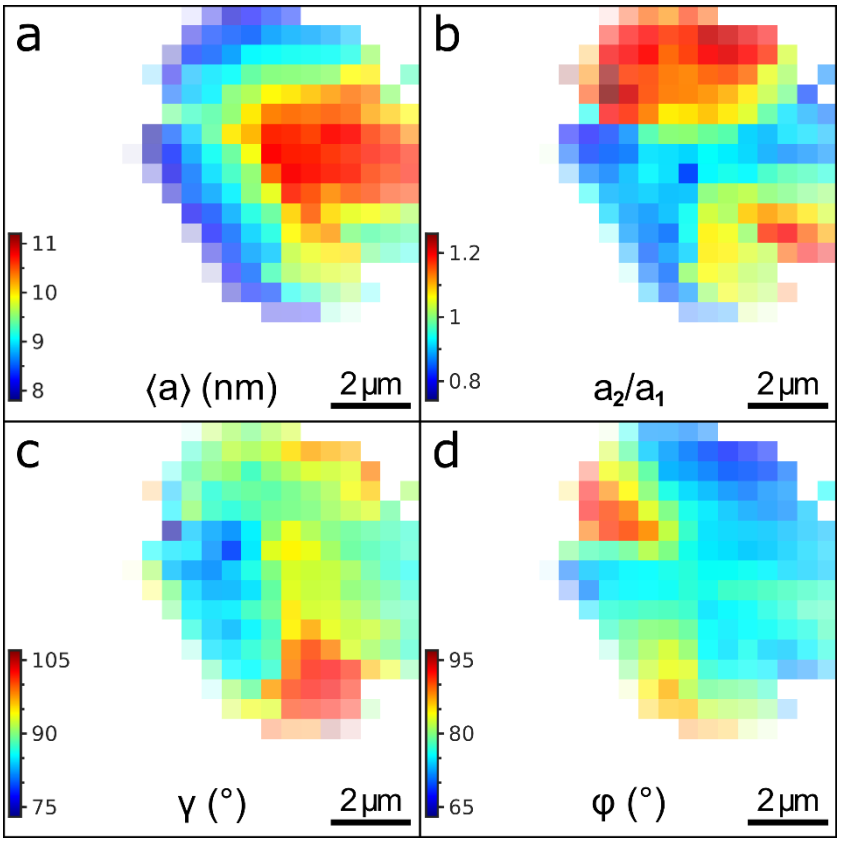

Figure S3.24: Extracted superlattice parameters: a) average unit cell parameter $\langle a \rangle = (a_1+a_2)/2$; b) ratio a_2/a_1 of the NC spacings along the basis vectors $\boldsymbol{a_2}$ and $\boldsymbol{a_1}$; c) angle γ between the basis vectors $\boldsymbol{a_1}$ and $\boldsymbol{a_2}$; d) azimuthal position φ of the mean line $\boldsymbol{M}$ between the basis vectors $\boldsymbol{a_1}$ and $\boldsymbol{a_2}$. The pixel size is 500 nm.

The main extracted parameters of the atomic lattice are shown in **Fig. S3.25**. The main difference with the sample described in the main text is the homogeneous intensity of the WAXS Bragg peaks decreasing on the edges. It indicates absence of the out-of-plane rotations of the NCs. But the NCs rotate in-plane correlated with the mean line $\boldsymbol{M}$ between the $\boldsymbol{a_1}$ and $\boldsymbol{a_2}$ superlattice vectors as can be seen from the difference angle $\Delta = \psi - \varphi$. The angular disorder of the NCs grows on the edges the same way as for the sample described in the main text.

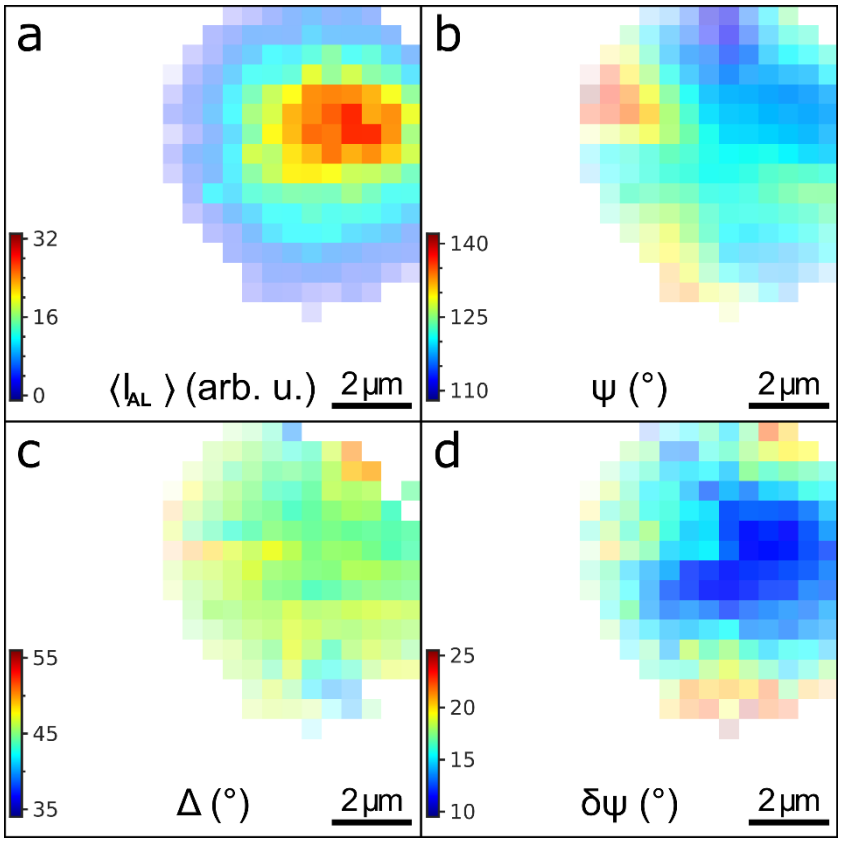

Figure S3.25: Extracted atomic lattice parameters: a) Average intensity of the WAXS Bragg peaks $<I_{AL}>$; b) azimuthal position ψ of the 100_{AL} crystallographic directions of the NCs; c) the relative angle Δ between the $[010]_{AL}$ axis and the mean line $\boldsymbol{M}$ between the $\boldsymbol{a_1}$ and $\boldsymbol{a_2}$ basic vectors of the SL; d) FWHM $\delta\psi$ of the angular disorder of the NCs around the mean azimuthal position ψ. The pixel size is 500 nm.

The calculated unit cell parameter of the atomic lattice from the q-values of the WAXS Bragg peaks is shown in **Fig. S3.26**. It doesn't show any correlation with the spatial position within the supercrystal and remains constant at the value of a_{AL} = 0.576±0.002 nm.

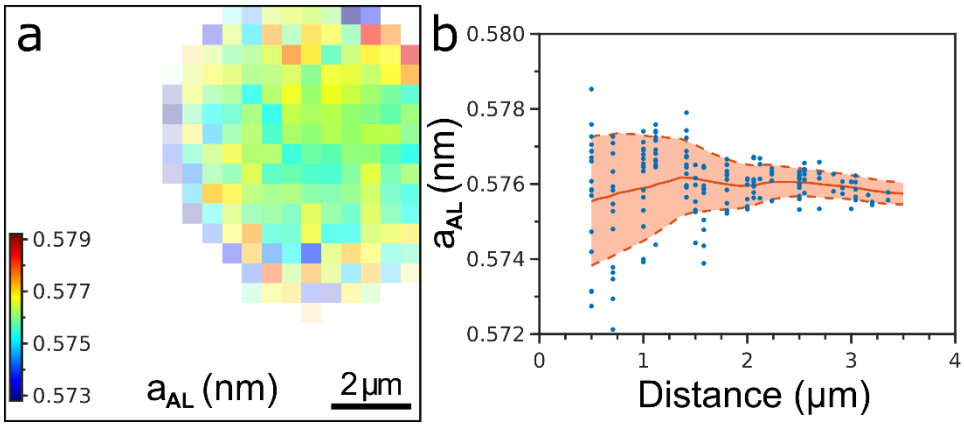

Figure S3.26: a) Calculated unit cell parameter a_{AL} of the pseudo-cubic atomic lattice of the NCs and b) the same value for each pixel against the distance from this pixel to the nearest edge of the supercrystal. The red line shows the mean value, the dashed lines indicate the confidence interval of ±σ. The pixel size in a) is 500 nm.

The atomic lattice distortion was calculated from the FWHMs of the present WAXS Bragg peaks by the Williamson-Hall method (**Eq. S3.10**). The resulting values of the atomic lattice distortion

are shown in **Figure S3.27**. The distortion gets slightly higher on the edges of the supercrystal that can be explained by the contraction of the NCs together with the superlattice. The atomic lattice distortion grows from about 0.5% in the middle of the supercrystal up to about 2.5% on the edges.

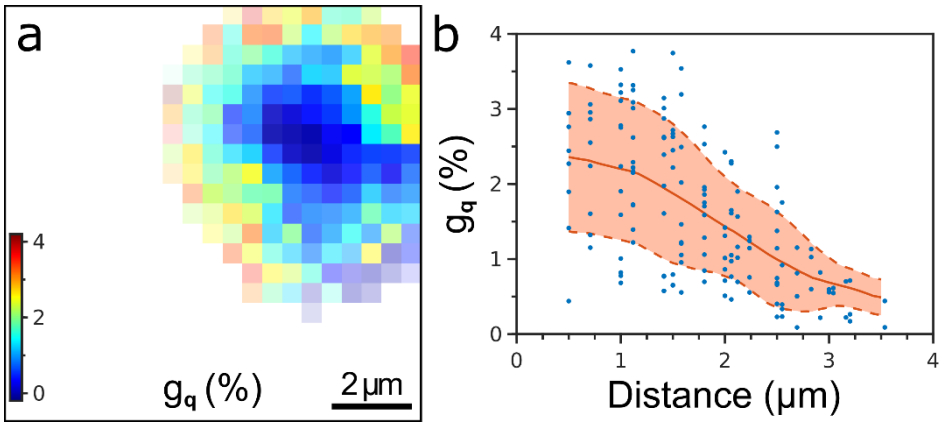

Figure S3.27: a) Atomic lattice distortion g_q extracted from the radial FWHMs of the WAXS Bragg peaks by the Williamson-Hall method and b) the same value for each pixel against the distance from this pixel to the nearest edge of the supercrystal. The red line shows the mean value, the dashed lines indicate the confidence interval of ±σ. The pixel size in a) is 500 nm.

Section S3.8. DFT-computed structures

Computation protocol used in this work is described in the main text. Cartesian coordinates of all computed structures can be accessed from the coordinate file (.xyz).

4. Quasielastic Neutron and Small Angle Scattering Reveal Highly Dynamic Surface Equilibrium on L-α-Lecithin Functionalized $CsPbBr_3$ Nanocrystals

Jan Wahl[1], Tilo Seydel[2,3], Ivan Zaluzhnyy[2], Christian Beck[2,3], Olga Matsarskaia[3], Lionel Porcar[3], Ezzeldin Metwalli[4], Frank Schreiber[2], Marcus Scheele[1,5]

[1] *Institut für physikalische und theoretische Chemie, Universität Tübingen, Auf der Morgenstelle 18, D-72076 Tübingen, Germany*

[2] *Institut für Angewandte Physik, Universität Tübingen, Auf der Morgenstelle 10, D-72076 Tübingen, Germany*

[3] *Institut Max von Laue – Paul Langevin, 71 avenue des Martyrs, F-38042 Grenoble, France*

[4] *Institut für Physik der Kondensierten Materie, Universität Erlangen-Nürnberg, Staudtstrasse 3, D-91058 Erlangen*

[5] *Center for Light-Matter Interaction, Sensors & Analytics LISA*$^+$*, Universität Tübingen, Auf der Morgenstelle 15, D-72076 Tübingen, Germany*

This chapter is based on a manuscript, which is about to be submitted to the Journal of Physical Chemistry Letters (as of 16.03.2022).

ArXiv Preprint: n.a. (as of 16.03.2022)

4.1. Abstract

All-inorganic perovskite nanocrystals (NC) in liquid toluene suspensions were investigated with a range of complementary scattering techniques and nuclear magnetic resonance to reveal their surface chemistry, solution structure, and diffusive dynamics. Two distinct diffusion coefficients were determined and analyzed, the center-of-mass diffusion of the NCs and that of micelles, as well as the lateral diffusion coefficient of the L–α–lecithin surface ligand on the NC surface and when located inside micelles. We find a highly dynamic surface equilibrium, represented by a tunable lateral diffusion coefficient dependent on the ligand surface density. This phenomenon can be rationalized by the extraordinary binding of this zwitterionic ligand and its ability to bind *via* two different binding sites. These results highlight the highly dynamic nature of the interface of this system.

4.2. Materials and Methods

Materials

1-Octadecene (ODE), technical grade, 90%, Sigma Aldrich; Trioctylphosphin (TOP), 95%, Acros Organics; Bromine, pure, chemical supply department, University of Tübingen; Toluene, HPLC grade, 99.8%, chemical supply department, University of Tübingen; Acetone, pure, chemical supply department, University of Tübingen; Caesium carbonate (Cs_2CO_3), 99.99% (trace metal basis), Acros Organics; Lead(II)acetate trihydrate ($Pb(ac)_2 \cdot 3\ H_2O$), 99%, Acros Organics; Oleic acid, 97%, Acros Organics; L–α–Lecithin, granular, from soybean oil, Acros Organics; deuterated Toluene (d_8-Tol), 99 atom-% D, Sigma Aldrich; custom made aluminium sample containers with indium sealing rings from the metal workshop at the University of Tübingen; 15×15 mm^2 silicon field-effect transistor (FET) substrates with gold contacts, obtained from Fraunhofer IPMS, Dresden. All chemicals were used as received.

$CsPbBr_3$ nanocrystal synthesis

The synthesis of the nanocrystals (NC) was carried out following Krieg *et al.* [24] with slight deviations. During the first step, the precursor solutions were prepared by keeping mixtures of Cs_2CO_3 (1.628 g, 5 mmol) and $Pb(ac)_2 \cdot 3\ H_2O$ (4.607 g, 12 mmol) with oleic acid (5 mL, 16 mmol for Cs_2CO_3 and 7.6 mL, 24 mmol for $Pb(ac)_2$) in ODE at 120 °C under vacuum until completion of gas formation. Simultaneously, 6 mL (13 mmol) of TOP were mixed with 0.6 mL (11.5 mmol) bromine in a separate flask. After the formation of a colorless solid was complete, the flask was cooled to room temperature in a water bath. The product was subsequently dissolved in 18.7 mL toluene.

The nanocrystal synthesis was carried out in a three-neck flask containing 0.324 g (0.432 mmol) L-α-lecithin, 4 mL Cs-oleate (1.6 mmol) and 5 mL Pb-oleate (2.5 mmol) in 10 mL ODE. The

mixture was heated to 150 °C under vacuum and the atmosphere was changed to nitrogen upon reaching the desired temperature. 5 mL of TOP-Br_2 was quickly injected into the solution and the reaction was allowed to take place for 5–10 s. Afterwards, the solution was cooled to room temperature with an ice bath.

The product was precipitated by adding two equivalents of acetone and centrifuging at 7000 rpm for 12 min. Following centrifugation, the pellet was redispersed in toluene, and a second centrifugation cycle was performed. Subsequently, the solution was centrifuged at 4000 rpm in toluene to remove unwanted aggregates.

Thin film preparation

Thin films of the nanocrystals for SEM measurements were prepared on silicon/silicon oxide FET substrates. 100 µl of NC solution were drop–casted onto the substrate and subsequently spin-coated at 34 rpm for 30 s, after completion of the first cycle, the substrate was spun again to remove remaining solvent at the edges.

Scanning electron microscopy (SEM)

SEM was carried out with a HATACHI SU8030 electron microscope operating with an acceleration voltage of 30 kV.

UV-vis and photoluminescence measurements

Optical analysis was carried out on an UV-vis-NIR spectrometer (Agilent Technologies, Cary 5000) and a fluorescence spectrometer (PerkinElmer FL8500). Both systems are equipped with an exchangeable sample holder for solid state and solution measurements.

Nuclear magnetic resonance spectroscopy (NMR)

NMR measurements were carried out on a Bruker Avance III HDX 400 at the NMR department of the University of Tübingen, with a frequency of 400 MHz. The spectra were analyzed with the Bruker TopSpin 4.0.2 as well as the Mnova NMR software. Peaks were fitted in the Mnova NMR software with convoluted Lorentzian and Gaussian line shapes, *i.e.*, a Voigt profile. All measurements were conducted with 1,3-dioxolane-2,4-dione as a standard. All samples were measured at room temperature.

Quasielastic neutron scattering (QENS)

Samples for neutron backscattering (NBS) measurements were prepared in deuterated toluene with NC concentrations ranging from 180 mg/ml to 360 mg/ml. In addition, a solvent reference (pure d_8–toluene) and a L–α–lecithin reference in deuterated toluene (22.8 mg/ml) were measured. All samples were prepared under inert atmosphere (N_2) due to sample aggregation in air (see supplementary information section S6).

QENS spectra were recorded on the IN16B beamline of the Institute Laue-Langevin (ILL) at Grenoble, France. IN16B was used in the BATS configuration with a suppressor chopper speed of 4731 rpm and a counter-rotating pulse chopper speed of 18924 rpm and an energy resolution of approximately 3.5 μeV full width at half maximum. The samples (total volume ~ 1 ml) were measured in 14 mm outer diameter double-walled cylindrical Al samples holders. The liquid suspension samples were filled in the gap (width ΔR = 0.3 mm) between the Al walls. The sample holders were hermetically sealed with In wire and inserted in a standard Orange cryofurnace for data acquisition. BATS scans were carried out at temperatures of 295 K, 250 K, and 200 K. The QENS data were reduced using Mantid and fitted using python scripts employing scipy.curvefit. [127] The convolution with the Gaussian instrument resolution function was performed using Voigt functions.

Small angle X-ray and neutron scattering (SAXS and SANS)

The samples were first measured by QENS and subsequently by SAXS/SANS. For the SAXS/SANS measurements, the samples were transferred from the sealed Al containers employed for QENS into dedicated SAXS/SANS cuvettes. All samples were measured at room temperature.

Simultaneous SAXS/SANS measurements were carried out at a customized system within the D22 beamline of the ILL. [291,292] SAXS data was acquired using a laboratory X-ray source with a Copper/Molybdenium (Kα, 8.0/17.4 keV; Rigaku MM007 HF DW generator) source combined with a Dectris EIGER2 X 1M detector in a vacuum tube. For Cu radiation (λ = 1.54 Å; beam size 0.5 x 0.5 mm), a q-range of 0.005 – 0.5 $Å^{-1}$ was covered by changing the sample-to-detector distance (0.55 – 1.63 m). The system could be moved in its entirety to focus on the same spot as the neutron beam, provided by the D22 beamline. The neutron beam wavelength was λ = 6 Å with Δλ/λ = 10 %, the sample-to-detector distance was tuned from 1.4 m, 5.6 m, 8 m, and 17.6 m, thus enabling measurements in the q-range from 10^{-3} – 0.7 $Å^{-1}$. The SANS signal was recorded with a large (96 x 96 cm) detector, composed of 16000 pixels. Both data sets, *i.e.*, SAXS and SANS, were collected simultaneously and subsequently analyzed using the SASFit software. [210] A more detailed discussion of the custom setup can be found in Metwalli *et al.* [292]

4.3. Introduction

Lead halide perovskite (LHP) nanocrystals (NC) are promising for application in novel optoelectronic devices. [51] Besides the LHP itself, the organic ligand shell of the NCs has a dramatic effect in this respect. [293] For instance, the quantum yield (QY) of LHP NCs can be tuned by utilizing specific ligand shells. [294,295] In light-emitting diodes, this effect as well as the equally ligand-dependent charge injection barrier are exploited to enhance the performance of LHP NC-based devices. [296,297] One of the major drawbacks of LHP NCs, their limited stability, can also be tailored by the ligand shell. By

utilizing proper ligands and fine tuning the surface ligand density, the stability of LHP-based NCs was shown to increase largely. [294,298,299] Chemical modifications of the ligand shell are either carried out *in situ* or by post-synthetic treatment. [296] Especially the latter case is advantageous for optoelectronic applications, as the ligands can be selected to fit specific needs without developing a novel synthetic route. [296] Any rational design of such ligand exchange procedures requires detailed knowledge of the surface chemistry of the NCs, including its dynamics. [300] Here, we study the surface chemistry of L–α–lecithin covered all-inorganic $CsPbBr_3$ NCs in deuterated toluene and reveal a highly dynamic surface equilibrium. To this end, we combine information from NMR, which probes angular correlations, with simultaneous SAXS and SANS for probing spatial correlations on a mesoscopic scale, as well as QENS, which probes both spatial and time correlations simultaneously on a scale commensurate with molecule dimensions. All of the above methods are well suited for optically opaque liquid samples, where other techniques relying on optical transmission would fail. The simultaneous SAXS and SANS setup as well as the IN16B-BATS spectrometer option at the ILL constituted novel instrumentation used in this work. QENS benefits from the dominant incoherent scattering signal of the lecithin ligands against the deuterated solvent in the investigated *q*-range. I thus probes the self-diffusion of the ligands in their different configurations, *i.e.*, on the NCs, free, or inside lecithin micelles, respectively. Due to the nanosecond coherence time of the QENS experiment, this self-diffusion is observed on the diffusive short-time scale on which the NCs displace by only a small fraction of their radius. On this scale, collisions between the NCs can be neglected, and the center-of-mass diffusion can be assumed to be governed by hydrodynamic interactions. Due to the large momentum transfer accessed by the QENS experiment, both the lateral diffusion of the lecithin, as well as the superimposed center-of-mass diffusion of the ligand-decorated micelles and NCs are simultaneously probed. [125] The QENS experiment also allows to easily access a wide sample temperature range. The significantly increased energy range investigated with keeping a good energy resolution of the IN16B-BATS option allows to separate unambiguously the apparent global diffusion from the faster diffusive processes within the ligand shell.

4.4. Results

Nanocrystal characterization

The as-synthesized NCs covered by L–α–lecithin exhibit an absorption onset at 510 nm and a corresponding photoluminescence (PL) signal at 513 nm (**Figure 4.1 a**). Scanning electron microscopy reveals an average diameter of 8.25 ± 1.2 nm (**Figure 4.1 b + c**), which is in good agreement with a size of roughly 9 nm inferred from the PL center wavelength. [24,57]

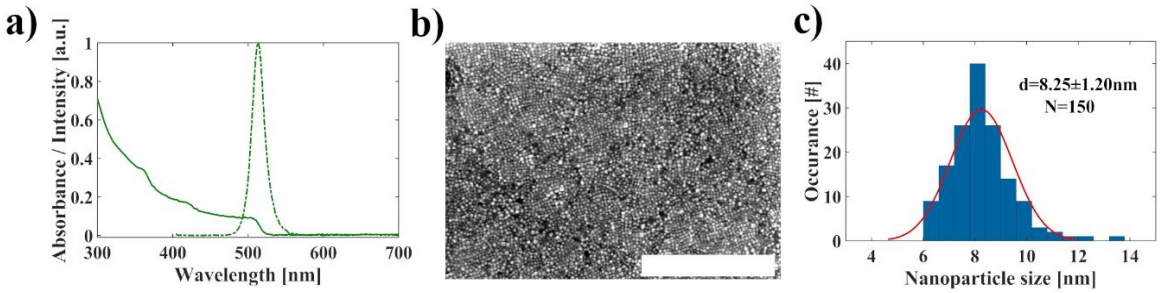

Figure 4.1: a) Absorption and photoluminescence of lecithin functionalized $CsPbBr_3$ nanocrystals in toluene at room temperature. Absorption and photoluminescence are depicted as solid and dotted lines, respectively. b) SEM micrograph of the NCs. The scale bar is 500 nm. c) Size distribution measured *via* SEM for 150 analyzed particles.

To characterize the ligand shell, we carried out NMR on three types of samples, namely the L–α–lecithin covered NCs, an L–α–lecithin reference, and an NC sample in which excess L–α–lecithin was added. The ligand content for the as-synthesized samples was 18 mg/ml, whereas the sample with excess ligand had a ligand concentration of 38 mg/ml, *i.e.*, roughly twice the ligand amount. L–α–lecithin exhibits a characteristic peak at ~ 5.5 ppm associated with the alkyl chains attached to the phosphatidylcholine head group. This peak behaves similarly to the characteristic peak of oleic acid in the alkene region (5 – 6 ppm), which is already thoroughly characterized. [191,192,197] A typical NMR signal, in-detail analysis, as well as overview spectra are given in the Supplementary Information, Section S4.1. All samples, and respective references (solvent and pure ligand), were subsequently utilized in further experiments.

NMR Fitting and multiple Lecithin species

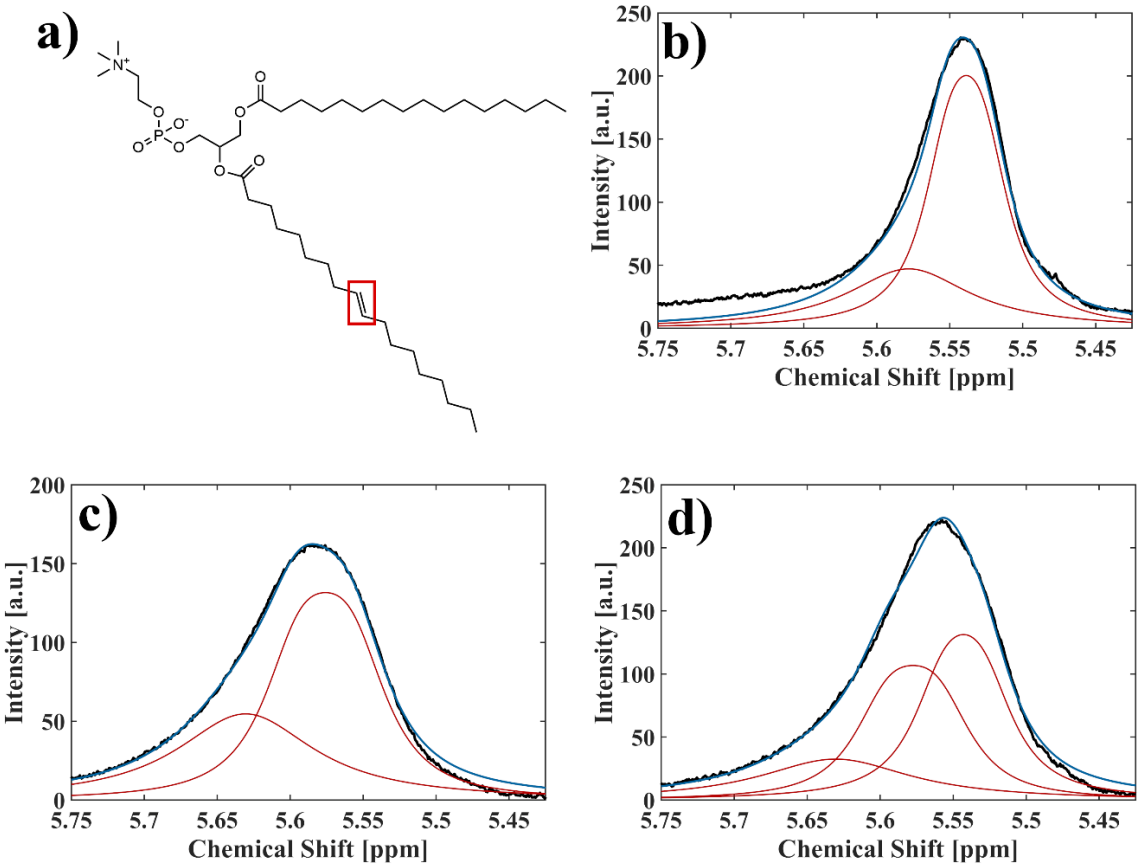

Figure 4.2: a) Structure of lecithin, the analyzed protons are highlighted in red. NMR spectra of the lecithin alkene region (5.4 – 5.7 ppm) with corresponding fits of b) lecithin reference, c) as-synthesized NCs and d) excess ligand sample. All measured peaks were found to be asymmetric. The lecithin and NC reference was fitted with two peaks, whereas for the excess sample three peaks were necessary. The fitting parameters for the displayed fits are given in **Table 4.1**.

First, the NMR spectra were evaluated, *i.e.*, the alkene peak was fitted specifically since the shape was found to be asymmetric (see **Figure 4.2** and **Figure S4.1**). This suggests multiple species of the ligand in the respective solutions. The assignment of the peaks was carried out following similar considerations for colloidal NC samples, commonly exemplified in literature with the oleic acid alkene peak. [191,192,197] In this context, a downfield shift in NMR of colloidal NC samples can be attributed to a ligand molecule which is in proximity to either the NC or other ligand molecules, *i.e.*, bound to the NC surface or attached in a micelle. [192] Therefore, the chemical shift of the respective peaks was investigated, and three distinct peaks could be identified. All of them occurred in the excess ligand sample, which thus was used to obtain the peak positions. The positions were subsequently held constant. A summary of the chemical shifts can be found in the second column of **Table 4.1**. The second important property of the alkene peaks is the full-width-at-half-maximum (FWHM), which is reciprocally linked to the decay constant (T_2*) of the free induction decay (FID) signal which gives a measure for the freedom of movement of a molecule. [192] The signals displayed in **Figure 4.2** exhibit a clear trend in the FWHM, as the signal broadens with increasing downfield shift. A broader signal in

NMR can be associated with a more confined movement of the molecule. Therefore, the peaks found in NMR could be assigned to 3 species of lecithin as follows: the peak at 5.54 ppm corresponds to free lecithin and small ligand aggregates, the peak at 5.58 ppm can be assigned to a weakly bound ligand species, and finally the peak at 5.63 ppm arises due to strongly bound lecithin. A more precise discussion of these species will be given further below (section on small angle scattering) and especially in the discussion section.

Table 4.1: Fitting results of the ^{1}H NMR alkene peak at 5.4 – 5.7 ppm for the respective samples. Given are chemical shifts, the corresponding peak assignment, peak full-width-at-half-maximum (FWHM), reduced relaxation times T_2^* and the relative peak area. All peaks are fitted with Voigt functions.

Sample	Chemical shift [ppm]	Assignment	FWHM [Hz]	T_2^* [ms]	Relative Area [a.u.]
NC	5.578	Micelles & weakly bound	31.65	10.10	0.5857
	5.631	Tightly bound	45.34	7.02	0.4143
Lecithin ref	5.539	Free Lecithin & small clusters	22.94	13.88	0.6743
	5.578	Micelles & weakly bound	40.94	7.78	0.3257
Excess	5.543	Free Lecithin & small clusters	27.01	11.79	0.4122
	5.578	Micelles & weakly bound	31.65	10.10	0.3721
	5.631	Tightly bound	49.86	6.39	0.2157

Small angle X-ray and neutron scattering

For further analysis of the structure of the ligand shell, we conducted simultaneous small angle X-ray (SAXS) and neutron scattering (SANS) measurement, exemplarily shown in **Figure 4.3 a**. The differing intensities are due to the sensitivity of the methods towards the inorganic core and organic ligand shell. [31,125,202] While SAXS is most sensitive towards heavy atoms (here: particularly Pb), the SANS signal originates predominantly from the hydrogen atoms in the ligand and their scattering length density (SLD), which invokes a strong scattering contrast against the background of the deuterated solvent. [125,202] A model-independent analysis *via* Kratky plots (**Figure 4.3 b**) of the SAXS data revealed two findings: All samples are of spherical morphology and the radius of gyration is increased after the addition of excess ligand. The radius increased by ~ 0.5 nm, from 5.2 nm to 5.7 nm, which was deducted from the peak position in the Kratky plots **(Figure 4.3 b**). Additionally, the bell shape in **Figure 4.3 b** and the asymptotic behavior of the scattering intensity decay ($\propto q^{-4}$, **Figure 4.3 a**) indicates a sharp and smooth surface. [301]

Utilizing the information obtained from SAXS, the intensity decay of the SANS data was specifically modelled by applying an appropriate model in the SASfit software. [210] Generally, the scattered intensity is proportional to the number of scatterers N_{scat}, the form factor $P(q)$ and the structure factor $S(q)$:

$$I(q) \propto N_{scat} P(q) S(q). \tag{4.1}$$

Where q is the absolute value of the momentum transfer:

$$q = |\vec{q}| = \frac{4\pi}{\lambda} \sin\theta, \tag{4.2}$$

with the incoming wavelength λ and the scattering angle θ.

As the samples showed some sign of aggregation from the q-dependence of the intensity decay, the SANS data was fitted with a model containing free and aggregated NCs as well as micelles. A more detailed description of the fitting procedure is given in the Supplementary Information Section S4.2. The parameters to model the SANS intensity decay, *i.e.*, the necessary radii, were set as obtained from SEM and SAXS. Specifically, for the inorganic core d_{core} = 8.25 ± 1.25 nm from SEM, as well as the overall NC diameter (core + ligand) d_{NC} = 10.4 nm. However, modelling the form factor with solely a core-shell sphere model proofed insufficient (see Supplementary Information **Figure S4.10**). Other reasonable morphologies, *e.g.*, parallelepipeds, also resulted in insufficient fits (see Supplementary Information Section S4.2 for further details). Therefore, to obtain proper fitting, the model was extended by a second contribution, namely another spherical form factor. [302] The additional form factor can be rationalized by the presence of micelles in the samples, as lecithin has two distinct critical micelles concentrations (CMC) in benzene, which is very similar to toluene. [303] At already very low concentrations lecithin starts to form aggregates of 3 – 4 molecules, and above concentrations of 0.73 mg/ml the formation of larger micelles commences, with a molecular weight of 55000 – 57000 Dalton. [303] Combining all contributions results in the overall scattering intensity being modeled by:

$$I(q) = I_{core-shell} + I_{aggregated} + I_{micelle} + I_{OZ} + I_{bkg}, \tag{4.3}$$

with the scattered intensity from free NCs $I_{coreshell}$, from aggregated NCs $I_{aggregated}$, from micelles $I_{micelle}$, an Ornstein-Zerneke contribution I_{OZ} and a constant background I_{bkg}.

The Ornstein-Zerneke contribution was added in all fitting procedures as it appeared necessary for colloidal systems to describe indirect interparticle interactions not included in the structure factor. [125,304] From fitting it was found that the spheres, *i.e.*, the micelles, have a radius of 6.2 nm. The molecular weight of lecithin micelles from literature corresponds to micelles consisting of 75 lecithin molecules and a radius of ~ 3 nm, which is in reasonable agreement with the experimental findings from SANS as the theoretical radius includes a variety of assumptions. [303] The discrepancy between the theoretical and experimental value can be explained by the fact that the theoretical value was calculated from literature values and does not take into account the environment of the micelles as well as deviations from ideality in solution.

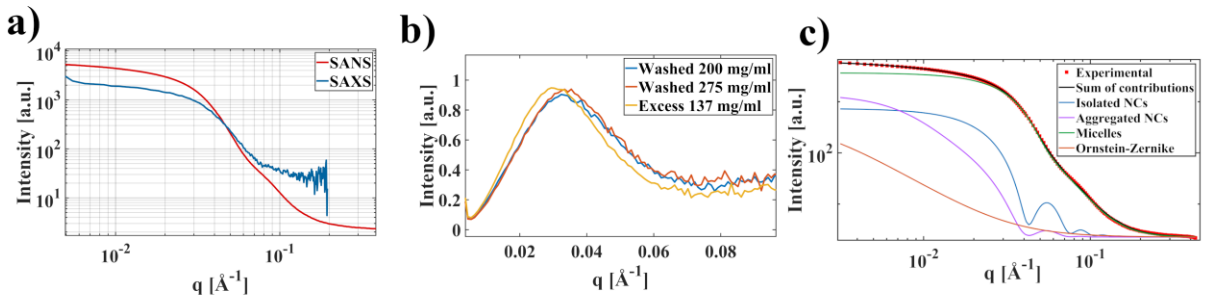

Figure 4.3: a) Results of the simultaneous SAXS and SANS measurements on D22, with SANS and SAXS shown in blue and red, respectively. The different intensities arise due to the different sensitivity of the methods towards the used compounds. An increase at low *q* is visible in the SAXS data, which could hint at clustering of the NCs. b) Kratky plots of the SAXS measurements for 3 different samples. The samples of the as-synthesized NCs exhibit the same maximum despite having different concentrations (red and blue), whereas the sample with additional lecithin experiences a shift of the maximum to lower *q*-values (yellow). c) Fitting model for the SANS measurement, experimental data is given in red, the core-shell sphere contribution in blue, aggregated NCs in purple, micelle contribution in green, and the final fit (**Equation (4.3)**) in black.

Quasielastic neutron scattering

To complement the steady-state information obtained from NMR and small angle scattering (SAS) with information about the dynamics at the surface of the NCs, we conducted QENS. By employing deuterated toluene as a solvent, but protonated ligands, the QENS experiment is sensitive to the dominant incoherent scattering of the ligand protons. In this way, the self-diffusion of the ligand molecules is probed on an observation, *i.e.*, coherence time of 1 ns. Through this method, it was possible to determine the diffusion coefficients in the system, namely the center-of-mass diffusion (D) of the NCs as well as the lateral diffusion of the ligand (D_{jump}) on the nanocrystal surface. Of particular interest is the elastic incoherent structure factor (EISF) A_0, as it gives a measure for the mean free path within the geometrical confinement of the lateral diffusion process. Experimentally, the diffusion coefficients can be accessed *via* *q*-dependent line broadenings of the QENS signal due to the molecular diffusion. The information on the EISF is contained within the intensity ratio of the Lorentzians accounting for the center-of-mass and lateral diffusion. More specifically, a line broadening in the Lorentzian FWHM of multiple components contribute to an overall broadening (exemplarily shown in **Figure 4.4 a +b**). Models of different complexity, with correspondingly different levels of assumptions on the system, may be considered. Here we describe the most straightforward approach, other models are explained in the Supplementary Information. In this model, the components can be attributed to the average center-of-mass diffusion of the NCs and lecithin micelles, accounting for the Lorentzian with the width $\Lambda(q)$, average lateral ligand diffusion associated with a Lorentzian of width $\gamma(q)$, solvent Lorentzian having the width $\zeta(q)$, and an apparent elastic contribution of the sample container, accounted for by a Lorentzian with zero with width $\varepsilon(q) = 0$. The sum of these components results in the of the model scattering function (**Equation (4.4)**).

$$S_\Gamma(q,\omega) = \sum_\Gamma S_\Gamma(q,\omega) = \sum_\Gamma A_\Gamma \frac{1}{\pi} \frac{\Gamma(\mathrm{q})}{\omega^2 + \Gamma(\mathrm{q})^2}, \tag{4.4}$$

with the line broadening of the respective component $\Gamma = \Lambda, \gamma, \zeta, \varepsilon$ and associated amplitude A_Γ was convoluted with the spectrometer resolution function and fitted to the data.

To obtain the solvent broadening, a reference sample of d_8-toluene was measured, and this pure solvent fit result was rescaled and fixed in the subsequent fits of spectra from samples containing NCs and lecithin, while the other parameters were utilized as free parameters during the fitting procedure. A more precise discussion of the fitting and the EISF is given in the Supplementary Information Section S3, along with the presentation of alternative models. Finally, the q-dependent Lorentzian widths could be used to calculate the apparent average nanoparticle and lecithin micelle center-of-mass diffusion $D = \Lambda/q^2$ and ligand, D_{jump}:

$$\Gamma(\mathrm{q}) = \frac{\mathrm{D_{jump}q^2}}{1 + D_{jump}q^2\tau}, \tag{4.5}$$

with the jump diffusion coefficient D_{jump} and the residence time τ.

The residence time τ, describes the time a component remains at a certain site, which for the center-of-mass diffusion is assumed to be zero, thus $D = \Lambda/q^2$. This model is denoted Fickian diffusion ($\Gamma = Dq^2$) for the NCs. We note that, due to the large momentum transfers of the QENS experiment, D is an implicit function of both translational and rotational diffusion. However, the residence time for the lateral ligand diffusion had to be specifically fitted. The values are almost zero for the ligand diffusion as well, with a maximum of 7 ps (see supplementary information **Figure S4.11**), which means Fickian diffusion can also be assumed for the lateral ligand movement, in agreement with related observations on oleic acid on PbS nanoparticles. [125] The diffusion coefficients calculated following **Equation (4.5)** are summarized for all samples in **Figure 4.4 c**. Additionally, the temperature dependence of the diffusion coefficient was determined for two samples, namely the lecithin reference and the excess sample (see **Figure 4.4 c + d**).

The presented results are obtained from a model with only few parameters, this specifically means that the lecithin species are approximated as an average and are thus fitted by a single contribution for lateral and center-of-mass diffusion, each. This effectively means the fitting results average over all possible binding situations of the lecithin ligand. However, the EISF for the lecithin and NC mixtures was found not to follow the expected monotonous decay with rising q (**Figure S4.5 a**). In contrast, the EISF of the pure lecithin suspensions displays a reasonable behavior consistent with diffusion in spatial confinement. To address the inconsistent EISF of the NC/lecithin mixtures additional models were tested. In the first additional approach, a physically meaningful EISF was forcefully implemented in the previously described fit of the averages. For the second model, not only the toluene fit results, but also the pure lecithin solution fit results were held fixed, before fitting

the NC suspension spectra. The relative weight of the signals from the lecithin-decorated NCs and the fit results were fixed. From NMR the existence of multiple lecithin species is known (*cf.* **Table 4.1**). Therein, to achieve a stable fit of the QENS spectra, the weakly bound lecithin and lecithin in micelles as well as small clusters were averaged by the single lecithin contribution in the model. The results of this approach are shown in the Supplementary Information Section S4.4. The EISF in this case behaves reasonably with, notably, rather large diffusive mean free paths of the ligands, indicating a very weak diffusive confinement. Moreover, the ratio of bound and free lecithin is consistent with the NMR results (*cf.* **Table 4.1**). However, the results for the line broadening accounting for the ligand diffusion appeared to be less reliable since the fit result for the residence time was somewhat unstable. We attribute this instability to the existence of the different ligand species, which are measurable in NMR, but would exceedingly increase the number of free fit parameters in the QENS model. For this reason, we can only account for the average lecithin population as stated above. Due to the presence of the NCs, there might be even more species contributing to these peaks, which could be described as a continuum of lecithin species. Therefore, fixing the fitting parameters to 2 very distinct species prevents a fully consistent fitting. It appears that averaging over all species provides more robust results.

By consulting the averaged fitting results, several main observations from QENS were made. On the other hand, the center-of-mass diffusion exhibited a somehow expected behavior, as the lecithin micelles (**Figure 4.4 c**, cyan) diffuse faster than the NCs (**Figure 4.4 c**, green). However, if excess lecithin was added, an apparent diffusion coefficient between the extreme values was observed (**Figure 4.4 c**, blue). On the other hand, the lateral diffusion exhibited a counterintuitive result, as the lateral diffusion for the lecithin molecules in micelles as well as on the NC surface appears to be similar **(Figure 4.4 d**, cyan and green at 295 K) but the excess sample showed significantly faster diffusion coefficients, as shown in **Figure 4.4 d**, blue line at 295 K. However, it may be difficult to dissociate the contributions by the different dynamic equilibria since a fast diffusion process results in different lecithin species (*cf.* **Table 4.1** and Discussion section) to this average fit.

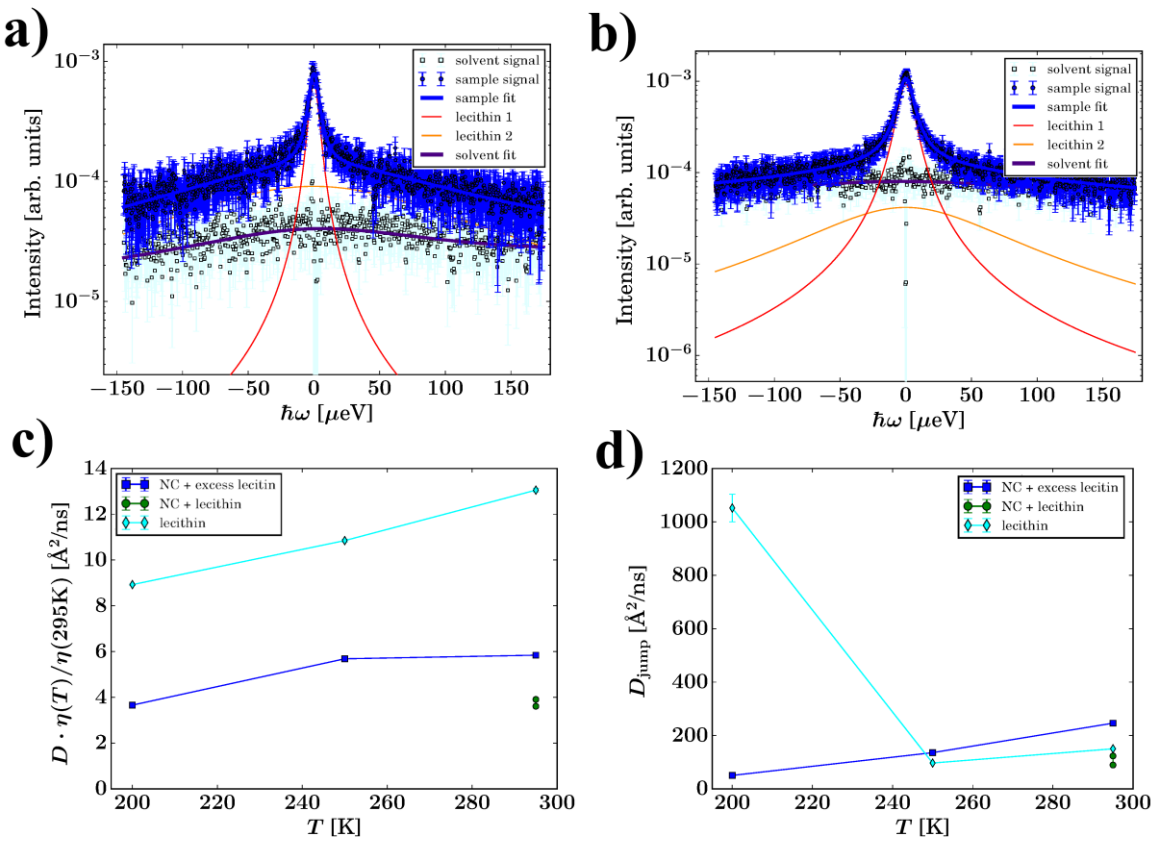

Figure 4.4: Quasielastic neutron scattering results for the used samples. a) + b) Example QENS spectra at certain momentum transfers ($q = 0.98\ \text{Å}^{-1}$ and $q = 1.56\ \text{Å}^{-1}$ for a) and b), respectively) with corresponding contributions at 295 K, as described in the main text. A broadening due to an elastic contribution was subtracted after fitting. Solvent, NC center-of-mass (lecithin 1) and ligand lateral diffusion (lecithin 2) contributions are shown. c) Calculated center-of-mass diffusion for the as-synthesized NCs (green), the lecithin reference (cyan) and the sample with additional ligand (blue) at different temperatures. d) The lateral diffusion coefficient of the lecithin reference (cyan), as-synthesized NCs (green) and the sample with excess ligand (blue) at different temperatures. The much larger diffusion of the reference sample can possibly be explained by overfitting due to freezing of the sample. The viscosity correction for all diffusion coefficients was done by fitting literature values, as explained in the Supplementary Information Section S5. The error bars on the fit parameters denote σ confidence bounds from the diagonal elements of the covariance matrix. They are mostly smaller than the symbols, because a global fit of the spectra for all measured momentum transfers at once was performed.

4.5. Discussion

To discuss the results described in the sections above, it is convenient to base the discussion on the dynamic properties obtained from QENS. The first crucial finding is the center-of-mass diffusion coefficient *D*, which is distinct for the lecithin *vs.* NC reference. We found an almost 3 times larger diffusion coefficient for the lecithin, which we attribute to the smaller diameter of the lecithin micelles

compared to the NCs. Therefore, the hydrodynamic radius was calculated by using the Einstein-Stokes relation:

$$r_h = \frac{k_b T}{6\pi\eta(T)D}. \tag{4.6}$$

With the Boltzmann constant k_B, temperature T, and solvent viscosity of d_8-toluene $\eta(295\ K)$ = $5.39 \cdot 10^{-4}$ $kgm^{-1}s^{-1}$. For details on the temperature dependent viscosity, see supplementary information section S4.5.

By utilizing **Equation (4.6)**, we found a hydrodynamic radius for the lecithin micelles of 3.71 nm and for the NCs a radius of 10.1 nm, which is in reasonable agreement with the other size-determining methods. Generally, micelles of lecithin are present in the sample, and they are found to be smaller than the NCs, which is in good agreement with literature as well. [24,303] The sizes, and thus, the different diffusion coefficients can also explain the behavior of the excess lecithin sample, where a center-of-mass diffusion in between the reference samples was found (**Figure 4.4 c**). We rationalize this by an apparent diffusion coefficient, which occurs due to the pronounced presence of both species in this sample.

The second result of interest is the behavior of the lateral diffusion, where seemingly counterintuitive results were obtained. **Figure 4.4 d** displays D_{jump}, and the diffusion of the ligand in the excess sample is significantly higher. To explain this, the precise surface chemistry needs to be considered. From the fitted NMR areas, the ratio of the different species, assigned as shown in **Table 4.1**, was calculated. The ratio can directly be correlated to an equilibrium constant that describes the binding situation of the different ligand species. However, the model of the QENS spectra averages over the two different equilibria and probes lateral diffusion rather than the angular correlations measured by NMR. The first dynamic equilibrium is between free and weakly bound lecithin (*e.g.*, in micelles or on the NC surface), in the following denoted as K_1. In the case of the as-synthesized, washed NCs, K_1 equals nearly zero, *i.e.*, almost all ligands are attached to the NC surface. On the other hand, if excess ligand is added, this equilibrium is distorted, and we find a ratio of free to attached lecithin of 0.7013 (see **Figure 4.5**). This means that more ligand is bound to the NC, effectively increasing the ligand surface density. On the other hand, in this situation more ligand molecules are present in solution, inducing the formation of further micelles. As more micelles are present, the average apparent center-of-mass diffusion coefficient, from the faster micelle and slower NC coefficient, must increase. This is the behavior displayed in **Figure 4.4 c**.

Furthermore, a second equilibrium (K_2) exists which is associated with the ligands that are attached to the surface. The associated species from **Table 4.1** are the weakly and tightly bound species, and K_2 describes the ratio of weakly to tightly bound lecithin. We propose the following model to define these two species in more detail: Lecithin intrinsically is a zwitterionic ligand with two functional groups that are able to bind to a surface, namely the amine ($N(CH)_3^+$) and phosphate

(PO_4^-) groups. We propose the weakly attached species to be a lecithin molecule bound with only one of the respective groups, whereas the tightly bound lecithin would be attached with both groups at the same time (Schematic, **Figure 4.5**). For the as-synthesized NC reference K_2 was found to equal 1.4137, this value could be increased to $K_2' = 1.7251$ by adding more ligand. Effectively, this means after more ligand is added, more lecithin is attached weakly to the NC surface, *i.e.*, only bound with one functional group. This implies two important changes, firstly the effective radius of the ligand shell must increase. This is due to the fact that less surface area per ligand is available and therefore more lecithin is bound with the amine group. This functional group is at a terminal position, which means the rest of the molecule must stand out into the solution away from the surface (Schematic, **Figure 4.5**, bottom). This view is consistent with SAXS and SANS, where an increase in size of 0.5 nm was found. This is almost exactly the length which would be expected by the "stretching" of the molecule. The second implication is that, since one bond is broken easily than two, lecithin bound in a monodentate fashion can be removed more easily and can thus diffuse faster. This explains the counterintuitive behavior found from the lateral diffusion coefficient (**Figure 4.4 d**).

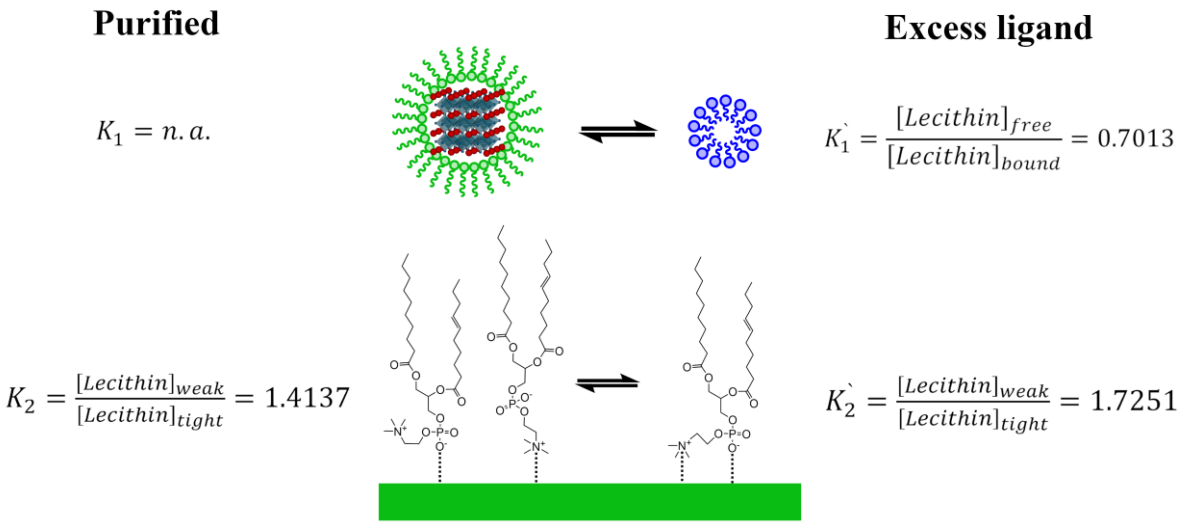

Figure 4.5: Model for the surface chemistry of lecithin on $CsPbBr_3$ NCs, the left side displays the equilibrium constant(s) for the purified case, *i.e.*, the as-synthesized sample. The right side shows the same equilibrium constants, however for the case of the excess lecithin sample. The first equilibrium (K_1) describes the situation of the ligand molecules, they are either present in the form of micelles, attached to a NC surface or free. The equilibrium constants are thoroughly calculated from the areas shown in **Table 4.1**. For the as-synthesized case, this could not be obtained, as no NMR signal for the free ligand could be measured. The second equilibrium (K_2 and K_2') describes the binding of the ligand to the NC surface. The middle section shows a cartoon of the binding situation of the zwitterionic ligand in micelles and NCs (top) as well as on the surface (bottom) with the bonds between NC and ligand shown as dotted lines.

4.6. Conclusion

To conclude, by combining NMR with small angle X-ray and neutron as well as quasielastic neutron scattering the surface chemistry and solution structure of L–α–lecithin functionalized $CsPbBr_3$ NCs in liquid toluene suspensions could be revealed. From SAS it was found that all samples contained ligand micelles (**Figure 4.3 b** and **Figure 4.4 d**) with a size of roughly 4 – 5 nm. In combination with the presence of the NCs this led to an apparent average center-of-mass diffusion in the samples, revealed by QENS. Effectively, this means in a sample with free ligand only the average diffusion coefficients can be obtained in a straightforward was. Modelling separate populations of NCs and micelles is also possible but requires drastic assumptions on the dynamic behavior of the system. However, in a thoroughly washed sample, the number of micelles could be minimized and the center-of-mass diffusion of the NCs could be approximated (**Figure 4.4 c**, green symbols). Additionally, from NMR it was known that multiple surface species of the ligand must be present (**Figure 4.2**), which can be rationalized by accounting for the size increase, measured in the excess sample by SAXS. The lecithin can be attached by either both of its two functional groups or only by one. Upon increasing the ligand density, the latter case becomes more probable as less surface area per ligand is available. The highly dynamic equilibrium identified by NMR is consistent with a fast average lateral diffusion process identified by QENS. Even though this lateral diffusion cannot be further dissociated into different dynamic contributions with the present QENS data, the nearly unrestricted geometrical character of this diffusion seen in the nearly vanishing residence time and large mean free path seen in the EISF are consistent with this highly dynamic picture. Thus, in summary, the lecithin functionalized $CsPbBr_3$ NCs exhibited a highly dynamic surface equilibrium confirmed in both QENS and NMR, which could be tuned by varying the ligand density *via* excess lecithin. Ultimately, the tuning of the surface equilibrium, and thus the binding situation, could be exploited during ligand exchange procedures.

Author information

The manuscript was written through contributions of all authors. All authors have given approval to the final version of the manuscript.

Acknowledgment

This work was supported by the DFG under grants SCHE1905/8-1 (project no. 424708673) and SCHE1905/9-1. The German Ministry of Research and Education BMBF (05K19VTB, ...) is acknowledged for funding the BATS option on IN16B as well as the in-situ SAXS option on D22, both located at the ILL. F.S. acknowledges funding by the BMBF.

4.7. Supplementary Information

Supplementary Information

Quasielastic Neutron and Small Angle Scattering Reveals Highly Dynamic Surface Equilibrium on L-α-Lecithin Functionalized $CsPbBr_3$ Nanocrystals

Jan Wahl[1], Tilo Seydel[2,3], Ivan Zaluzhnyy[2], Christian Beck[2,3], Olga Matsarskaia[3], Lionel Porcar[3], Ezzeldin Metwalli[4], Frank Schreiber[2], Marcus Scheele[1,5]

[1] *Institut für physikalische und theoretische Chemie, Universität Tübingen, Auf der Morgenstelle 18, D-72076 Tübingen, Germany*

[2] *Institut für Angewandte Physik, Universität Tübingen, Auf der Morgenstelle 10, D-72076 Tübingen, Germany*

[3] *Institut Max von Laue – Paul Langevin, 71 avenue des Martyrs, F-38042 Grenoble, France*

[4] *Institut für Physik der Kondensierten Materie, Universität Erlangen-Nürnberg, Staudtstrasse 3, D-91058 Erlangen*

[5] *Center for Light-Matter Interaction, Sensors & Analytics LISA*$^+$*, Universität Tübingen, Auf der Morgenstelle 15, D-72076 Tübingen, Germany*

S4.1: NMR overview and alkene region of L-α-Lecithin for the measured samples

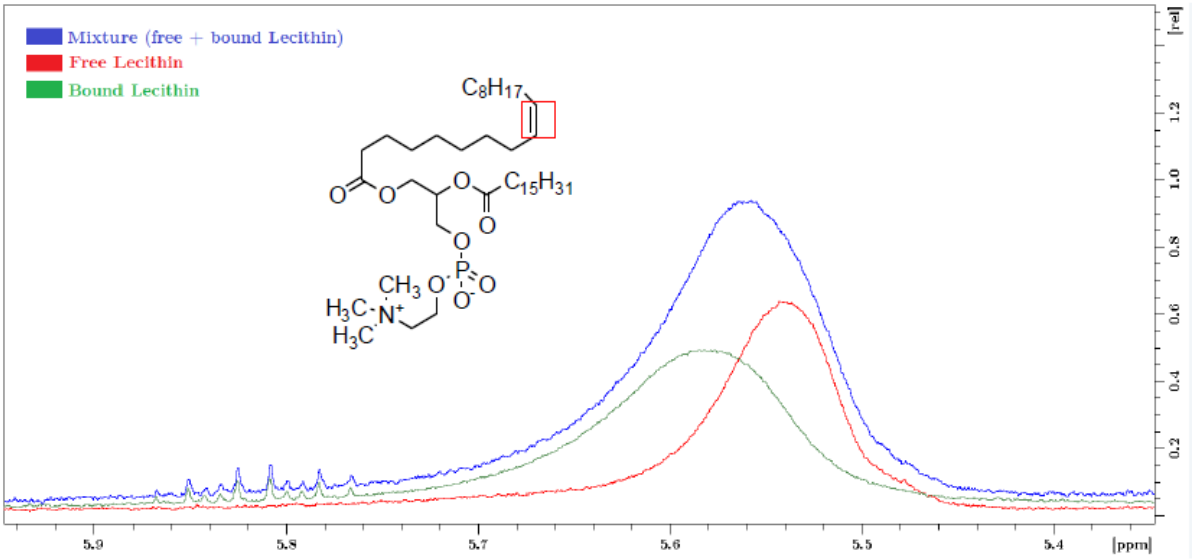

Figure S4.1: NMR spectra of the vinyl peak for three samples mentioned in the text. Shown are a lecithin reference (red), as-synthesized NCs (green) and a sample with excess ligand (blue). The measurement of the sample with excess ligand is multiplied with a factor of 2 for better visibility.

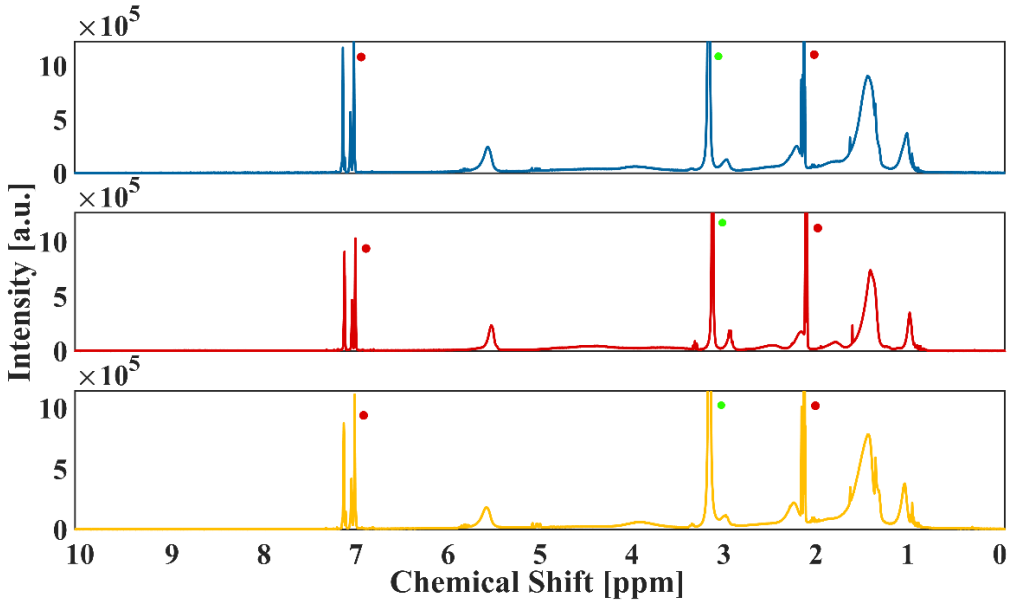

Figure S4.2: NMR overview spectra of the used samples in this work, namely the excess lecithin sample (blue), the lecithin reference (red) and as-synthesized NCs (orange). The solvent peaks of d_8-toluene and standard peaks are marked with red and green dots, respectively.

All samples were equipped with a standard to perform a quantitative analysis which can reveal the ligand content of each sample. The corresponding concentrations were calculated using following expression:

$$c_{Lecithin} = \frac{A_{Lecithin}}{A_{standard}} \cdot \frac{N^H_{Lecithin}}{N^H_{standard}} \cdot c_{standard}, \tag{S4.1}$$

With the concentrations of lecithin and standard c, the area underneath the NMR peak A and the number of protons N^H. The results of the quantitative NMR analysis are given in **Table S4.1**.

Table S4.1: Results of the quantitative NMR analysis, given are the concentrations of the standard $c_{standard}$, the relative area of the lecithin peak $A_{lecithin}$, as well as the calculated concentration of lecithin in the measured sample and the lecithin concentration of the stock solution. This was done since the samples for the NMR measurements were diluted by a factor of 5. The area of the standard peak was set to equal unity. A molar mass of 750 g/mol for lecithin was used to transform the concentrations from M to mg/ml.

Sample	$c_{standard}$ [M]	$A_{lecithin}$ [a.u.]	$c_{lecithin}$ [mg/ml]	$c_{lecithin}^{stock}$[mg/ml]
As-synthesized	0.0941	0.1	3.53	18
Lecithin reference	0.1067	0.19	7.61	38
Excess lecithin	0.1302	0.09	4.39	22

S4.2: Analysis and fitting of small angle neutron (SANS) and X-ray (SAXS) scattering data‡‡

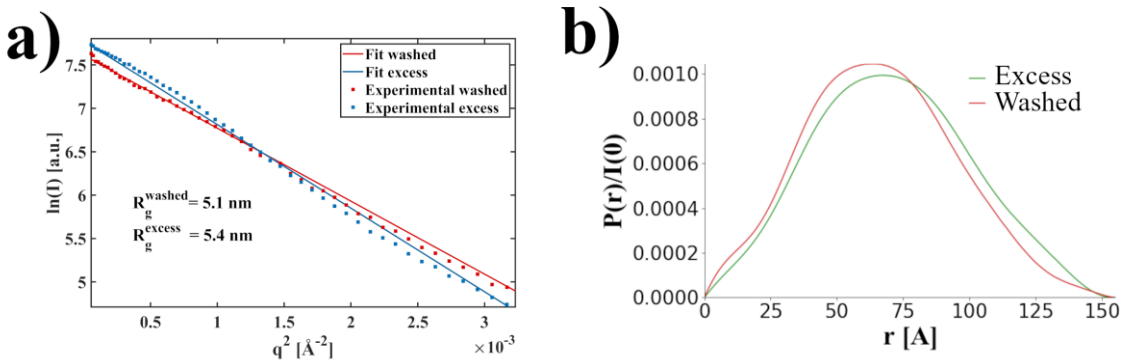

Figure S4.3: Additional model independent SAXS Analysis. a) Guinier plot and fit for a washed (blue) and excess lecithin (orange) sample. The fit results, *i.e.*, the radius of gyration is given for both cases. b) Indirect Fourier transformation of the small angle scattering data provides the size distributions for the aforementioned cases. An increase in diameter is seen for the excess sample in both cases.

Additional SAXS Analysis *via* a Guinier Fit for the NC containing samples revealed a similar behavior as observed in the Kratky plot (**Figure 4.3**). The intensity decay in the Guinier plot was fitted as follows to obtain the radius of gyration: [302]

$$\ln(I) = \ln(I_0) - \left(\frac{R_g^2}{3}\right) q^2, with\ r_H = 1.29\ R_g\ (for\ spheres) \qquad \text{(S4.2)}$$

With the scattered intensity $I(q)$, the radius of gyration R_g, the hydrodynamic radius r_H, and the momentum transfer q. [305]

The Guinier radii of gyration were found to equal 5.1 nm and 5.4 nm for the as-synthesized and excess ligand sample, respectively. This means we find comparable values to the Kratky analysis, which in turn fit to the proposed model, as shown in **Figure 4.5**. A comparable result was found upon performing a Fourier transform of the intensity signal, the size distribution function (**Figure S4.3 b**) confirms the findings from Guinier and Kratky analysis, *i.e.*, the increase in radius of roughly 0.4 – 0.5 nm.

‡‡ Remark from the author: The exact fitting procedure for the publication might still be subject to change due to revisions of the absolute calibration in the scattering data.

Next to the model free analysis, the following procedure was carried out on an as-synthesized sample of L–α–lecithin covered $CsPbBr_3$ nanocrystals (NCs) to verify the existence of ligand micelles in solution. Only the SANS data was explicitly fitted due to the fact that the micelles are more susceptible to neutron radiation in the presence of inorganic NCs. The fitting procedure was carried out based on the supporting information by Seydel *et al.* [125]

Fitting was carried out with SASFit 0.94.11, and the scattering length densities were calculated using the SASFit calculation tool (**Table S4.2**). [210] Each fit was repeated multiple times, with each repetition consisting of 10 iterations, until the fit remained stable.

Table S4.2: Summary of parameters to calculate the SLDs of used compounds.

Material	Density [g/cm^3]	M [g/mol]	$\lambda_{X\text{-}ray}$ (Cu Kα) [Å]	$\lambda_{neutron}$ [Å]	$SLD_{X\text{-}ray}$ [cm^{-2}]	$SLD_{neutron}$ [cm^{-2}]
$CsPbBr_3$	4.42	580	1.54	6 ± 0.6	$1.6164 \cdot 10^{10}$	$3.045 \cdot 10^{11}$
L–α–lecithin	1.3	758	1.54	6 ± 0.6	$4.2266 \cdot 10^{9}$	$1.217 \cdot 10^{11}$
d_8-Toluene	0.943	100	1.54	6 ± 0.6	$7.8055 \cdot 10^{10}$	$1.101 \cdot 10^{11}$

For the NC and micelle contribution the intensity was assumed to be follow $I(q) \propto NP(q)S(q)$, with the scatterer number *N*, as well as the form *P(q)* and structure factor *S(q)*. The structure factor was assumed to be unity and the form factor was subsequently explicitly fitted. For the NCs the form factor was fitted by 3 different models: 1) averaged sphere 2) core-shell sphere and 3) averaged parallelepiped with equal side lengths and angles of 90°. Averaged refers to the average SLD of core and ligand.

The form factor for model 1) was as follows: [302]

$$P_{sphere}\left(q, r_{NC+lig}, SLD_{NC/lig}, SLD_0\right) = \left(\frac{4}{3}\pi r^3 \Delta SLD \times 3\,\frac{\sin(qr_{NC+lig}) - qr_{NC+lig}\cos(qr_{NC+lig})}{(qr_{NC+lig})^3}\right)^2, \qquad \text{(S4.3)}$$

wherein r_{NC+lig} is the radius of the NC and the ligand shell, $SLD_{NC/lig}$ is the averaged scattering length density of NC and ligand, and SLD_0 is the scattering length density of the solvent.

For the core-shell sphere model 2), the form factor was taken as: [125,302]

$$P(q, r_{core}, t, SLD_{core}, SLD_{lig}, SLD_0) = \left[K(q, r_{core} + t, SLD_{lig} - SLD_0) + K(q, r_{core}, SLD_{core} - SLD_0)\right]^2, \qquad \text{(S4.4)}$$

with the core radius r_{core}, ligand shell thickness *t*, and scattering length densities of core, ligand shell and solvent SLD_{core}, SLD_{lig}, SLD_0, respectively.

Furthermore:

$$K(q, r, \Delta SLD) = \frac{4}{3}\,\pi\, r^3 \Delta SLD\ \times 3\frac{\sin(qr) - qr\cos(qr)}{(qr)^3}. \qquad \text{(S4.5)}$$

This model was considered, as the Kratky plots (**Figure 4.3 b** in the manuscript and **Figure S4.5 a**) exhibited a bell shape which is evidence for a spherical scatterer.

On the other hand, the parallelepiped model 3) was fitted by:

$$P_{Parallelepiped}(\vec{q}) = \left[\frac{\sin\left(\frac{1}{2}qA\ cos(\alpha)\right)}{\frac{1}{2}qA\cos(\alpha)}\right]^2 \left[\frac{\sin\left(\frac{1}{2}qB\ cos(\beta)\right)}{\frac{1}{2}qB\cos(\beta)}\right]^2 \left[\frac{\sin\left(\frac{1}{2}qC\ cos(\gamma)\right)}{\frac{1}{2}qC\cos(\gamma)}\right]^2. \quad \text{(S4.6)}$$

With the lengths of the parallelepiped *A*, *B*, and *C*, and therefore the Volume *V=A*B*C*. The angles between the sides α, β, and γ. [212,306,307]

Initially, the intensity was fitted by:

$$I(q) = I_{NC} + I_{OZ} + I_{bkg}, \quad \text{(S4.7)}$$

with the scattered intensity from the NCs I_{NC}, an Ornstein-Zernike contribution I_{OZ}, and a constant background I_{bkg}. I_{OZ} was used to account for (indirect) correlations of the NCs, which are not included in explicit form and structure factors, and was fitted as: [125,304]

$$I_{OZ}(q) = \frac{I_{OZ}(0)}{1 + q^2\xi_{OZ}^2}, \quad \text{(S4.8)}$$

Therein the intensity at $q = 0$, $I_{OZ}(0)$, and the correlation length ξ_{OZ} were used as parameters.

During the first fitting iteration, only NCs were considered to check if the intensity can be fitted solely by applying the from factors from **Equations (S4.3), (S4.4)** and **(S4.6)**. The parameters of the fits were obtained as shown in **Table S4.3**. The radii were deduced from SEM measurements for the inorganic core (8.25 nm) and the thickness of the ligand shell (2 nm, from SEM FFT analysis depicted in **Figure S4.5 b**). The scattering length density differences were calculated from the values given in **Table S4.2**. The radii were assumed to be distributed as a gaussian normal distribution, with the mean held fixed. From **Figure S4.4** it can be seen that all applied fitting models are insufficient, however the core-shell model appears most suitable and was used for subsequent steps (lowest variance). This can additionally be rationalized by looking at the Kratky plots of the SANS experiments (**Figure S4.5 a**), which shows a pronounced bell shape indicating spherical scatterers. Additionally, the tunability of the core-shell model enables a more detailed fit.

Table S4.3: Fitting parameters of the first iteration. $^{\Delta}$ From size distribution determined *via* SEM. All angles in model 3 are set to 90°. σ^2 is the variance of the fit. *Averaged SLDs are calculated from the arithmetic mean.

Model 1: Averaged sphere (σ^2 = 1.772)				
Contribution	Parameter	Unit	Fitted	Value
Spherical NC	N	cm^{-3}	Yes	$3.62 \cdot 10^{-29}$
	r_{NC+lig}	nm	No	$6.125 \pm 0.6125^{\Delta}$
	ΔSLD_{core-0}	cm^{-2}	No	$1.03 \cdot 10^{10}$ *
Ornstein-Zernike	$I(0)$	cm^{-1}	Yes	209.95
	ξ_{OZ}	Å	Yes	951
Background	I_{bkg}	cm^{-1}	Yes	2.51

Continuation Table S4.3: Fitting parameters of the first iteration. $^{\Delta}$ From size distribution determined *via* SEM. All angles in model 3 are set to 90°. σ^2 is the variance of the fit. *Averaged SLDs are calculated from the arithmetic mean.

Model 2: Core-shell sphere (σ^2 = 2.890)

Core-shell NC	N	cm^{-3}	Yes	$1.98 \cdot 10^{-30}$
	r_{core}	nm	No	$4.125 \pm 0.6125^{\Delta}$
	$r_{core} + t$	nm	No	6.125
	ΔSLD_{core-0}	cm^{-2}	No	$3.589 \cdot 10^{10}$
	ΔSLD_{lig-0}	cm^{-2}	No	$4.831 \cdot 10^{10}$
Ornstein-Zernike	$I(0)$	cm^{-1}	Yes	209.95
	ξ_{OZ}	Å	Yes	951
Background	I_{bkg}	cm^{-1}	Yes	2.51

Model 3: Averaged parallelepiped (σ^2 = 10.200)

Contribution	Parameter	Unit	Fitted	Value
Parallelepiped NC	N	cm^{-3}	Yes	$1.01 \cdot 10^{-30}$
	A	nm	No	$8.25 \pm 1.2^{\Delta}$
	B	nm	No	$8.25 \pm 1.2^{\Delta}$
	C	nm	No	$8.25 \pm 1.2^{\Delta}$
	ΔSLD_{core-0}	cm^{-2}	No	$1.03 \cdot 10^{10\,*}$
Ornstein-Zernike	$I(0)$	cm^{-1}	Yes	209.95
	ξ_{OZ}	Å	Yes	951
Background	I_{bkg}	cm^{-1}	Yes	2.51

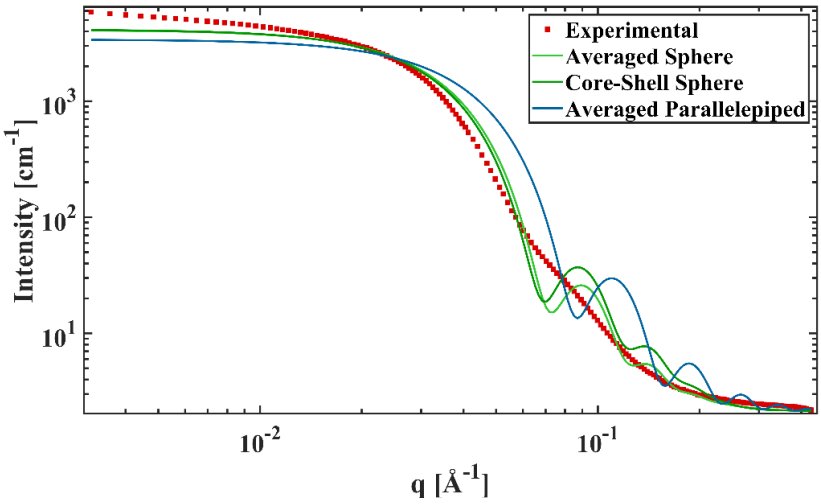

Figure S4.4: Plots of the results from the initial fitting iteration, the measurement data is shown in red, the sphere and core-shell sphere are shown in light and dark green, respectively. The parallelepiped from model 3) is shown in blue.

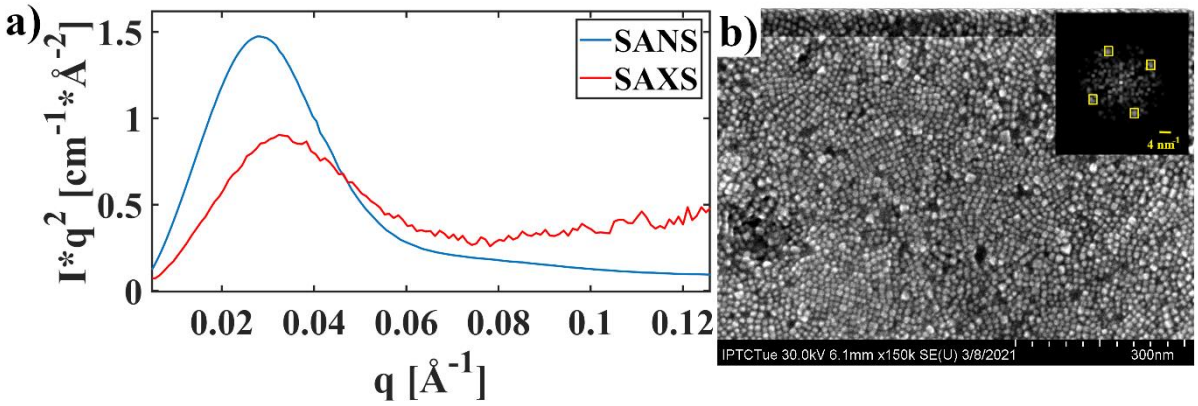

Figure S4.5: a) Kratky plots of SANS and SAXS shown in blue and red, respectively. The SAXS signal shows some indication for multidomain behavior, which could hint towards aggregation. Such a behavior is not visible in SANS. b) SEM micrograph of a thin film prepared with the as-synthesized NCs, the scale bar corresponds to 300 nm. The inset shows the fast Fourier transform (FFT) of the film, revealing a nearest-neighbor distance of 4 nm. This corresponds to a thickness of the ligand shell of ~ 2 nm.

For the second iteration micelles were added as a spherical form factor: [125,302]

$$P_{sphere}\left(q, r_{micelle}, SLD_{lig}, SLD_0\right) = \left(\frac{4}{3}\pi r^3 \Delta SLD \times 3\,\frac{\sin(qr_{micelle}) - qr_{micelle}\cos(qr_{micelle})}{(qr_{micelle})^3}\right)^2, \quad \text{(S4.9)}$$

with the radius of the micelles $r_{micelle}$. The corresponding result of the second iteration are given in **Table S4.4**.

Table S4.4: Fitting parameters of the second iteration. $^{\Delta}$ Fitted size distribution. * Sizes obtained *via* SEM. σ^2 is the variance of the fit.

Model 2: Core-shell sphere (σ^2 = 0.380)				
Contribution	Parameter	Unit	Fitted	Value
Core-shell NC	N	cm^{-3}	Yes	$1.50 \cdot 10^{-31}$
	r_{core}	nm	No	$4.125 \pm 0.74^{*\Delta}$
	$r_{core} + t$	nm	No	6.125^{*}
	ΔSLD_{core-0}	cm^{-2}	No	$3.589 \cdot 10^{10}$
	ΔSLD_{lig-0}	cm^{-2}	No	$4.831 \cdot 10^{10}$
Spherical micelles	N	cm^{-3}	Yes	$1.32 \cdot 10^{-30}$
	$r_{micelle}$	nm	Yes	5.69 ± 1.6
	ΔSLD_{lig-0}	cm^{-2}	No	$4.831 \cdot 10^{10}$
Ornstein-Zernike	$I(0)$	cm^{-1}	Yes	209.95
	ξ_{OZ}	Å	Yes	951
Background	I_{bkg}	cm^{-1}	Yes	2.29

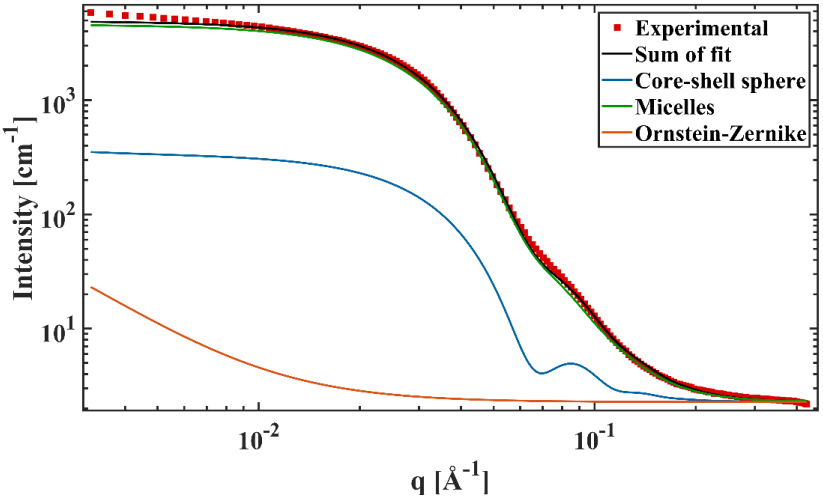

Figure S4.6: Fitting results after the second iteration (black), the components are shown explicitly. Namely, the NC scattering intensity (blue), the micelle contribution (green), and Ornstein-Zernike (orange).

The best model was a combination of a core-shell sphere (NCs) with additional spheres (lecithin micelles). The contribution of all components is shown in **Figure S4.6**. Subsequently, a hard sphere structure factor for the NCs as well as micelles was added. The hard sphere model was chosen due to the large repulsion energy of the lecithin-functionalized particles. [24] The radius of NCs was held fixed for this iteration and used as repulsion radius for the structure factor. The volume fractions were calculated from UV-vis concentration measurements in the case of $CsPbBr_3$ and fitted for the micelles. The structure factor for a liquid of structureless particles is given by: [302]

$$S_{HS}(q, R_{HS}, f_p) = \frac{1}{1 + 24\, f_p \dfrac{G(f_p, 2R_{HS}q)}{2R_{HS}q}}. \tag{S4.10.1}$$

Therein, f_p is the volume fraction, R_{HS} the repulsion radius. The Fourier transform of the direct correlation function is:

$$\begin{aligned} &G(f_p, 2R_{HS}q) \\ &= \alpha \frac{\sin(2R_{HS}q) - 2R_{HS}q\cos(2R_{HS}q)}{(2R_{HS}q)^2} + \beta \frac{4R_{HS}q\sin(2R_{HS}q) + (2 - 2R_{HS}q)^2\cos(2R_{HS}q) - 2}{(2R_{HS}q)^3} \\ &+ \gamma \frac{-(2R_{HS}q)^4\cos(2R_{HS}q) + 4((3(2R_{HS}q)^2 - 6)\cos(2R_{HS}q) + ((2R_{HS}q)^3 - 12R_{HS}q)\sin(2R_{HS}q) + 6)}{(2R_{HS}q)^5}, \end{aligned} \tag{S4.10.2}$$

wherein

$$\begin{aligned} \alpha &= \frac{(1 + 2f_p)^2}{(1 - f_p)^4} \\ \beta &= -6f_P \frac{(1 + f_p/2)^2}{(1 - f_p)^4} \\ \gamma &= f_p\alpha/2. \end{aligned} \tag{S4.10.3}$$

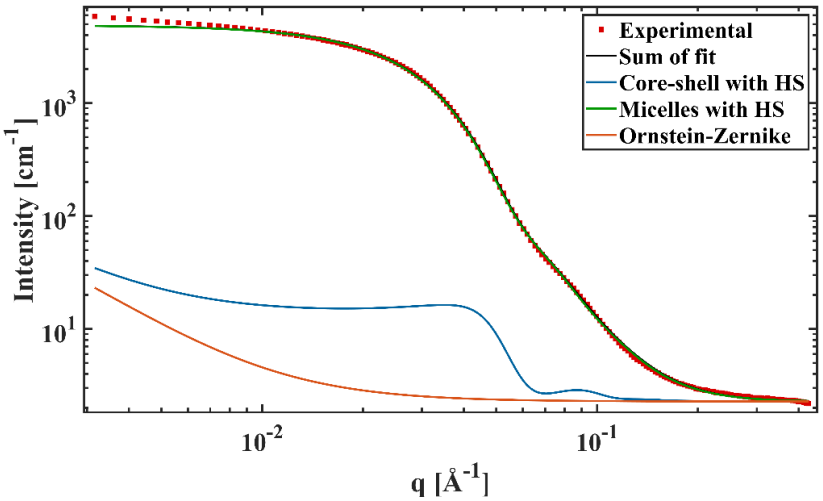

Figure S4.7: Contributions to the fit after applying hard sphere structure factors to NCs and micelles. The contributions of the NCs, micelles and Ornstein-Zernike are given in blue, green, and orange, respectively.

Table S4.5: Fitting parameters of the third iteration. $^{\Delta}$ Fitted size distribution. * Sizes obtained *via* SEM. σ^2 is the variance of the fit.

Model 2: Core-shell sphere (σ^2 = 0.011)				
Contribution	Parameter	Unit	Fitted	Value
Core-shell NC	N	cm^{-3}	Yes	$3.44 \cdot 10^{-32}$
	r_{core}	nm	No	$4.125 \pm 0.81^{*\Delta}$
	$r_{core} + t$	nm	No	6.125^{*}
	ΔSLD_{core-0}	cm^{-2}	No	$3.589 * 10^{10}$
	ΔSLD_{lig-0}	cm^{-2}	No	$4.831 * 10^{10}$
	R_{HS}	nm	No	6.125
	f_p	n.a.	No	0.242
Spherical micelles	N	cm^{-3}	Yes	$1.37 \cdot 10^{-30}$
	$r_{micelle}$	nm	Yes	5.99 ± 1.8
	ΔSLD_{lig-0}	cm^{-2}	No	$4.831 \cdot 10^{10}$
	R_{HS}	nm	Yes	4.80
	f_p	n.a.	Yes	0.05
Ornstein-Zernike	$I(0)$	cm^{-1}	Yes	209.95
	ξ_{OZ}	Å	Yes	951
Background	I_{bkg}	cm^{-1}	Yes	2.28

Independent of applying a structure factor, the size of the micelles was found to be ~ 6 nm. The intensity decay could not be fitted solely with the form and structure factor of the NCs, which were modelled with parameters obtained from independent experiments (*e.g.*, UV-vis and SEM). Therefore, the conclusion arises that micelles of lecithin in solution are present, which is also in accordance to the literature on lecithin micelles in benzene. [303] The critical micelle concentration (0.73 mg/ml) lies significantly below the concentration which were used during the experiments. [303] Additionally, the reported weight of the micelles from literature results in a radius of 3 nm:

$$
\begin{aligned}
&M_{Lecithin} = 750\,\frac{g}{mol}\\
&\rho_{Lecithin} = 1.3\,\frac{g}{cm^3}\\
&V_m^{Lecithin} = 577\,\frac{cm^3}{mol}\\
&n_{micelle} = 1.24 * 10^{-22} mol\\
&V_{micelle} = \frac{4}{3}\pi r^3 = 72\ nm^3\\
&r_{micelle} = 3nm.
\end{aligned}
\tag{S4.11}
$$

Notably, this diameter does not include the solvation shell of the micelles and is completely derived from theoretical / literature values. Therefore, this value fits reasonably well to the obtained diameter from the fits (*cf.* **Table S4.4** and **Table S4.5**).

Lastly, the fit was extended to contain an aggregation contribution of the NCs (evident from **Figure S4.5**, SAXS measurement) and the absence of distinct features in SAXS. Effectively, the intensity was modelled by:

$$I_{ges}(q) = I_{NC}^{free} + I_{NC}^{agg} + I_{micelle} + I_{OZ} + I_{bkg}. \tag{S4.12}$$

Therein I_{NC}^{free} and I_{NC}^{agg} is the scattering from dispersed and aggregated NCs.

The contribution of aggregated NCs is explicitly fitted by a mass fractal structure factor, for which the NCs dimensions of the free and aggregated NCs, *i.e.*, the size and heterogeneity as well as scattering length densities, were held fixed. The mass fractal structure factor is given by: [125]

$$S(q) = 1 + \frac{D_f}{r_0^{D_f}} \int_0^{\infty} r^{D_f - 3} \exp\left[-\left(\frac{r}{\xi_f}\right)^{\alpha}\right] \frac{\sin(qr)}{qr}\, r^2 dr, \tag{S4.13}$$

with the radius of the individual NC r_0, the cut-off characteristic length of the fractal correlations ξ_f, fractal dimension D_f, and fractal exponent α. The fractal dimension for diffusion-limited cluster aggregates was assumed and set to be 1.8. [125]

Table S4.6: Fitting parameters of the last iteration. $^{\Delta}$ Fitted size distribution. * Sizes obtained *via* SEM. σ^2 is the variance of the fit.

Model 2: Core-shell sphere (σ^2 = 0.009)				
Contribution	Parameter	Unit	Fitted	Value
Core-shell NC	N	cm^{-3}	Yes	$7.02 \cdot 10^{-32}$
	r_{core}	nm	No	$4.125 \pm 0.74^{*\,\Delta}$
	$r_{core} + t$	nm	No	6.125^{*}
	ΔSLD_{core-0}	cm^{-2}	No	$3.589 \cdot 10^{10}$
	ΔSLD_{lig-0}	cm^{-2}	No	$4.831 \cdot 10^{10}$
	R_{HS}	nm	No	6.125
	f_p	n.a.	Yes	0.24
NC Aggregates	N	cm^{-3}	Yes	$3.37 \cdot 10^{-32}$
	r_{core}	nm	No	$4.125 \pm 0.74^{*\,\Delta}$

Continuation Table S4.6: Fitting parameters of the last iteration. $^{\Delta}$ Fitted size distribution. * Sizes obtained *via* SEM. σ^2 is the variance of the fit.

	$r_{core} + t$	nm	No	6.125 *
	ΔSLD_{core-0}	cm^{-2}	No	$3.589 \cdot 10^{10}$
	ΔSLD_{lig-0}	cm^{-2}	No	$4.831 \cdot 10^{10}$
	r_0	nm	No	6.125
	ξ_f	nm	Yes	33.5
	D	n.a.	No	1.8
	α	n.a.	No	2.2
Spherical micelles	N	cm^{-3}	Yes	$1.16 \cdot 10^{-30}$
	$r_{micelle}$	nm	Yes	6.2 ± 2.1
	ΔSLD_{lig-0}	cm^{-2}	No	$4.831 \cdot 10^{10}$
	R_{HS}	nm	Yes	6.23
	f_p	n.a.	Yes	0.09
Ornstein-Zernike	$I(0)$	cm^{-1}	Yes	209.95
	ξ_{OZ}	Å	Yes	951
Background	I_{bkg}	cm^{-1}	Yes	2.28

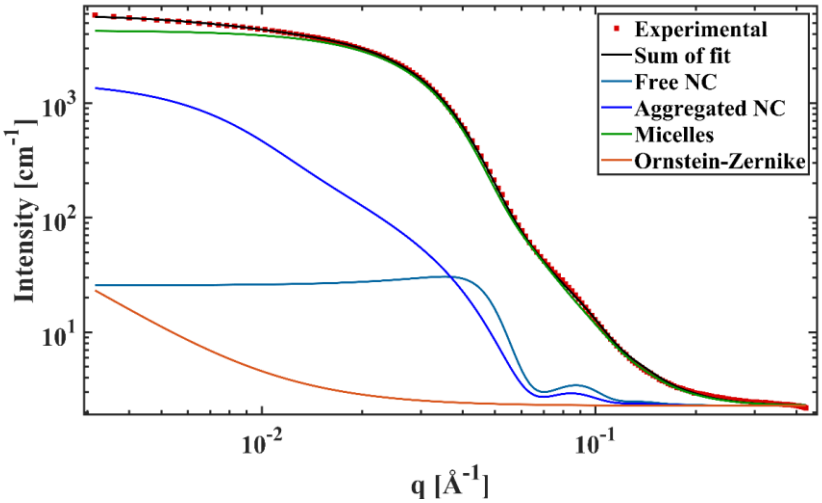

Figure S4.8: Fitting results upon considering NC aggregation and free NCs as well as micelles. The NCs are fitted by two contributions, free (light blue) and aggregated (dark blue) NCs. The micelle contribution is depicted in green, and the Ornstein-Zernike contribution in orange.

Fitting showed the formation of clusters with a size of ~32 nm, this is in good agreement with the DLS results showing a cluster species with a size of roughly 30 nm (*cf.* supporting information section S6). From the number densities it was found that 32 % of NCs are aggregated as clusters.

The above-described fitting model was additionally applied to the SAXS data to check the consistency of the model. The results are summarized in **Table S4.7**. Within this fit only the number densities and volume fractions of the scatterers are used as parameters, all other quantities are held fixed.

Table S4.7: Fitting parameters of SAXS fitting. $^{\Delta}$ Fitted size distribution. * Sizes obtained *via* SEM. σ^2 is the variance of the fit.

Model 2: Core-shell sphere (σ^2 = 58.924)				
Contribution	Parameter	Unit	Fitted	Value
Core-shell NC	N	cm^{-3}	Yes	$1.18 \cdot 10^{-33}$
	r_{core}	nm	No	$4.125 \pm 0.74^{*\,\Delta}$
	$r_{core} + t$	nm	No	6.125^{*}
	ΔSLD_{core-0}	cm^{-2}	No	$6.1891 \cdot 10^{10}$
	ΔSLD_{lig-0}	cm^{-2}	No	$3.485 \cdot 10^{10}$
	R_{HS}	nm	No	6.125
	f_p	n.a.	Yes	0.165
NC Aggregates	N	cm^{-3}	Yes	$3.22 \cdot 10^{-34}$
	r_{core}	nm	No	$4.125 \pm 0.74^{*\,\Delta}$
	$r_{core} + t$	nm	No	6.125^{*}
	ΔSLD_{core-0}	cm^{-2}	No	$6.1891 \cdot 10^{10}$
	ΔSLD_{lig-0}	cm^{-2}	No	$3.485 \cdot 10^{10}$
	r_0	nm	No	6.125
	ξ_f	nm	No	33.5
	D	n.a.	No	1.8
	α	n.a.	No	2.2
Spherical micelles	N	cm^{-3}	Yes	$1.86 \cdot 10^{-32}$
	$r_{micelle}$	nm	No	6.2 ± 2.1
	ΔSLD_{lig-0}	cm^{-2}	No	$3.485 \cdot 10^{10}$
	R_{HS}	nm	No	6.23
	f_p	n.a.	Yes	0.177
Ornstein-Zernike	$I(0)$	cm^{-1}	No	209.95
	ξ_{OZ}	Å	No	951
Background	I_{bkg}	cm^{-1}	Yes	26.1

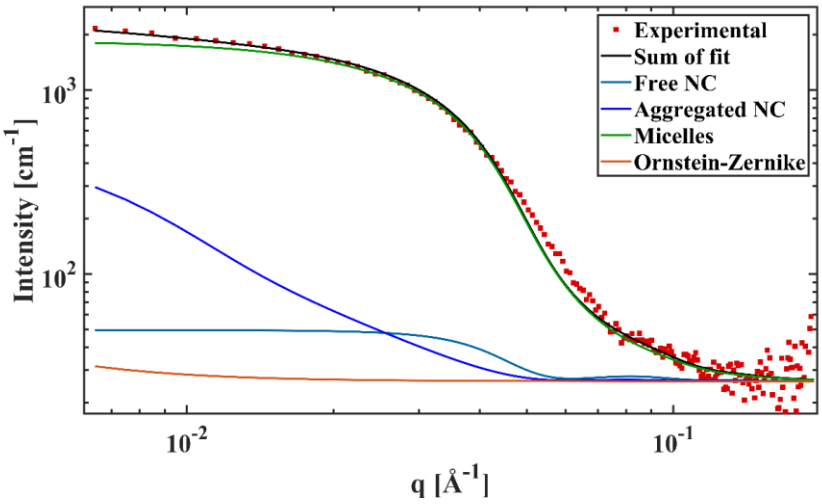

Figure S4.9: SAXS fitting results with the contributions explicitly shown. The contributions of the NCs are given in light and dark blue for the free and aggregated NCs, respectively. The micelles are depicted in green and the Ornstein-Zernike contribution in orange.

Overall, the applied model fits the measured SAXS data very well, the large variance of the fit probably originates in the large noise of the signal at large *q*. From fitting the amount of aggregated NCs is found to be 21 %, which differs from the findings in SANS still can be considered in reasonable range. This is due to the larger variance of the fit and the SAXS fit is not perfect in all regions of the data.

To further cross check the obtained results, a fit was carried out without the micelles to check if the aggregates are able to describe the intensity decay (**Figure S4.10**). During this fit, the number densities, volume fractions, and cluster sizes were used as fitting parameters. Only the NC dimensions were held fixed.

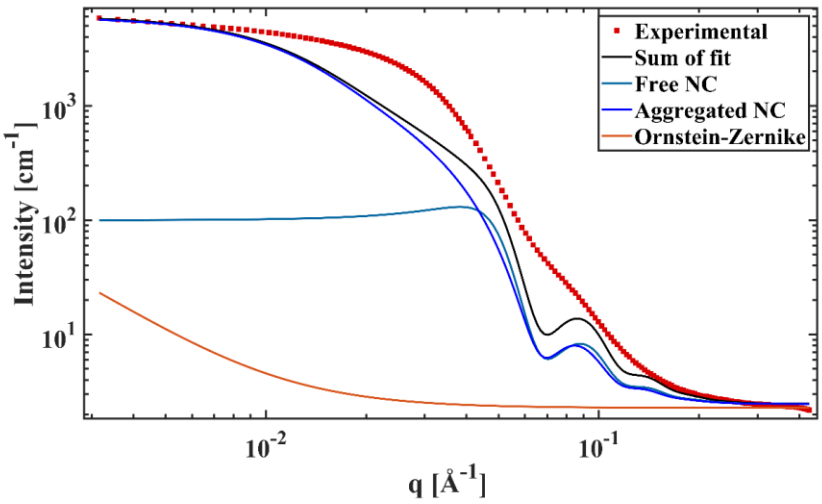

Figure S4.10: Fitting without spherical ligand micelles, the explicit contributions are shown. The NCs are again modelled as free (light blue) and aggregated (dark blue) species.

From this fit it can be seen that only applying aggregates and free NCs the intensity curve cannot be approximated, therefore lecithin micelles are highly likely to be present in the sample. As the sample is a washed, as-synthesized one, the number density of micelles in samples with excess ligand must be larger than in this case.

S4.3: Fitting of the QENS Data

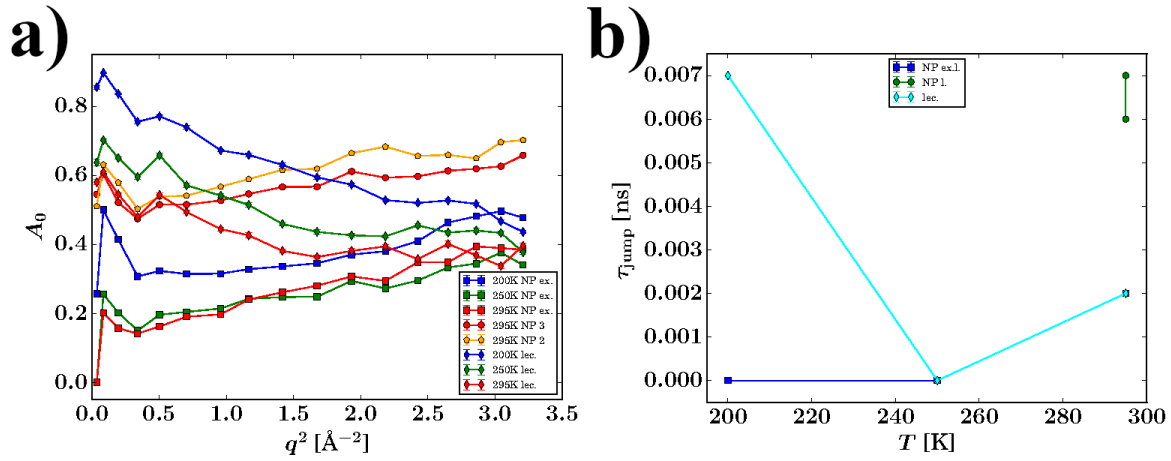

Figure S4.11: a) The elastic incoherent structure factor (EISF) resulting from the fitting model utilized in the main text that averages over the lecithin micelle and lecithin/NC contributions but allows for a free fit of the EISF (model (1)a below). The lecithin reference sample shows a strictly monotonic decay, whereas this changes when the NCs are present, where no such decay can be observed. This unphysical EISF for the mixture samples is assumed to be a result of taking the average. b) Fitted jump times of the samples discussed in the main text. The jump times at different temperatures for all samples are given, namely the as-synthesized, excess lecithin, and lecithin reference sample.

Data Reduction

Reference measurements of an empty sample holder (Aluminium sample holder sealed with an Indium ring), the empty cryofurnace and a Vanadium standard (foil inside a cylinder) were carried out on IN16B/BATS. Standard data reductions to account for the channel-dependent incident flux measured by a monitor device, for background scattering and detector efficiencies were carried out. The data were converted from the time-of-flight and scattering angle to a dynamic structure factor $S(q,\omega)$ as shown in **Equation (4.4)** of the manuscript, using the software package Mantid (www.mantidproject.org), and the as obtained data was then fitted using python as discussed below. The python scripts involved scipy.curvefit for the fitting, employing an analytical convolution of the model with the Gaussian energy resolution function using Voigt functions, based on code derived from github.com/seydel/QENS_utilities.

Fitting

The fitting procedure started with the pure solvent (d_8-toluene) spectra, which included the Lorentzian function $L(\gamma_{tol})$ due to the presence of the solvent, an elastic contribution of the sample container as well as a sloped affine background. This procedure was carried out for all q-values independently. From here on these solvent fit parameters were held fixed for the subsequent fitting steps. The intensity of the solvent contribution was scaled according to the excluded volume by the added components. This value is accessible *via* the concentrations of both additions as described in the

nanocrystal characterization of the main text and section S1. Subsequently, the pure lecithin reference sample was fitted for all momentum transfer values simultaneously. In this fit, 2 Lorentzian contributions to the line broadening were assumed, namely the center-of-mass and lateral diffusion broadenings. Lastly, the NC containing samples were fitted by fixing the solvent and, optionally, pure lecithin contributions, by following different approaches:

1) An averaging model (**Equation (S4.14)**), where the lecithin contributions were averaged over the lecithin bound to the NCs, the lecithin in vesicles, and free lecithin. This average is based on the assumption that the various lecithin species cannot be further distinguished, and that most lecithin is subject to a change in the diffusive dynamics in the presence of the NCs. The equation below reports the above model prior to the convolution with the spectrometer resolution function, without the container contribution and without the background:

$$S(q,\omega) = \beta(q)\{A_0(q)L(\gamma) + (1 - A_0(q))L(\gamma + \Gamma)\} + \beta_{tol}(q)L(\gamma_{tol}) \quad \text{(S4.14)}$$

Therein, $\beta(q)$ is a scalar parameter that corresponds to the thermal Debye-Waller factor of the sample, $A_0(q)$ is the Elastic Incoherent Structure Factor (EISF), $\beta_{tol}(q)$ is the scaling factor for the d-toluene solvent contribution and the L denote Lorentzian functions with q-dependent widths. This model (**Equation (S4.14)**) was fitted in two variants:

   1) a) In one variant of this model, the q-dependence of the EISF $A_0(q)$ in **Equation (S4.14)** was left free in the fit, resulting in unphysical average EISFs for the NC-containing samples (**Figure S4.11 a**).

   1) b) In another variant of this model, the EISF $A_0(q)$ in **Equation (S4.14)** was imposed according to **Equation (S4.16)** with the q-independent scalar fit parameters p, f, and R.

2) A model in which 2 distinct lecithin species are allowed (**Equation (S4.15)**). Therein, to reduce the number of fit parameters for a feasible fit, (i) an EISF as in model 1(b) above (**Equation (S4.16)**) was imposed for each species, and (ii) the Lorentzian widths and EISF for the first species were fixed from the fit result for the pure lecithin solutions. This model accounts for separate populations of NCs and Lecithin vesicles with their distinct center-of-mass diffusion coefficients. Along both the NC and vesicle surfaces, the Lecithin may undergo a separate lateral diffusion process (described in section S4 and the main text). The equation below reports the above model prior to the convolution with the spectrometer resolution function, without the container contribution and without the background. Therein, the scalar fit parameter r accounts for the ratio between the lecithin-vesicle and lecithin-NC species. $A_0(q)$ denotes the second EISF associated with the second species.

$$\begin{aligned} S(q,\omega) = {} & \beta(q)r\{A_0(q)L(\gamma_0) + (1 - A_0(q))L(\gamma_0 + \Gamma_0)\} \\ & + \beta(q)(1 - r)\{A_1(q)L(\gamma_1) + (1 - A_1(q))L(\gamma_1 + \Gamma_1)\} \\ & + \beta_{tol}(q)L(\gamma_{tol}) \end{aligned} \quad \text{(S4.15)}$$

For the models 1(b) and (2), the functional form of the EISF for each population is imposed as:

$$A_i(q) = f_i exp\left(-R_i^2 q^2\right) + p_i. \tag{S4.16}$$

Therein the index i denotes the respective lecithin species in the model (**Equation (S4.15)**), fi, R_i, and p_i are scalar fit parameters. Therein, p is the fraction of immobile scatterers within the instrument resolution, and R the average mean free path of confined diffusion,

For both models and all populations, the q-dependences of the 2 Lorentzian widths are imposed as:

$$\begin{aligned} &\Gamma_i = D_i q^2 \text{ , } i.e.\text{, Fickian diffusion for the center-of-mass diffusion, and} \\ &\Gamma_i = \frac{D_{jump,i} q^2}{(1+D_{jump,i} q^2 \tau_i)}\text{, } i.e.\text{, jump diffusion for the lateral lecithin diffusion} \end{aligned} \tag{S4.17}$$

These fitting procedures were carried out for each temperature separately. We remark that none of the above models explicitly accounts for the association or dissociation equilibrium dynamics of the lecithin from the NC surfaces. However, at present, we do not know if this equilibrium dynamics falls within the approximately 10 ps to 1 ns time scale accessed by our QENS experiment.

S4.4: Alternative fitting model with fewer degrees of freedom

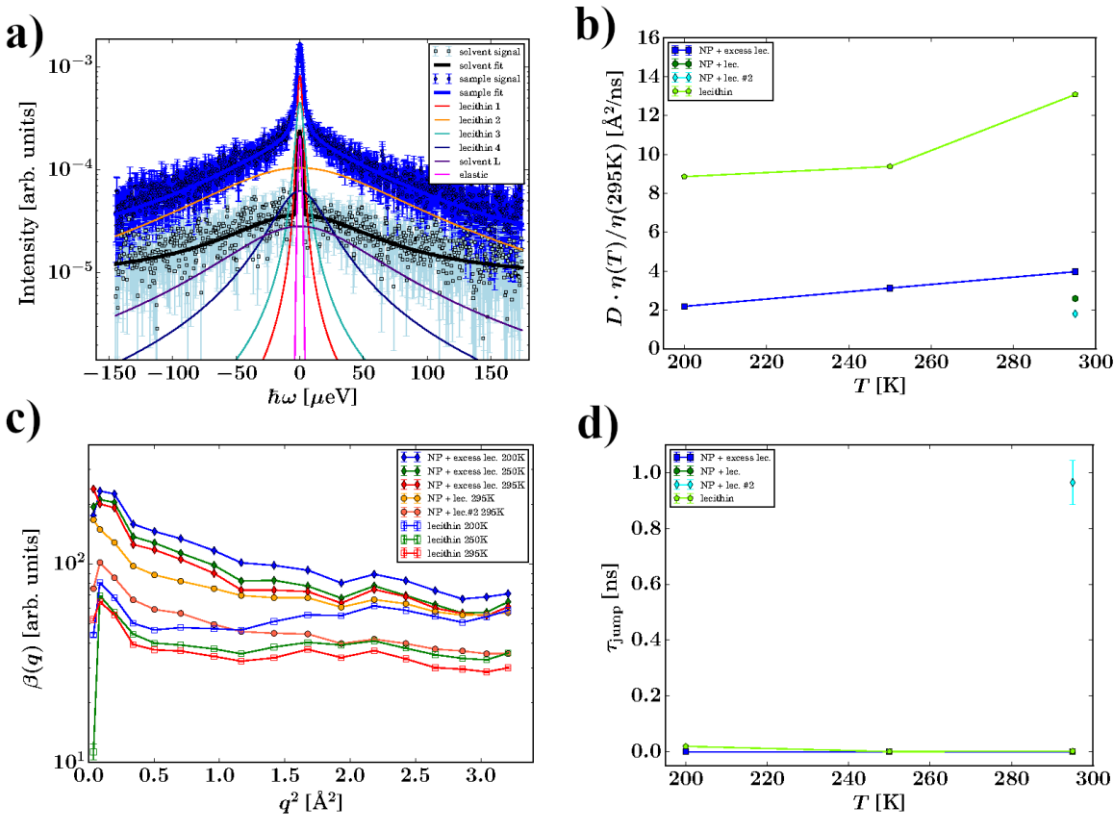

Figure S4.12: Fit results of the QENS model (2) explained on the previous page assuming two distinct lecithin species. a) The contributions obtained from the model (lines) and experimental data for an example at one momentum transfer and T = 298 K. The broadening contributions are given in the main text. b) Results for the center-of-mass diffusion coefficient within this model, obtained by utilizing **Equation (4.5)** in the main text. c) The apparent Debye-Waller factor for a variety of samples at different temperatures. d) The jump time for the lateral diffusion. Notably, one of the NC reference samples shows a significantly higher jump time.

The general fitting procedure for the alternative models (1)b and (2) was the same as for the model (1)a described in the main text. However, as stated in the section above some additional fitting parameters were kept fixed, *viz* the *q*-dependence of the EISF according to **Equation (S4.16)**. This resulted in a physically meaningful elastic incoherent structure factor compared to the averaging model (1)a from the main manuscript. Additionally, the results for the center-of-mass diffusion are comparable to the results of the other fit as shown in **Figure S4.12 b**. However, despite showing a meaningful EISF and apparently reasonable diffusion coefficients some possible inconsistencies occurred. Especially the consistency of the jump time fitting was questionable. The results for this value are shown in **Figure S4.12 d** and upon comparing the jump times for two similar washed NC samples we found a significant difference. Both samples should exhibit roughly the same values, but one sample shows an increased jump time by orders of magnitude.

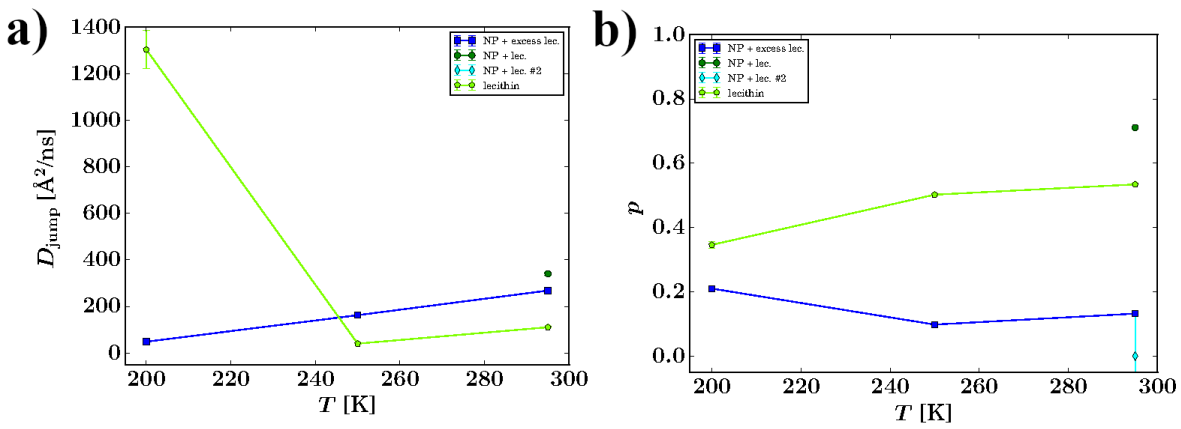

Figure S4.13: Detailed analysis of the fitting results obtained by applying the alternative model. a) The results of the lateral diffusion coefficient. b) The ratio of tightly and weakly bound lecithin *p*, which was calculated from the 2 distinct contributions from QENS fitting. Note: The *p* value is the reciprocal value of the equilibrium constants depicted in Figure 5.

This led us to further analyze the obtained values of the fit and compare them to independently measured values, which were obtained from other experiments. Firstly, the trend of the lateral diffusion for the lecithin reference showed a non-physical behavior of the temperature dependence, *i.e.*, the lateral diffusion at the lowest temperature is significantly larger than at higher temperatures (**Figure S4.13 a**). Typically, this value should be lower, because the movement of the ligand must be hindered at lower temperatures. Secondly, the ratio of tightly and weakly bound lecithin from QENS (**Figure S4.13 b**) can be compared to the values obtained from NMR. From NMR we find ratios of 0.59 and 0.71 for the washed and excess ligand samples, respectively (*cf.* **Figure 4.5** of the main text). This does not fit to the obtained results from the fit within the framework of model 2. Additionally, we again found a large discrepancy between the two similar washed NC samples, which should not occur.

These findings led to the conclusion, that the fitting model with higher degrees of freedom, *i.e.*, averaging over the lecithin species, is more suitable than the one discussed in this section.

S4.5: Temperature dependent viscosity of d_8-Toluene

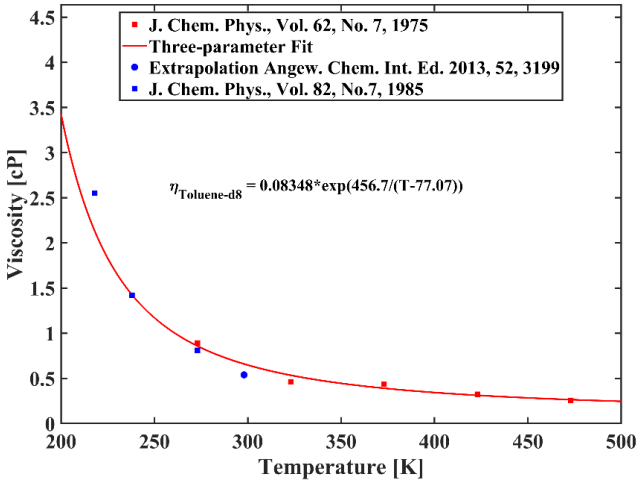

Figure S4.14: Temperature dependent viscosity of deuterated toluene. Data from literature is given as red and blue dots and the conducted three-parameter fit, as shown in **Equation (S4.18)**, is given as a solid red line.

$$\eta = A \cdot \exp\left(\frac{B}{T - C}\right) \tag{S4.18}$$

With the viscosity η, free fitting parameters A, B, C, and temperature T. Data from literature was taken to apply a three-parameter fit to the temperature dependency of deuterated toluene. [308–310]

S4.6: Dynamic light scattering (DLS) and aging after air exposure

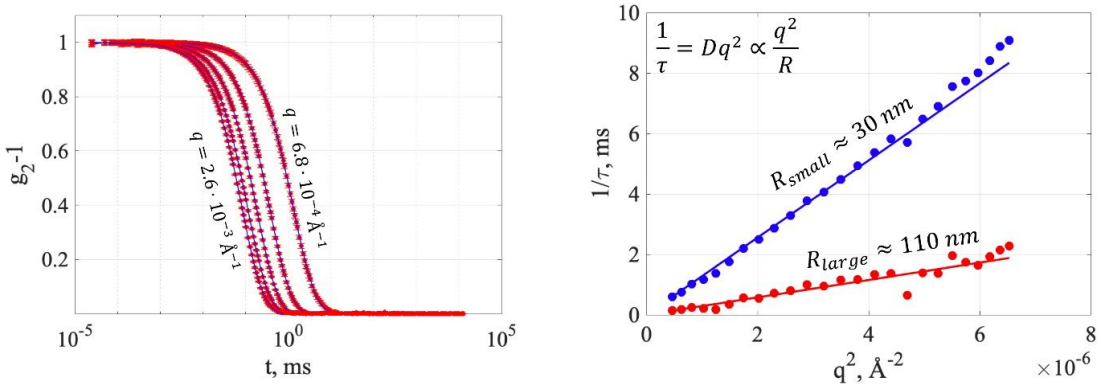

Figure S4.15: DLS measurements of a sample which was kept under air. a) Autocorrelation function at different q-values, with the maximum values given for the lowest and highest value.[§§] b) Fits of the decay times for 2 different samples. Both samples show differently sized aggregates.

To investigate the aging behavior of the samples, DLS measurements were conducted and the autocorrelation function g_2 was fitted with an exponential decay and the result was analyzed with the help of the Stokes-Einstein equation (**Equation (4.6)** of the main text). It was found that, when stored under air, the nanocrystals are aggregating, therefore, all samples were kept under nitrogen until completion of the experiments.

[§§] Remark from the author: Shown is the second order autocorrelation function $g^2(q,\tau) - 1 = \frac{\langle I(t)I(t+\tau)\rangle}{\langle I(t)\rangle^2} - 1 = \beta \exp(-2q^2 D\tau)$.

5. Porphyrin-Functionalization of $CsPbBrI_2/SiO_2$ Core-Shell Nanocrystals Enhances the Stability and Efficiency in Electroluminescent Devices

***Jan Wahl**, Manuel Engelmayer, Mukunda Mandal, Tassilo Naujoks, Philipp Haizmann, Andre Maier, Heiko Peisert, Denis Andrienko*, Wolfgang Brütting*, Marcus Scheele**

J. Wahl, P. Haizmann, Dr. A. Maier, Prof. Dr. H. Peisert, Prof. Dr. M. Scheele
Institute of Theoretical and Physical Chemistry, Eberhard-Karls University of Tübingen, 72076 Tübingen, Germany
E-Mail: marcus.scheele@uni-tuebingen.de

Prof. Dr. M. Scheele
Center for Light-Matter Interaction, Sensors & Analytics $LISA^+$, Eberhard-Karls University of Tübingen, 72076 Tübingen, Germany

M. Engelmayer, T. Naujoks, Prof. Dr. W. Brütting
Institute of Physics, University of Augsburg, 86135 Augsburg, Germany
E-Mail: bruetting@physik.uni-augsburg.de

Dr. M. Mandal, Dr. D. Andrienko
Max Planck Institute for Polymer Research, 55128 Mainz, Germany
E-Mail: denis.andrienko@mpip-mainz.mpg.de

Keywords

Perovskites, Ligand Exchange, Electroluminescence, LEDs, Porphyrins, Nanocrystals

This chapter is based on the publication published in Advanced Optical Materials: Adv. Optical Mater. 2022, 10, 2101945, DOI: 10.1002/adom.202101945.

ArXiv Preprint: https://doi.org/10.48550/arXiv.2109.05501

5.1. Abstract

Surface ligand exchange on all-inorganic perovskite nanocrystals of composition $CsPbBrI_2$ reveals improved optoelectronic properties due to strong interactions of the nanocrystal with mono-functionalized porphyrin derivatives. The interaction is verified experimentally with an array of spectroscopic measurements as well as computationally by exploiting density functional theory calculations. The enhanced current efficiency is attributed to a lowering of the charging energy by a factor of 2–3, which is determined by combining electronic and optical measurements on a selection of ligands. The coupled organic-inorganic nanostructures are successfully deployed in a light emitting device with higher current efficacy and improved charge carrier balance, magnifying the efficiency almost fivefold compared to the native ligand.

5.2. Introduction

Lead-halide perovskite-based light-emitting devices (LEDs), both all-inorganic (*e.g.*, $CsPbX_3$; X=Cl, Br, I) and hybrid (*e.g.* $MAPbX_3$; MA = methylammonium) variants, recently made significant advances with regards to efficiency. [311,312] Perovskite nanocrystals (NCs) are particularly promising for realizing LEDs due to their unique properties. Specifically, the large surface area of NCs offers numerous possibilities for functionalization with a variety of surface ligands. Therefore, a major challenge towards advancing nanocrystal-based LEDs is the search for a suitable functionalization. A suitable ligand can modify the NCs, and *vice versa*, in a variety of ways, which can be exploited to prepare novel materials that fit specific needs. This has previously been shown on well-characterized nanoparticle systems and is providing the foundation of the present work, which focuses on the enhancement of the optoelectronic properties by exchanging the native ligand shell with porphyrin-based ligands. [31,32,218,313] In the case of perovskite nanocrystals, a ligand exchange is inherently difficult due to the instability of the particles against polar environments. However, it holds the potential of improving crucial parameters like conductivity, stability and device efficiency. [311] In practice, this is realized by introducing a ligand with a higher binding affinity to the surface, which can lead to more stable NCs. [24] Additionally, the electronic coupling between NC and ligand can be adjusted and subsequently used to modify the optoelectronic properties at the interface. [22,32,218] Following this rationale, we introduce a series of novel surface ligands, *i.e.,* the semiconducting 5-monocarboxyphenyl-10,15,20-triphenylporphyrin and its metalated analogs, in an attempt to improve both stability and current efficiency. Porphyrins have already shown improved efficiency in perovskite-based light harvesting devices as an intermediate layer, which makes them a suitable candidate for functionalized hybrid materials. [314,315] Here, we investigate how this surface ligand

affects key parameters of $CsPbBrI_2$ NC-based LEDs, namely the current efficacy and turn-on voltage. To this end, we demonstrate how exchange with this porphyrin surface ligand becomes possible without deteriorating the perovskite nanocrystal. We show the effects of the porphyrin on the absorption, fluorescence, and electrical transport in macroscopic thin films of the exchanged NCs and find a significant suppression of parasitic ionic transport, an increased crystal phase stability, reduced fluorescence lifetime as well as bright and narrow electroluminescence at 650 nm. In LEDs, these $CsPbBrI_2$ NC/porphyrin hybrid materials exhibit improved current efficacies, which we attribute to a reduction of exciton quenching and an improved charge carrier balance.

5.3. Results and Discussion

5.3.1. Structure and Core-Shell Synthesis

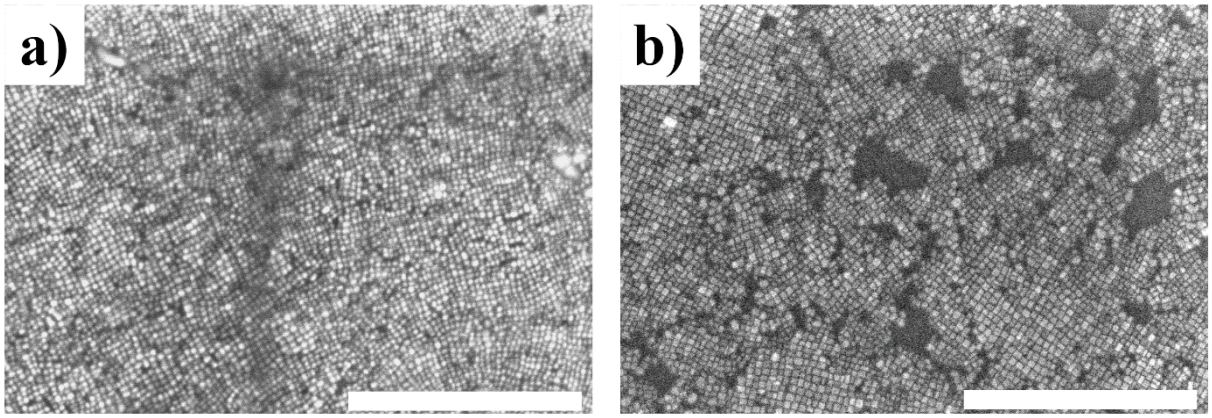

Figure 5.1: SEM micrographs of $CsPbBrI_2$ nanocrystals showing the preservation of the structural integrity during the preparation and ligand exchange processes. a) Untreated NCs without inorganic shell, and b) after the shell synthesis and ligand exchange with mZnTPP. Scale bars correspond to 500 nm.

We find that exchange with ligands bearing polar functional groups on perovskite NCs is inherently difficult. To overcome this, we synthesized a silica shell (SiO_x) around the perovskite core to enhance its stability (Details in **Figure S5.3**). [93] To monitor the particle and superstructure morphology during the preparation process, SEM and AFM measurements were taken before and after the shell growth, which displayed homogeneous, well-defined thin films with a thickness of ~15–19 nm, corresponding to approximately one monolayer of NCs. By comparing the micrographs before and after the shell growth, we find an increase of the particle diameter from d_0 = 8.9±1.2 nm to d_1 = 10.9±1.4 nm. This suggests that a silica shell with a thickness of approximately 1 nm was synthesized (**Figure S5.1 a – b**). Further micrographs, size distributions and spectroscopic analyses are given in the SI (**Figure S5.1 and S5.3**). The expected improvement in stability is especially beneficial for the functionalization with a polar ligand, like metal-(5-monocarboxyphenyl-10,15,20-triphenylporphyrin) (mMTPP, see

Figure 5.2 b). The semiconducting character and interaction as an intermediate layer in perovskite devices predestine this porphyrin as a promising surface ligand. [314,315] After functionalization with the organic semiconductor, no apparent changes in morphology could be observed as the particles kept their cubic shape and size (**Figure 5.1 b**), indicating that the ligand preserves the structural integrity. The nearest neighbor distance did not change during the SiO_x-shell synthesis nor during the ligand exchange. In the following all characterization methods were carried out on core-shell NCs, except DFT calculations, which were done without consideration of the shell due to a lower time effort as well as the fact that the exact structure, homogeneity and coverage of the silica shell is unknown.

5.3.2.Ligand Exchange

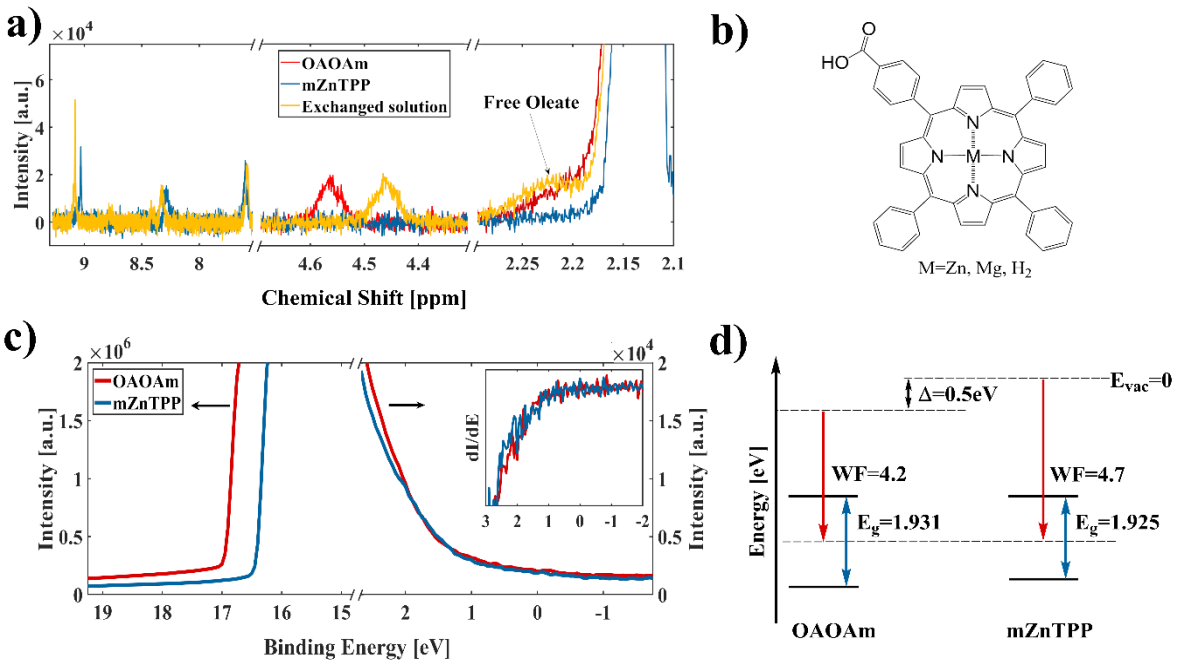

Figure 5.2: a) NMR analysis of the ligand exchange with mZnTPP. Shown are the regions for the characteristic porphyrin (7.5–9 ppm), amide proton (4.4–4.6 ppm) and the caesium oleate (2.2–2.25 ppm) peaks. b) Structure of the metal-(5-monocarboxyphenyl-10,15,20-triphenylporphyrin) derivatives described throughout this work. c) UPS of thin films before (blue) and after (red) ligand exchange. The inset displays the derivative. d) Corresponding electronic structure of the films, shown are the work functions (red) and band gap energies (blue). The values are referenced against the instrument Fermi level. Overview spectra of the NMR and UPS measurements can be found in **Figure S5.4 and S5.5**.

The solution-based ligand exchange with different mMTPP derivatives (**Figure 5.2 b**) was monitored by NMR (**Figure 5.2 a**). Conveniently, a peculiarity of the iodide containing perovskites is the catalysis of amide formation, [300] which we use here to monitor the exchange. The characteristic amide peak at ~4.6 ppm experienced a clearly visible upfield shift, which is commonly attributed to a

detachment of the native ligand. [191] Additionally, a downfield shift for the proton peaks in the characteristic porphyrin region (7.5–9 ppm) suggests successful binding of the desired ligand.

Since mMTPP is significantly more polar than oleic acid (OA) and oleylamine (OAm), the surface dipole moment is expected to change upon introducing the novel ligand, hence shifting the absolute energy levels depending on the strength and orientation of said dipole moment. [218] Generally, a reduction of the surface dipole, *i.e.*, if it is (partially) lowered by the attached ligand, the energy levels of the NC are shifted to lower energies. [218] Since mMTPP has a pronounced π-system and an asymmetric functionalization, it provides an intrinsic dipole moment. This dipole is directed contrary to the surface dipole moment of the NCs and is thus able to partially compensate it. We find a shift of the Fermi level by 0.5 eV to lower energies in the case of mZnTPP (**Figure 5.2 c – d**), confirming the electronic interaction of the NCs and the novel ligand. In both cases, the Fermi level remained in the middle of the respective band gap, indicated by the same onset of the valence band maximum (inset of **Figure 5.2 c**), which can be understood as an indicator for preservation of the valence electronic structure.

5.3.3.Optical Properties

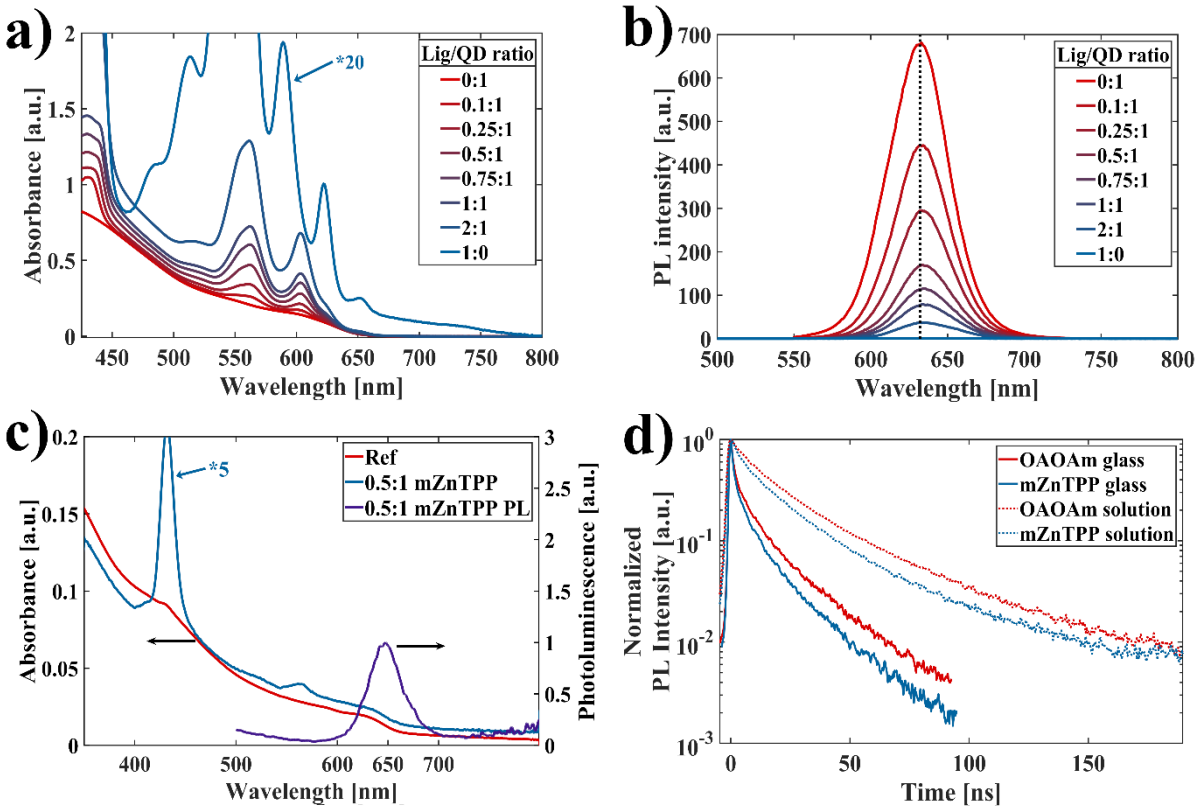

Figure 5.3: a) UV-vis and b) PL in toluene with different stoichiometric amounts of mZnTPP added. c) Solid state absorption and photoluminescence. d) Exciton lifetime measurement of native and exchanged samples in both solution and on a glass substrate.

The native $CsPbBrI_2$ sample exhibits the typical spectroscopic features for this composition and a quantum yield of ~60%. The absorption spectra (**Figure 5.3 a**) confirm the preservation of the first excitonic transition from the valence state ($1S_h$) to the conduction state ($1S_e$) of the NCs as the onset of the absorption is independent of the amount of ligand added. Nevertheless, increasing the ligand content leads to more pronounced characteristic absorption peaks, namely the Q-bands of the porphyrin. Strikingly, these bands are shifted to lower energies when compared to an isolated mZnTPP sample. This can be attributed to a pronounced interaction between the particle and ligand since porphyrins are very sensitive towards electronic changes in their periphery.

By comparison with the photoluminescence (PL) spectrum of pure mZnTPP (spectra shown in SI, **Figure S5.6**), we verify that the emission of the mixed solution originates purely from the perovskite NCs. Upon addition of mZnTPP, we observe a redshift in the emission by 6 meV and a decrease in quantum yield (QY) as indicated by the reduced emission intensity (**Figure 5.3 b**). Moreover, fluorescence lifetime measurements display 30% shorter lifetimes after ligand exchange (**Table 5.1**), indicating an enhanced interaction between particle and ligand. The redshift in the emission spectra can be explained by a spatial extension of the exciton wavefunction onto the ligand, a changed dielectric environment or a combination of both. Likewise, the shorter fluorescence lifetime can be rationalized as follows: by extending the excitonic wavefunction onto the ligand, the quantum confinement is lowered which results in decreased exciton binding energies. [316,317] The lowering destabilizes the exciton, yielding decreased PL lifetimes. This is consistent with the observed behavior in the solid state where the nearest neighbor interaction enhances the said effect, resulting in a bathochromic shift from 635 nm to 650 nm (**Figure 5.3 c**) and a further reduction of the lifetime by a factor of 2–3 (**Figure 5.3 d and Table 5.1**). Additionally, a separation of excitons can occur in the system, as the conduction state ($1S_e$) is shifted onto the ligand in the mZnTPP functionalized NCs (see **Figure 5.5 d**). Long-lived excitons can thus be split and are able to recombine non-radiatively on the ligand. Especially porphyrins are known for providing a variety of radiationless transitions. [318–320] This scenario would also invoke a decrease in lifetime and QY.

Table 5.1: Measured photoluminescence lifetimes (τ_i) of $CsPbBrI_2$ samples on glass and in solution. The values were obtained by fitting the PL decay with a triexponential function. The goodness of the fit is given as the R-squared factor (R^2).

Ligand	Solution				Solid state			
	Lifetime τ_i [ns]			R^2	Lifetime τ_i [ns]			R^2
	τ_1	τ_2	τ_3		τ_1	τ_2	τ_3	
OAOAm	2.89	13.82	39.27	0.99985	1.09	6.59	22.46	0.99971
mZnTPP	2.25	12.93	34.06	0.99983	0.84	4.80	17.34	0.99957

5.3.4.Electronic Properties

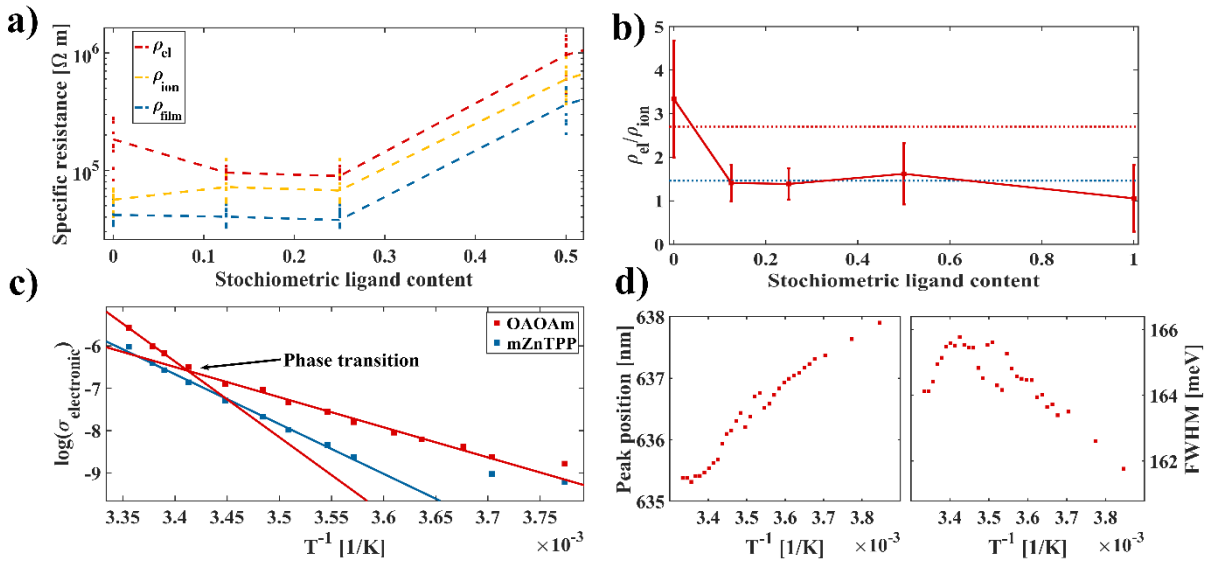

Figure 5.4: a) Specific resistances of thin films with different ligand compositions. The electronic (red) and ionic (orange) contributions to the overall ohmic resistance (blue) are shown. b) Ratio of electronic and ionic resistance at different stoichiometric values. Dotted lines represent the ratio of electronic and ionic activation energies obtained from temperature dependent conductivity measurements. c) Temperature dependence of the electronic contribution with the corresponding fitting functions. The ionic contribution is given in **Figure S5.7** d) Temperature dependent PL measurements. Position (left) and FWHM (right) of the PL peak in dependence of temperature.

Since perovskites are both electronic and ionic conductors, both transport pathways need to be considered. This can be effectively described by a parallel connection of an electronic (ρ_{el}) and ionic resistance (ρ_{ion}). [321,322]

$$\frac{1}{\rho_{film}} = \frac{1}{\rho_{el}} + \frac{1}{\rho_{ion}} \tag{5.1}$$

To derive ρ_{el} from **Equation (5.1)**, the ionic part has to be eliminated. Since the ionic contribution behaves like a capacitor, it can be saturated by a potentiostatic measurement, *i.e.*, if a constant voltage over a prolonged period of time is applied. By combining a standard current-voltage curve to obtain the film resistance (ρ_{film}) and the potentiostatic measurement for ρ_{el}, the specific resistances with varying ligand content were analyzed (**Figure 5.4 a**). The resistance of the system increases dramatically if 0.5 or more equivalents of mZnTPP are added. The most probable reason is a saturation of the NC surface and the allocation of free, excess ligand between the particles. At lower stoichiometric additions, the ratio ρ_{el}/ρ_{ion} decreases, while the overall film resistance stays constant (**Figure 5.4 b**). To validate these findings and further explore the conduction mechanism, temperature dependent conductivity measurements were carried out. The results were fitted using an Arrhenius type nearest neighbor hopping (NNH) model:

$$\sigma(T) = \sigma_0 exp\left\{-\frac{E_A}{k_B T}\right\}, \tag{5.2}$$

with the conductivity σ_0, Boltzmann's constant k_B, temperature T and the hopping activation energy E_A. Upon mZnTPP-functionalization, the activation energy in the exchanged system was reduced by over 33% for the electron hopping, whereas the energy for the ion transport did not change significantly (**Figure 5.4 c, Table 5.2, and Figure S5.7**). Which further supports our claim of improved electrical properties of the mZnTPP ligand system.

Table 5.2: Results of the Arrhenius type NNH fit of the temperature dependent conductivities. The electronic activation energy (E_A^{el}) and ionic activation energy (E_A^{ion}) were measured. In the case of the native OAOAm ligand shell the higher temperature fit was used. The ratio of the energies was compared to the measured specific resistance ratio (SRR) as shown in **Figure 5.4 b.**

	OAOAm	mZnTPP
E_A^{el} [eV]	3.56	2.34
E_A^{ion} [eV]	1.38	1.41
E_A^{el}/E_A^{ion}	2.57	1.65
ρ_{el}/ρ_{ion}	3.2	1.5

We note that the temperature-dependent conductivity of the native system cannot be described with a single linear fit, which we tentatively attribute to a phase transition at around 290 K. To verify this assumption, the PL was additionally monitored over the same temperature range (**Figure 5.4 d**). Two observations were evident, the emission peak shifted to lower energies upon cooling the sample and the full width at half maximum (FWHM) exhibited a maximum at 290K. The shift arises due to the thermal compression of the lattice and an increased interaction between lead and halides, resulting in a broadening of states at the valence band edge which reduces the size of the band gap, this is consistent with previous reports on perovskites. [161,323] Further, as the FWHM of the PL signal is phonon-dependent and typically increases with temperature $FWHM \propto exp\{E_{LO}/(k_B T)\}^{-1}$, a necessity of the decrease in broadening with higher temperature is a phase transition. Tang *et al.* have investigated the electron-phonon coupling of different perovskite phases and their temperature dependent behavior. [323] They found the energy of the longitudinal optical phonon in cubic nanoparticles to be two times larger than in the corresponding orthorhombic counterparts, therefore, a transition from predominantly cubic (T > 290 K) to orthorhombic (T < 290K) could explain the decrease of FWHM as observed in **Figure 5.4**. [56,324]

5.3.5.Charging Energy

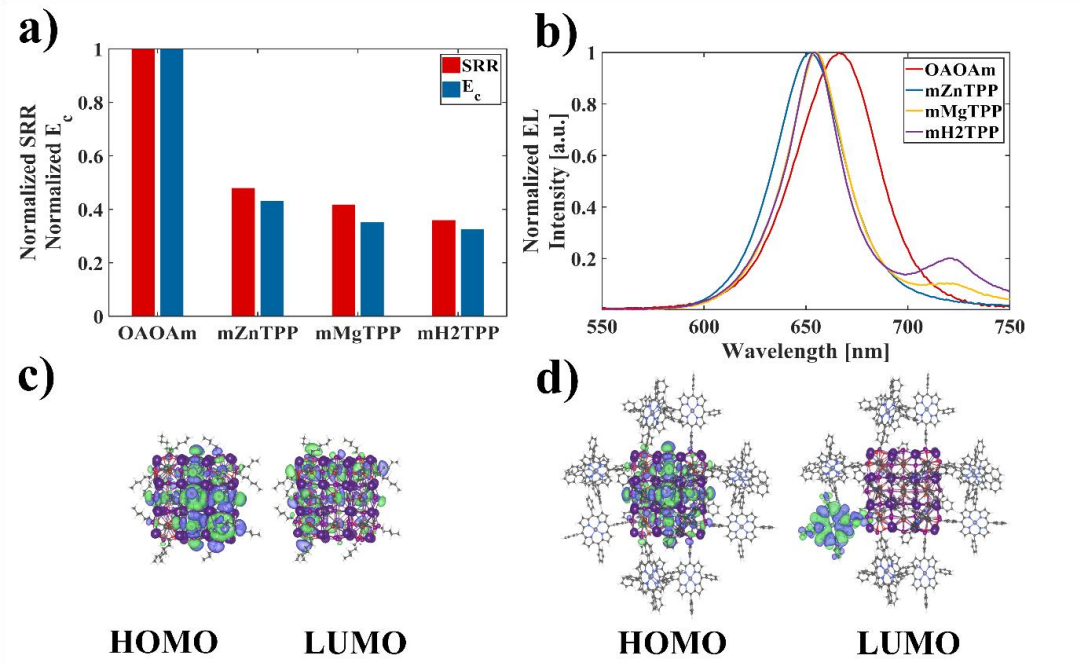

Figure 5.5: a) Normalized charging energy (E_C) and measured specific resistance ratios (SRR) for OAOAm and mMTPP (M = Zn, Mg, H_2). b) Electroluminescence spectra of devices built with differently functionalized NCs. Note that samples prepared with mMgTPP and mH2TPP exhibit parasitic emission at ~725 nm. Frontier molecular orbitals of $CsPbBrI_2$ NC decorated with c) hexanoic acid as a mimic for oleic acid and d) mZnTPP ligands.

To clarify the origin of the altered optoelectronic properties, the dependence of the conductivity on the charging energy E_C was considered, which describes the energy required to introduce charges in a nanocrystal. Following the modified Laikhtman-Wolf model E_C is defined as: [173]

$$E_C = \frac{e^2}{2(C_S + n\,C_m)}, \tag{5.3}$$

with the elementary charge e, self-capacitance C_s, number of nearest neighbors n and the mutual capacitance C_m. A more detailed derivation of the components can be found in the SI (**section S5.9**).

Table 5.3: The calculated molecular polarizabilities of the different ligands in atomic units [au], OAOAm refers to the native system, mZnTPP, mMgTPP, mH2TPP refer to the zinc, magnesium, and metal free derivative, respectively. The calculated dielectric constants as well as the charging energies **(Equation (5.3))** are shown as well.

	Polarizability [au]	**Dielectric constant**	**Charging energy [meV]**
OAOAm	~240	2.5	8.62
mZnTPP	808	4.4	4.38
mMgTPP	809	4.9	3.72
mH2TPP	797	5.1	3.49

To evaluate the main influence of the charging energy on the charge carrier dynamics, the NCs were functionalized with mMTPP derivatives. Upon comparing the measured, normalized specific resistance ratios (SRR) with the charging energy E_C of the different systems, it becomes clear that the improvement of the electronic properties follows the same trend as E_C (**Figure 5.5 a**), suggesting that the charging energy has the main influence. Quantitatively, the charging energy of the exchanged samples, displayed in **Figure 5.5 a**, is lowered by a factor of ~2.4–3 compared to the native NCs. We note that although mMgTPP and mH2TPP showed beneficial electrical properties compared to mZnTPP, such as a better SRR and lower E_C, they were found unsuitable for light emitting devices due to parasitic emission at longer wavelength (**Figure 5.5 b**).

To probe the effect of the ligand used for surface functionalization on the electronic structure of the NC/ligand hybrid system, density functional calculations were carried out (see SI, **section S5.10** for computational details). As shown briefly in **Figure 5.5 c – d**, and in the supporting information (**Figure S5.9 – S5.12**) in more detail, a significant change in the nature of the frontier orbital can be observed as a function of ligand. For the aliphatic hexanoic acid ligand we find that, both occupied and empty molecular orbitals (MOs) reside over the inorganic core (**Figure 5.5 c**). The introduction of the porphyrin ligand and its metalated derivatives, however, changes this significantly, and we see that the low-lying vacant orbitals are exclusively over the porphyrin moiety (**Figure 5.5 d**). This shift of the $1S_e$ state onto the ligand and hence reduced exciton confinement can lead to the aforementioned reduction in PL lifetime, and a decrease in surface dipole moment (compare **Figure 5.2**). Considering the porphyrin-functionalized NCs on themself, we see that in the case of the mZnTPP system, the occupied orbitals H, H–1, and H–2 (H ≡ highest occupied MO or HOMO) reside almost entirely over the NC core (**Figure S5.10**). However, the scenario changes once we switch to the other two porphyrin-based systems. Accordingly, even for the occupied MOs, we find significant density over the ligand for both the mMgTPP (see the H-1 and H-2 orbitals; **Figure S5.11**) and the mH2TPP system (refer to the H, H–1 and H–2 orbitals; **Figure S5.12**). We hypothesize that this partial extension of the occupied orbital over the ligand can contribute towards the slightly favorable optoelectronic properties of mMgTPP and mH2TPP compared to those of mZnTPP. However, we hold these high-lying, ligand-based occupied orbitals in mMgTPP and mH2TPP responsible for the parasitic emission observed near 725 nm, more so since the low-lying unoccupied orbitals, *i.e.*, the $1S_h$ state, is always located over the ligand in the porphyrin-exchanged systems.

5.3.6.Optoelectronic Devices

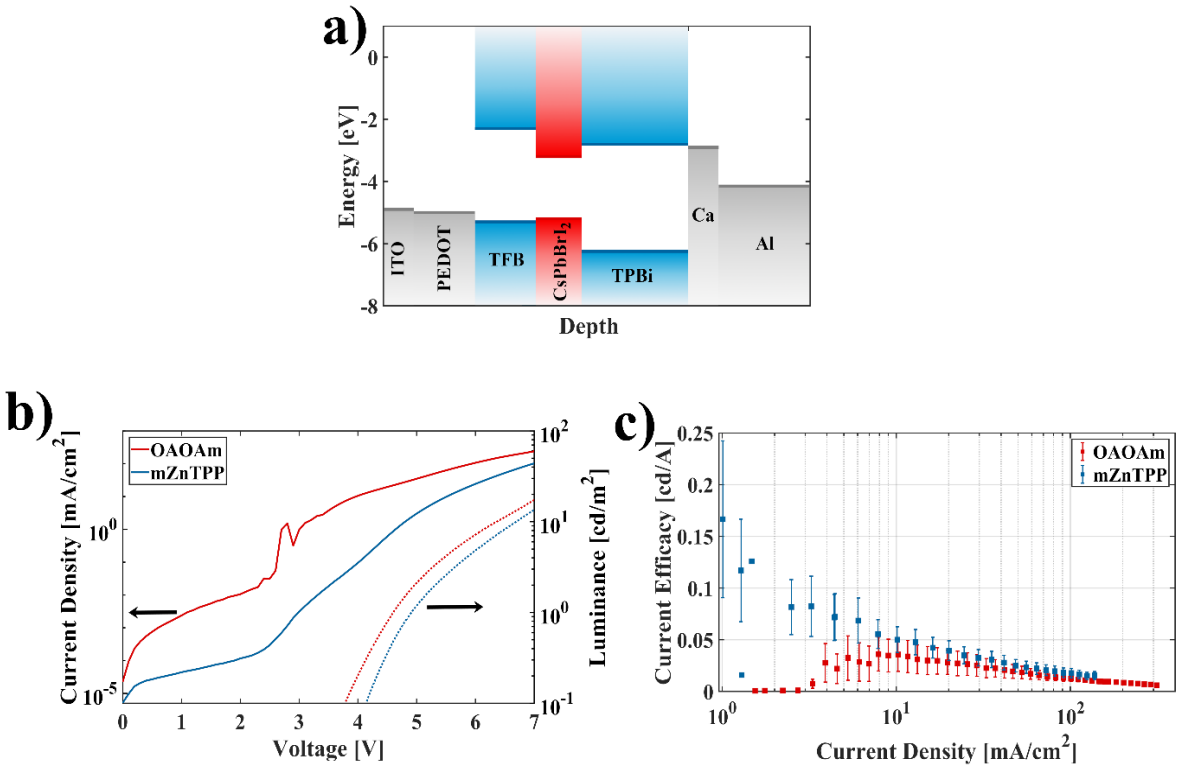

Figure 5.6: a) Typical stack design used for the characterization of $CsPbBrI_2$-based light emitting devices. b) Typical current-voltage-luminance (jVL) characterization curve, with the current density and luminance shown as a solid and dashed line, respectively. c) Measured current efficacies of native and exchanged perovskites in electroluminescent light emitting devices. The efficiency curves were obtained by averaging over five different samples, each consisting of four pixels.

The perovskite NCs with and without ligand exchange were deposited as the emitter material in the device stacks, shown in **Figure 5.6 a**, with a homogeneous perovskite NC film as an emitting layer (see AFM image in **Figure S5.13**). We obtained electroluminescent devices with a turn-on voltage of the current of ~2.5 V (**Figure 5.6 b**) and a turn-on voltage of the luminance in the range of 3–4.5 V. From this comparison, we find that the ligand exchanged NCs exhibit almost the same luminance, but at lower current densities, which results in an improved current efficacy (**Figure 5.6 c**). Overall, the peak current efficacy could be enhanced by a factor of 4.65 and the necessary current density to reach the peak efficacy was also lowered by approximately one order of magnitude. This could indicate that the ligand exchange leads to reduced quenching of excitons, *i.e.*, the injected charge carriers are not lost during injection. Additionally, we find that the maximum current efficacy for the systems was located either at the onset or at higher current densities for mZnTPP and OAOAm, respectively. A possible explanation is an improved charge carrier balance in the exchanged system. We attribute both phenomena to the lower charging energy in the porphyrin-functionalized system.

5.4. Conclusion

To summarize, we successfully performed ligand exchange with mMTPP derivatives on all-inorganic core-shell $CsPbBrI_2/SiO_x$ nanocrystals with a core size of 9 nm while maintaining the structural integrity of the particles. We found the optoelectronic properties of the system to be highly controllable with the nature and amount of ligand, suggesting significant electronic interaction between nanoparticle and ligand. This is also evidenced by a decrease of the first excitonic transition energy and photoluminescence lifetimes, where a dislocation of the $1S_e$ state onto the ligand could be identified as the main driving force. Additionally, the composition of the measured current, namely the electronic and ionic contribution, was found to be dependent on the dielectric constant of the ligand. We hold a decrease of the charging energy and the manifestation of a compensating dipole moment at the NC interface responsible for the observed smaller electrical resistance. Temperature-dependent photoluminescence measurements indicated an increased phase stability of the ligand-exchanged perovskite nanocrystals. These improvements of the optoelectronic properties could be used to prepare light-emitting devices with enhanced current efficacy.

5.5. Experimental Section

Materials: 1-Octadecene (ODE), technical grade, 90%, Sigma Aldrich; Oleic acid (OA), 97%, Acros Organics; Oleylamine (OAm), 80–90%, Acros Organics; Caesium carbonate (Cs_2CO_3), 99.99% (trace metal basis), Acros Organics; Lead(II)iodide (PbI_2), 99.999% (trace metal basis), Sigma Aldrich; Lead(II)bromide ($PbBr_2$), ≥98%, Sigma Aldrich; Tetramethyl orthosilicate (TMOS), 99%, Acros Organics; Toluene, HPLC grade, 99.8%; Toluene, 99.8%, extra dry, AcroSeal, Acros Organics; Ethyl acetate, ACS reagent, ≥99.5%, Sigma Aldrich; zinc-(5-monocarboxyphenyl-10,15,20-triphenylporphyrin) (mZnTPP), TriPorTech; magnesium-(5-monocarboxyphenyl-10,15,20-triphenylporphyrin), 98%min, PorphyChem; (5-monocarboxyphenyl-10,15,20-triphenylporphyrin), 98%min, PorphyChem; poly(3,4-ethylenedioxythiophene) polystyrene sulfonate (PEDOT:PSS) (AI4083 or CH8000), Clevios™, Heraeus Epurio; poly[(9,9-dioctylfluorenyl-2,7-diyl)-co-(4,4'-(N-(4-sec-butylphenyl)diphenylamine)] (TFB), M_W=10,000-30,000, Lumtec; 1,3,5-Tris(1-phenyl-1HBenzimidazol-2-yl)benzene) (TPBi), >99.5% (HPLC), Lumtec

Synthesis: The $CsPbBrI_2$ nanocrystals in this work are prepared by following the literature on arrested metathesis reported by Protesescu *et al.* with slight modifications. [19] In a typical synthesis, two precursors were prepared in separate flasks, one containing 203.5 mg (0.624 mmol) Cs_2CO_3 and 0.7 ml oleic acid (OA) in 10 ml octadecene (ODE). The second flask contained 116 mg (0.252 mmol) PbI_2 and 46 mg (0.125 mmol) $PbBr_2$ in 5 ml ODE, both flasks were dried under vacuum at 120 °C for 2 h. Immediately after the addition of OA to the first flask, gas evolution was observed due to the

formation of carbonic acid which decomposes to water and carbon dioxide, ultimately indicating the formation of caesium oleate. After completion of the drying process, the flasks were set under nitrogen.

The caesium oleate flask was then heated to 150 °C to ensure completion of the caesium oleate formation, visually observable by a yellow-brownish color. Before injection, said solution was cooled to 120 °C. To dissolve the lead salts, 1 ml OA and 1 ml OAm was added to the flask, the solution was heated to 160 °C after the salts were dissolved. Subsequently, 0.8 ml of caesium oleate precursor were quickly injected into the lead halide solution under vigorous stirring. After allowing the reaction to proceed for 5 s, the reaction was quenched by placing it in an ice-bath.

The purification was carried out *via* centrifugation at 4000 rpm for 12 min, the pellet was afterwards redispersed in dry toluene under nitrogen atmosphere.

The general procedure for the silica shell was based upon the procedure published for $CsPbBr_3$ particles. [93] The thickness of the as synthesized shell could be tuned by using different amounts of tetramethoxyorthosilicate (TMOS), commonly a ratio of 5:1 (TMOS:NC) was used. A 1:1 mixture of wet and dry toluene was used as a solvent, since water is the initiator for the polymerization. After 72 h reaction time, the solution was again centrifuged at 2000 rpm for 2 min to remove unwanted larger particles and agglomerates. The supernatant was subsequently transferred to a fresh vial to obtain a stable colloidal nanoparticle dispersion. If necessary, the nanoparticle dispersion was afterwards filtered with a 200 nm syringe filter.

Ligand exchange: The ligand exchange was carried out in solution by utilizing a defined solution of metal-(5-monocarboxyphenyl-10,15,20-triphenylporphyrin) (mMTPP) in toluene and adding specific volumina to the NC dispersion. Upon addition, an immediate color change was observed. The solutions, exchanged as well as native, were then used as prepared or washed with ethyl acetate (EtAc), depending on the desired analysis method. The washing step was carried out by adding 2 volumetric equivalents of EtAc to the NC dispersion followed by centrifugation. The resulting precipitate was redispersed in toluene.

Spin-coating and vacuum drying: Most characterization techniques presented in this work are carried out in thin films of the as prepared NCs. The method of choice was spin–coating under inert atmosphere. Usually, 100 µl of a ~2 мм solution (particle concentration ~0.7 µм) was casted onto a substrate (silica, gold, or device stack) and left at rest for 30 s. The substrate was spun at 600 rpm for 30 s with a ramp of 3 s. Since low spinning speeds were used, the spin-coater was repeatedly started 2–3 times after the initial 30 s to remove any residual solvent which remained at the edges. Subsequently, the substrate was placed in vacuum for 15 min for drying.

Conductivity measurements: Conductivity measurements were carried out on 15×15mm^2 silicon field-effect transistor (FET) substrates with gold contacts of different channel lengths 2.5 µm, 5 µm, 10 µm

and 20 µm obtained from the Fraunhofer IPMS, Dresden. Prior to the film preparation, the substrates were rinsed with acetone and subsequently cleaned with acetone, deionized water, and ethanol in an ultrasonic bath for 5min each. Following the film preparation, the substrates were mounted on a custom build sample holder under inert atmosphere which was connected to a Keithley 2634B SYSTEM SourceMeter® with 10^{-9} A (nA) accuracy. Temperature dependent conductivity measurements were carried out inside a Lake Shore Cryotronics CRX-6.5K Probe Station attached to a Keithley 2636B SYSTEM Source Meter® with 10^{-12} A (pA) accuracy. In a typical film characterization, custom measurement scripts were used.

Scanning electron microscopy (SEM): SEM was carried out with a HITACHI SU8030 electron microscope operating with an acceleration voltage of 30 kV.

Ultraviolet electron spectroscopy (UPS): UPS measurements were performed using a multi-chamber UHV system with a base pressure of $2 \cdot 10^{-10}$ mbar, equipped an Ultraviolet source (UVS 300 SPECS) and a Phoibos 150 hemispherical photoelectron analyzer with DLD detector. Measurements were carried out with Helium I radiation (21.22 eV). The films for UPS were prepared on silicon/silicon oxide or gold substrates.

Nuclear magnetic resonance (NMR) spectroscopy: NMR measurements were performed on a Bruker Avance III HDX 400, with a frequency of 400 MHz. Spectra are analyzed with the Bruker TopSpin 4.0.2 software and plotted with MatLab R2020.

UV-vis and photoluminescence spectroscopy (in solution and solid state): Optical measurements were performed on a UV-vis-NIR spectrometer (Agilent Technologies, Cary 5000) and a fluorescence spectrometer (PerkinElmer FL8500). Both systems contain interchangeable sample holders for measurements in solution and solid state. The fluorescence spectrometer additionally provides the possibility of absolute quantum yield measurements in an integrating sphere.

Fluorescence lifetime measurements: The samples were excited *via* a picosecond pulsed laser system (EKSPLA PT400) and measured with an Acton Spectra-Pro 2300i spectrograph coupled to a Hamamatsu Streak Camera C5680 for time-resolved spectral information.

Device characterization and current-voltage-luminance (jVL) curves: The electroluminescent devices were prepared on prestructured indium tin oxide (ITO) which was cleaned with acetone and isopropanol in an ultrasonic bath. Subsequently, a layer of poly(3,4-ethylenedioxythiophene) polystyrene sulfonate (PEDOT:PSS) was spin-coated. On top, a layer of poly[(9,9-dioctylfluorenyl-2,7-diyl)-co-(4,4'-(N-(4-sec-butylphenyl)diphenylamine)] (TFB) was applied, a solution of 5 mg/ml in chlorobenzene was spin-coated at 3000 rpm and dried at 175 °C for 30 min. The perovskite layer was prepared as described before. Above the perovskite emitters, a layer of 1,3,5-Tris(1-phenyl-1HBenzimidazol-2-yl)benzene) (TPBi) was deposited. As a top electrode, calcium and aluminium were thermally evaporated onto the sample. The substrates are divided to 4 subsections, each with an

active area of 2×2mm^2. The devices were measured in a custom-made sample box attached to a calibrated photodiode for luminance, a two-channel Keithley 2602B source-measure unit for powering the LED and probing the electrical as well as optical output, and a JETI specbos 1211 for spectroscopic measurements. Data acquisition was carried out with a custom written LabView program.

Atomic force microscopy (AFM): AFM was carried out with a Bruker MultiMode 8-HR and a Bruker Dimension Icon, the obtained images were analyzed using Gwyddion.

DFT calculations: All computations are performed using the CP2K 8.1 program suite [283] employing the PBE exchange correlation functional [284], MOLOPT [286] DZVP basis-set and GTH pseudopotentials [287] for core electrons. A dual basis of localized Gaussians and plane waves (GPW) with a 350 Ry plane-wave cutoff are used for all calculations. Grimme's DFT-D3 protocol [285] was used to account for van der Waals (VDW) interaction. SCF convergence criterion was set at 10^{-6} for all calculations. Initial geometries of $CsPbBrI_2$ nanocrystals were obtained by cutting small cubes (~1.7 nm) from the bulk, exposing the CsX layer (X = Br, I) at the surface and maintaining overall charge neutrality of the particle. [288] All calculations invoked a periodic boundary condition. However, to avoid spurious interaction with its periodic image, nanoparticles were placed inside a large box of size 75×75×75 Å^3 ensuring large vacuum layer above the surface of the NC. All structures were then optimized in vacuum using the BFGS optimizer, setting a maximum force of 5 meV Å^{-1} (1.0×10^{-04} hartree/bohr) as convergence criteria. The polarizabilities of native ligands as well as the different metal-(5-monocarboxyphenyl-10,15,20-triphenylporphyrin) derivatives was carried out at the PW91/def2-TZVP level with the ORCA software. [325] The geometries were optimized using a SCF convergence criterion of 10^{-7}.

Supporting Information

Supporting Information is available from the Wiley Online Library or from the author.

Cartesian coordinates of all computed structures can be accessed from the coordinate file (.xyz).

Acknowledgements

This work was supported by the DFG under grants SCHE1905/8-1, AN680/6-1, BR1728/21-1 (project no. 424708673) and SCHE1905/9-1. The authors would like to thank Dr. Kai Braun from the Institut für Physikalische und Theoretische Chemie, Universität Tübingen for his help with the measurements of the temperature-dependent photoluminescence spectra.

Conflict of Interest

The authors declare no conflict of interest.

5.6. Supplementary Information

Porphyrin-functionalization of $CsPbBrI_2/SiO_2$ core-shell nanocrystals enhances the stability and efficiency in electroluminescent devices

Supplementary information

Jan Wahl[1], Manuel Engelmayer[2], Mukunda Mandal[3], Tassilo Naujoks[2], Philipp Haizmann[1], Andre Maier[1,4], Heiko Peisert[1], Denis Andrienko[3], Wolfgang Brütting[2], Marcus Scheele[1,4,+]

[1] *Institut für physikalische und theoretische Chemie, Universität Tübingen, Auf der Morgenstelle 18, D-72076 Tübingen, Germany*

[2] *Max Planck Institute for Polymer Research, Ackermannweg 10, D-55128 Mainz, Germany*

[3] *Institute of Physics, University of Augsburg, D-86135 Augsburg, Germany*

[4] *Center for Light-Matter Interaction, Sensors & Analytics LISA*$^+$*, Universität Tübingen, Auf der Morgenstelle 15, D-72076 Tübingen, Germany*

[+] *To whom correspondence should be addressed*

S1. SEM and HRTEM micrographs of silica coated $CsPbBrI_2$ nanocrystals

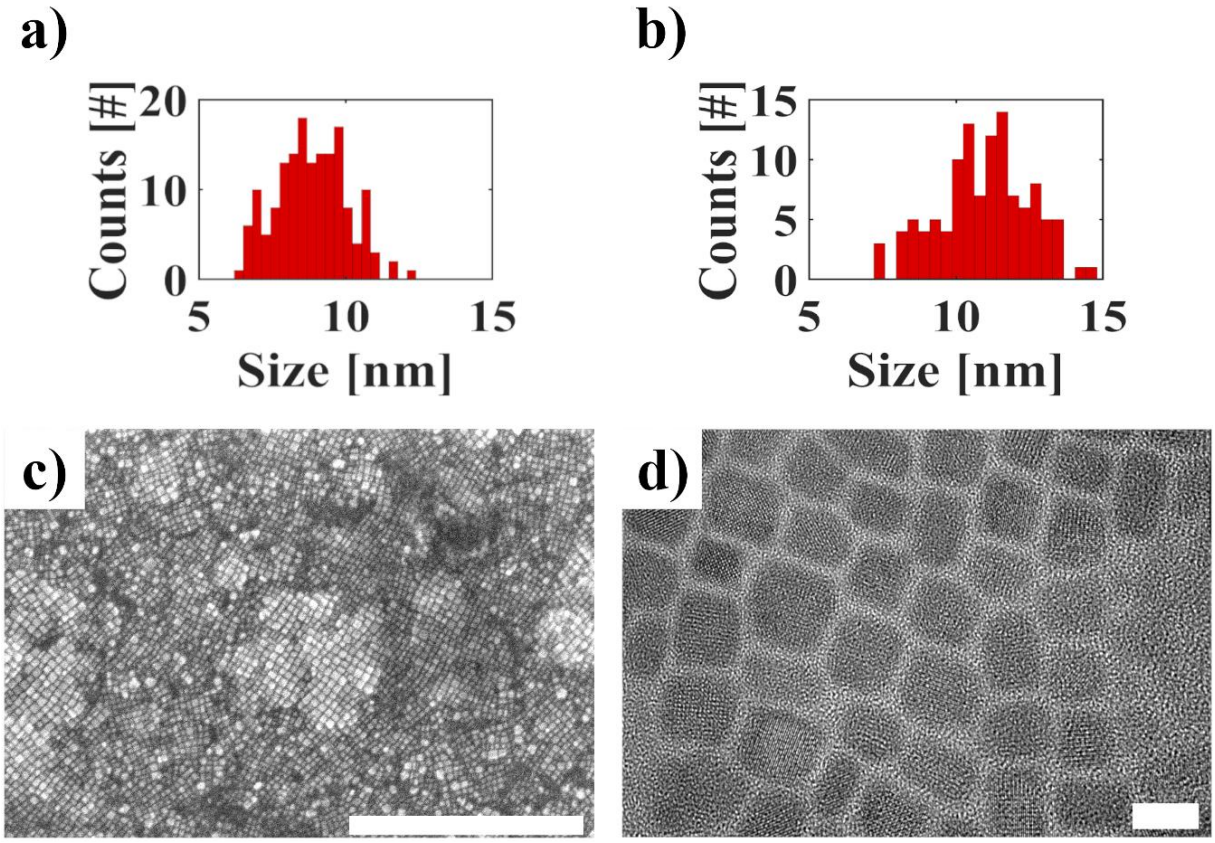

Figure S5.1: a) Size distribution determined from SEM micrographs of untreated $CsPbBrI_2$ nanocrystals. b) Size distribution after applying a 5:1 molar ratio of TMOS. c) SEM micrograph of silica coated NCs. d) HRTEM of silica coated NCs. The scale bars are 500 nm and 10 nm, respectively.

S5.2. AFM of spin-coated perovskite thin films with corresponding height determination

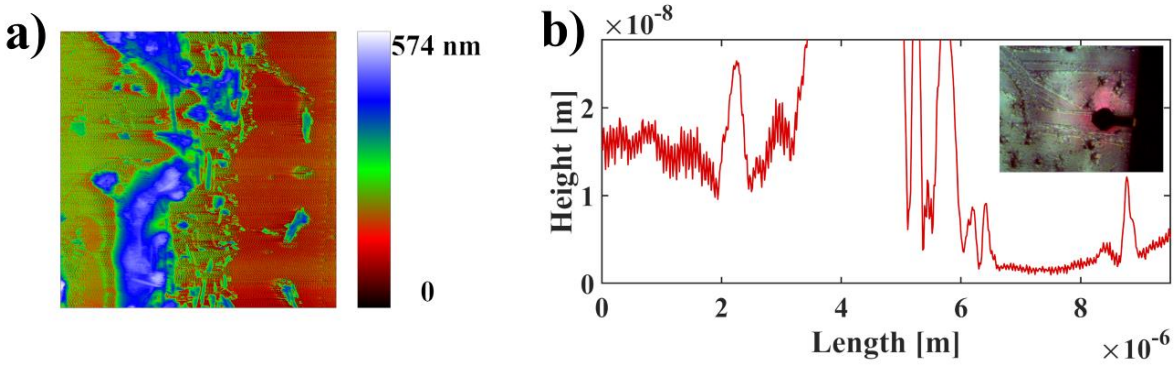

Figure S5.2: a) AFM image of a typical NC thin film, on the left the unharmed film is shown, whereas on the right a scratch was made to measure the absolute film height. The size of the micrograph is 10µmx10µm. b) Corresponding height profile of the NC thin film. The inset shows the different areas (scratch and unharmed) in a microscopic image. The large peak in between is due to dislocated material during the scratching process.

In order to determine the film thickness of a typical NC thin film, a film was prepared following the as described spin-coating method. Subsequently, a scratch was made with a syringe to remove the film in a certain area. The AFM tip was located onto the edges of the scratch and the measurement range was set to include the scratch as well as the unharmed thin film. Thereafter, the film was analyzed using Gwyddion and the film thickness was determined to be 15-19 nm, which corresponds to approximately one monolayer.

S5.3. Silica shell characterization and stability against polar solvents

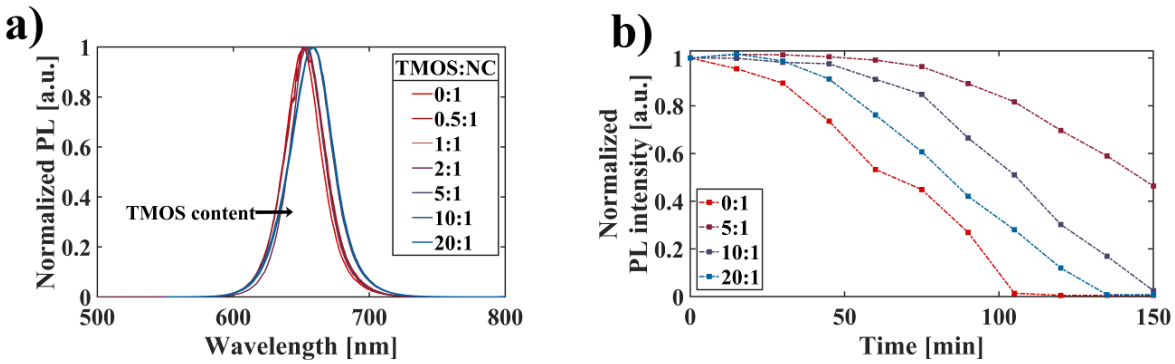

Figure S5.3: a) Normalized PL spectra of $CsPbBrI_2$ nanocrystals that were treated with different amounts of TMOS. The stochiometric ratio was ranging up to 20-fold. b) Stability of spectroscopic samples against water. In a typical experiment, 100 µl deionized water was added to a sample with spectroscopic concentration.

A hypochromic shift due to exciton leakage was observed when treating the $CsPbBrI_2$ samples with TMOS over the duration of 72 h. The extend of the shift is dependent on the amount of TMOS added and can be directly correlated to the shell thickness. The shift increases until the stochiometric ratio of 5:1 (TMOS:NC) is applied, adding additional TMOS does not shift the emission to lower energies.

The silica shell was subsequently probed for improved stability by adding 100 µl deionized water to a spectroscopic sample with µM concentrations. It was found that the stability was maximized for a sample prepared with a 5:1 TMOS:NC ratio. Higher TMOS concentrations lead to a less stable silica shell, a possible explanation are incompletely reacted TMOS species that are activated upon water addition and hence form another highly reactive, polar species in solution which damage the particles.

S5.4. Overview spectra of NMR and UPS

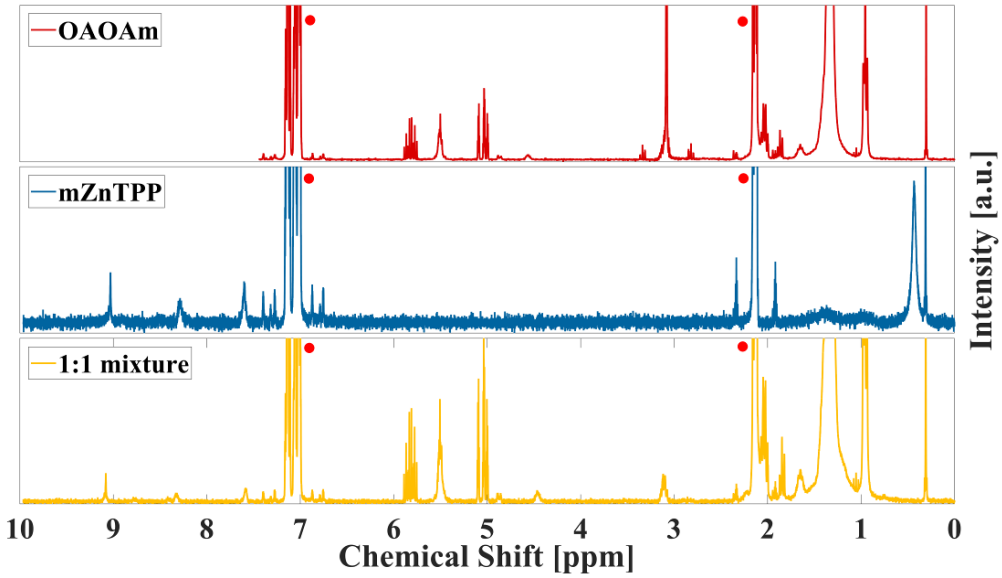

Figure S5.4: Overview NMR spectra of Top: Native $CsPbBrI_2$ functionalized with OA and OAm. Middle: Reference measurement of pure mZnTPP. Bottom: 1:1 stochiometric mixture of $CsPbBrI_2$ nanocrystals with mZnTPP. All spectra are taken in toluene, the solvent peaks are indicated by a red spot.

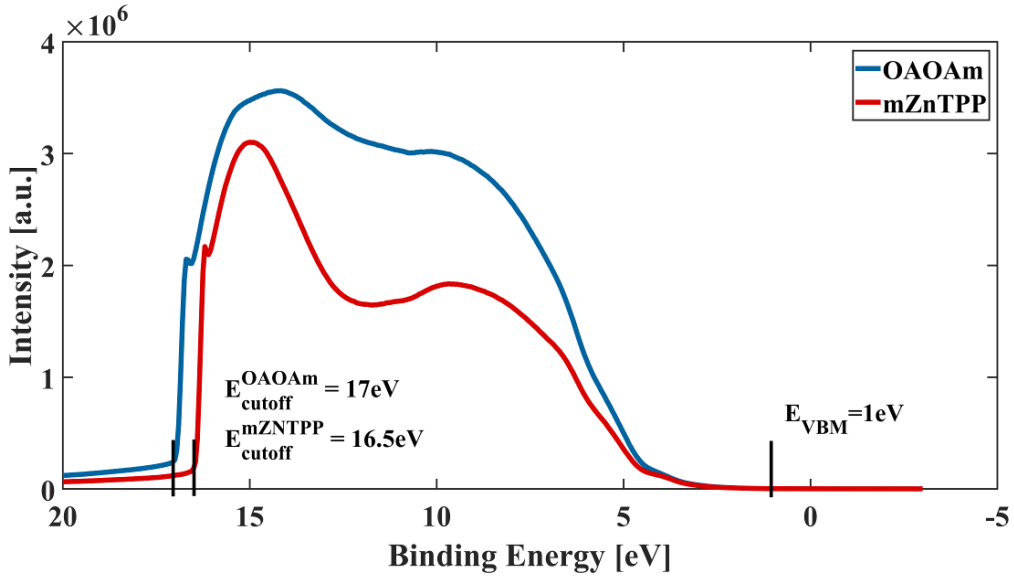

Figure S5.5: Overview UPS spectrum, indicated are the onset of the valence band maximum (VBM) as well as the cutoff energies.

S5.5. Extinction coefficient of $CsPbBrI_2$

The concentration of the perovskite solutions was determined by absorption spectroscopy, the extinction coefficient of $CsPbBrI_2$ thin films was taken as a reference. [326] Since $CsPbBrI_2$ nanocrystals with a size of 9 nm are in the weak confinement regime (Exciton Bohr diameter ~10 nm), the extinction coefficients derived from thin films are of sufficient accuracy. The absorbance can then easily be transformed to the molar extinction coefficient ε_{mol} by multiplying with the molar volume.

$$\varepsilon_{mol}^{600} = \alpha_{600} \cdot V_{mol} = 7263\ cm^{-1}\ M^{-1}, \quad \text{(S5.1)}$$

with the absorption coefficient at 600 nm α_{600} and the molar volume of $CsPbBrI_2$ V_{mol} = 0.14973 l/mol.

S5.6. Photoluminescence spectra of mZnTPP and a stoichiometric mixture with NCs

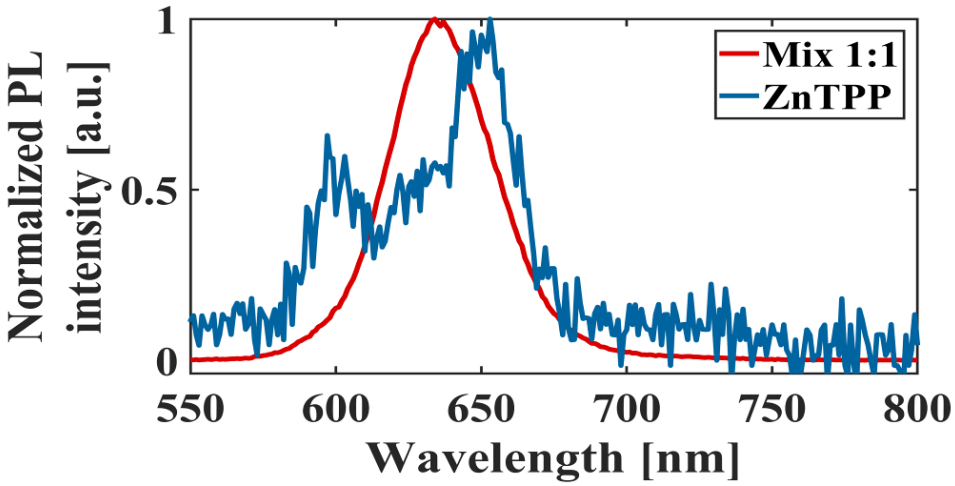

Figure S5.6: Normalized photoluminescence spectra of a 1:1 stochiometric mixture of $CsPbBrI_2$ NCs and mZnTPP (red) and pure mZnTPP (blue) in toluene.

S5.7. Lifetime fitting model and parameters

As a general model for fitting the lifetime decay a triexponential function was used, as described by **Equation (S5.2)**, and the results and explicit fitting parameters are summarized in **Table S5.1**.

$$I(t) = I(0) + A_1 exp\left\{-\frac{t-t_0}{\tau_1}\right\} + A_2 exp\left\{-\frac{t-t_0}{\tau_2}\right\} + A_3 exp\left\{-\frac{t-t_0}{\tau_3}\right\} \quad \text{(S5.2)}$$

With Intensity I, preexponential factors A_i, time t and lifetimes τ_i.

Table S5.1: Complete fitting parameters for the triexponential function utilized to obtain the photoluminescence lifetimes. With Intensity I, preexponential factors A_i, lifetimes τ_i and the R^2 value to control the goodness of the fit.

		OAOAm	mZnTPP
Solution	I(0)	0.00590	0.00639
	A_1	0.08880	0.20708
	τ_1	2.88499	2.24639
	A_2	0.49359	0.43820
	τ_2	13.81641	12.93177
	A_3	0.34807	0.28029

Continuation Table S5.1: Complete fitting parameters for the triexponential function utilized to obtain the photoluminescence lifetimes. With Intensity I, preexponential factors A_i, lifetimes τ_i and the R^2 value to control the goodness of the fit.

	τ_3	39.26681	34.06298
	R^2	0.99985	0.99983
		OAOAm	mZnTPP
Solid state	I(0)	0.00146	0.00152
	A_1	0.51995	0.58755
	τ_1	1.09208	0.84141
	A_2	0.30650	0.30570
	τ_2	6.58622	4.79796
	A_3	0.15721	0.15050
	τ_3	22.46031	17.34084
	R^2	0.99971	0.99957

S5.8. Temperature-dependent ionic conductivity and fitting results

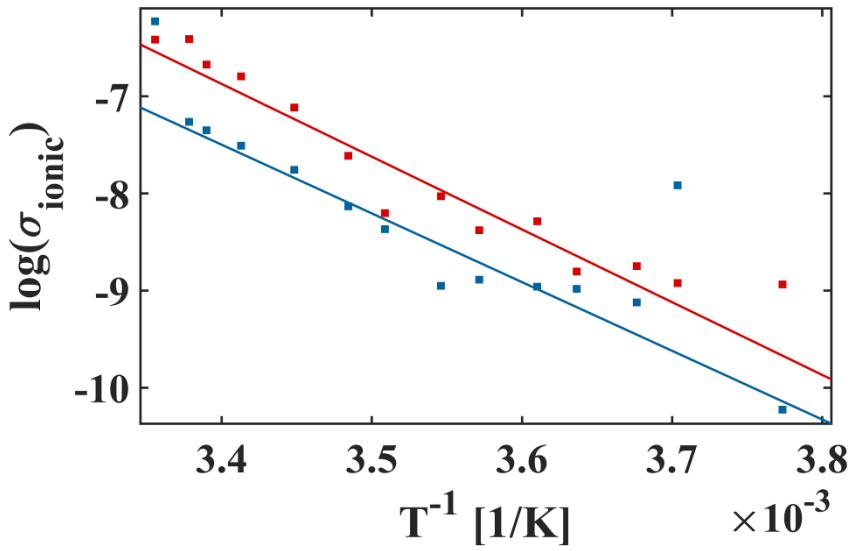

Figure S5.7: Temperature dependent ionic conductivity of native (red) and mZnTPP functionalized (blue) $CsPbBrI_2$ perovskites. The corresponding Arrhenius type NNH fits are shown as solid lines.

The results of the Arrhenius type NNH model are as follows: [***]

Electronic contribution native

$$\sigma_{el}^{OAOAm}(T) = -17850\,T^{-1} + 54.32\ (higher\ T)$$
$$\sigma_{el}^{OAOAm}(T) = -7106\,T^{-1} + 17.66\ (lower\ T) \quad \text{(S5.3)}$$

[***] Remark from the author: All conductivities are given as their decadic logarithm (log).

The higher temperature part of the fit corresponds to the predominantly cubic and the lower temperature fit to the predominantly orthorhombic phase. [56,324]

Ionic contribution native $$\sigma_{ion}^{OAOAm} = -6926\,T^{-1} + 16.68 \quad \text{(S5.4)}$$

Electronic contribution mZnTPP $$\sigma_{el}^{mZnTPP} = -11750\,T^{-1} + 33.28 \quad \text{(S5.5)}$$

Ionic contribution mZnTPP $$\sigma_{ion}^{mZnTPP} = -7073\,T^{-1} + 16.55 \quad \text{(S5.6)}$$

S5.9. Calculation of the charging energy

The conductivity of a nanocrystal thin film is dependent on the transfer integral β, which describes the dependence of the conductivity on the coupling between neighboring particles:

$$\beta = E_0 \cdot f(\Delta V, d_{NN}), \quad \text{(S5.7)}$$

with the activation energy E_0, containing the charging energy E_C as well as fluctuations due to size distributions, and a contribution of the energy barrier with height ΔV and width d_{NN}. [22,170,327] To access the charging energy in **Equation (S5.7)**, the molecular polarizability and dielectric constant of different ligands was calculated with the Claussius-Mosotti equation in **Equation (S5.8)**.

$$\varepsilon_r = 1 + \frac{3N_A\rho\alpha}{3M_m\varepsilon_0 - N_A\rho\alpha}, \quad \text{(S5.8)}$$

with Avogadro's constant N_A, density ρ, molecular polarizability α, molecular mass M_m and vacuum permittivity ε_0.

On the other hand, the dielectric constant of the NCs is size-dependent and has to be adjusted following a generalized Penn model: [328]

$$\varepsilon_{Penn}(r) = 1 + \frac{\varepsilon_{bulk} - 1}{1 + \frac{18.05}{r^{1.8}}} \quad \text{(S5.9)}$$

$$with\ \varepsilon_{bulk} = 17.$$

Finally, the charging energy was calculated following the modified Laikhtman-Wolf model in **Equation (S5.10)**. [173]

$$E_C = \frac{e^2}{2(C_S + nC_m)}, \quad \text{(S5.10)}$$

with the self-capacitance

$$C_S^{-1} = \frac{1}{4\pi\varepsilon_0 r}\,\frac{\varepsilon_{QD}-\varepsilon_m}{\varepsilon_{QD}\varepsilon_m} + \frac{0.94}{4\pi\varepsilon_{QD}\varepsilon_0 r}\,\frac{\varepsilon_{QD}-\varepsilon_m}{\varepsilon_{QD}+\varepsilon_m}, \tag{S5.11}$$

and the mutual capacitance

$$C_m = 2\pi\varepsilon_0\,\frac{\varepsilon_{QD}\varepsilon_m}{\varepsilon_{QD}-\varepsilon_m} r \ln\left\{\frac{D}{D-2r}\right\} \tag{S5.12}$$

Since the description of the charging energy, precisely the capacities, only hold true for spherical nanocrystals the calculated values had to be corrected by a constant factor which corresponds to the change to cubic morphologies. It has been shown for the unit cube that the capacitance must be adjusted by a factor of ~0.6607. [329]

Besides adjusting the capacities, a correction was made to properly apply the Penn model to the cubic NCs. The volume of the perovskite NCs was calculated and subsequently used to calculate the radius of a corresponding sphere with equivalent volume, which radius was inserted into the Penn model. Additionally, the value for the static dielectric constant was required, values for $CsPbI_3$ and $CsPbBr_3$ are known from literature. [330,331] Linear behavior of the mixed halide system was assumed and used to calculate the static dielectric constant.

Table S5.2: Static dielectric constants of iodide and bromide containing cubic perovskites used throughout this work.

	Static dielectric constant
$CsPbI_3$ [331]	18.1
$CsPbBr_3$ [330]	15
$CsPbBrI_2$	17

S5.10. DFT calculations

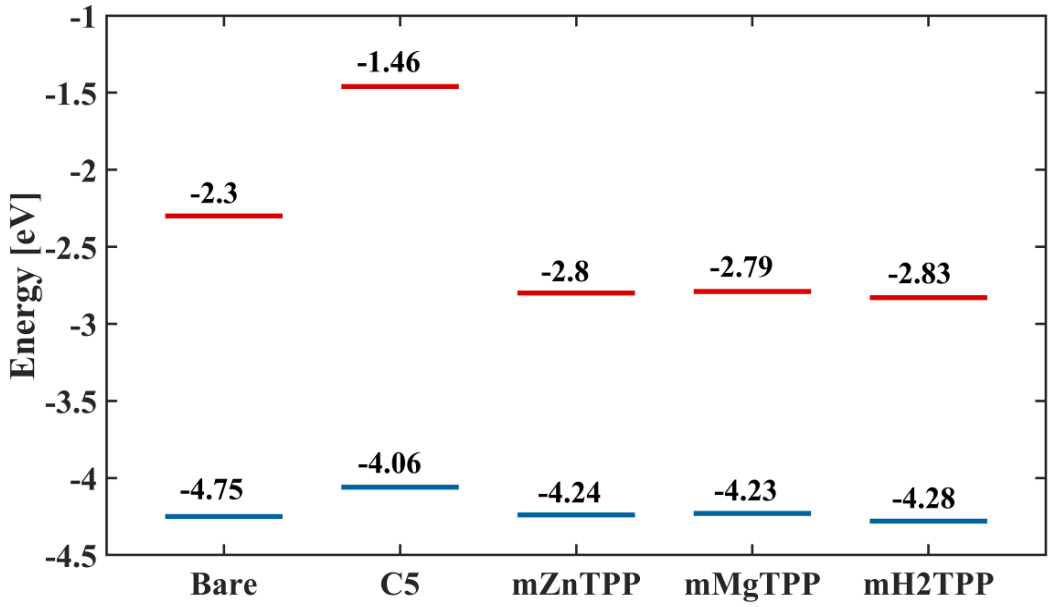

Figure S5.8: Energy levels obtained from calculations at the PBE/DZVP level for NCs functionalized with various ligands: aliphatic hexanoic acid (HexAcid; mimic for oleic acid), and porphyrin derivatives: mZnTPP, mMgTPP and mH2TPP.

Upon comparing experimental data with the results of density functional theory (DFT) calculations, it was found that the experimental trend could be confirmed. However, the magnitude of the effects induced by the novel ligand shell are not comparable, since calculations were run on a nanocrystal with 1.7nm edge length, whereas the particles used in practice were roughly five times larger. Nevertheless, DFT results exhibited a shift to lower energies upon exchanging the aliphatic ligand with semiconducting tetraphenylporphyrin derivatives, as measured with UPS. Additionally, the band gap decreases, which was also found in absorption and fluorescence measurements.

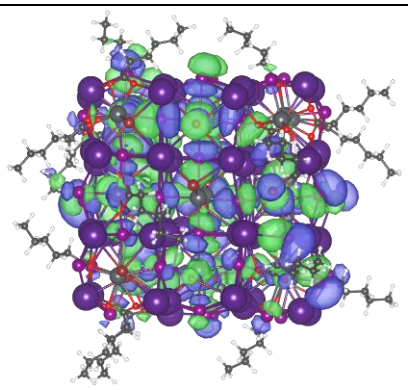	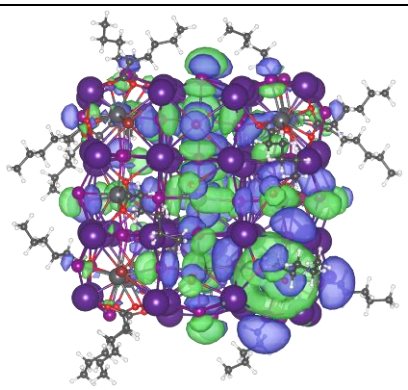	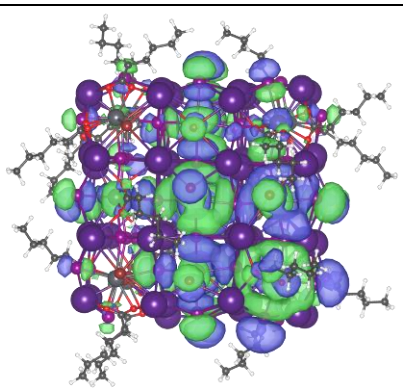
HOMO – 2 (–4.57 eV)	HOMO – 1 (–4.51 eV)	HOMO (–4.47 eV)
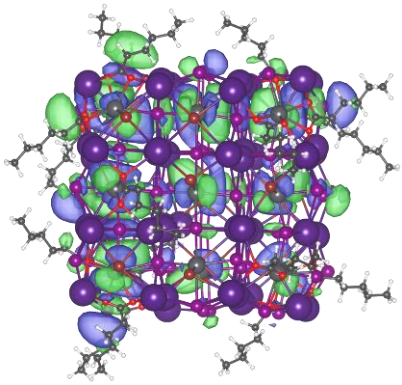	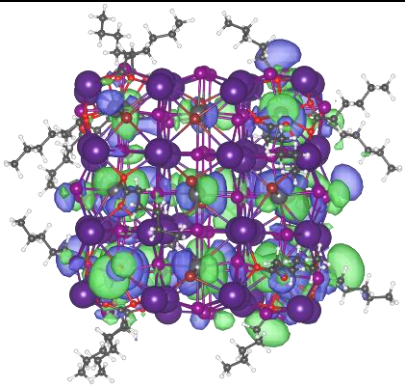	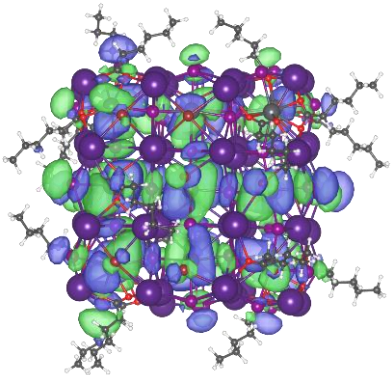
LUMO (–1.86 eV)	LUMO + 1 (–1.78 eV)	LUMO + 2 (–1.75 eV)

Figure S5.9: Calculated frontier molecular orbitals of hexanoic acid functionalized NCs.

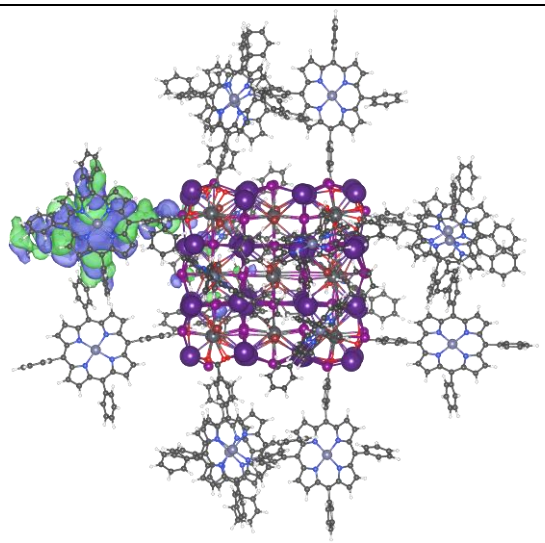	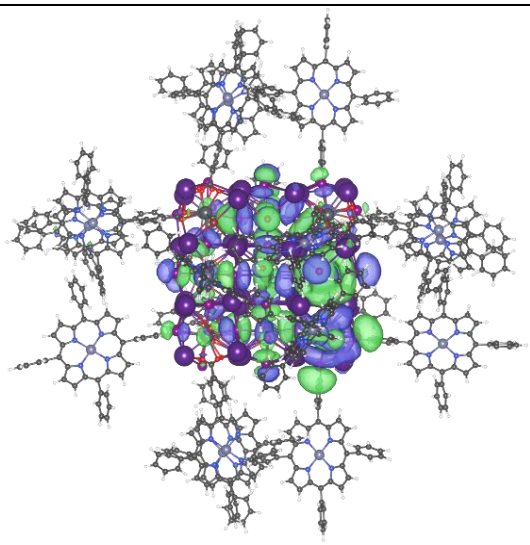
HOMO – 3 (–4.36 eV)	HOMO – 2 (–4.34 eV)
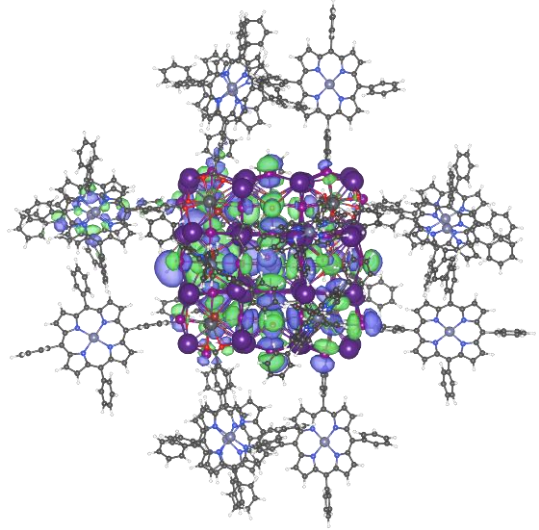	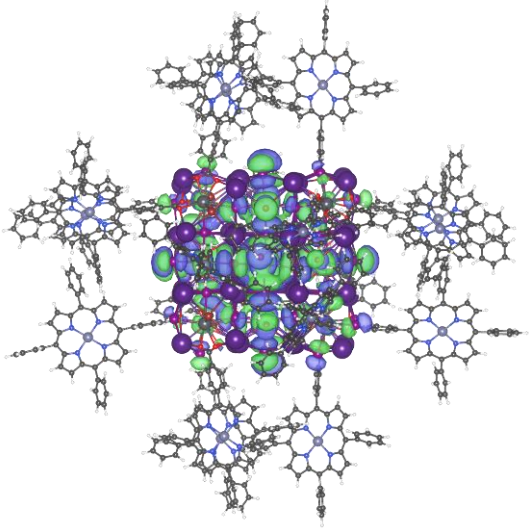
HOMO – 1 (–4.32 eV)	HOMO (–4.24 eV)
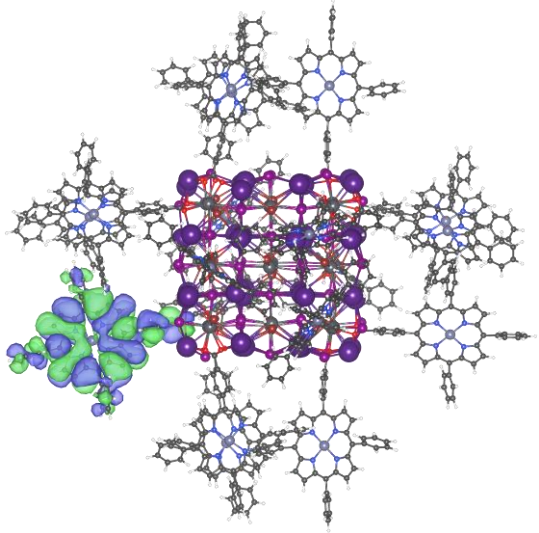	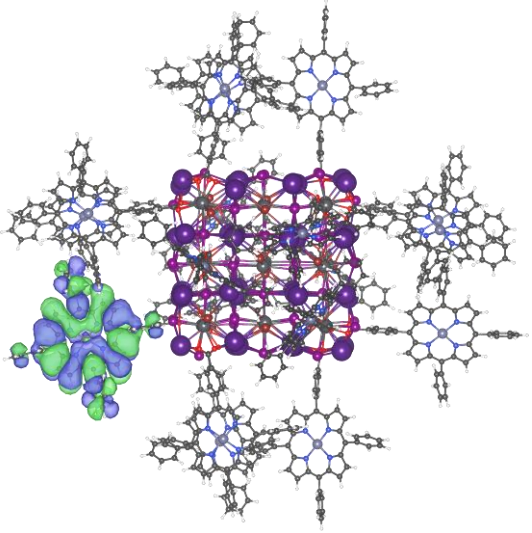
LUMO (–2.80 eV)	LUMO + 1 (–2.77 eV)

Figure S5.10: Calculated frontier molecular orbitals of mZnTPP functionalized NCs.

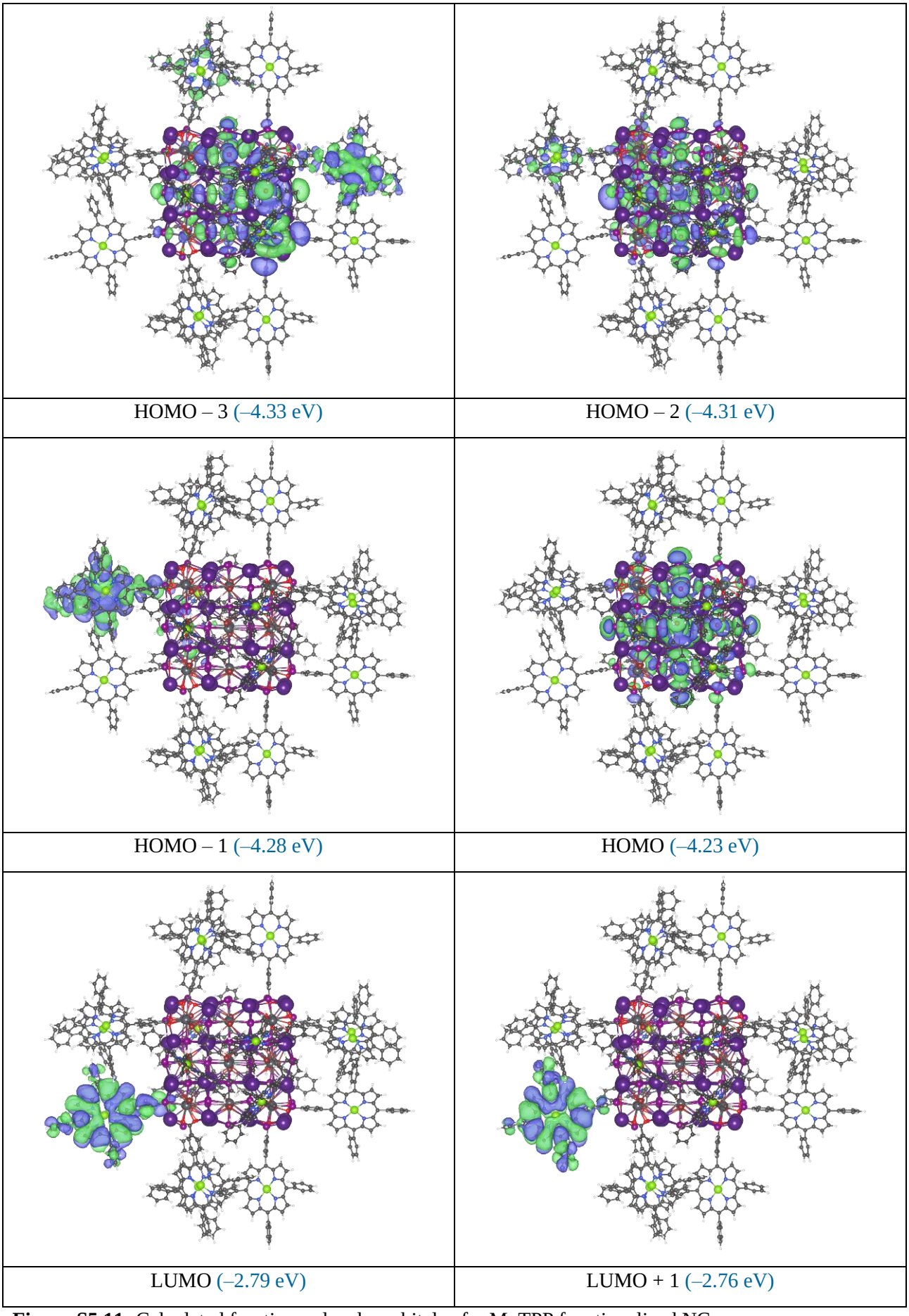

Figure S5.11: Calculated frontier molecular orbitals of mMgTPP functionalized NCs.

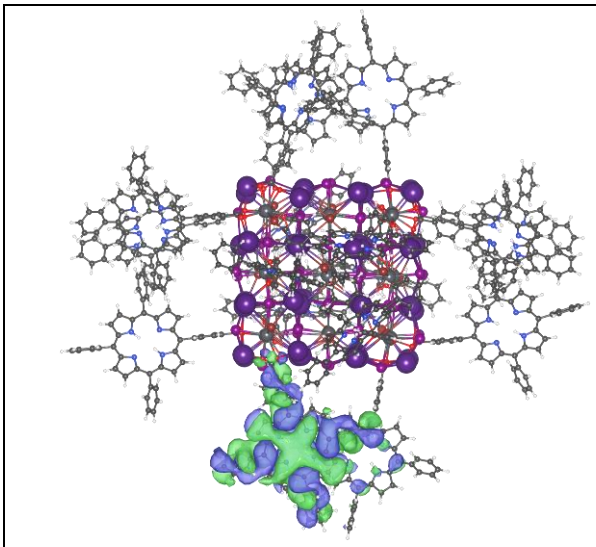

HOMO – 3 (–4.33 eV)

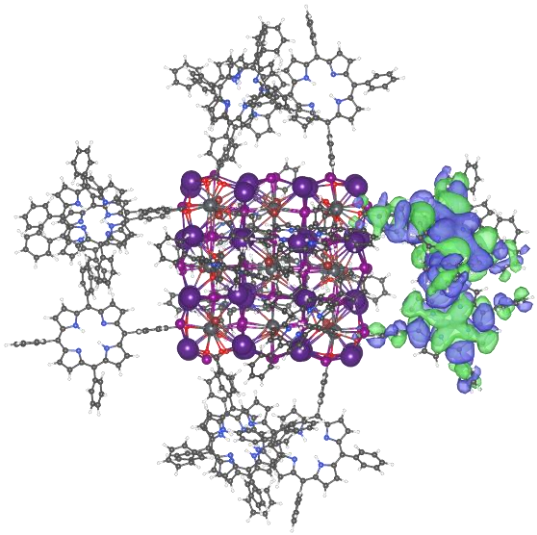

HOMO – 2 (–4.33 eV)

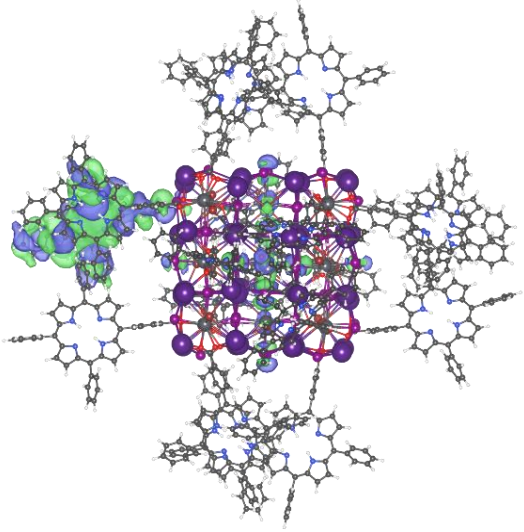

HOMO – 1 (–4.28 eV)

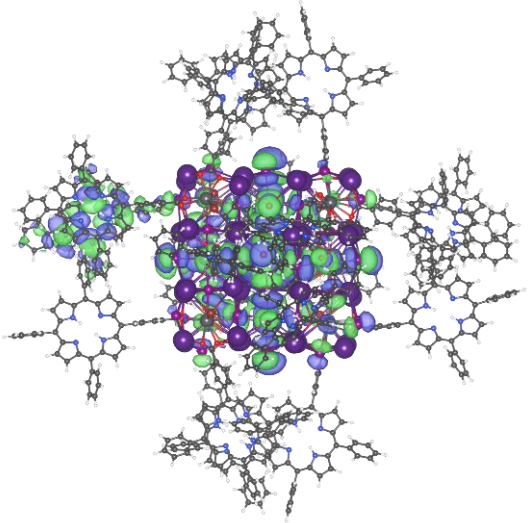

HOMO (–4.28 eV)

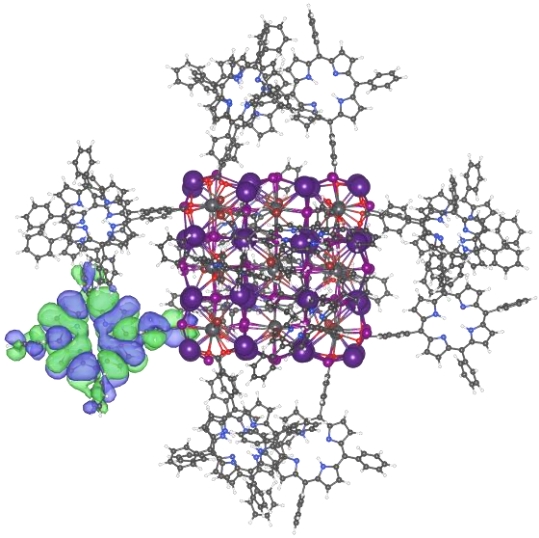

LUMO (–2.83 eV)

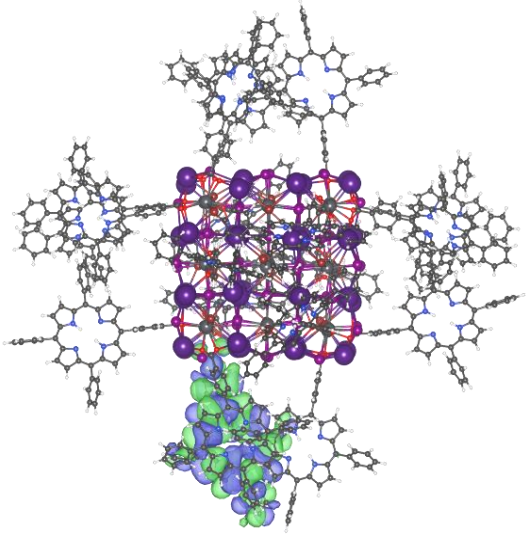

LUMO + 1 (–2.83 eV)

Figure S5.12: Calculated frontier molecular orbitals of mH2TPP functionalized NCs.

S5.11. AFM of the film coverage on TFB

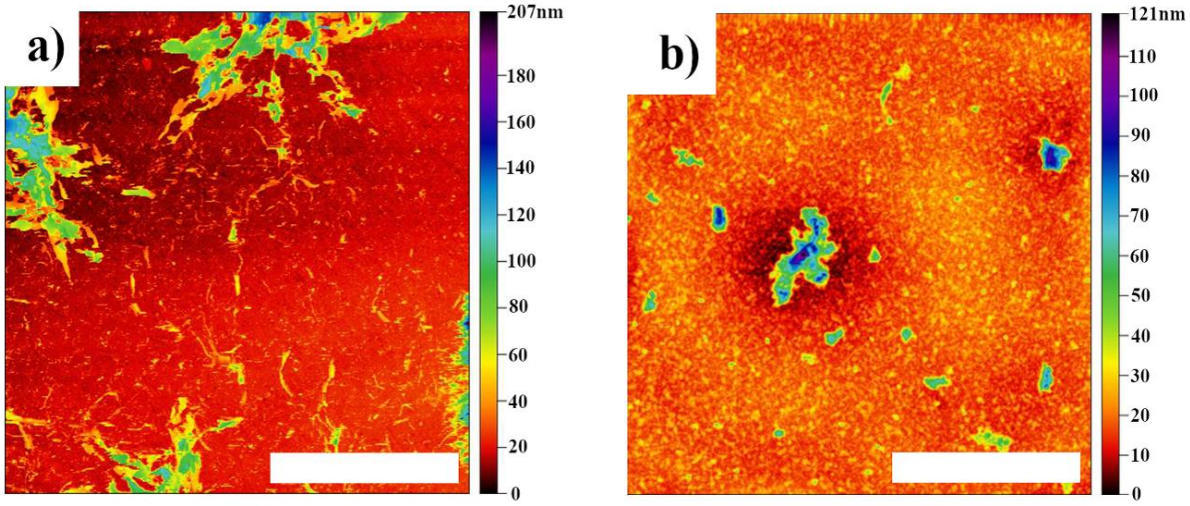

Figure S5.13: AFM images of the perovskite film coverage on a TFB coated substrate. a) Native $CsPbBrI_2$ nanoparticles on TFB. b) Exchanged $CsPbBrI_2$ nanoparticles on TFB. Scale bars are 4µm in both cases.

6. Mitigating the Photodegradation of All-Inorganic Mixed-Halide Perovskite Nanocrystals by Ligand Exchange

Jan Wahl[$,‡], *Philipp Haizmann*[$,‡], *Christopher Kirsch*[$], *Rene Frecot*[$], *Nastasia Mukharamova*[#], *Dameli Assalauova*[#], *Young Yong Kim*[#], *Ivan Zaluzhnyy*[+], *Thomas Chassé*[$,ß], *Ivan A. Vartanyants*[#], *Heiko Peisert*[$,]*, *Marcus Scheele*[$,ß,]*

[$] Institut für physikalische und theoretische Chemie, Universität Tübingen, Auf der Morgenstelle 18, 72076 Tübingen, Germany

[#] Deutsches Elektronen-Synchrotron DESY, Notkestraße 85, 22607 Hamburg, Germany

[+] Institut für Angewandte Physik, Universität Tübingen, Auf der Morgenstelle 10, 72076 Tübingen, Germany

[ß] Center for Light-Matter Interaction, Sensors & Analytics LISA[+], Universität Tübingen, Auf der Morgenstelle 15, 72076 Tübingen, Germany

[‡] These authors contributed equally

Perovskites, Stability, Ligand Exchange, XPS, Structure

This chapter is based on a publication published in Physical Chemistry Chemical Physics (PCCP): Phys. Chem. Chem. Phys., 2022, 24, 10944–10951, DOI: 10.1039/d2cp00546h

Arxiv Preprint: https://doi.org/10.48550/arXiv.2112.10004

6.1. Abstract

We show that the decomposition of caesium lead halide perovskite nanocrystals under continuous X-ray illumination depends on the surface ligand. For oleic acid/oleylamine, we observe a fast decay accompanied by the formation of elemental lead and halogen. Upon surface functionalization with a metal porphyrin derivate, the decay is markedly slower and involves the disproportionation of lead to Pb^0 and Pb^{3+}. In both cases, the decomposition is preceded by a contraction of the atomic lattice, which appears to initiate the decay. We find that the metal porphyrin derivative induces a strong surface dipole on the nanocrystals, which we hold responsible for the altered and slower decomposition pathway. These results are important for application of lead halide perovskite nanocrystals in X-ray scintillators.

6.2. Introduction

Lead halide perovskites are an important class of materials for use in light harvesting and light emitting devices. [51,332] Another promising application of perovskites are scintillators, where they have already shown good performance in X-ray detection. [333–335] However, the instability of perovskite-based materials is a significant drawback for the application in optoelectronic and scintillating devices. [24,35,38,39,334,336,337] To address this issue, the photodegradation of methylammonium lead iodide ($MAPbI_3$) thin films has been thoroughly investigated, including the postulation of a decay mechanism. [22,338,339] Recently, these photodegradation studies have been extended to caesium mixed-halide perovskites ($CsPbX_3$) [55,340,341] in view of their improved stability against long-term light exposure. [342] However, even the most stable mixed halide perovskites, such as $CsPbBrI_2$, undergo slow photodegradation in intense visible light. [55,340,341] The aim of this work is to use the tunable surface chemistry of nanocrystals (NCs) to further mitigate this instability with a particular focus on photodegradation with X-ray photons to aid the application in scintillators. [22,24] To this end, we introduce zinc-(5-monocarboxyphenyl-10,15,20-triphenylporphyrin) (mZnTPP) as surface ligand and investigate its effect on the decomposition of the NCs under X-ray illumination. As NCs, we use two model systems, namely $CsPbBrI_2$ and $CsPbBr_2Cl$, based on their light emitting properties hereafter referred to as red and blue perovskites, respectively. If not explicitly stated otherwise, these NCs are surface-functionalized with oleic acid/oleylamine, referred here to as the “native ligand”. As previously reported, perovskites experience drastic changes under continuous X-ray exposure. [36,37] One analytical method that utilizes X-ray irradiation is X-ray photoelectron spectroscopy (XPS). Here, a sample is continuously irradiated with X-rays, and electrons, released from the sample due to the external photoelectric effect, are detected based on their kinetic energy. The core-level binding energy of an emitted electron is directly related to the detected kinetic energy. Previous XPS experiments on

perovskites reported a shift of the binding energies to higher values with ongoing measurement time. This was mostly attributed to either surface, substrate or charging effects. [39] In this work, we observe a similar shift for the red and blue perovskite NCs. However, we demonstrate by a combination of XPS and wide-angle X-ray scattering (WAXS) that the core-level energy shift originates from a contraction of the atomic lattice. For the red and blue perovskite NCs with native ligands, we find a similar decay mechanism as recently postulated for thin films. [55] While morphology and chemical composition are maintained in the red perovskites, the blue perovskites exhibit a loss of chlorine and undergo recrystallization. Most importantly, we observe a greatly altered and slower decay mechanism after surface functionalization with the porphyrin derivative mZnTPP.

6.3. Results

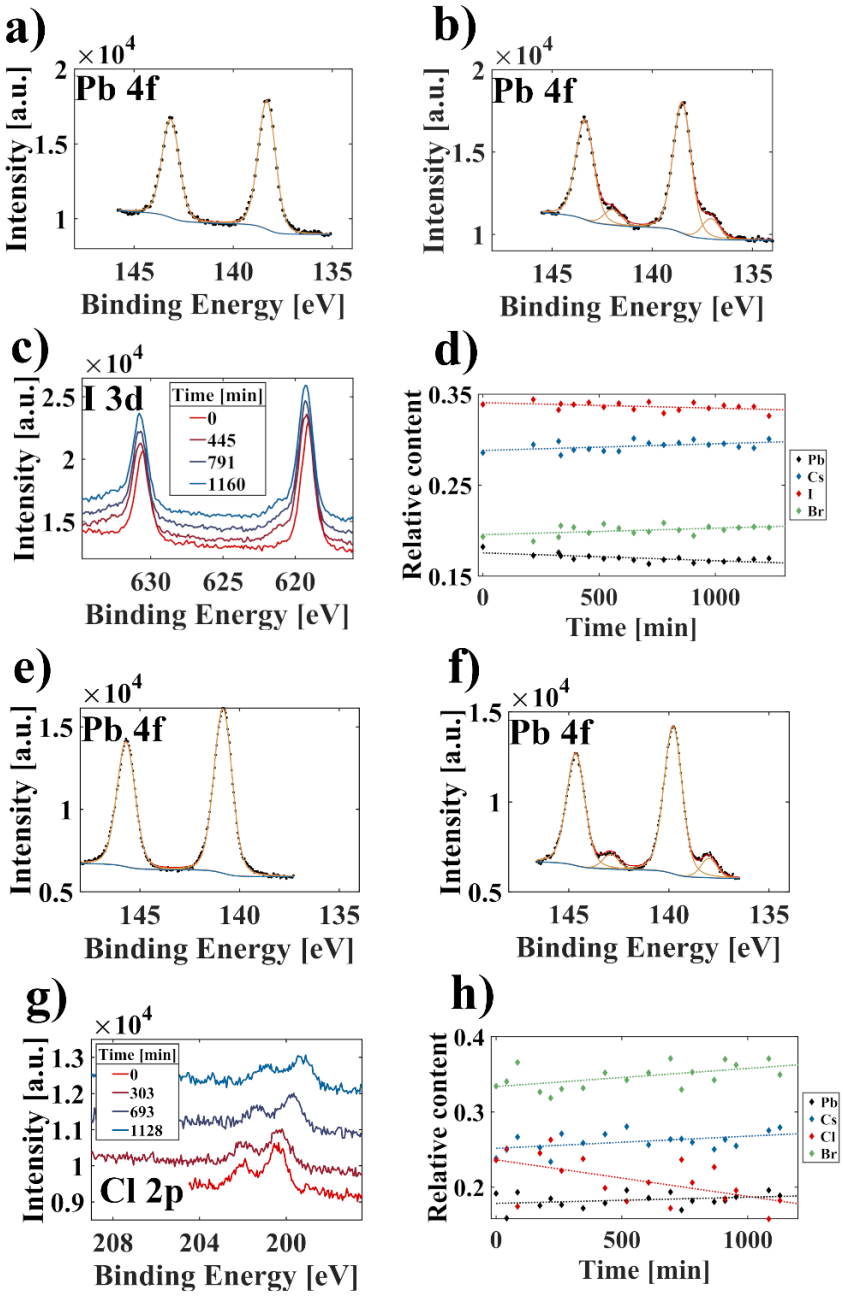

Figure 6.1: Pb 4f core level XPS spectra of $CsPbBrI_2$ a) at the start (0 min) and b) after 1160 min of X-ray exposure. Fit components are shown in orange, the overall fit is depicted in red. All spectra were fitted by applying a Shirley-type background (blue). c) I 3d spectra at different times during the illumination with the evolution of a shoulder at higher binding energy (621 eV). d) Relative stoichiometric content and linear regression (dotted lines) during the exposure for $CsPbBrI_2$. Pb 4f spectra of $CsPbBr_2Cl$ e) at the start (0 min) and f) after 1128 min of exposure. g) Cl 2p spectra (~ 200 eV) exhibit a decrease over time without the formation of a novel peak. h) Relative stoichiometric content for $CsPbBr_2Cl$ during the experiment.

The decomposition of both perovskite systems was analyzed under continuous X-ray illumination for at least 20 h by XPS and ultraviolet photoelectron spectroscopy (UPS). Core level and valence spectra were recorded at regular time intervals. Exemplarily, spectra of Pb 4f doublet peaks recorded at the beginning and end of the illumination are shown in **Figure 6.1 a + b**. The Pb 4f main peak at a binding energy of 138.25 eV in **Figure 6.1 a** corresponds to Pb^{2+} in the red perovskites. Over the course of this investigation, all samples, independent of stoichiometry and ligand shell, developed an additional Pb species visible in the corresponding Pb 4f-core level spectra of **Figure 6.1 a + b**. The signal occurred at lower binding energies (~137 eV), which indicates a lowering of the oxidation state. Therefore, and in agreement with literature, we attribute this peak to the formation of elemental lead (Pb^0). [39,338,343] The formation of the Pb^0 component is detected after illuminating the sample for few hours. The intensity of the Pb^0 peak increases continuously with time, the relative Pb^0/Pb^{2+} content as a function of the illumination time is summarized in **Figure S6.3** for the red perovskites. Corresponding peak fits are shown for the first and last measurement of the experiment in **Figure 6.1 a + b**, respectively. Additionally, we tracked the lead content over the course of the experiment, as shown in **Figure S6.3**. After 20 h, we observe the formation of 13.2 % Pb^0 for the red perovskites (**Figure S6.3**). As a source of electrons for the reduction of Pb^{2+}, we consider the halides in the NCs. While the bromide peak in all samples experienced no significant change (see **Figure S6.1**), we find strong changes in the core level spectra of the other halides, *i.e.*, I^- for the red perovskites (**Figure 6.1 c + g**. We observe the formation of a distinct shoulder at high binding energy in the I 3d region for the red perovskites, suggesting that I^- is indeed oxidized during the reduction of Pb^{2+} (**Figure 6.1 c**). By tracking the stoichiometric composition, we find the iodide content to stay constant throughout the experiment (**Figure 6.1 d**), suggesting that the new iodine/iodide species remains in the sample during the decomposition even in ultra-high vacuum. To calculate the amount of newly formed species, we first determined the percentages of such from the detail spectra fits. However, the intensities therein are not directly comparable, therefore we multiplied the percentage with the survey spectrum intensities, *i.e.*, peak areas, to calculate a comparable value for the amount of all newly formed species. The ratio of the novel iodine (621 eV) to Pb^0 (137 eV) species is 1.61 ± 0.23, *i.e.*, close to 2:1, supporting our hypothesis of a redox reaction between I^- and Pb^{2+}. For a more detailed derivation of the ratio, see supporting information section S6.2.

We observed similar changes in the XPS core level spectra for the blue perovskites, *e.g.*, the formation of Pb^0 (**Figure 6.1 e + f**), however to a lesser extent compared to the red perovskites. After 20 h of irradiation, a total of 10.2 % Pb^0 was observed for the blue perovskites (**Figure S6.3**). Additionally, we measured a drastic decrease by ~20–25 % (**Figure 6.1 h**) in the Cl 2p peak intensity, suggesting chloride as the redox partner for Pb^{2+} since this is roughly twice the amount of Pb^0 formed. Finally, the Cs 4d orbital was monitored and no formation of novel peaks could be observed (**Figure 6.1 d + h**), suggesting that Cs remains in a relatively stable environment in both cases.

We probed the morphology of both NC samples after X-ray exposure by scanning electron microscopy (SEM). While the red perovskites maintained the cubic, nanocrystalline morphology, the blue perovskites recrystallized to larger agglomerates (see **Figure S6.4**). Therefore, we determine the structure before (**Figure 6.2 a**) and after X-ray exposure by WAXS. (Note that the flux and exposure times during synchrotron-based WAXS are vastly different from those during XPS, and the cross-section is substantially higher for the XPS experiments with their lower photon energies, such that a quantitative comparison is not possible. We believe, however, that qualitative considerations may still be made.) We index the WAXS patterns observed here according to the cubic perovskite phase, although previous scattering experiments have shown a pseudocubic annotation to be more appropriate. [56,324] However, the limited *q*-range and the broad reflections, which are typical for NCs, prevent such a refinement. From **Figure 6.2 b** one can see that one of the 200 peaks shifted to higher *q* values, while another remains at the same position. This indicates a contraction of this part of the sample. For further analysis, we integrate the diffraction maps over all angular coordinates to obtain an azimuthally-independent scattering pattern. In **Figure 6.2 c**, we display the differential intensity, obtained by subtracting the azimuthally integrated diffraction pattern after X-ray exposure from the first pattern. In this Figure, positive differential intensities refer to reflections which weakened during X-ray exposure, while negative differential intensities indicate newly evolved reflections. From the differential pattern, a change of the lattice constant from 6.11 Å to 5.67 Å could be obtained (see **Figure 6.2 c**) and Supporting information, S6.5, for more details).

Upon exposing the red perovskites to X-rays during XPS, we observed a shift of all sample peaks to higher binding energies (**Figure 6.3**). We argue that this shift is not primarily caused by electric charging since 1) the Au 4f substrate peaks remain at constant energies throughout the experiment (**Figure 6.3 a + b**), 2) the perovskite films were rather thin to enable the release of a large number of secondary electrons from the Au substrate underneath to suppress charging, [344,345] and 3) the magnitude of the shift of the sample peaks was different for different elements (Pb 4f: +0.63 eV, Cs 4d: +0.71 eV). The shifts remained constant after illumination for approximately 7 h (**Figure 6.3 c + d**).

We probed the influence of X-ray irradiation on the work function by measuring UPS before and after 20 h exposure (**Figure S6.5**). We find a shift of the high binding cutoff by 0.12 eV to higher energies, indicating a decrease of the work function. At the same time, the energy of the valence state maximum ($1S_h$) referenced to the Fermi level remains constant (see **Figure S6.8**). These findings suggest that the energy levels of the nanocrystal are shifted by 0.12 eV toward the vacuum level.

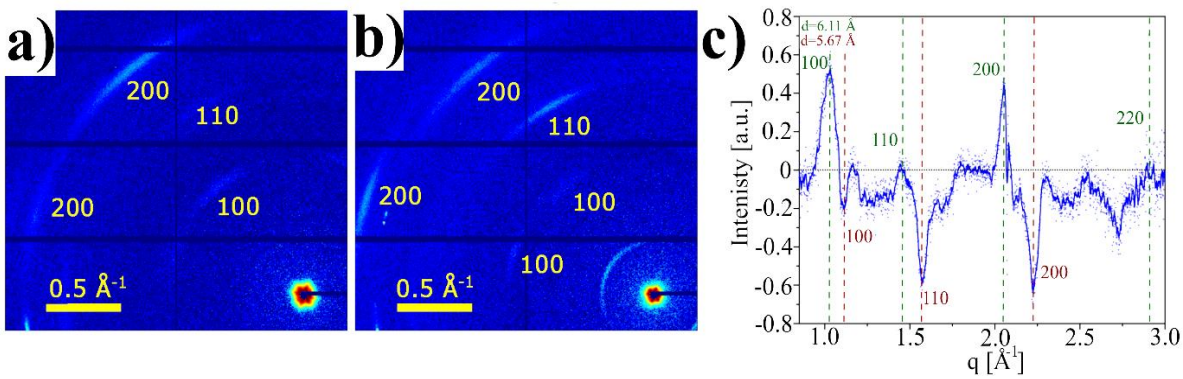

Figure 6.2: a) First WAXS measurement of $CsPbBrI_2$ nanocrystal superlattices and b) subsequent measurement after the spot was already exposed to radiation. c) Differential scattering intensity obtained by subtracting the azimuthally integrated diffraction pattern after X-ray exposure from the first pattern. Positive differential intensities refer to reflections which weakened during X-ray exposure, while negative differential intensities indicate newly evolved reflections. Indexing of old (green) and new (brown) peaks according to a cubic perovskite phase.

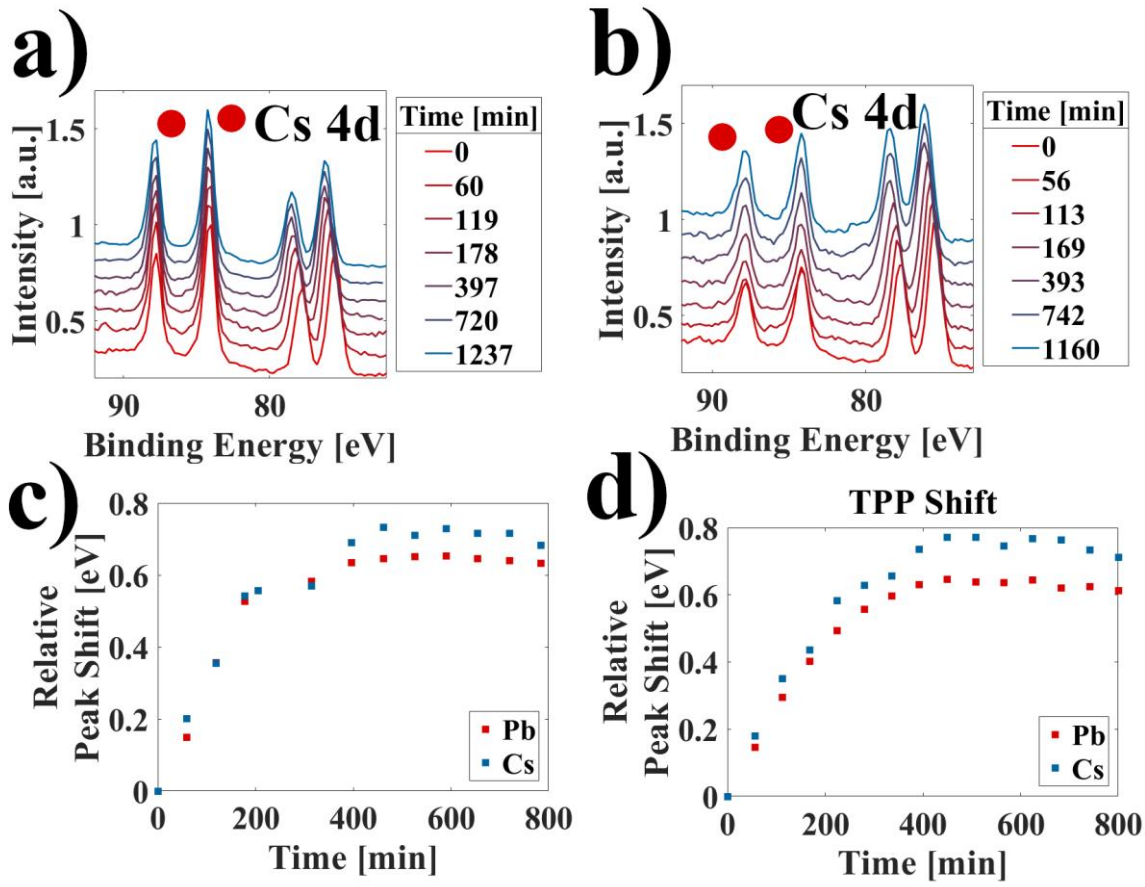

Figure 6.3: Cs 4d (75 eV) and Au 4f (84 eV) XPS spectra for a) native ligands and b) mZnTPP exchanged samples after different X-ray radiation exposure times. The substrate-related Au signals are denoted by red dots and did not change throughout the experiment in both cases. Relative peak position of the Pb 4f and Cs 3d signals compared to the binding energy at the start of the experiment for c) native and d) mZnTPP exchanged samples.

Motivated by the previous finding that ligand exchange with mZnTPP can enhance the stability of red perovskites in light emitting devices, [296] we studied the effect of this ligand on the

decomposition of the red perovskites under X-ray illumination. (Note: the loss of structural integrity of the blue perovskites due to chlorine evaporation did not allow for an analogous analysis.) With the mZnTPP ligand shell, we again found the formation of Pb^0, but its formation is slower and yields only 8.1 % compared to 13.2 % after 20 h for the native ligand. An additional lead species occurred at higher binding energy for this ligand at ~140.9 eV, indicating a higher oxidation state than Pb^{2+} (**Figure 6.4 a + b**). The intensity ratio between this new peak and the evolving Pb^0 peak in the Pb 4f spectrum is roughly 2:1 for all irradiation times, implying that their formation is correlated (**Figure 6.4 e**). In contrast to the sample stabilized with the native ligand (*cf.* **Figure 6.1**), we did not find a similar shoulder in the iodide signal (Supporting information section S6.7), suggesting a different decomposition mechanism as a result of the ligand exchange. Before investigating this mechanism in more detail, we verify by SEM the structural integrity of the mZnTPP-stabilized red perovskites after X-ray exposure (**Figure 6.4 c**) and note that the stoichiometric composition remained roughly constant (**Figure 6.4 d**). We found the same shift in binding energies for all core-level peaks of the sample as already described for the red perovskites with the native ligand, suggesting that the shift is independent of the ligand shell and related to the NCs itself. UPS measurements before X-ray exposure revealed a shift to lower cutoff binding energies by ~0.5 eV compared to the NCs with native ligand stabilization (**Figure S6.7**). After X-ray exposure, the cutoff binding energies increase by 0.1 eV (**Figure S6.5**), reproducing the same effect as observed with the native ligand.

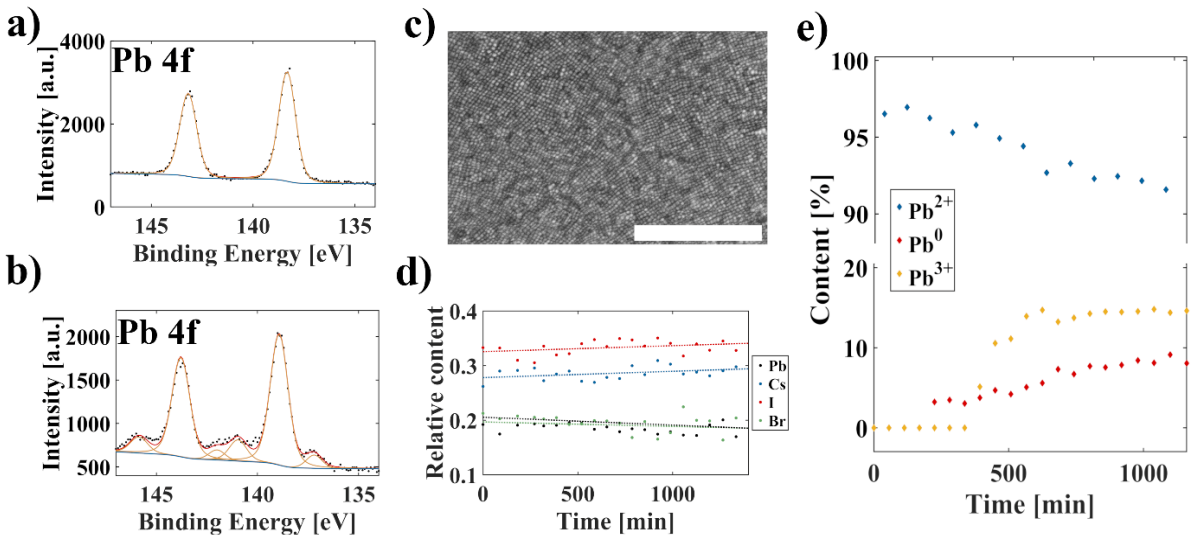

Figure 6.4: XPS of the Pb 4f orbital for $CsPbBrI_2$ with an mZnTPP ligand shell at the a) start and b) end of the experiment. Two new lead species occurred, at lower and higher binding energies. c) SEM micrograph of the mZnTPP exchanged sample after X-ray exposure for approximately 20h. Scale bar corresponds to 500 nm. d) Relative stoichiometric content and linear regression (dotted lines) of the exchanged $CsPbBrI_2$ sample over time. e) Temporal evolution of the observed lead species, the novel formed peaks are attributed to Pb^0 (~ 137 eV) and Pb^{3+} (~ 141 eV).

6.4. Discussion

Based on the XPS and WAXS results, we now propose a mechanism for the X-ray radiation-related degradation of the red and blue perovskite NCs with their native ligands. Our findings suggest a redox reaction during which Pb^0 and molecular iodine ($CsPbBrI_2$) or chlorine ($CsPbBr_2Cl$) are formed. While iodine resides within the sample after 20 h in ultra-high vacuum, chlorine is removed. This suggests the following decomposition reaction for the red perovskites:

$$\begin{aligned} CsPbBrI_2(xl) &\rightarrow CsBr(s) + PbI_2(s) \\ PbI_2(s) &\rightarrow Pb^0(s) + I_2(s)\,, \end{aligned} \tag{6.1}$$

where (xl) refers to the crystalline and (s) to the solid state. Similar mechanisms are postulated for $MAPbI_3$ and $CsPbBrI_2$ thin films, where a comparable Pb peak was found. [35,37,55,340,341] The first reaction is facilitated by the low enthalpy of formation for $CsPbBrI_2$ as shown by calorimetry. [54] We believe that the second reaction is enabled by the high energy radiation. In view of the high volatility of I_2, particular in ultra-high vacuum, we note that the formation of polyiodides, such as I_3^-, is possible under these conditions which greatly reduces its volatility. [55,346]

We suggest a similar decay mechanism for the blue perovskites based on the analogous formation of a Pb^0 signal (**Figure 6.1 f**). We interpret the absence of a novel chlorine peak (**Figure 6.1 g**) and the strong decrease in chlorine content (**Figure 6.1 h**) as indirect evidence for the oxidation of chloride, since Cl_2 is highly volatile and polychlorides are less stable than polyiodides. In this scenario, chlorine would immediately evaporate and remain undetected by XPS. The crystal decomposition expected from such a loss in material is consistent with the greatly altered morphology found by SEM (**Figure S6.4**). Our finding that, in the red and blue perovskites alike, bromide is neither oxidized nor removed from the sample, can be rationalized in terms of the oxidation potentials and enthalpies of decomposition for all three halides. Firstly, the oxidation potential of bromide (E^0 = -1.087 V) is larger than that of iodide (E^0 = -0.5355 V) and triiodide (E^0 = -0.536 V), favoring the oxidation of the latter. In contrast, the oxidation potential of chloride (E^0 = -1.396 V) is higher than for bromide. However, the enthalpy of decomposition is roughly 0.22 eV larger for $CsPbBr_3$ than for $CsPbCl_3$, which we hold responsible for the observed overall oxidation and removal of chloride. [347] We now discuss the shift of the core-levels in XPS upon X-ray illumination, for which we focus on the red-emitting perovskites since the decomposition of the blue perovskites prevents a similar analysis. A core-level shift in XPS is generally attributed to a variety of origins, such as changes in the chemical environment of specific atoms, an altered electrostatic or Madelung potential, surface effects at the sample substrate interface or charging effects. [22,39,338,339] Firstly, we rule out any surface effects due to the very prominent gold substrate signal (**Figure 6.3**) which remains unaltered throughout the entire experiment. Secondly, charging effects are unlikely due to several reasons: The gold substrate signal is clearly visible, indicating a very thin perovskite film that can be assumed to be grounded. Closely

related is the high secondary electron count, originating from the substrate that we correlate to a suppression of sample charging. Lastly, the conductivities of the native as well as the mZnTPP exchanged sample are known. [296] The electric resistance in the porphyrin-containing sample is lower and should result in a smaller shift. However, we find the same shifts independent of the ligand shell and can thus assume that the shift does not originate from charging. Therefore, only two possible explanations remain: changes in either the electrostatic potential or the chemical environment. We argue that a change of the electrostatic potential in the sample is the origin of the peak shifts, which is justified in the following. The electrostatic potential in an ionic solid for an ion *i* is given as

$$V_i = \frac{e^2}{4\pi\epsilon_0 r_0} \sum_{j \neq i} \frac{z_j}{r_{ij}/r_0} = \frac{e^2}{4\pi\epsilon_0 r_0} M_i \qquad 6.2)$$

with the elementary charge *e*, vacuum permittivity ε_0, equilibrium lattice constant r_0, effective charge z_j of the *j*-th atom, the distance between the respective atoms r_{ij} and the Madelung constant M_i. To quantify the change in V_i for Pb and Cs according to **Equation (6.2)**, we calculate the changes of the radii during the contraction of the unit cell by 0.44 Å as determined from WAXS (**Figure 6.2 a**) and compare the results to the core-level shifts in XPS. The excellent agreement suggests that the lattice contraction is the reason for the measured core-level shift. We attribute the remaining small discrepancies to the inhomogeneous composition of the mixed halide system, as well as the simultaneously occurring decomposition mechanisms.

Table 6.1: Influence of irradiation by X-rays on the lattice constants and resulting distances for the $CsPbBrI_2$ NCs. The calculated electrostatic potential for Pb and Cs as well as the difference are given, experimental value in brackets.

	$CsPbBrI_2$					
	a_0=6.11Å	**a_1=5.67Å**	**Difference [eV]**	**a_0=6.11Å**	**a_1=5.67Å**	**Difference [eV]**
Atom		**Pb**			**Cs**	
d_{CsA} [Å]	5.2395	4.8497		n.a.	n.a.	
d_{AX} [Å]	3.025	2.8		4.2780	3.9598	
d_{PbA} [Å]	n.a.	n.a.		5.2395	4.8497	
V_{el} [eV]	7.5	8.1	0.6 (0.630)	8.9	9.6	0.7 (0.711)

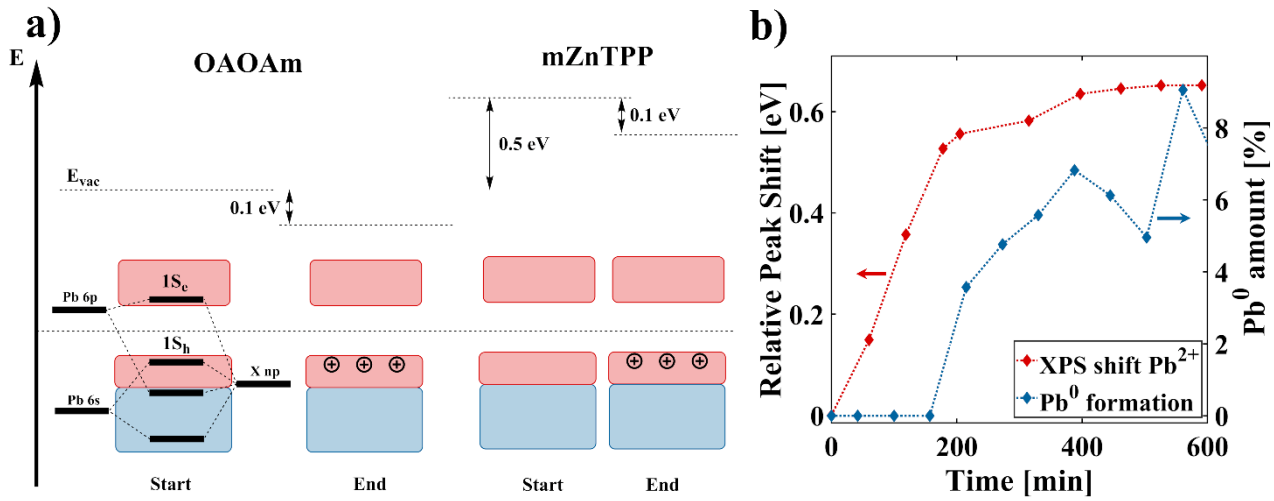

Figure 6.5: a) Energy level scheme obtained from UPS measurements for the native shell (left) and mZnTPP functionalized nanocrystals (right), all energies are referenced against the Fermi level of the instrument. The conduction state minimum ($1S_e$) and valence state maximum ($1S_h$) are indicated, respectively. The character of the states is depicted as red and blue for antibonding and bonding orbitals, respectively. The contraction of the crystal lattice resulted in a shift to higher energies by 0.1 eV for the native ligand as well as for mZnTPP. In addition, mZnTPP functionalization lowered the binding energy by 0.5 eV compared to the native functionalization. b) Temporal evolution of the XPS shift induced by the lattice contraction (red) and the formation of elemental lead (blue).

We now discuss the effect of ligand exchange with mZnTPP on the stability of the red perovskites under X-ray irradiation. Based on our XPS results, which involve the occurrence of two novel lead species (**Figure 6.4 b**), supposedly Pb^0 and Pb^{3+}, and a constant Pb^0:Pb^{3+} ratio of 1:2 during the experiment (**Figure 6.4 e**), we suggest the following disproportionation reaction:

$$3\ CsPbBrI_2 \rightarrow Cs_3Pb_2Br_3I_6 + Pb^0 \qquad (6.3)$$

This disproportionation is consistent with our finding that no other iodide species occurred (**Figure S6.9**) under these conditions, that is, this degradation pathway does not involve halide oxidation. Despite the low stability of Pb^{3+}, this oxidation state has previously been postulated for perovskites. [339,348] In addition, the specialized experimental conditions (continuous X-ray radiation in ultra-high vacuum) may facilitate its detection. Most notably, this new degradation pathway is substantially slower than the degradation with native ligand functionalization (compare **Figure S6.3** with **Figure 6.4 e**) and proceeds solely via the reaction of lead. To rationalize this surprising effect of the mZnTPP ligand, we note a recent work on the stabilizing effect of ligands with strong (surface) dipoles on CdSe NCs against irreversible reduction during charging. [349] During XPS, the NCs are subject to substantial charging and, while not all considerations for the reduction of Cd in CdSe may be transferable to Pb in $CsPbBrI_2$, we argue that the general rational outlined by du Fossé *et al.* is of central importance also in the present case: mZnTPP invokes a 0.5 eV increase in work function (**Figure 6.5 a**) and provides better dielectric screening (a higher permittivity) [296] compared to the native ligand. As du Fossé *et al.* have shown, a reduced work function affects primarily the overall crystal and only to a lesser extent a localized state, such as Pb^0. [349] This stabilizes the NCs during charging and inhibits the irreversible

reduction of lead. Thus, a promising strategy to further enhance the stability of perovskite NCs is the search for ligands that induce even larger work functions.

We note that both degradation pathways – with and without mZnTPP – are preceded by the same core level energy shifts of Pb and Cs (**Figure 6.3 c + d**), which we were able to correlate with a lattice contraction (**Figure 6.2 a** and **Table 6.1**). A likely scenario for such a contraction could be either a phase transition or halide segregation. [341] The latter is a well-known phenomenon in $CsPbI_2Br$, leading to bromine-enriched crystal domains (of smaller lattice constant) with iodine-rich segregations at the boundaries. [55] **Figure 6.5 b** suggests that this transformation is a prerequisite for the redox reaction of Pb^{2+} to occur according to either **Equation (6.1)** or **(6.3)**.

Upon comparing the decomposition of our samples with the response of mixed-halide perovskites under UV radiation some similarities were found. The phase segregation / lattice contraction and iodine evaporation were found for superlattices of $CsPb(Br_xI_{1-x})_3$ NCs and could be reproduced under X-ray illumination. [115] However, we did not observe the formation of distinct $CsPbBr_3$ nanocrystals under the presented conditions, which we rationalize by the possibility of forming triiodide under the extreme environment of XPS. [55,346] Mainly this can be seen in the reduction of the photoluminescence signal and absence of bright green emission (**Figure S6.10**).

In conclusion, we have shown that the mechanism of photodegradation under X-ray radiation of all-inorganic mixed lead halide perovskite nanocrystals depends on the ligand shell. With the ligands oleic acid/oleylamine, we found a fast decomposition into elemental lead and halogen, similar to previous studies on bulk thin films. After ligand exchange with a metal porphyrin derivative, photodegradation was significantly slower and progressed *via* a disproportionation of Pb^{2+} to Pb^0 and Pb^{3+}. We hold an increase in work function of the nanocrystal film by 0.5 eV responsible for the altered photodegradation behavior, which was induced by the metal porphyrin derivative. This work highlights the advantageous tunability of the ligand shell of lead halide perovskite nanocrystals as an additional means to improve their photostability and suggests surface ligands that introduce strong dipoles as a general paradigm toward mitigating photodegradation.

Author information

The manuscript was written through contributions of all authors. All authors have given approval to the final version of the manuscript.

Acknowledgments

This work was supported by the DFG under grants SCHE1905/8-1 (project no. 424708673) and SCHE1905/9-1 as well as the Carl Zeiss Stiftung (Forschungsstrukturkonzept "Interdisziplinäres nanoBCP-Lab"). I.A.V. acknowledges the financial support of the Russian Federation represented by the Ministry of Science and Higher Education of the Russian Federation (Agreement No. 075-15-2021-1352). The Authors would like to thank Dmitry Lapkin and Jerome Carnis for help with the

WAXS measurements. We acknowledge DESY (Hamburg, Germany), a member of the Helmholtz Association HGF, for the provision of experimental facilities. Parts of this research were carried out at PETRA III synchrotron facility and we would like to thank the beamline staff for assistance in using the Coherence Application P10 beamline.

6.5. Supplementary Information

Mitigating the Photodegradation of All-Inorganic Mixed-Halide Perovskite Nanocrystals by Ligand Exchange

Supplementary Information

Jan Wahl[$,‡], *Philipp Haizmann*[$,‡], *Christopher Kirsch*[$], *Rene Frecot*[$], *Nastasia Mukharamova*[#], , *Dameli Assalauova*[#], *Young Yong Kim*[#], *Ivan Zaluzhnyy*[+], *Thomas Chassé*[$,ß], *Ivan A. Vartanyants*[#], *Heiko Peisert*[$,]*, *Marcus Scheele*[$,ß,]*

[$] Institut für physikalische und theoretische Chemie, Universität Tübingen, Auf der Morgenstelle 18, D-72076 Tübingen, Germany

[#] Deutsches Elektronen-Synchrotron DESY, Notkestraße 85, D-22607 Hamburg, Germany

[+] Institut für Angewandte Physik, Universität Tübingen, Auf der Morgenstelle 10, D-72076 Tübingen, Germany

[ß] Center for Light-Matter Interaction, Sensors & Analytics LISA[+], Universität Tübingen, Auf der Morgenstelle 15, D-72076 Tübingen, Germany

[‡] These authors contributed equally

Materials and methods

Materials

1-Octadecene (ODE), technical grade, 90%, Sigma Aldrich; Oleic acid (OA), 97%, Acros Organics; Oleylamine (OAm), 80-90%, Acros Organics; Caesium carbonate (Cs_2CO_3), 99.99% (trace metal basis), Acros Organics; Lead(II)iodide (PbI_2), 99.999% (trace metal basis), Sigma Aldrich; Lead(II)bromide ($PbBr_2$), ≥98%, Sigma Aldrich; Lead(II)chloride ($PbCl_2$), Puratronic™, 99.999% (metal trace), Crystalline, Alfa Aesar; Toluene, HPLC grade, 99.8%; Toluene, 99.8%, extra dry, AcroSeal, Acros Organics; zinc-(5-monocarboxyphenyl-10,15,20-triphenylporphyrin) (mZnTPP), TriPorTech; Tetrachloroethylene (TCE), ≥99%, Acros Organics; Kapton® polyimide membranes (125 µm thickness), DuPont

$CsPbX_3$ nanocrystal synthesis

The used nanocrystals were synthesized with two different stoichiometries, namely $CsPbBrI_2$ and $CsPbBr_2Cl$, following the published synthesis route by Protesescu *et al.* [19] with slight adjustments. For $CsPbBrI_2$ a 20ml glass reaction vial was used which could be heated to the reaction temperature of 160°C in a custom-made aluminum heating block. Generally, the syntheses were carried out with twice the concentration of precursors compared to literature.

Ligand exchange and thin film preparation

Following the purification, the nanocrystals (NC) were either used as obtained or post-synthetically modified by ligand exchange with zinc-(5-monocarboxyphenyl-10,15,20-triphenylporphyrin) (mZnTPP). The exchange was effectively carried out in solution by adding 0.25 stoichiometric equivalents of mZnTPP to the NC solution. An immediate color change was observed upon addition. The ligand exchange procedure and corresponding analysis is given in more detail in another paper. [296]

The as-synthesized and exchanged NCs were subsequently spin-coated onto custom-made gold substrates under nitrogen atmosphere to prepare thin films. The coating parameters were chosen to be 10 rps for 30 s with a 3 s ramp.

The used substrates were custom made at the $LISA^+$ center Tübingen. A commercially available four-inch silicon wafer with native oxide layer was coated with 10 nm chromium in an evaporation chamber, followed by deposition of a 50 nm gold layer.

Self-assembly into superlattices

To prepare superlattices for the X-ray scattering measurements, the perovskite samples were prepared as 1-3 mM solutions in toluene ($CsPbBrI_2$) or tetrachloroethylene ($CsPbBr_2Cl$) and drop-casted onto Kapton® substrates under inert atmosphere. The substrates were placed inside a petri dish

with an additional reservoir of solvent (1-2 ml) to slow down the evaporation process and covered with a lid. The samples were allowed to dry for 24 h before the lid was removed and an additional drying process for 5–6 h was allowed.

Scanning electron microscopy (SEM)

SEM was carried out at a HITACHI SU8030 electron microscope, utilizing an acceleration voltage of 30 kV. SEM micrographs were taken of thin film samples.

X-ray photoelectron spectroscopy and ultraviolet photoelectron spectroscopy

The thin film samples were analyzed inside an ultrahigh vacuum chamber (base pressure: 2 x 10^{-10} mbar) with a XR-50M X-ray source from SPECS utilizing monochromatic Al Kα radiation ($h\nu$ = 1486.7 eV) with a flux of $2.3 \cdot 10^{11}$ photons/s. For photoelectron detection a Phoibos 150 DLD hemispherical photoelectron energy analyzer (SPECS) was used. The spectrometer was calibrated to reproduce the binding energy of Au $4f_{7/2}$ (84.0 eV) and Cu $2p_{3/2}$ (932.6 eV) signals, with photoionization cross sections of 0.2511 and 0.3438, respectively. [350] Measurements were performed under fixed analyzer transmission mode, with an energy resolution of 400 meV and 150 meV for XPS and Ultraviolet photoelectron spectroscopy (UPS), respectively. Custom written scripts were used to measure overview and detailed spectra at specified times during the experiment. Peak fitting was done using the Unifit software package. [351] Peaks are expected to show Voigt profile, meaning a convolution of Lorentzian and Gaussian peaks. The background was modeled with an iterative algorithm to apply Shirley background.

UPS was carried out with similar conditions as XPS measurements. A helium ultraviolet source with an energy of 21.22 eV was used in combination with a Phoibos 150 DLD electron analyzer.

XPS and UPS experiments were conducted on thin film samples.

Small- and wide-angle X-ray scattering

The small- and wide-angle X-ray scattering (SAXS and WAXS) were carried out at the Coherence Applications beamline P10 of the PETRA III synchrotron source at the Deutsche Elektronen-Synchrotron (DESY). The X-ray source provided a beam with a wavelength of λ=0.0898nm or an energy of 13.8 keV, the beam was focused on a spot size of roughly 400x400 nm^2 with a focal depth of 0.5 mm. A two-dimensional EIGER X4M (Dectris) detector with 2070x2167 pixels of size 75x75 μm^2 was used, it was located 412 mm away from the sample plane. The detector was positioned in a way to allow simultaneous measurements of SAXS and WAXS. The exposure time of the samples was 0.5 s. The obtained diffraction patterns were analyzed by Bragg peak assignment and radial profiles could be achieved by averaging over the angular coordinates. For SAXS and WAXS measurements superlattice samples were used.

S6.1: Low Binding energy survey from XPS

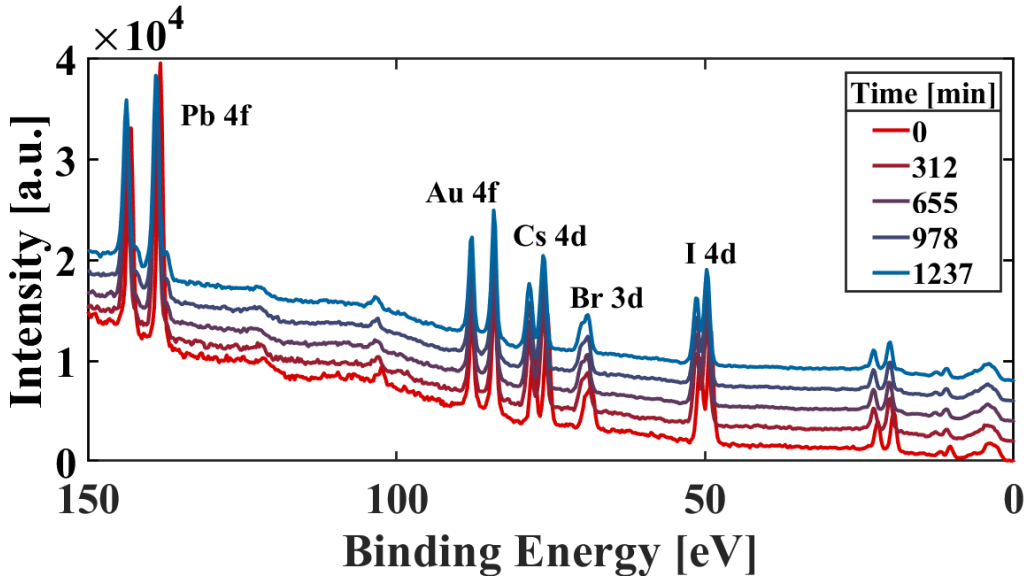

Figure S6.1: Survey spectra at different times during the X-ray illumination. A shift in peak position for all elements associated with the perovskites can be observed. As the perovskites were deposited on a gold substrate, the Au 4f core level peak serves as a reference for the binding energies. Another interesting feature is the occurrence of an additional novel peak in the Pb 4f region, visible at lower binding energies after illumination, indicating the decomposition of the nanocrystals (*cf.* **Figure 6.1** of the manuscript). Beside of the energetic shift of the Br 3d peak no further change could be observed, *i.e.*, it was not possible to detect an additional species for this element arising from the degradation.

S6.2: Calculation of the I:Pb ratio and temporal evolution of novel lead species

As detail XPS spectra are generally not comparable, the ratio of formed elemental lead and iodine was calculated as follows. The percentages were taken from the ratio of the areas fitted to the detail spectra as shown in **Figure S6.2**. Subsequently, the areas from the survey spectra were fitted as described in the methods section. The as obtained areas were then multiplied with the percentages from the detail spectra, resulting in areas that are quantitatively comparable.

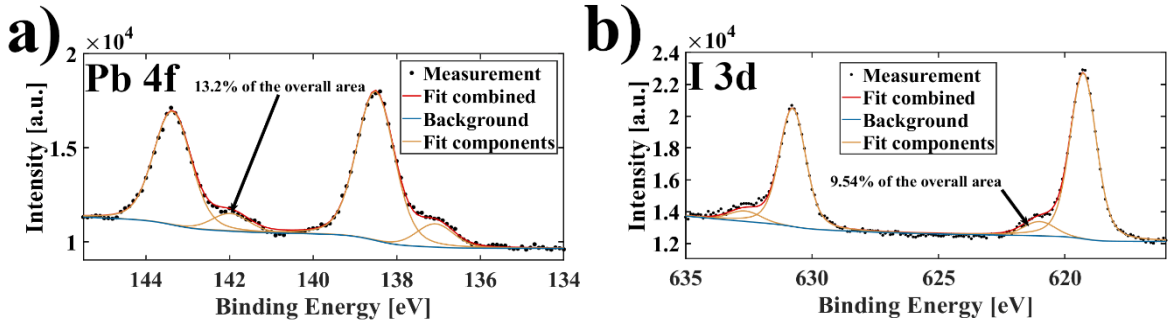

Figure S6.2: Percentages of the novel formed species after illuminating the native sample for ~20h for a) lead and b) iodide. The amount of newly formed species is given as a percentage of the overall peak area in both cases.

Generally, an error of 10% per fitted peak area is assumed. [352] Additionally, a Gaussian error propagation was carried out since multiple calculations were done with the measured values. The precise error calculation is given by:

$$\Delta\left(\frac{I_2}{Pb^0}\right) = \Delta R = \sqrt{\left(\frac{\partial R}{\partial A_{I_2}} * \Delta A_{I_2}\right)^2 + \left(\frac{\partial R}{\partial A_{Pb^0}} * \Delta A_{Pb^0}\right)^2} \tag{S6.1}$$

With the ratio of formed iodine to elemental lead R, the Area of iodine A_{I2} and elemental lead A_{Pb0} as well as the corresponding uncertainties denoted by Δ. The error calculation resulted in an error of the ratio of 0.23.

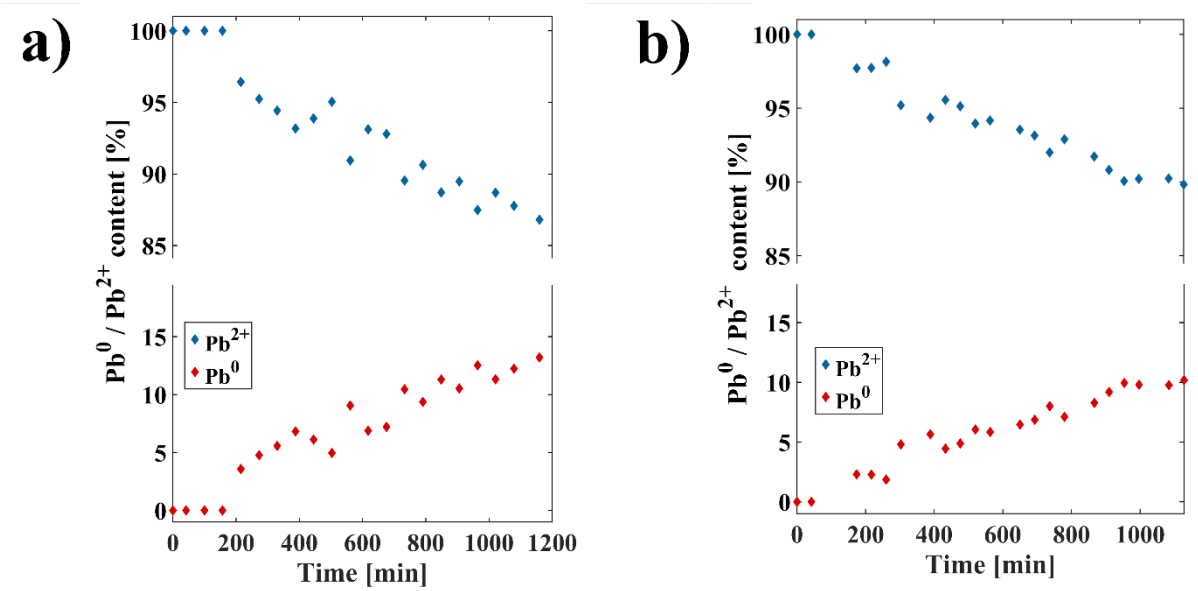

Figure S6.3: Temporal evolution of elemental lead (Pb^0) for a) $CsPbBrI_2$ and b) $CsPbBr_2Cl$ obtained by fitting the Pb 4f XPS spectra in **Figure 6.1** of the manuscript.

S6.3: Structural integrity probed by SEM for $CsPbBrI_2$ and $CsPbBr_2Cl$

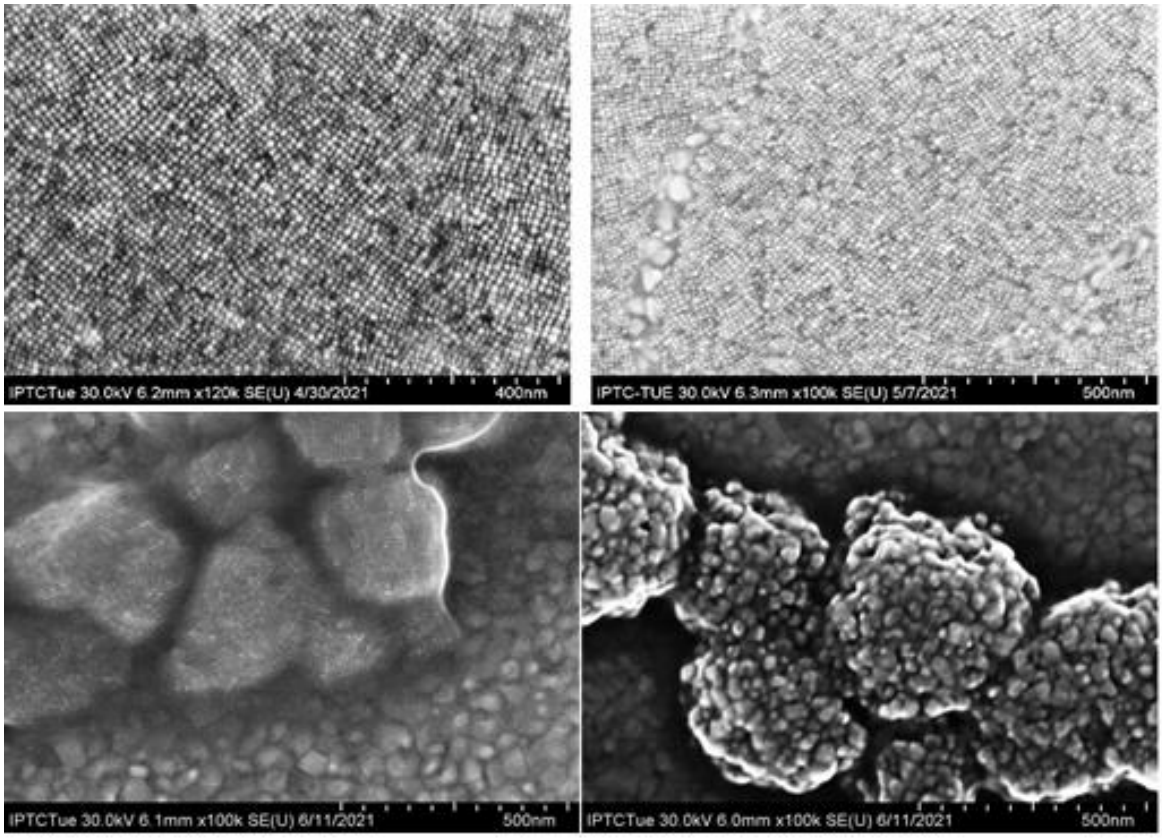

Figure S6.4: SEM of $CsPbBrI_2$ (top) and $CsPbBr_2Cl$ (bottom) before (left) and after (right) X-ray exposure.

S6.4: UPS of native and exchanged $CsPbBrI_2$ before and after X-ray illumination

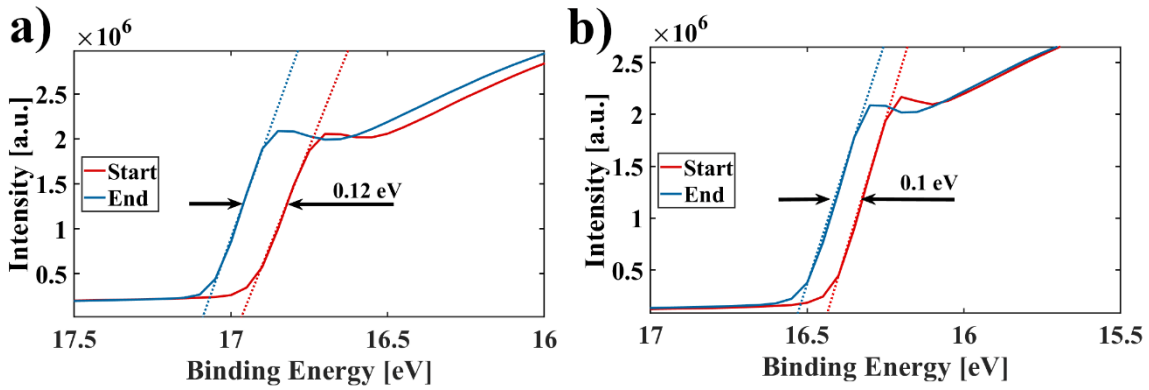

Figure S6.5: UPS cut-off energies of a) native and b) exchanged $CsPbBrI_2$. The shift in the cut-off energy of ~0.1 eV in both cases is found from a linear extrapolation, the shift indicates a reduction of the work function by the same amount. The fits are indicated as dotted lines.

The shifts of the UPS onset were found to be $\Delta_{native} = 0.12333\ eV$ and $\Delta_{TPP} = 0.0947\ eV$ from fitting. However, as UPS has a resolution limit of one decimal, the value for both shifts was taken to be ~ 0.1 eV.

S6.5: Further example of the lattice contraction

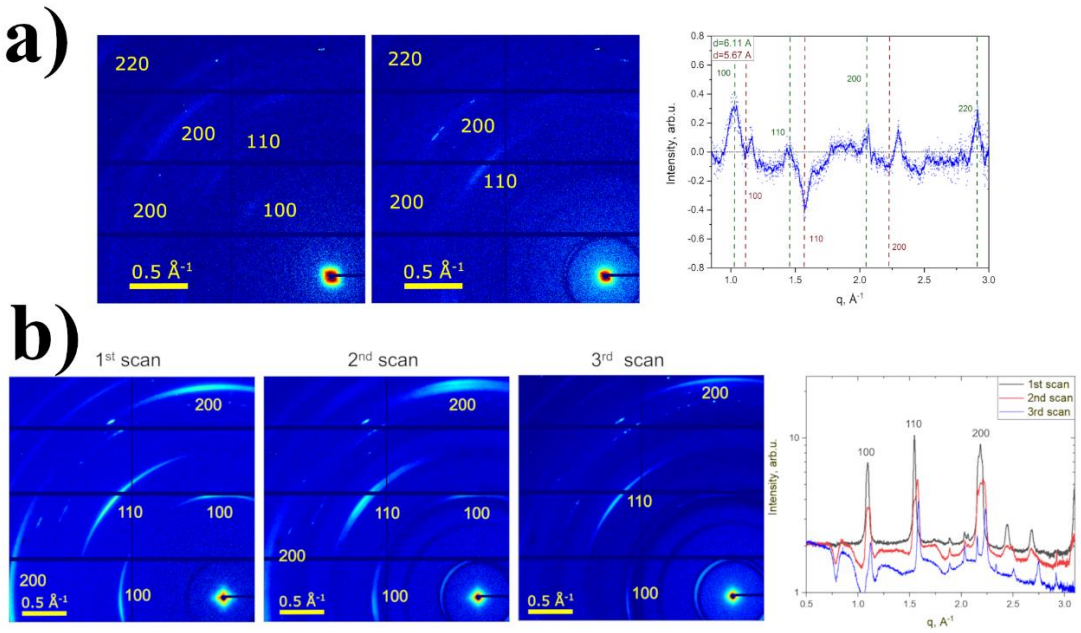

Figure S6.6: More examples of the isotropic lattice contraction for a) $CsPbBrI_2$ and b) $CsPbBr_2Cl$

S6.6: UPS overview spectra and onset

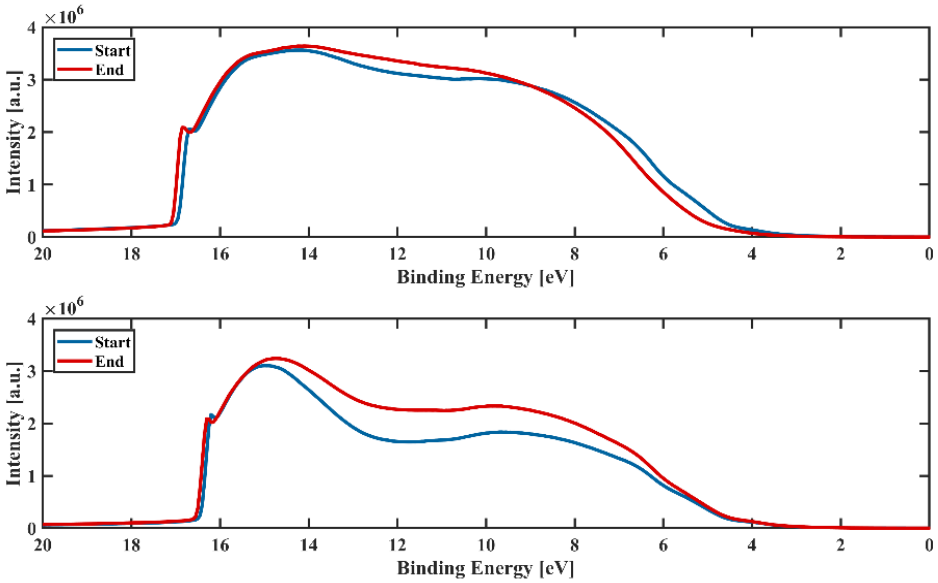

Figure S6.7: UPS overview spectra of the native $CsPbBrI_2$ sample (top) and the mZnTPP exchanges sample (bottom). The cutoff energies are shifted by ~0.5 eV.

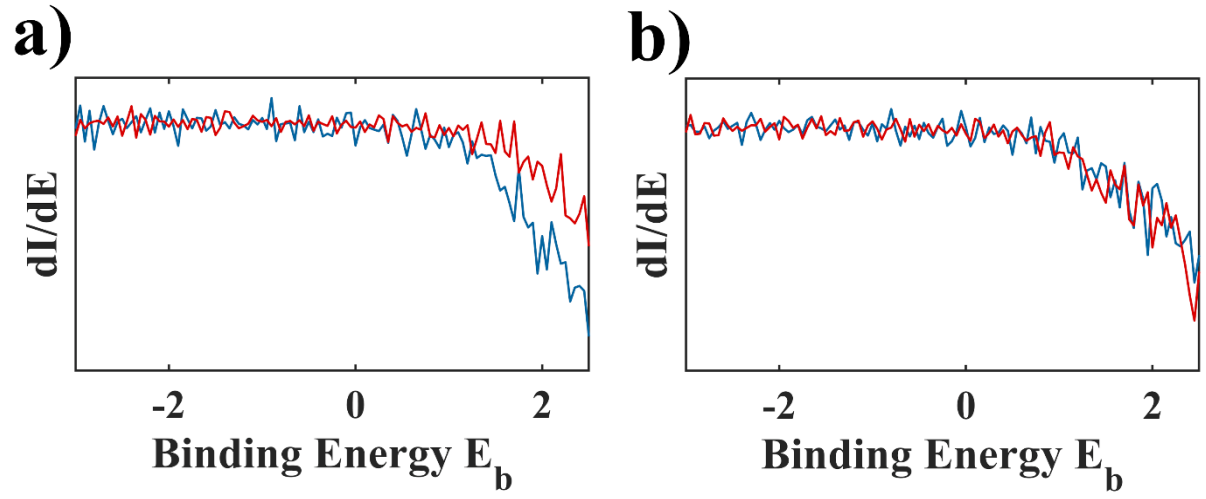

Figure S6.8: The onset remained constant at ~1 eV, shown by the derivative of the UPS spectrum for a) native and b) mZnTPP functionalized $CsPbBrI_2$. The constant onset refers to the Fermi level being located in the middle of the band gap before and after the illumination. Therefore, a shift of the energy states in their entirety is at hand.

S6.7: Iodide preservation for CsPbBrI2 functionalized with mZnTPP

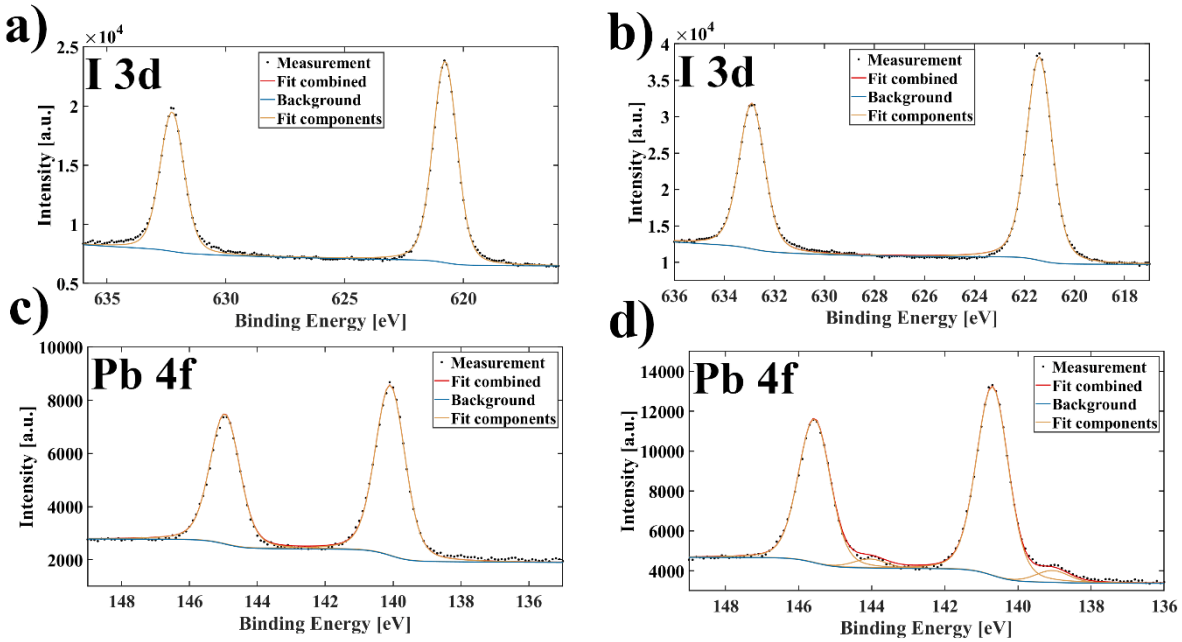

Figure S6.9: I 3d (a + b) and Pb 4f (c + d) XPS detail spectra for the mZnTPP exchanged sample. The decomposition of the NCs started as indicated by the formation of elemental lead. However, there are no novel peaks for the iodide signal.

S6.8: Photoluminescence loss after X-ray illumination

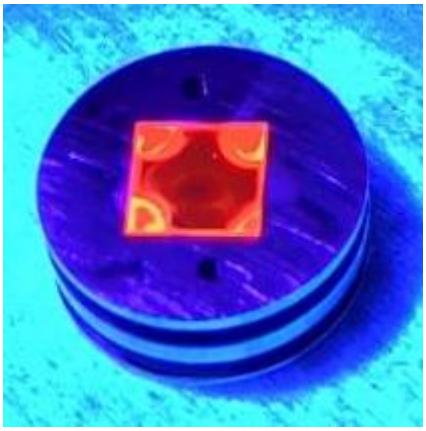

Figure S6.10: $CsPbBrI_2$ sample after exposure to X-ray radiation for ~21 h. The middle of the sample was illuminated, the area exhibits a darker spot corresponding to a loss of PL response.

7. Conclusion

Within chapters 1 and 2 the crucial parameters for an optimized light emitting diode have been introduced, *viz.* the structure, optical properties, electrical transport / charge injection, and stability. The optimization of each parameter, as well as the interplay define the efficiency of a material for LEDs. Every aspect affecting the efficiency in itself comes with intrinsic difficulties and estimating the effect on the interplay with other influences is extremely complicated, if not impossible. The results presented in this work provide experimental insights on approaches to tackle these problems and prepare diodes with better performance.

In the beginning, the implications of the solid-state structure on optical properties were discussed. It was found that upon assembling perovskite NCs in superlattices, the interparticle interactions are no longer negligible. The structural coherence of the individual NCs inside the SL has major implications on their emission. It could be shown that the edges of SLs exhibit a distortion from a perfect simple cubic lattice, whereas these imperfections are almost absent in the center of the SL. The distortions can reach magnitudes of up to 2–3 %, resulting in an increased interaction of NCs located at the center. The effect on the photoluminescence signal was probed as a hypsochromic shift of up to ~20 meV near the edges. This shift originates in a lower nearest neighbor count at the edges, along with a larger interparticle spacing due to misalignment, and an increased strain. These findings emphasize the importance of structural coherence for perovskites-based LEDs, and how preparative methods can affect the performance of an optical device.

In a subsequent step, the organic ligand shell of perovskites was investigated to gain deeper insight on the dynamics of the NCs and the ligands tethered to the surface. L–α–lecithin functionalized LHP NCs and ligand micelles were found to exhibit Fickian diffusion in solution, which could be used to confirm micelles of 4–5 nm diameter in the solution. On the other hand, a highly dynamic surface equilibrium was found on the NC-ligand interface. The diffusion of lecithin on the surface also follows Fickian´s laws of diffusion, however the diffusion coefficient is tunable with the ligand concentration. Upon increasing the concentration of L–α–lecithin in the samples, the ligand density at the surface increases as well and this alters the binding situation of the zwitterionic ligand. A higher ligand density results in more ligands being tethered with only one of the two functional headgroups (amine and phosphonate), which in turn facilitates the lateral movement. This phenomenon is reflected in a lateral diffusion coefficient almost twice as large as in a sample without excess ligand. Effectively, this highly dynamic system can be utilized during ligand exchange reactions.

The aforementioned surface dynamics could then be exploited to exchange the native ligand shell on mixed-halide LHP NCs and introduce an organic semiconductor to the particle surface. This novel ligand partially compensated the surface dipole through extending the excitonic wavefunction

onto the ligand and a more effective dielectric screening. This effectively lowered the charge injection energy, which resulted in a 2–3 times lower electronic resistance. Additionally, after applying these NCs to a LED the current efficacy of the device was enhanced almost fivefold. The enhancement can be rationalized by a better charge carrier balance and less quenching in the emitter layer, induced by the lower charging energy.

Lastly, the NCs with the novel functionalization were probed for the stability under X-ray illumination. A first main finding was a decelerated decay for this novel system, which can be explained by the surface dipole compensation mentioned before. The Fermi level is shifted to lower energies, *i.e.*, the system is stabilized against oxidation. Therefore, the decay mechanism of the native system is no longer accessible, and the system chooses another pathway. The exchanged organic semiconductor induces a disproportionation of Pb^{2+} to Pb^{0} and Pb^{3+} during the decomposition, whereas the native system in contrast decays into the respective halide salts. A second major finding was a lattice contraction under X-ray exposure, correlated to a phase segregation of iodide and bromide. The contraction precedes the decay in both the native and exchanged system and appears as a likely energy source for the decay, since the electrostatic potential in the crystal is altered *via* lattice contractions.

To summarize, within the framework of this thesis the influences mentioned at the beginning could suitable be tackled. By carefully tuning the properties of LHP-based light emitting materials it was possible to prepare more stable and efficient devices. Additionally, the results presented here encourage the search for other surface ligands to further improve the optoelectronics of such systems. This enables a new approach, based on coupled organic-inorganic nanostructures, for optimization. For example, the utilization of multidentate organic semiconductors could benefit from the chelate effect to further improve the structural coupling of the NCs in a superstructure and lowering the tunneling barrier. Also, the fine tuning of the dielectric properties of NC and ligand might further decrease the charging energy and charge carrier screening, which would benefit the LED characteristics. Overall, the importance of the ligand shell for optoelectronic applications was discussed throughout this text and methods were presented to carefully tailor the properties of the system, which can be further improved in the future.

List of Abbreviations

$1S_e$	Conduction band state
$1S_h$	Valence band state
AFM	Atomic force microscopy
AL	Atomic lattice
Al	Aluminium
AO	Atomic orbital
BATS	Backscattering and time-of-flight spectroscopy
bcc	Body-centered cubic
BF_4^-	Tetrafluoroborate anion
Ca	Calcium
$CaTiO_3$	Calcium titanate
cf.	*conferatur* (compare)
CdSe	Cadmium selenide
CIE	Commission Internationale de l´Éclairage (International commission on illumination)
Cl	Chlorine / chloride
CMC	Critical micelle concentration
CNT	Classical nucleation theory
CO_2	Carbon dioxide
COIN	Coupled organic-inorganic nanostructure
COVID	Corona virus disease
Cs	Caesium
Cs_2CO_3	Caesium carbonate
CsCl	Caesium chloride
$CsPbX_3$	All-inorganic caesium lead perovskites
d_8-Tol	Deuterated toluene
DESY	Deutsches Elektronen Synchrotron (German electron synchrotron)
DFG	Deutsche Forschungsgemeinschaft (German research foundation)
DFT	Density functional theory
DLS	Dynamic light scattering
DLVO theory	Derjaguin Landau Verwey Overbeek theory
DOS	Density of states

DOSY	Diffusion ordered nuclear magnetic resonance spectroscopy
e.g.	*exempli gratia* (for example)
EISF	Elastic incoherent structure factor
ELQLED	Electroluminescent quantum dot light emitting diode
EQE	External quantum efficiency
et al.	*et alia* (and others)
Et_3OBF_4	Meerwein´s reagent Triethyl oxonium tetrafluoroborate
EtAc	Ethyl acetate
ETL	Electron transmitting layer
fcc	Face-centered cubic
FCF	Franck-Condon factor
FET	Field-effect transistor
FID	Free induction decay
FLIM	Fast fluorescence lifetime imaging microscopy
FRET	Förster resonance energy transfer
FT	Fourier transform
FWHM	Full width at half maximum
hcp	Hexagonal closed packed
HexAcid	Hexanoic acid
HOMO	Highest occupied molecular orbital
HRTEM	High-resolution transmission electron microscopy
HTL	Hole transmitting layer
I	Iodine / iodide
i.e.	*id est* (that is to say)
ILL	Institute Laue-Langevin
InP	Indium phosphide
IPTC	Institut für physikalische und theoretische Chemie (Institute of physical and theoretical chemistry)
IRF	Instrument response function
ISC	Intersystem crossing
ITO	Indium tin oxide
LED	Light emitting diode
LHP	Lead halide perovskite
LO	Longitudinal optical

LUMO	Lowest unoccupied molecular orbital
$MAPbX_3$	Methylammonium lead perovskites
MeOH	Methanol
Mg	Magnesium
mMTPP	Monocarboxy metal-tetraphenylporphyrin
MO	Molecular orbital
NC	Nanocrystal
Ni4APc	Ni-tetraaminophthalocyanine
NNH	Nearest-neighbor hopping
NMR	Nuclear magnetic resonance spectroscopy
$NOBF_4$	Nitrosonium tetrafluoroborate
NP	Nanoparticle
NTSC	National television systems committee
O	Oxygen
OA	Oleic acid
OAm	Oleylamine
ODE	1-Octadecene
OSC	Organic semiconductor
PEDOT:PSS	Poly(3,4-ethylenedioxythiophene) polystyrene sulfonate
Pb	Lead
$Pb(ac)_2$	Lead acetate
PbS	Lead sulfide
PbSe	Lead Selenide
$PbBr_2$	Lead bromide
$PbCl_2$	Lead chloride
PbI_2	Lead iodide
PL	Photoluminescence
PTCDA	Perylenetetracarboxylic dianhydride
PTFE	Polytetrafluoroethylene
QENS	Quasielastic neutron scattering
QD	Quantum dot
QDLED	Quantum dot light emitting diode
QY	Quantum yield
ROI	Region of interest

S	Sulfur
SALC	Symmetry adapted linear combinations
SANS	Small-angle neutron scattering
SAS	Small-angle scattering
SAXS	Small-angle X-ray scattering
sc	Simple cubic
SEM	Scanning electron microscopy
SI	Supplementary information
SILAR	Successive ion layer adsorption and reaction
SiO_2	Crystalline silicon oxide
SiO_x	Amorphous silicon dioxide
SL	Superlattice
SLD	Scattering length density
SOC	Spin-orbit coupling
SRR	Specific resistance ratio
TAC	Thermally activated conduction
TCE	Tetrachloroethylene
TCSPC	Time-correlated single photon counting
TFB	Poly[(9,9-dioctylfluorenyl-2,7-diyl)-co-(4,4'-(N-(4-sec-butylphenyl)diphenylamine)]
TDM	Transition dipole moment
TMOS	Tetramethoxy orthosilicate
ToF	Time-of-flight
TOP	Trioctylphosphin
TPBi	1,3,5-Tris(1-phenyl-1HBenzimidazol-2-yl)benzene)
TV	Television
tZnTPP	Zn-tetracarboxyphenylporphyrin
UPS	Ultraviolet photoelectron spectroscopy
UV	Ultraviolet
UV-vis	Ultraviolet-visible
v. v.	*vice versa* (in reverse)
vdW	van der Waals
via	through
viz.	*videlicet* (namely)

VRH	Variable range hopping
vs.	*versus* (in contrast)
WAXS	Wide-angle X-ray scattering
X	Halogen
XPS	X-ray photoelectron spectroscopy
Zn	Zinc
ZnS	Zinc sulfide

List of Figures and Tables

Bibliography

[1] D. Chew, M. Azizi, *The state of video conferencing 2022*, https://www.dialpad.com/blog/video-conferencing-report/. (Last accessed 25.02.2022).

[2] S. Sridharan, S. KJ, *How the cryptocurrency rush added to the semiconductor crisis* **2022**, https://www.moneycontrol.com/news/opinion/how-the-cryptocurrency-rush-added-to-the-semiconductor-crisis-7787791.html. (Last accessed 25.02.2022).

[3] G. Migiro, *10 of the World's Most Traded Goods* **2018**, https://www.worldatlas.com/articles/10-of-the-world-s-most-traded-goods.html. (Last accessed 25.02.2022).

[4] B. Blanchard, M. Anantharaman, *Taiwan's TSMC says to comply with export control rules on Russia* **2022**, https://www.reuters.com/technology/taiwans-tsmc-says-comply-with-export-control-rules-russia-2022-02-25/. (Last accessed 25.02.2022).

[5] European Commission, *COMMISSION RECOMMENDATION of 18 October 2011 on the definition of nanomaterial* **2011**.

[6] S. Hamilton, *Computer* **1999**, *32*, 43.

[7] K. S. Subramanian, V. Karthika, M. Praghadeesh, A. Lakshmanan, *Nanotechnology for Mitigation of Global Warming Impacts*, Springer Singapore **2020**.

[8] Nature, *Nature Nanotechnology* **2007**, *2*, 325.

[9] T. Hornigold, *How Can Nanotechnology Be Used to Help Limit Climate Change?* **2018**, https://www.azonano.com/article.aspx?ArticleID=4895. (Last accessed 25.02.2022).

[10] Clarivate, *Analyze results: "light emitting diode"*, https://www.webofscience.com/wos/woscc/analyze-results/1935c798-16d4-431b-ae68-79460cda10a1-25e0c7d0. (Last accessed 25.02.2022).

[11] A. Maier, F. Strauß, P. Kohlschreiber, C. Schedel, K. Braun, M. Scheele, *ArXiv Preprint* **2021**, https://arxiv.org/abs/2112.11987.

[12] T. Smith, J. Guild, *Transactions of the Optical Society* **1932**, *33*, 73.

[13] G. J. Supran, Y. Shirasaki, K. W. Song, J.-M. Caruge, P. T. Kazlas, S. Coe-Sullivan, T. L. Andrew, M. G. Bawendi, V. Bulović, *MRS Bulletin* **2013**, *38*, 703.

[14] Z. Wu, P. Liu, W. Zhang, K. Wang, X. W. Sun, *ACS Energy Letters* **2020**, *5*, 1095.

[15] avantama, *Are Quantum Dot TVs Outperforming OLEDs?*, https://avantama.com/quantum-dot-tvs-outperforming-oleds/. (Last accessed 01.03.2022).

[16] Oled Display Info, *What is a QDLED*, http://www.oled-display.info/what-is-a-qdled. (Last accessed 01.03.2022).

[17] Y.-H. Won, O. Cho, T. Kim, D.-Y. Chung, T. Kim, H. Chung, H. Jang, J. Lee, D. Kim, E. Jang, *Nature* **2019**, *575*, 634.

[18] Samsung Group, *QLED TVs*, https://www.samsung.com/de/tvs/qled-tv/. (Last accessed 01.03.2022).

[19] L. Protesescu, S. Yakunin, M. I. Bodnarchuk, F. Krieg, R. Caputo, C. H. Hendon, R. X. Yang, A. Walsh, M. V. Kovalenko, *Nano Letters* **2015**, *15*, 3692.

[20] J. Wahl, *Coupled organic inorganic nanostructures (COIN) of core-shell Indium Phosphide / Zinc Sulfide qunatum dots prepared via reactive surface passivation* **2018**. Master thesis, Eberhard Karls Universität Tübingen.

[21] M. Scheele, *Bunsen Magazin* **2014**, *4*, 168.

[22] M. Scheele, W. Brütting, F. Schreiber, *Physical Chemistry Chemical Physics PCCP* **2015**, *17*, 97.

[23] A. Thomas, K. Sandeep, S. M. Somasundaran, K. G. Thomas, *ACS Energy Letters* **2018**, *3*, 2368.

[24] F. Krieg, Q. K. Ong, M. Burian, G. Rainò, D. Naumenko, H. Amenitsch, A. Süess, M. J. Grotevent, F. Krumeich, M. I. Bodnarchuk, I. Shorubalko, F. Stellacci, M. V. Kovalenko, *Journal of the American Chemical Society* **2019**, *141*, 19839.

[25] Q. A. Akkerman, L. Manna, *ACS Energy Letters* **2020**, *5*, 604.

[26] H. Kim, L. Zhao, J. S. Price, A. J. Grede, K. Roh, A. N. Brigeman, M. Lopez, B. P. Rand, N. C. Giebink, *Nature Communications* **2018**, *9*, 4893.

[27] Y.-H. Kim, S. Kim, A. Kakekhani, J. Park, J. Park, Y.-H. Lee, H. Xu, S. Nagane, R. B. Wexler, D.-H. Kim, S. H. Jo, L. Martínez-Sarti, P. Tan, A. Sadhanala, G.-S. Park, Y.-W. Kim, B. Hu, H. J. Bolink, S. Yoo, R. H. Friend, A. M. Rappe, T.-W. Lee, *Nature Photon* **2021**, *15*, 148.

[28] J. Zhang, C. Yin, F. Yang, Y. Yao, F. Yuan, H. Chen, R. Wang, S. Bai, G. Tu, L. Hou, *The Journal of Physical Chemistry Letters* **2021**, *12*, 2437.

[29] A. Kogo, Y. Sanehira, Y. Numata, M. Ikegami, T. Miyasaka, *ACS Applied Materials & Interfaces* **2018**, *10*, 2224.

[30] TU Graz, *MOSFET Gradual Channel Approximation*, http://lampx.tugraz.at/~hadley/psd/L10/gradualchannelapprox.php. (Last accessed 01.03.2022).

[31] A. Maier, D. Lapkin, N. Mukharamova, P. Frech, D. Assalauova, A. Ignatenko, R. Khubbutdinov, S. Lazarev, M. Sprung, F. Laible, R. Löffler, N. Previdi, A. Bräuer, T. Günkel, M. Fleischer, F. Schreiber, I. A. Vartanyants, M. Scheele, *Advanced Materials* **2020**, *32*, e2002254.

[32] A. André, M. Weber, K. M. Wurst, S. Maiti, F. Schreiber, M. Scheele, *ACS Applied Materials & Interfaces* **2018**, *10*, 24708.

[33] A. André, D. Zherebetskyy, D. Hanifi, B. He, M. Samadi Khoshkhoo, M. Jankowski, T. Chassé, L.-W. Wang, F. Schreiber, A. Salleo, Y. Liu, M. Scheele, *Chemistry of Materials* **2015**, *27*, 8105.

[34] B. Kundu, A. J. Pal, *Journal of the Physical Chemistry C* **2018**, *122*, 11570.

[35] B. Conings, J. Drijkoningen, N. Gauquelin, A. Babayigit, J. D'Haen, L. D'Olieslaeger, A. Ethirajan, J. Verbeeck, J. Manca, E. Mosconi, F. D. Angelis, H.-G. Boyen, *Advanced Energy Materials* **2015**, *5*, 1500477.

[36] C. Das, M. Wussler, T. Hellmann, T. Mayer, W. Jaegermann, *Physical Chemistry Chemical Physics PCCP* **2018**, *20*, 17180.

[37] J. D. McGettrick, K. Hooper, A. Pockett, J. Baker, J. Troughton, M. Carnie, T. Watson, *Materials Letters* **2019**, *251*, 98.

[38] S. Mazumdar, Y. Zhao, X. Zhang, *Frontiers in Electronics* **2021**, *2*, 2572.

[39] W. Xiang, S. Liu, W. Tress, *Energy & Environmental Science* **2021**, *14*, 2090.

[40] G. Rose, *De novis quibusdam fossilibus, quae in montibus uraliis inveniuntur. I. De Perowskite, fossili novo.*, Berlin **1839**.

[41] G. Rose, *Journal für praktische Chemie* **1840**, *19*, 459.

[42] T. F. W. Barth, *Norwegian Journal of Geology* **1925**, *08*, 201.

[43] V. M. Goldschmidt, *Naturwissenschaften* **1926**, *14*, 477.

[44] N. S. Arul, V. D. Nithya, *Revolution of Perovskite*, Springer Singapore, Singapore **2020**.

[45] H. L. Wells, *Zeitschrift für anorganische Chemie* **1893**, *3*, 195.

[46] Q. A. Akkerman, G. Rainò, M. V. Kovalenko, L. Manna, *Nature Materials* **2018**, *17*, 394.

[47] J. Kang, L.-W. Wang, *The Journal of Physical Chemistry Letters* **2017**, *8*, 489.

[48] H. Zhu, K. Miyata, Y. Fu, J. Wang, P. P. Joshi, D. Niesner, K. W. Williams, S. Jin, X.-Y. Zhu, *Science (New York, N.Y.)* **2016**, *353*, 1409.

[49] Q. A. Akkerman, V. D'Innocenzo, S. Accornero, A. Scarpellini, A. Petrozza, M. Prato, L. Manna, *Journal of the American Chemical Society* **2015**, *137*, 10276.

[50] W. Zhihai, W. Jiao, S. Yanni, W. Jun, H. Yafei, W. Pan, W. Nengping, Z. Zhenfu, *Journal of Material Science* **2019**, *54*, 6917.

[51] L. N. Quan, B. P. Rand, R. H. Friend, S. G. Mhaisalkar, T.-W. Lee, E. H. Sargent, *Chemical Reviews* **2019**, *119*, 7444.

[52] H. J. Snaith, *Nature Materials* **2018**, *17*, 372.

[53] A. L. Wani, A. Ara, J. A. Usmani, *Interdisciplinary Toxicology* **2015**, *8*, 55.

[54] B. Wang, A. Navrotsky, *Journal of Physical Chemistry C* **2020**, *124*, 8639.

[55] L. A. Frolova, S. Y. Luchkin, Y. Lekina, L. G. Gutsev, S. A. Tsarev, I. S. Zhidkov, E. Z. Kurmaev, Z. X. Shen, K. J. Stevenson, S. M. Aldoshin, P. A. Troshin, *Advanced Energy Materials* **2021**, *11*, 2002934.

[56] F. Bertolotti, L. Protesescu, M. V. Kovalenko, S. Yakunin, A. Cervellino, S. J. L. Billinge, M. W. Terban, J. S. Pedersen, N. Masciocchi, A. Guagliardi, *ACS nano* **2017**, *11*, 3819.

[57] L. Brus, *Journal of Physical Chemistry* **1986**, *90*, 2555.

[58] M. J. Jurow, T. Morgenstern, C. Eisler, J. Kang, E. Penzo, M. Do, M. Engelmayer, W. T. Osowiecki, Y. Bekenstein, C. Tassone, L.-W. Wang, A. P. Alivisatos, W. Brütting, Y. Liu, *Nano Letters* **2019**, *19*, 2489.

[59] M. Wautelet, B. Hoppe, *Nanotechnologie*, Oldenbourg, München **2008**.

[60] N. Baig, I. Kammakakam, W. Falath, *Materials Advances* **2021**, *2*, 1821.

[61] H. W. Kroto, J. R. Heath, S. C. O'Brien, R. F. Curl, R. E. Smalley, *Nature* **1985**, *318*, 162.

[62] H. Li, J. Wu, Z. Yin, H. Zhang, *Accounts of Chemical Research* **2014**, *47*, 1067.

[63] Y. Hernandez, V. Nicolosi, M. Lotya, F. M. Blighe, Z. Sun, S. De, I. T. McGovern, B. Holland, M. Byrne, Y. K. Gun'Ko, J. J. Boland, P. Niraj, G. Duesberg, S. Krishnamurthy, R. Goodhue, J. Hutchison, V. Scardaci, A. C. Ferrari, J. N. Coleman, *Nature Nanotechnology* **2008**, *3*, 563.

[64] F. Fetzer, C. Schrenk, N. Pollard, A. Adeagbo, A. Z. Clayborne, A. Schnepf, *Chemical Communications* **2021**, *57*, 3551.

[65] S. Kenzler, F. Fetzer, C. Schrenk, N. Pollard, A. R. Frojd, A. Z. Clayborne, A. Schnepf, *Angewandte Chemie (International ed. in English)* **2019**, *58*, 5902.

[66] J. Shamsi, A. S. Urban, M. Imran, L. de Trizio, L. Manna, *Chemical Reviews* **2019**, *119*, 3296.

[67] D. Battaglia, X. Peng, *Nano Letters* **2002**, *2*, 1027.

[68] M. W. G. de Bolster, *Pure and Applied Chemistry* **1997**, *69*, 1251.

[69] J. E. Lennard-Jones, *Proceedings of the Physical Society* **1931**, *43*, 461.

[70] W. D. Knight, K. Clemenger, W. A. de Heer, W. A. Saunders, M. Y. Chou, M. L. Cohen, *Physical Review Letters* **1984**, *52*, 2141.

[71] P. G. Debenedetti, *Metastable liquids: Concepts and principles*, Princeton Univ. Press, Princeton, N.J **1996**.

[72] R. P. Sear, *Journal of Physics: Condensed Matter* **2007**, *19*, 33101.

[73] V. K. LaMer, R. H. Dinegar, *Journal of the American Chemical Society* **1950**, *72*, 4847.

[74] C. B. Murray, D. J. Norris, M. G. Bawendi, *Journal of the American Chemical Society* **1993**, *115*, 8706.

[75] Peng, Manna, Yang, Wickham, Scher, Kadavanich, Alivisatos, *Nature* **2000**, *404*, 59.

[76] L. Cademartiri, G. A. Ozin, J.-M. Lehn, *Concepts of nanochemistry*, Wiley-VCH Verlag GmbH & Co. KGaA, Weinheim **2009**.

[77] D. Zherebetskyy, M. Scheele, Y. Zhang, N. Bronstein, C. Thompson, D. Britt, M. Salmeron, P. Alivisatos, L.-W. Wang, *Science* **2014**, *344*, 1380.

[78] C. R. Bealing, W. J. Baumgardner, J. J. Choi, T. Hanrath, R. G. Hennig, *ACS Nano* **2012**, *6*, 2118.

[79] G. Wulff, *Zeitschrift für Krystallographie und Mineralogie*, *1901*, 449.

[80] A. Pan, B. He, X. Fan, Z. Liu, J. J. Urban, A. P. Alivisatos, L. He, Y. Liu, *ACS Nano* **2016**, *10*, 7943.

[81] G. Almeida, L. Goldoni, Q. Akkerman, Z. Dang, A. H. Khan, S. Marras, I. Moreels, L. Manna, *ACS Nano* **2018**, *12*, 1704.

[82] W. Ostwald, *Zeitschrift für Physikalische Chemie* **1900**, *34U*, 495.

[83] K.-K. Kang, B. Lee, C.-S. Lee, *Journal of the Taiwan Institute of Chemical Engineers* **2019**, *98*, 2.

[84] H. Zheng, R. K. Smith, Y.-W. Jun, C. Kisielowski, U. Dahmen, A. P. Alivisatos, *Science* **2009**, *324*, 1309.

[85] D. Li, M. H. Nielsen, J. R. I. Lee, C. Frandsen, J. F. Banfield, J. J. de Yoreo, *Science* **2012**, *336*, 1014.

[86] Y. Dong, T. Qiao, D. Kim, D. Parobek, D. Rossi, D. H. Son, *Nano Letters* **2018**, *18*, 3716.

[87] S. Sharma, N. Weiden, A. Weiss, *Zeitschrift für Physikalische Chemie* **1992**, *175*, 63.

[88] B. Wang, N. Novendra, A. Navrotsky, *Journal of the American Chemical Society* **2019**, *141*, 14501.

[89] K. Wang, Z. Jin, L. Liang, H. Bian, D. Bai, H. Wang, J. Zhang, Q. Wang, S. Liu, *Nature Communications* **2018**, *9*, 4544.

[90] C. L. Jackson, G. B. McKenna, *The Journal of Chemical Physics* **1990**, *93*, 9002.

[91] Y. Chen, W. Xing, Y. Liu, X. Zhang, Y. Xie, C. Shen, J. G. Liu, C. Geng, S. Xu, *Nanomaterials* **2020**, *10*.

[92] H. T. Minden, *The Journal of Chemical Physics* **1955**, *23*, 1948.

[93] F. Zhang, Z.-F. Shi, Z.-Z. Ma, Y. Li, S. Li, Di Wu, T.-T. Xu, X.-J. Li, C.-X. Shan, G.-T. Du, *Nanoscale* **2018**, *10*, 20131.

[94] P. Reiss, M. Protière, L. Li, *Small* **2009**, *5*, 154.

[95] J. J. Li, Y. A. Wang, W. Guo, J. C. Keay, T. D. Mishima, M. B. Johnson, X. Peng, *Journal of the American Chemical Society* **2003**, *125*, 12567.

[96] Y. Cheng, H. Wan, T. Liang, C. Liu, M. Wu, H. Hong, K. Liu, H. Shen, *Journal of Physical Chemistry Letters* **2021**, *12*, 5967.

[97] C. Shen, Y. Zhu, Z. Li, J. Li, H. Tao, J. Zou, X. Xu, G. Xu, *Journal of Materials Chemistry C* **2021**, *9*, 9599.

[98] K. Boldt, *Zeitschrift für Physikalische Chemie* **2017**, *231*, 77.

[99] C. Kittel, *Introduction to Solid State Physics*, John Wiley & Sons **2005**.

[100] Hinckley, Singh, *Physical reviews B, Condensed matter* **1990**, *42*, 3546.

[101] S. Kasap, P. Capper (Eds.), *Springer Handbook of Electronic and Photonic Materials*, Springer International Publishing, Cham **2017**.

[102] P. Mandracci (Ed.), *Crystalline and Non-crystalline Solids*, InTech **2016**.

[103] M. Moreno, M. Domínguez, R. Ambrosio, A. Torres, A. Torres, P. Rosales, A. Itzmoyotl, in *Crystalline and Non-crystalline Solids* (Ed.: P. Mandracci), InTech **2016**.

[104] S. D. Brotherton, *Introduction to thin film transistors: Physics and technology of TFTs*, Springer, Heidelberg u.a **2013**.

[105] W. Pauli, *Exclusion principle and quantum mechanics* **1946**, Nobel lecture.

[106] F. London, *Transactions of the Faraday Society* **1937**, *33*, 8b.

[107] J. N. Israelachvili, *Intermolecular and surface forces*, Academic Press, Burlington, MA **2011**.

[108] W. H. Keesom, *Proceedings of the Royal Netherlands Academy of Arts and Sciences*.

[109] A. D. McLachlan, *Proceedings of the Royal Society of London. Series A* **1963**, *271*, 387.

[110] A. D. McLachlan, *Discussions of the Faraday Society* **1965**, *40*, 239.

[111] E. M. Lifshitz, *Journal of Experimental Theoretical Physics USSR* **1956**, *29*, 94.

[112] H. Yukawa, *Proceedings of the Physico-Mathematical Society of Japan* **1935**, *3rd*, 48.

[113] S. Asakura, F. Oosawa, *The Journal of Chemical Physics* **1954**, *22*, 1255.

[114] J. Griffin, H. Hassan, E. Spooner, *Spin Coating: Complete Guide to Theory and Techniques*, https://www.ossila.com/pages/spin-coating. (Last accessed 05.03.2022).

[115] M. C. Brennan, S. Toso, I. M. Pavlovetc, M. Zhukovskyi, S. Marras, M. Kuno, L. Manna, D. Baranov, *ACS Energy Letters* **2020**, *5*, 1465.

[116] V. M. Yuwono, N. D. Burrows, J. A. Soltis, R. L. Penn, *Journal of the American Chemical Society* **2010**, *132*, 2163.

[117] V. J. Anderson, H. N. W. Lekkerkerker, *Nature* **2002**, *416*, 811.

[118] M. Bartelmann, B. Feuerbacher, T. Krüger, D. Lüst, A. Rebhan, A. Wipf, F. Modler, M. Kreh, *Theoretische Physik*, Springer Spektrum, Berlin **2015**.

[119] M. Born, *Zeitschrift für Physik* **1926**, *37*, 863.

[120] B. A. Lippmann, J. Schwinger, *Physical Reviews* **1950**, *79*, 469.

[121] O. Glatter, O. Kratky, *Small angle x-ray scattering: Edited by O. Glatter and O. Kratky*, Academic Press, London, New York **1983**.

[122] R. E. Dinnebier (Ed.), *Powder diffraction: Theory and practice*, Royal Society of Chemistry, Cambridge **2009**.

[123] W. H. Bragg, W. L. Bragg, *Proceedings of the Royal Society of London. Series A* **1913**, *88*, 428.

[124] Helmholtz Gemeinschaft, *P10 Coherence Beamline User Guide* **2016**, https://photon-science.desy.de/facilities/petra_iii/beamlines/p10_coherence_applications/instructions_documentation/p10_documentation/index_eng.html. (Last accessed 27.01.2022).

[125] T. Seydel, M. M. Koza, O. Matsarskaia, A. André, S. Maiti, M. Weber, R. Schweins, S. Prévost, F. Schreiber, M. Scheele, *Chemical Science* **2020**, *11*, 8875.

[126] K. Venkateswarlu, A. Chandra Bose, N. Rameshbabu, *Physica B: Physics of Condensed Matter* **2010**, *405*, 4256.

[127] O. Arnold, J. C. Bilheux, J. M. Borreguero, A. Buts, S. I. Campbell, L. Chapon, M. Doucet, N. Draper, R. Ferraz Leal, M. A. Gigg, V. E. Lynch, A. Markvardsen, D. J. Mikkelson, R. L. Mikkelson, R. Miller, K. Palmen, P. Parker, G. Passos, T. G. Perring, P. F. Peterson, S. Ren, M. A. Reuter, A. T. Savici, J. W. Taylor, R. J. Taylor, R. Tolchenov, W. Zhou, J. Zikovsky, *Nuclear Instruments and Methods in Physics Research Section A: Accelerators, Spectrometers, Detectors and Associated Equipment* **2014**, *764*, 156.

[128] D. Richard, M. Ferrand, G. J. Kearley, *Journal of Neutron Research* **1996**, *4*, 33.

[129] F. Bloch, *Zeitschrift für Physik* **1929**, *52*, 555.

[130] R. D. L. Kronig, W. G. Penney, *Proceedings of the Royal Socitey of London. Series A* **1931**, *130*, 499.

[131] F. Zu, P. Amsalem, D. A. Egger, R. Wang, C. M. Wolff, H. Fang, M. A. Loi, D. Neher, L. Kronik, S. Duhm, N. Koch, *Journal of Physical Chemistry Letters* **2019**, *10*, 601.

[132] M. D. Al-Amri, M. El-Gomati, M. S. Zubairy, *Optics in Our Time*, Springer International Publishing, Cham **2016**.

[133] S. Mohan, S. O. Oluwafemi, N. Kalarikkal, S. Thomas, *Synthesis of Inorganic Nanomaterials: Advances and Key Technologies*, Elsevier Science & Technology, San Diego **2018**.

[134] P. W. Atkins, R. Friedman, *Molecular quantum mechanics*, Oxford Univ. Press, Oxford **2011**.

[135] J. Franck, E. G. Dymond, *Transactions of the Faraday Society* **1926**, *21*, 536.

[136] E. Condon, *Physical Reviews* **1926**, *28*, 1182.

[137] P. M. Morse, *Physical Reviews* **1929**, *34*, 57.

[138] A. Jablonski, *Nature* **1933**, *131*, 839.

[139] G. Rainò, M. A. Becker, M. I. Bodnarchuk, R. F. Mahrt, M. V. Kovalenko, T. Stöferle, *Nature* **2018**, *563*, 671.

[140] J. Frenkel, *Physical Reviews* **1931**, *37*, 17.

[141] G. H. Wannier, *Physical Reviews* **1937**, *52*, 191.

[142] H. Ibach, H. Lüth, *Festkörperphysik: Einführung in die Grundlagen; mit 18 Tafeln und 104 Übungen*, Springer, Berlin **2009**.

[143] J.-C. Blancon, A. V. Stier, H. Tsai, W. Nie, C. C. Stoumpos, B. Traoré, L. Pedesseau, M. Kepenekian, F. Katsutani, G. T. Noe, J. Kono, S. Tretiak, S. A. Crooker, C. Katan, M. G. Kanatzidis, J. J. Crochet, J. Even, A. D. Mohite, *Nature Communications* **2018**, *9*, 2254.

[144] L. Hou, P. Tamarat, B. Lounis, *Nanomaterials* **2021**, *11*.

[145] M. Baranowski, P. Plochocka, *Advanced Energy Materials* **2020**, *10*, 1903659.

[146] P. Tamarat, L. Hou, J.-B. Trebbia, A. Swarnkar, L. Biadala, Y. Louyer, M. I. Bodnarchuk, M. V. Kovalenko, J. Even, B. Lounis, *Nature Communications* **2020**, *11*, 6001.

[147] M. A. Becker, R. Vaxenburg, G. Nedelcu, P. C. Sercel, A. Shabaev, M. J. Mehl, J. G. Michopoulos, S. G. Lambrakos, N. Bernstein, J. L. Lyons, T. Stöferle, R. F. Mahrt, M. V. Kovalenko, D. J. Norris, G. Rainò, A. L. Efros, *Nature* **2018**, *553*, 189.

[148] J. Even, L. Pedesseau, J.-M. Jancu, C. Katan, *Journal of Physical Chemistry Letters* **2013**, *4*, 2999.

[149] T. Förster, *Annalen der Physik* **2006**, *437*, 55.

[150] Y. Kanemitsu, *The Journal of Chemical Physics* **2019**, *151*, 170902.

[151] N. Yarita, T. Aharen, H. Tahara, M. Saruyama, T. Kawawaki, R. Sato, T. Teranishi, Y. Kanemitsu, *Physical Review Materials* **2018**, *2*.

[152] H. Fröhlich, *Advances in Physics* **1954**, *3*, 325.

[153] H. Fröhlich, H. Pelzer, S. Zienau, *The London, Edinburgh, and Dublin Philosophical Magazine and Journal of Science* **2009**, *41*, 221.

[154] T. Holstein, *Annals of Physics* **1959**, *8*, 343.

[155] T. Holstein, *Annals of Physics* **1959**, *8*, 325.

[156] F. Urbach, *Physical Reviews* **1953**, *92*, 1324.

[157] R. Vettumperumal, S. Kalyanaraman, B. Santoshkumar, R. Thangavel, *Materials Research Bulletin* **2016**, *77*, 101.

[158] B. Choudhury, A. Choudhury, *Physica E: Low-dimensional Systems and Nanostructures* **2014**, *56*, 364.

[159] G. D. Cody, T. Tiedje, B. Abeles, B. Brooks, Y. Goldstein, *Physical Review Letters* **1981**, *47*, 1480.

[160] Rudin, Reinecke, Segall, *Physical Reviews B, Condensed Matter* **1990**, *42*, 11218.

[161] J. Yi, X. Ge, E. Liu, T. Cai, C. Zhao, S. Wen, H. Sanabria, O. Chen, A. M. Rao, J. Gao, *Nanoscale Advances* **2020**, *2*, 4390.

[162] R. Saran, A. Heuer-Jungemann, A. G. Kanaras, R. J. Curry, *Advanced Optical Materials* **2017**, *5*, 1700231.

[163] D. Bozyigit, V. Wood, *MRS Bulletin* **2013**, *38*, 731.

[164] M. T. Frederick, V. A. Amin, N. K. Swenson, A. Y. Ho, E. A. Weiss, *Nano Letters* **2013**, *13*, 287.

[165] R. H. Dicke, *Physical Reviews* **1954**, *93*, 99.

[166] P. Drude, *Annalen der Physik* **1900**, *306*, 566.

[167] P. W. Atkins, J. de Paula, J. Keeler, *Physical Chemistry*, Oxford Univ. Press, Oxford **2018**.

[168] Y. Liu, M. Gibbs, J. Puthussery, S. Gaik, R. Ihly, H. W. Hillhouse, M. Law, *Nano Letters* **2010**, *10*, 1960.

[169] P. Guyot-Sionnest, *Journal of Physical Chemistry Letters* **2012**, *3*, 1169.

[170] R. A. Marcus, *Angewandte Chemie (International ed. in English)* **1993**, *32*, 1111.

[171] C. B. Murray, C. R. Kagan, M. G. Bawendi, *Annual Review of Materials Science* **2000**, *30*, 545.

[172] D. V. Talapin, J.-S. Lee, M. V. Kovalenko, E. V. Shevchenko, *Chemical Reviews* **2010**, *110*, 389.

[173] A. J. Quinn, P. Beecher, D. Iacopino, L. Floyd, G. de Marzi, E. V. Shevchenko, H. Weller, G. Redmond, *Small* **2005**, *1*, 613.

[174] F. Remacle, R. D. Levine, *ChemPhysChem* **2001**, *2*, 20.

[175] N. Mott, *Metal-Insulator Transitions*, Chapman and Hall/CRC, Boca Raton **1990**.

[176] P. W. Anderson, *Physical Reviews* **1958**, *109*, 1492.

[177] Z. Wang, C. Schliehe, K. Bian, D. Dale, W. A. Bassett, T. Hanrath, C. Klinke, H. Weller, *Nano Letters* **2013**, *13*, 1303.

[178] I. A. Zaluzhnyy, R. P. Kurta, A. André, O. Y. Gorobtsov, M. Rose, P. Skopintsev, I. Besedin, A. V. Zozulya, M. Sprung, F. Schreiber, I. A. Vartanyants, M. Scheele, *Nano Letters* **2017**, *17*, 3511.

[179] A. P. Kaushik, B. Lukose, P. Clancy, *ACS nano* **2014**, *8*, 2302.

[180] N. Yazdani, S. Andermatt, M. Yarema, V. Farto, M. H. Bani-Hashemian, S. Volk, W. M. M. Lin, O. Yarema, M. Luisier, V. Wood, *Nature Communications* **2020**, *11*, 2852.

[181] S. Arrhenius, *Zeitschrift für Physikalische Chemie* **1889**, *4U*, 226.

[182] E. R. Viana, J. C. González, G. M. Ribeiro, A. G. d. Oliveira, *Physica Status Solidi – Rapid Research Letters* **2012**, *6*, 262.

[183] N. F. Mott, *Philosophical Magazine* **1969**, *19*, 835.

[184] H. Liu, A. Pourret, P. Guyot-Sionnest, *ACS Nano* **2010**, *4*, 5211.

[185] A. L. Efros, B. I. Shklovskii, *Journal of Physics C: Solid State Physics* **1975**, *8*, L49.

[186] H.-L. Le Châtelier, *Comptes Rendus de l´Académie des Sciences* **1884**, *99*, 786.

[187] F. Braun, *Zeitschrift für Physikalische Chemie* **1887**, *1U*, 259.

[188] R. W. Crisp, N. Kirkwood, G. Grimaldi, S. Kinge, L. D. A. Siebbeles, A. J. Houtepen, *ACS Applied Energy Materials* **2018**, *1*, 6569.

[189] A. Dong, X. Ye, J. Chen, Y. Kang, T. Gordon, J. M. Kikkawa, C. B. Murray, *Journal of the American Chemical Society* **2011**, *133*, 998.

[190] E. L. Rosen, R. Buonsanti, A. Llordes, A. M. Sawvel, D. J. Milliron, B. A. Helms, *Angewandte Chemie (International ed. in English)* **2012**, *51*, 684.

[191] B. Fritzinger, R. K. Capek, K. Lambert, J. C. Martins, Z. Hens, *Journal of the American Chemical Society* **2010**, *132*, 10195.

[192] M. Wu, A. M. Vartanian, G. Chong, A. K. Pandiakumar, R. J. Hamers, R. Hernandez, C. J. Murphy, *Journal of the American Chemical Society* **2019**, *141*, 4316.

[193] M.L.H. Green, *Journal of Organometallic Chemistry* **1995**, *500*, 127.

[194] M. A. Boles, D. Ling, T. Hyeon, D. V. Talapin, *Nature Materials* **2016**, *15*, 141.

[195] Z. Lingley, S. Lu, A. Madhukar, *Nano Letters* **2011**, *11*, 2887.

[196] I. Fedin, D. V. Talapin, *Journal of the American Chemical Society* **2014**, *136*, 11228.

[197] J. de Roo, N. Yazdani, E. Drijvers, A. Lauria, J. Maes, J. S. Owen, I. van Driessche, M. Niederberger, V. Wood, J. C. Martins, I. Infante, Z. Hens, *Chemistry of Materials* **2018**, *30*, 5485.

[198] M. Hapka, M. Jaszuński, *Magnetic Resonance in Chemistry* **2020**, *58*, 245.

[199] F. A. L. Anet, A. J. R. Bourn, *Journal of the American Chemical Society* **1965**, *87*, 5250.

[200] X. Liu, M. Yu, H. Kim, M. Mameli, F. Stellacci, *Nature Communications* **2012**, *3*, 1182.

[201] L. D. Landau, E. M. Lifšic, *Quantum mechanics: Non-relativistic theory*, Elsevier, Singapore **2007**.

[202] V. F. Sears, *Neutron News* **2006**, *3*, 26.

[203] M. Bée, *Physica B: Condensed Matter* **1992**, *182*, 323.

[204] A. Einstein, *Annalen der Physik* **1905**, *322*, 549.

[205] M. von Smoluchowski, *Annalen der Physik* **1906**, *326*, 756.

[206] C. M. Wolf, L. Guio, S. C. Scheiwiller, R. P. O'Hara, C. K. Luscombe, L. D. Pozzo, *Macromolecules* **2021**, *54*, 2960.

[207] G. Porod, *Kolloid-Zeitschrift* **1951**, *124*, 83.

[208] A. Guinier, G. Fournet, C. B. Walker, K. L. Yudowitch, *Small-Angle Scattering of X-Rays*, John Wiley & Sons, New York **1955**.

[209] M. H. Koch, P. Vachette, D. I. Svergun, *Quarterly Reviews of Biophysics* **2003**, *36*, 147.

[210] I. Breßler, J. Kohlbrecher, A. F. Thünemann, *Journal of Applied Crystallography* **2015**, *48*, 1587.

[211] L. S. Ornstein, F. Zernike, *Koninklijke Nederlandse Akademie van Wetenschappen Amsterdam Proceeding of Akademic Science* **1914**, *17*, 793.

[212] R. Nayuk, K. Huber, *Zeitschrift für Physikalische Chemie* **2012**, *226*, 837.

[213] J. S. Pedersen, *Advances in Colloid and Interface Science* **1997**, *70*, 171.

[214] B. Sjöberg, *Journal of Applied Crystallography* **1999**, *32*, 917.

[215] E. Estrada, D. Avnir, *Journal of the American Chemical Society* **2003**, *125*, 4368.

[216] H. Zabrodsky, S. Peleg, D. Avnir, *Journal of the American Chemical Society* **1992**, *114*, 7843.

[217] G. Herzberg, *Infrared and Raman spectra of polyatomic molecules*, van Nostrand, New York **ca. 1987**.

[218] (i) P. R. Brown, D. Kim, R. R. Lunt, N. Zhao, M. G. Bawendi, J. C. Grossman, V. Bulović, *ACS Nano* **2014**, *8*, 5863.

(ii) L. Canil, T. Cramer, B. Fraboni, D. Ricciarelli, D. Meggiolaro, A. Singh, M. Liu, M. Rusu, C. M. Wolff, N. Phung, Q. Wang, D. Neher, T. Unold, P. Vivo, A. Gagliardi, F. De Angelis, A. Abate, *Energy & Environmental Science*, **2021**, 14, 1429.

[219] W. Nolting, *Grundkurs theoretische Physik: 3: Elektrodynamik*, Springer Spektrum, Berlin, Heidelberg **2013**.

[220] R. T. Tung, *Applied Physics Reviews* **2014**, *1*, 11304.

[221] H. Hasegawa, *Japanese Journal of Applied Physics* **1999**, *38*, 1098.

[222] M. Samadi Khoshkhoo, H. Peisert, T. Chassé, M. Scheele, *Organic Electronics* **2017**, *49*, 249.

[223] R. L. Anderson, *IBM Journal of Research & Development* **1960**, *4*, 283.

[224] J. Tersoff, *Physical reviews B, Condensed matter* **1984**, *30*, 4874.

[225] M. Scheele, *Bunsen Magazin* **2020**, *3*, 57.

[226] H. Li, Z. Wu, T. Zhou, A. Sellinger, M. T. Lusk, *Energy & Environmental Science* **2014**, *7*, 1023.

[227] S. R. Yost, E. Hontz, S. Yeganeh, T. van Voorhis, *Journal of Physical Chemistry C* **2012**, *116*, 17369.

[228] V. Coropceanu, J. Cornil, D. A. da Silva Filho, Y. Olivier, R. Silbey, J.-L. Brédas, *Chemical Reviews* **2007**, *107*, 926.

[229] W. Brütting, C. Adachi, et. al. (Eds.), *Physics of organic semiconductors*, Wiley-VCH, Weinheim **2012**.

[230] H. Hu, T. Salim, B. Chen, Y. M. Lam, *Scientific Reports* **2016**, *6*, 33546.

[231] A. Kurzmann, A. Ludwig, A. D. Wieck, A. Lorke, M. Geller, *Nano Letters* **2016**, *16*, 3367.

[232] M. J. Jurow, T. Lampe, E. Penzo, J. Kang, M. A. Koc, T. Zechel, Z. Nett, M. Brady, L.-W. Wang, A. P. Alivisatos, S. Cabrini, W. Brütting, Y. Liu, *Nano Letters* **2017**, *17*, 4534.

[233] T. Morgenstern, C. Lampe, T. Naujoks, M. Jurow, Y. Liu, A. S. Urban, W. Brütting, *Journal of Luminescence* **2020**, *220*, 116939.

[234] H. Wu, J. Qiu, J. Wang, Y. Wen, Q. Wang, Z. Long, D. Zhou, Y. Yang, D. Wang, *Inorganic Chemistry Frontiers* **2021**, *8*, 658.

[235] T. Wu, J. Li, Y. Zou, H. Xu, K. Wen, S. Wan, S. Bai, T. Song, J. A. McLeod, S. Duhm, F. Gao, B. Sun, *Angewandte Chemie (International ed. in English)* **2020**, *59*, 4099.

[236] H. H. Ku, *Journal of Research of the National Bureau of Standards, Section C: Engineering and Instrumentation* **1966**, *70C*, 263.

[237] S. Toso, D. Baranov, D. Altamura, F. Scattarella, J. Dahl, X. Wang, S. Marras, A. P. Alivisatos, A. Singer, C. Giannini, L. Manna, *ACS Nano* **2021**, *15*, 6243.

[238] X. Ye, J. Chen, M. Eric Irrgang, M. Engel, A. Dong, S. C. Glotzer, C. B. Murray, *Nature Materials* **2017**, *16*, 214.

[239] N. Goubet, M. P. Pileni, *Journal of Physical Chemistry Letters* **2011**, *2*, 1024.

[240] M. Cargnello, A. C. Johnston-Peck, B. T. Diroll, E. Wong, B. Datta, D. Damodhar, V. V. T. Doan-Nguyen, A. A. Herzing, C. R. Kagan, C. B. Murray, *Nature* **2015**, *524*, 450.

[241] A. Dreyer, A. Feld, A. Kornowski, E. D. Yilmaz, H. Noei, A. Meyer, T. Krekeler, C. Jiao, A. Stierle, V. Abetz, H. Weller, G. A. Schneider, *Nature Materials* **2016**, *15*, 522.

[242] F. Fetzer, A. Maier, M. Hodas, O. Geladari, K. Braun, A. J. Meixner, F. Schreiber, A. Schnepf, M. Scheele, *Nature Communications* **2020**, *11*, 6188.

[243] N. Yazdani, M. Jansen, D. Bozyigit, W. M. M. Lin, S. Volk, O. Yarema, M. Yarema, F. Juranyi, S. D. Huber, V. Wood, *Nature Communications* **2019**, *10*, 4236.

[244] Y. Tong, E.-P. Yao, A. Manzi, E. Bladt, K. Wang, M. Döblinger, S. Bals, P. Müller-Buschbaum, A. S. Urban, L. Polavarapu, J. Feldmann, *Advanced Materials* **2018**, e1801117.

[245] I. Cherniukh, G. Rainò, T. Stöferle, M. Burian, A. Travesset, D. Naumenko, H. Amenitsch, R. Erni, R. F. Mahrt, M. I. Bodnarchuk, M. V. Kovalenko, *Nature* **2021**, *593*, 535.

[246] R. Hoffmann, *Angewandte Chemie (International ed. in English)* **2013**, *52*, 93.

[247] G. A. Somorjai, Y. Li, *Introduction to Surface Chemistry and Catalysis*, Wiley, Hoboken, NJ **2010**.

[248] C. Kastl, R. J. Koch, C. T. Chen, J. Eichhorn, S. Ulstrup, A. Bostwick, C. Jozwiak, T. R. Kuykendall, N. J. Borys, F. M. Toma, S. Aloni, A. Weber-Bargioni, E. Rotenberg, A. M. Schwartzberg, *ACS Nano* **2019**, *13*, 1284.

[249] H. Y. Jeong, Y. Jin, S. J. Yun, J. Zhao, J. Baik, D. H. Keum, H. S. Lee, Y. H. Lee, *Advanced Materials* **2017**, *29*.

[250] H. R. Gutiérrez, N. Perea-López, A. L. Elías, A. Berkdemir, B. Wang, R. Lv, F. López-Urías, V. H. Crespi, H. Terrones, M. Terrones, *Nano Letters* **2013**, *13*, 3447.

[251] M. S. Kim, S. J. Yun, Y. Lee, C. Seo, G. H. Han, K. K. Kim, Y. H. Lee, J. Kim, *ACS Nano* **2016**, *10*, 2399.

[252] M. R. Rosenberger, H.-J. Chuang, K. M. McCreary, C. H. Li, B. T. Jonker, *ACS Nano* **2018**, *12*, 1793.

[253] H. Ding, Y. Dong, S. Li, N. Pan, X. Wang, *Optics express* **2018**, *26*, 7797.

[254] D.-D. Ren, J.-K. Qin, Y. Li, P. Miao, Z.-Y. Sun, P. Xu, L. Zhen, C.-Y. Xu, *Optical Materials* **2018**, *80*, 203.

[255] J. G. Bohnet, Z. Chen, J. M. Weiner, D. Meiser, M. J. Holland, J. K. Thompson, *Nature* **2012**, *484*, 78.

[256] K. D. B. Higgins, S. C. Benjamin, T. M. Stace, G. J. Milburn, B. W. Lovett, E. M. Gauger, *Nature Communications* **2014**, *5*, 4705.

[257] F. Mattiotti, M. Kuno, F. Borgonovi, B. Jankó, G. L. Celardo, *Nano Letters* **2020**, *20*, 7382.

[258] F. Krieg, P. C. Sercel, M. Burian, H. Andrusiv, M. I. Bodnarchuk, T. Stöferle, R. F. Mahrt, D. Naumenko, H. Amenitsch, G. Rainò, M. V. Kovalenko, *ACS Central Science* **2021**, *7*, 135.

[259] S. Toso, D. Baranov, C. Giannini, S. Marras, L. Manna, *ACS Materials Letters* **2019**, *1*, 272.

[260] J. S. van der Burgt, J. J. Geuchies, B. van der Meer, H. Vanrompay, D. Zanaga, Y. Zhang, W. Albrecht, A. V. Petukhov, L. Filion, S. Bals, I. Swart, D. Vanmaekelbergh, *Journal of Physical Chemistry C* **2018**, *122*, 15706.

[261] N. Mukharamova, D. Lapkin, I. A. Zaluzhnyy, A. André, S. Lazarev, Y. Y. Kim, M. Sprung, R. P. Kurta, F. Schreiber, I. A. Vartanyants, M. Scheele, *Small* **2019**, *15*, e1904954.

[262] M. Zhang, Z. Zheng, Q. Fu, Z. Chen, J. He, S. Zhang, L. Yan, Y. Hu, W. Luo, *CrystEngComm* **2017**, *19*, 6797.

[263] A. Swarnkar, R. Chulliyil, V. K. Ravi, M. Irfanullah, A. Chowdhury, A. Nag, *Angewandte Chemie* **2015**, *127*, 15644.

[264] T. G. Liashenko, E. D. Cherotchenko, A. P. Pushkarev, V. Pakštas, A. Naujokaitis, S. A. Khubezhov, R. G. Polozkov, K. B. Agapev, A. A. Zakhidov, I. A. Shelykh, S. V. Makarov, *Physical Chemistry Chemical Physics PCCP* **2019**, *21*, 18930.

[265] M. Kapuscinski, M. Agthe, Z.-P. Lv, Y. Liu, M. Segad, L. Bergström, *ACS Nano* **2020**, *14*, 5337.

[266] H. M. van der Kooij, G. T. van de Kerkhof, J. Sprakel, *Soft Matter* **2016**, *12*, 2858.

[267] A. Leineweber, *Journal of Applied Crystallography* **2016**, *49*, 1632.

[268] D.-J. Xue, Y. Hou, S.-C. Liu, M. Wei, B. Chen, Z. Huang, Z. Li, B. Sun, A. H. Proppe, Y. Dong, M. I. Saidaminov, S. O. Kelley, J.-S. Hu, E. H. Sargent, *Nature Communications* **2020**, *11*, 1514.

[269] D. Baranov, S. Toso, M. Imran, L. Manna, *Journal of Physical Chemistry Letters* **2019**, *10*, 655.

[270] D. Baranov, A. Fieramosca, R. X. Yang, L. Polimeno, G. Lerario, S. Toso, C. Giansante, M. D. Giorgi, L. Z. Tan, D. Sanvitto, L. Manna, *ACS Nano* **2021**, *15*, 650.

[271] Y. Tang, L. Gomez, A. Lesage, E. Marino, T. E. Kodger, J.-M. Meijer, P. Kolpakov, J. Meng, K. Zheng, T. Gregorkiewicz, P. Schall, *Nano Letters* **2020**, *20*, 5997.

[272] C. Stavrakas, A. A. Zhumekenov, R. Brenes, M. Abdi-Jalebi, V. Bulović, O. M. Bakr, E. S. Barnard, S. D. Stranks, *Energy & Environmental Science* **2018**, *11*, 2846.

[273] D. W. deQuilettes, S. M. Vorpahl, S. D. Stranks, H. Nagaoka, G. E. Eperon, M. E. Ziffer, H. J. Snaith, D. S. Ginger, *Science* **2015**, *348*, 683.

[274] Y. Wang, Z. Tang, M. A. Correa-Duarte, I. Pastoriza-Santos, M. Giersig, N. A. Kotov, L. M. Liz-Marzán, *Journal of Physical Chemistry B* **2004**, *108*, 15461.

[275] P. Asbeck, *Journal of Applied Physics* **1977**, *48*, 820.

[276] Y. Fang, H. Wei, Q. Dong, J. Huang, *Nature Communications* **2017**, *8*, 14417.

[277] L. M. Pazos-Outón, M. Szumilo, R. Lamboll, J. M. Richter, M. Crespo-Quesada, M. Abdi-Jalebi, H. J. Beeson, M. Vrućinić, M. Alsari, H. J. Snaith, B. Ehrler, R. H. Friend, F. Deschler, *Science* **2016**, *351*, 1430.

[278] D. Lapkin, C. Kirsch, J. Hiller, D. Andrienko, D. Assalauova, K. Braun, J. Carnis, Y. Y. Kim, M. Mandal, A. Maier, A. J. Meixner, N. Mukharamova, M. Scheele, F. Schreiber, M. Sprung, J. Wahl, S. Westendorf, I. A. Zaluzhnyy, I. A. Vartanyants, *Nature Communications* **2022**, *13*, 892.

[279] J. Maes, L. Balcaen, E. Drijvers, Q. Zhao, J. de Roo, A. Vantomme, F. Vanhaecke, P. Geiregat, Z. Hens, *Journal of Physical Chemistry Letters* **2018**, *9*, 3093.

[280] S. Kalbfleisch, H. Neubauer, S. P. Krüger, M. Bartels, M. Osterhoff, D. D. Mai, K. Giewekemeyer, B. Hartmann, M. Sprung, T. Salditt, I. McNulty, C. Eyberger, B. Lai, in *The Göttingen Holography Endstation of Beamline P10 at PETRA III/DESY* (Eds.: S. Kalbfleisch, H. Neubauer, S. P. Krüger, et al.), AIP **2011**, p. 96.

[281] G.K. Williamson, W.H. Hall, *Acta Metallurgica* **1953**, *1*, 22.

[282] J. I. Langford, A. J. C. Wilson, *Journal of Applied Crystallography* **1978**, *11*, 102.

[283] T. D. Kühne, M. Iannuzzi, M. Del Ben, V. V. Rybkin, P. Seewald, F. Stein, T. Laino, R. Z. Khaliullin, O. Schütt, F. Schiffmann, D. Golze, J. Wilhelm, S. Chulkov, M. H. Bani-Hashemian, V. Weber, U. Borštnik, M. Taillefumier, A. S. Jakobovits, A. Lazzaro, H. Pabst, T. Müller, R. Schade, M. Guidon, S. Andermatt, N. Holmberg, G. K. Schenter, A. Hehn, A.

Bussy, F. Belleflamme, G. Tabacchi, A. Glöß, M. Lass, I. Bethune, C. J. Mundy, C. Plessl, M. Watkins, J. VandeVondele, M. Krack, J. Hutter, *The Journal of Chemical Physics* **2020**, *152*, 194103.

[284] Perdew, Burke, Ernzerhof, *Physical Review Letters* **1996**, *77*, 3865.

[285] G. Lippert, M. Parrinello, Hutter, Jurg, *Molecular Physics* **2010**, *92*, 477.

[286] J. VandeVondele, J. Hutter, *The Journal of Chemical Physics* **2007**, *127*, 114105.

[287] M. Krack, *Theoretical Chemistry Accounts* **2005**, *114*, 145.

[288] S. Grimme, J. Antony, S. Ehrlich, H. Krieg, *The Journal of Chemical Physics* **2010**, *132*, 154104.

[289] S. ten Brinck, I. Infante, *ACS Energy Letters* **2016**, *1*, 1266.

[290] L. Genovese, T. Deutsch, A. Neelov, S. Goedecker, G. Beylkin, *The Journal of Chemical Physics* **2006**, *125*, 74105.

[291] E. Metwalli, K. Götz, S. Lages, C. Bär, T. Zech, D. M. Noll, I. Schuldes, T. Schindler, A. Prihoda, H. Lang, J. Grasser, M. Jacques, L. Didier, A. Cyril, A. Martel, L. Porcar, T. Unruh, *Journal of Applied Crystallography* **2020**, *53*, 722.

[292] E. Metwalli, K. Götz, T. Zech, C. Bär, I. Schuldes, A. Martel, L. Porcar, T. Unruh, *Applied Sciences* **2021**, *11*, 5925.

[293] K. Hills-Kimball, H. Yang, T. Cai, J. Wang, O. Chen, *Advanced science* **2021**, *8*, 2100214.

[294] F. Krieg, S. T. Ochsenbein, S. Yakunin, S. ten Brinck, P. Aellen, A. Süess, B. Clerc, D. Guggisberg, O. Nazarenko, Y. Shynkarenko, S. Kumar, C.-J. Shih, I. Infante, M. V. Kovalenko, *ACS Energy Letters* **2018**, *3*, 641.

[295] H. Wang, X. Zhang, N. Sui, Y. Hu, V. L. Colvin, W. W. Yu, Y. Zhang, *ACS Applied Materials & Interfaces* **2020**, *12*, 11769.

[296] J. Wahl, M. Engelmayer, M. Mandal, T. Naujoks, P. Haizmann, A. Maier, H. Peisert, D. Andrienko, W. Brütting, M. Scheele, *Advanced Optical Materials* **2021**, 10, 2101945.

[297] L. Zhao, Y.-W. Yeh, N. L. Tran, F. Wu, Z. Xiao, R. A. Kerner, Y. L. Lin, G. D. Scholes, N. Yao, B. P. Rand, *ACS Nano* **2017**, *11*, 3957.

[298] Y. Tan, Y. Zou, L. Wu, Q. Huang, Di Yang, M. Chen, M. Ban, C. Wu, T. Wu, S. Bai, T. Song, Q. Zhang, B. Sun, *ACS Applied Materials & Interfaces* **2018**, *10*, 3784.

[299] (i) J. Wahl, P. Haizmann, C. Kirsch, R. Frecot, N. Mukharamova, D. Assalauova, Y. Y. Kim, I. Zaluzhnyy, T. Chassé, I. A. Vartanyants, H. Peisert, M. Scheele, *Impact of the Ligand Shell on Structural Changes and Decomposition of All-Inorganic Mixed-Halide Perovskite (CsPbX3) Nanocrystals under X-Ray Illumination*. *ArXiv Preprint:* http://arxiv.org/pdf/2112.10004v1.

(ii) J. Wahl, P. Haizmann, C. Kirsch, R. Frecot, N. Mukharamova, D. Assalauova, Y. Y. Kim, I. Zaluzhnyy, T. Chassé, I. A. Vartanyants, H. Peisert, M. Scheele, *Physical Chemistry Chemical Physics* **2022**, (DOI: https://doi.org/10.1039/D2CP00546H)

[300] R. Grisorio, M. E. Di Clemente, E. Fanizza, I. Allegretta, D. Altamura, M. Striccoli, R. Terzano, C. Giannini, M. Irimia-Vladu, G. P. Suranna, *Nanoscale* **2019**, *11*, 986.

[301] G. L. Hura, A. L. Menon, M. Hammel, R. P. Rambo, F. L. Poole, S. E. Tsutakawa, F. E. Jenney, S. Classen, K. A. Frankel, R. C. Hopkins, S.-J. Yang, J. W. Scott, B. D. Dillard, M. W. W. Adams, J. A. Tainer, *Nature Methods* **2009**, *6*, 606.

[302] A. Guinier, G. Fournet, *Small-Angle Scattering of X-Rays*, John Wiley and Sons, New York **1955**.

[303] P. H. Elworthy, *Journal of the Chemical Society* **1959**, 1951.

[304] L. S. Ornstein, F. Zernike, *Proceedings of the Royal Netherlands Academy of Arts and Sciences* **1914**, *17*, 793.

[305] C. M. Kok, A. Rudin, *Die Makromolekulare Chemie, Rapid Communications* **1981**, *2*, 655.

[306] P. Mittelbach, G. Porod, *Acta Physica Austriaca* **1961**, 185.

[307] L. Onsager, *Annals of the New York Academy of Sciences* **1949**, *51*, 627.

[308] I. Artaki, J. Jonas, *The Journal of Chemical Physics* **1985**, *82*, 3360.

[309] R. Evans, Z. Deng, A. K. Rogerson, A. S. McLachlan, J. J. Richards, M. Nilsson, G. A. Morris, *Angewandte Chemie (International ed. in English)* **2013**, *52*, 3199.

[310] D. J. Wilbur, J. Jonas, *The Journal of Chemical Physics* **1975**, *62*, 2800.

[311] Y. Hassan, O. J. Ashton, J. H. Park, G. Li, N. Sakai, B. Wenger, A.-A. Haghighirad, N. K. Noel, M. H. Song, B. R. Lee, R. H. Friend, H. J. Snaith, *Journal of the American Chemical Society* **2019**, *141*, 1269.

[312] L. Cao, X. Liu, Y. Li, X. Li, L. Du, S. Chen, S. Zhao, C. Wang, *Frontiers of Physics* **2021**, *16*, 312.

[313] K. Kumar, J. Hiller, M. Bender, S. Nosrati, Q. Liu, M. Edelmann, S. Maier, T. Rammler, F. Wackenhut, A. J. Meixner, K. Braun, U. H. F. Bunz, M. Scheele, *ACS nano* **2021**, *15*, 480.

[314] X. Feng, Y. Huan, C. Zheng, C. Tan, H. Meng, B. Liu, D. Gao, W. Huang, *Organic Electronics* **2020**, *77*, 105522.

[315] K. Gkini, N. Balis, M. Papadakis, A. Verykios, M.-C. Skoulikidou, C. Drivas, S. Kennou, M. Golomb, A. Walsh, A. G. Coutsolelos, M. Vasilopoulou, P. Falaras, *ACS Applied Energy Materials* **2020**, *3*, 7353.

[316] P. Hui, *Chinese Physics Letters* **2004**, *21*, 160.

[317] K. Zheng, Q. Zhu, M. Abdellah, M. E. Messing, W. Zhang, A. Generalov, Y. Niu, L. Ribaud, S. E. Canton, T. Pullerits, *Journal of Physical Chemistry Letters* **2015**, *6*, 2969.

[318] A. Harriman, *Journal of the Chemical Socitey, Faraday Transactions 1* **1980**, *76*, 1978.

[319] J. Karolczak, D. Kowalska, A. Lukaszewicz, A. Maciejewski, R. P. Steer, *Journal of Physical Chemistry A* **2004**, *108*, 4570.

[320] J.-P. Strachan, S. Gentemann, J. Seth, W. A. Kalsbeck, J. S. Lindsey, D. Holten, D. F. Bocian, *Journal of the American Chemical Society* **1997**, *119*, 11191.

[321] Y.-C. Zhao, W.-K. Zhou, X. Zhou, K.-H. Liu, D.-P. Yu, Q. Zhao, *Light, Science & Applications* **2017**, *6*, e16243.

[322] A. Senocrate, J. Maier, *Journal of the American Chemical Society* **2019**, *141*, 8382.

[323] B. Tang, L. J. Ruan, C. Qin, A. Shu, H. He, Y. Ma, *Advanced Optical Materials* **2020**, *8*, 2000498.

[324] P. Cottingham, R. L. Brutchey, *Chemical Communications* **2016**, *52*, 5246.

[325] F. Neese, *WIREs Computational Molecular Science* **2012**, *2*, 73.

[326] S. Mariotti, O. S. Hutter, L. J. Phillips, P. J. Yates, B. Kundu, K. Durose, *ACS Applied Materials & Interfaces* **2018**, *10*, 3750.

[327] N. Prodanović, N. Vukmirović, Z. Ikonić, P. Harrison, D. Indjin, *Journal of Physical Chemistry Letters* **2014**, *5*, 1335.

[328] A. C. Sharma, *Journal of Applied Physics* **2006**, *100*, 84301.

[329] C.-O. Hwang, M. Mascagni, *Journal of Applied Physics* **2004**, *95*, 3798.

[330] C. Wolf, T.-W. Lee, *Materials Today Energy* **2018**, *7*, 199.

[331] H. Zhang, E. Debroye, J. A. Steele, M. B. J. Roeffaers, J. Hofkens, H. I. Wang, M. Bonn, *ACS Energy Letters* **2021**, *6*, 568.

[332] L. Chouhan, S. Ghimire, C. Subrahmanyam, T. Miyasaka, V. Biju, *Chemical Society Reviews* **2020**, *49*, 2869.

[333] Q. Chen, J. Wu, X. Ou, B. Huang, J. Almutlaq, A. A. Zhumekenov, X. Guan, S. Han, L. Liang, Z. Yi, J. Li, X. Xie, Y. Wang, Y. Li, D. Fan, D. B. L. Teh, A. H. All, O. F. Mohammed, O. M. Bakr, T. Wu, M. Bettinelli, H. Yang, W. Huang, X. Liu, *Nature* **2018**, *561*, 88.

[334] F. Zhou, Z. Li, W. Lan, Q. Wang, L. Ding, Z. Jin, *Small Methods* **2020**, *4*, 2000506.

[335] Y. Zhou, J. Chen, O. M. Bakr, O. F. Mohammed, *ACS Energy Letters* **2021**, *6*, 739.

[336] A. Xie, C. Hettiarachchi, F. Maddalena, M. E. Witkowski, M. Makowski, W. Drozdowski, A. Arramel, A. T. S. Wee, S. V. Springham, P. Q. Vuong, H. J. Kim, C. Dujardin, P. Coquet, M. D. Birowosuto, C. Dang, *Communications Materials* **2020**, *1*, 444.

[337] S. Kishimoto, K. Shibuya, F. Nishikido, M. Koshimizu, R. Haruki, Y. Yoda, *Applied Physics Letters* **2008**, *93*, 261901.

[338] J. Endres, M. Kulbak, L. Zhao, B. P. Rand, D. Cahen, G. Hodes, A. Kahn, *Journal of Applied Physics* **2017**, *121*, 35304.

[339] S. Colella, M. Todaro, S. Masi, A. Listorti, D. Altamura, R. Caliandro, C. Giannini, E. Carignani, M. Geppi, D. Meggiolaro, G. Buscarino, F. D. Angelis, A. Rizzo, *ACS Energy Letters* **2018**, *3*, 1840.

[340] A. F. Akbulatov, L. A. Frolova, N. N. Dremova, I. Zhidkov, V. M. Martynenko, S. A. Tsarev, S. Y. Luchkin, E. Z. Kurmaev, S. M. Aldoshin, K. J. Stevenson, P. A. Troshin, *Journal of Physical Chemistry Letters* **2020**, *11*, 333.

[341] L. A. Frolova, Q. Chang, S. Y. Luchkin, D. Zhao, A. F. Akbulatov, N. N. Dremova, A. V. Ivanov, E. E. M. Chia, K. J. Stevenson, P. A. Troshin, *Journal of Materials Chemistry C* **2019**, *7*, 5314.

[342] R. E. Beal, D. J. Slotcavage, T. Leijtens, A. R. Bowring, R. A. Belisle, W. H. Nguyen, G. F. Burkhard, E. T. Hoke, M. D. McGehee, *Journal of Physical Chemistry Letters* **2016**, *7*, 746.

[343] S. Tao, I. Schmidt, G. Brocks, J. Jiang, I. Tranca, K. Meerholz, S. Olthof, *Nature Communications* **2019**, *10*, 2560.

[344] D. R. Baer, K. Artyushkova, H. Cohen, C. D. Easton, M. Engelhard, T. R. Gengenbach, G. Greczynski, P. Mack, D. J. Morgan, A. Roberts, *Journal of Vacuum Science & Technology A* **2020**, *38*, 31204.

[345] J. Cazaux, *Journal of Electron Spectroscopy and Related Phenomena* **2000**, *113*, 15.

[346] P. S. Mathew, G. F. Samu, C. Janáky, P. V. Kamat, *ACS Energy Letters* **2020**, *5*, 1872.

[347] R. A. Evarestov, E. A. Kotomin, A. Senocrate, R. K. Kremer, J. Maier, *Physical Chemistry Chemical Physics PCCP* **2020**, *22*, 3914.

[348] D. Cortecchia, J. Yin, A. Bruno, S.-Z. A. Lo, G. G. Gurzadyan, S. Mhaisalkar, J.-L. Brédas, C. Soci, *Journal of Materials Chemistry C* **2017**, *5*, 2771.

[349] I. Du Fossé, S. Lal, A. N. Hossaini, I. Infante, A. J. Houtepen, *Journal of Physical Chemistry C* **2021**, *125*, 23968.

[350] J. J. Yeh, I. Lindau, *Atomic Data and Nuclear Data Tables* **1985**, *32*, 1.

[351] R. Hesse, M. Weiß, R. Szargan, P. Streubel, R. Denecke, *Journal of Electron Spectroscopy and Related Phenomena* **2013**, *186*, 44.

[352] K. Harrison, L. B. Hazell, *Surface and Interface Analysis* **1992**, *18*, 368.

List of publications

Peer-reviewed publications, which were written during the course of this thesis.

1. Dmitry Lapkin[*], Christopher Kirsch[*], Jonas Hiller[*], Denis Andrienko, Dameli Assalauova, Kai Braun, Jerome Carnis, Young Yong Kim, Mukunda Mandal, Andre Maier, Alfred J. Meixner, Nastasia Mukharamova, Marcus Scheele, Frank Schreiber, Michael Sprung, **Jan Wahl**, Sophia Westendorf, Ivan A. Zaluzhnyy, Ivan A. Vartanyants.
   ([*]: Equal contribution), Authors in alphabetical order.

   Spatially resolved fluorescence of caesium lead halide perovskite supercrystals reveals quasi-atomic behavior of nanocrystals
   Nature Communications 13, 892 (2022).
   DOI: 10.1038/s41467-022-28486-3

2. **Jan Wahl**, Manuel Engelmayer, Mukunda Mandal, Tassilo Naujoks, Philipp Haizmann, Andre Maier, Heiko Peisert, Denis Andrienko, Wolfgang Brütting, Marcus Scheele

   Porphyrin-functionalization of $CsPbBrI_2/SiO_2$ core-shell nanocrystals enhances the stability and efficiency in electroluminescent devices.
   Advanced Optical Materials 2022, 10, 2101945.
   DOI: 10.1002/adom.202101945

3. **Jan Wahl***, Philipp Haizmann*, Christopher Kirsch, Rene Frecot, Nastasia Mukharamova, Dameli Assalauova, Young Yong Kim, Ivan Zaluzhnyy, Thomas Chassé, Ivan A. Vartanyants, Heiko Peisert, Marcus Scheele
   ([*]: Equal contribution)

   Mitigating the Photodegradation of All-Inorganic Mixed-Halide Perovskite Nanocrystals by Ligand Exchange.
   Physical Chemistry Chemical Physics, 2022, 24, 10944–10951
   DOI: 10.1039/d2cp00546h

4. **Jan Wahl**, Ivan Zaluzhnyy, Christian Beck, Olga Matsarskaia, Lionel Porcar, Ezzeldin Metwalli, Frank Schreiber, Marcus Scheele, Tilo Seydel

   Quasielastic Neutron and Small Angle Scattering Reveals Highly Dynamic Surface Equilibrium on L-α-Lecithin Functionalized $CsPbBr_3$ Nanocrystals.
   To be submitted to the *Journal of Physical Chemistry Letters*.

5. Tassilo Naujoks, Roshini Jayabalan, Christopher Kirsch, Fengshuo Zu, Mukunda Mandal, **Jan Wahl**, Martin Waibel, Andreas Opitz, Norbert Koch, Denis Andrienko, Marcus Scheele, and Wolfgang Brütting

   Quantum Efficiency Enhancement of Lead-Halide Perovskite Nanocrystal LEDs by Organic Lithium Salt Treatment.
   ACS Applied Materials & Interfaces 2022, 14, 25, 28985–28996.
   DOI: 10.1021/acsami.2c04018

Other Scholarly Contributions

Conference Talks

1. **Jan Wahl**: “Electroluminescent perovskite nanocrystals – From tailor-made assemblies to opto-electronic properties”
   DFG SPP 2196 Workshop (Potsdam)
   01.03.2021

2. **Jan Wahl:** “The Devil is in the Details: Tailoring the Surface Chemistry of Perovskite Nanocrystals for Novel Optoelectronic Devices”
   NanoGe Spring Meeting (NSM) 2022
   09.03.2022

Supervision and Practical Courses

1. Frech, Philipp: „Gekoppelte organisch-anorganische Nanostrukturen: Elektrische und optische Eigenschaften InP basierter Quantenpunkte gekoppelt mit Metall-Phthalocyaninderivaten“ Bachelor thesis (2018)

2. Clemens Weig: “Enhancing Green Light Emitting Perovskite Quantum Dots in Stability”
   Bachelor Thesis (2020)

3. Höll, Nico: „Synthesis and ligand exchange of mixed methylammonium lead halide perocskite nanocrystals”
   Bachelor Thesis (2021)

4. Practical course PCP2 at the University of Tuebingen, Experiment: “Fluorescence”
   Lab course (2019-2022)

Declaration of Contribution

The following list describes the contributions to the papers discussed in this thesis.

Publication 1: Spatially resolved fluorescence of caesium lead halide perovskite supercrystals reveals quasi-atomic behavior of nanocrystals.

I synthesized and characterized samples for the measurements conducted at the DESY P10 beamline. The characterization mainly involved the determination of the size distribution, optical properties (absorption and photoluminescence), and structure analysis. The self-assembly into superlattices and corresponding characterization was carried out partly by me, including optical microscopy and sample preparation for scanning electron microscopy. Additionally, I synthesized multiple beamline samples and prepared them for shipping to the synchrotron.

Total estimated contribution: ~10 %

Publication 2: Porphyrin-functionalization of $CsPbBrI_2/SiO_2$ core-shell nanocrystals enhances the stability and efficiency in electroluminescent devices.

For this work I carried out the synthesis of the nanocrystals and performed the ligand exchange. Most preparative and analytical steps were carried out by me, including the optical, electrical, and structural measurements. The scientific idea, *i.e.*, using this specific ligand and conducting the published experiment was developed for the most part by me. I additionally prepared the samples for measurements, which could not be conducted in our lab, like SEM, NMR, and device measurements. I carried out the analysis of most experimental data and wrote the manuscript.

Total estimated contribution: ~90 %

Publication 3: Mitigating the Photodegradation of All-Inorganic Mixed-Halide Perovskite Nanocrystals by Ligand Exchange.

Herein, I prepared all samples from synthesizing the NCs as well as performing the ligand exchange. I prepared most of the thin films which were subsequently measured. The idea to perform these measurements was developed by me and the link between SAXS/WAXS and XPS data was discovered by me. I wrote the manuscript and analyzed the experimental data.

Total estimated contribution: ~65-70 %

Publication 4: Quasielastic Neutron and Small Angle Scattering Reveals Highly Dynamic Surface Equilibrium on L-α-Lecithin Functionalized $CsPbBr_3$ Nanocrystals.

For this publication I prepared the NC samples, including synthesis and characterization. The sample containers were prepared by me and subsequently shipped to the ILL, Grenoble. The theoretical model to describe the experimental findings from QENS and the link to NMR was develop by me. I am the author of the manuscript. I created the model for the SANS and SAXS measurements and performed the fitting procedure.

Total estimated contribution: ~70-75 %

Acknowledgments

During my PhD studies many people contributed to the presented results and without their help and support this project would have been impossible, and I want to thank all of them for making this possible.

First and foremost, I would like to express my deep gratitude to Prof. Dr. Marcus Scheele for providing me the possibility to perform this work in his group. The continuous support, scientifically and financially, as well as the vivid discussions during the project were extremely valuable. Despite the raging pandemic and more difficult communication, it was always possible to reach out, a fact that cannot be taken for granted. The continuous guidance and useful critique enabled me to find novel approaches to solving the difficulties which occurred whilst working on this thesis. I am especially thankful for the degree of freedom given to me as a student, this way I was able to develop scientifically as well as personally.

I want to thank my secondary supervisor Prof. Dr. Alfred J. Meixner for his support and the possibility to work with his students on the optical setups. Great appreciation belongs to Prof. Dr. Reinhold Fink for being the second reviewer of this thesis and being part of the board of examiners. Also, I want to thank Prof. Dr. Heiko Peisert and Prof. Dr. Thomas Chassé for their help with the XPS and UPS measurements. Thank you for enabling the access to the instruments and especially Heiko Peisert for very interesting and enlightening discussion on this topic. Additionally, I want to express my gratitude to Heiko Peisert for being part of the board of examiners.

Furthermore, I would like to thank my colleagues, Christopher Kirsch, and Philipp Haizmann, who were working with me through this exciting project. Without the discussions and vital exchange of information this dissertation would not have been possible. Not only during the working hours were we engaged in lively discussion, either of academic or non-academic nature. Thank you to Christopher Kirsch for proofreading this thesis. I want to express my gratitude towards Dr. Andre Maier for his outstanding work with the SEM images and always being enthusiastic about helping with these experiments. Additionally, I want to thank Andre Maier for the time during our studies here in Tübingen, which we started at the same time, and it was always an immense pleasure on and off campus. I especially want to thank Dr. Kai Braun for his help with the optical setups for temperature-dependent photoluminescence measurements and helpful insights on the technological setup. Thank you to all other members of our group, who were always supporting me with constructive discussions, ideas, and experiments: Kai Wurst, Christine Schedel, Philipp Frech, Theresa Hettinger, Dr. Björn Märker, Dr. Michelle Weber, Fabian Strauss, Sophia Westendorf, Dr. Krishan Kumar, Patrick Michel, and Jonas Hiller. It was an outstanding pleasure working with you. Also, I want to thank Dr. Ivan Zaluzhnyy and Prof. Dr. Frank Schreiber for their help with the scattering experiments, sample

preparation and worthwhile discussions on scattering and fitting of experimental data. Many thanks to Prof. Dr. Frank Schreiber for being part of the board of examiners.

Without the partners from Augsburg, Tassilo Naujoks, Manuel Engelmayer, Roshini Jayabalan, and Prof. Dr. Wolfang Brütting, this work would not have been possible, and I am very thankful for this thriving collaboration and the outstanding input on optoelectronic devices. I want to thank our partners from the Max Planck institute in Mainz, Dr. Mukunda Mandal, and Prof. Dr. Denis Andrienko for performing the DFT calculations which were an essential part of this work and greatly facilitated the interpretation of the results. Deep appreciations belong to the group of Prof. Dr. Ivan Vartaniants for working with us at the DESY beamline and doing an outstanding job with the data analysis. Several aspects within this work would not be possible without this support. I want to thank Dr. Tilo Seydel, Dr. Christian Beck, and Dr. Olga Matsarsakaia for performing the QENS experiments at the ILL. I want to explicitly express my gratitude to Tilo Seydel for doing an outstanding work concerning the fitting models. Without the lively discussions and your ideas for the models, this part of the work would have been impossible. Generally, I want to thank all of the collaborators for the wonderful discussions which we had during the joint meetings and the harmonic working environment which led to remarkable results.

Thank you to my fellow students and friends who I had the pleasure to spend my time in Tübingen with. Especially Dr. Florian Fetzer and Simon Trzmiel for providing support whenever necessary, at the institute and in private. I want to thank both of them for excellently proofreading this work.

Lastly, I want to thank my whole family for always supporting me and giving me the possibility to pursue my passion in science and their patience and encouragement along the way.